SURFACE MODIFICATION OF A TITANIUM ALLOY VIA ELECTROSPRAYING FOR BIOMEDICAL ENGINEERING APPLICATIONS

A thesis submitted for the degree of

Doctor of Philosophy

By

Theresa Mirembe Sebbowa

Department of Mechanical Engineering
University College London
Torrington Place
London
WC1E 7JE

October 2013

Declaration

I, Theresa Mirembe Sebbowa, confirm that the work presented in this thesis is my own. Where information has been derived from other sources, I confirm that this has been indicated in the thesis.

Theresa Mirembe Sebbowa

Abstract

Hydroxyapatite (HA) coated titanium (Ti) based dental and orthopaedic implants are widely utilized owing to their bone-bonding capability. However, the longevity of such implants is restricted by poor HA-Ti interfacial adhesion. Thus bioinert materials such as titania (TiO_2) and zirconia (ZrO_2) have been incorporated within the HA film in order to address this shortcoming.

This research investigated the development of novel electrosprayed bioceramic composite films with enhanced bioactivity and mechanical properties. Sol-gel derived TiO_2 and ZrO_2 nano-particles were synthesized using a range of precursors and solvents whereas nano-sized HA was synthesized by precipitation. Composite suspensions with a range of TiO_2 :HA and ZrO_2 :HA compositions were prepared by mixing. The liquid physical properties such as electrical conductivity and surface tension were affected by suspension composition and this in turn influenced the electrospray process.

Film morphology was optimized by varying deposition parameters such as needle-to-substrate distance and suspension flow rate as well as post deposition annealing. The *in vitro* cellular response to the electrospray films was generally enhanced by post deposition annealing temperature which affected the wettability and film roughness. Furthermore, the cellular response was enhanced by the addition of HA within the TiO_2 or ZrO_2 films. However, the TiO_2/HA composites displayed higher bioactivity compared to the ZrO_2/HA composites. The scratch resistance was affected by materials composition and was in the order ZrO_2>TiO_2>HA. Consequently, ZrO_2/HA composite films yielded superior mechanical properties. However, composite films with a composition of 50 wt% TiO_2: 50wt% HA gave a good combination of bioactivity and mechanical integrity. The scratch resistance was further enhanced via the deposition of HA-based bi-layer and functionally graded films with a comparable *in vitro* response to the electrosprayed single phase HA films. A film with graded ZrO_2 and HA phases gave a good combination of bioactivity and mechanical integrity.

This research demonstrated that electrospraying is a promising method for the deposition of novel bioceramic composite films for dental and orthopedic applications. Moreover, enhancement of the bioactivity and mechanical properties of the electrosprayed bioceramic composite coatings could be achieved through the combination of HA and ZrO_2.

Publications and conference presentations

Publications

Sebbowa, T., Edirisinghe, M., Salih, V. and Huang, J., (2011), Effect of deposition parameters and post annealing deposition on the morphology and cellular response of electrosprayed TiO_2 films, Biofabrication, 4, Article 045001.

Sebbowa, T.M., Edirisinghe, M, Salih, V, Bao, T., Gao, J. and Huang, J Deposition of novel electrosprayed titania and hydroxyapatite composite films on titanium alloy for hard tissue implants (under preparation)

Sebbowa, T.M., Edirisinghe, M., Salih, V., Bao, T., Gao, J. and Huang, J. Comparison of electrosprayed titania/hydroxyapatite and zirconia/hydroxyapatite films (under preparation)

Conference presentations

Morphology control of electrosprayed TiO_2 films, Theresa Sebbowa, Mohan Edirisinghe and Jie Huang, Oral presentation given at the UK society for Biomaterials society (UKSB) 2010 at the University of Glasgow, Scotland, UK.

Acknowledgements

First and foremost, I would like to thank my supervisors Dr Jie Huang and Professor Mohan Edirisinghe for offering me the wonderful opportunity to further my education and improve my career prospects. Their patience, guidance, encouragement, support and extreme patience over the past few years have been very invaluable to me and are very much appreciated.

I would like to thank the Department of Mechanical Engineering at University College London for awarding me the DTA PhD studentship that enabled me to undertake this research.

My collaborators from the Eastman Dental Institute (UCL), Dr Vehid Salih and Dr Nicki Mordan are thanked for granting me access to their cell culture lab facilities and their useful advice throughout the course of my research at the dental institute. Dr Graham Palmer is also thanked for his assistance with surface roughness measurement, water contact angle measurement and Raman spectroscopy.

I would also like to thank Professor Yuqing Bao and Dr Jiming Gao at London Southbank University for granting me access to their Materials testing facilities.

I further extend my gratitude to Mr Kevin Reeves at the UCL institute of Archeology for his assistance with the scanning electron microscopes.

I would also like to thank my colleagues in the Biomaterials research group for their friendship and for making my experience as a research student more interesting. My close friends Yvonne, Gabrielle, Maria and Gloria are so gratefully acknowledged for reminding me there's life outside the lab and for their prayers, and constant support and kind words of encouragement.

Last but by no means least; I would like to express my utmost love and gratitude to my dear parents who have so lovingly supported me emotionally and financially every step of the way. I am especially grateful for your unwavering belief in me and your prayers and encouragement. I also thank my brothers for their support. Finally, I extend my gratitude to my husband Onyedikachukwu for putting up with me and caring for and supporting me as I completed my thesis.

To my three parents; Dad, Mom and Auntie Gladys who have loved, nurtured and supported me over the years, my siblings who have continuously encouraged me, and my husband Onyedikachuwu and our two boys, Preston and Gabriel who have been sharing me with my studies for as long as they have known me.

Table of contents

List of Tables

List of Figures

Abbreviations

ACP Amorphous calcium phosphate

ALP Alkaline phosphatase

C Cubic

CaO Calcium oxide

CaP Calcium phosphate

CGO Cerium gadolinium oxide

Co Cobalt

CTE Coefficient of thermal expansivity

DMEM Dulbecco's modified eagle medium

DMSO Dimethyl sulfoxide

ECM Extracellular matrix

EG Ethylene glycol

ErK Extracellular signal regulated kinase

EtOH Ethanol

FAK Focal adhesion kinase

FDA Food and drug administration

FGC Functionally graded coating

FN Fibronectin

FTIR Fourier transform infrared spectroscopy

HA Hydroxyapatite

HCl Hydrochloric acid

HF Hydrofluoric acid

HMDS Hexamethyldisalazane

HOB Human osteoblast

ISO International organization for standardisation

M Monoclinic

MgO Magnesium oxide

NaCl	Sodium chloride
NaOH	Sodium hydroxide
NiO	Nickel oxide
NiTi	Nickel titanium
OHA	Oxyhydroxyapatite
PrOH	Propanol
RGD	Ariginine glycine aspartic acid peptide
SBF	Simulated body fluid
SEM	Scanning electron microscopy
T	Tetragonal
Tcp	tissue culture plastic
TCP	Tricalcium phosphate
Ti	Titanium
TiO_2	Titanium dioxide
TiP	Titanium phosphate
TTCP	Tetracalcium phosphate
TTIP	Titanium isopropoxide
VN	Vitronectin
XRD	X-ray diffraction
YSZ	Yttria stabilized zirconia
ZIP	Zirconium propoxide
ZrO_2	Zirconia

Chapter 1 Introduction

1.1 Background

Titanium and Titanium alloys are widely used as implant materials in dental and orthopaedic applications due to their superior biocompatibility, corrosion resistance and mechanical properties compared to other metals (Myer, 2003, Liu *et al*, 2004 and Teoh, 2004). However, these materials are unable to form a direct bond with the surrounding hard tissue. In order to improve implant-tissue osseointegration, several methodologies have been employed to modify the Ti implant surface. In particular, improved implant performance has been obtained due to the application of bioceramic films onto the metal implant surface. Hydroxyapatite (HA) has received a significant amount of attention in the fields of orthopedics and dentistry due to its chemical and crystallographic similarity with the naturally existing calcium phosphate phase in bone which renders HA biocompatible. HA is also bioactive and has been shown to bond directly with bone tissue. Therefore, HA coated implants facilitate fast, firm and long-lasting fixation of implants and also prevent the leakage of metal ions into the bodily environment (De Groot, 1987, Furlong and Osborn, 1991, Sousa and Barbosa, 1996 and Aebli *et al*, 2003). However, such implants are prone to failure due to HA-metal delamination (Yang *et al*, 1995, and Yang *et al*, 2003).

Implant bioactivity and cytocompatiblity have also been reported due to the application of bioceramic films such as titania (TiO_2) and zirconia (ZrO_2) on the metal implant surface (Vandrovcova *et al*, 2012 and Zhang *et al*, 2012). TiO_2 and ZrO_2 have attracted attention owing to their chemical stability, excellent corrosion resistance and superior mechanical properties such as high fracture toughness, wear resistance and hardness (Liu *et al*, 2004). Moreover, TiO_2 and ZrO_2 films have demonstrated superior adhesion to metal substrates in comparison with HA. However, despite their ability to initiate the formation of bone-like apatite and enhance cell attachment and proliferation *in vitro*, TiO_2 and ZrO_2 coated implants are generally bioinert and do not show direct bonding with the surrounding hard tissue but are instead encapsulated by fibrous tissue *in vivo*.

Enhanced mechanical and biological properties have been reported as a result of synthesizing composite films based on bioactive HA and the mechanically superior bioinert ceramics (Kim *et al*, 2004 and Li *et al*, 2004). Composite bioceramic films are typically deposited using a variety of techniques which include thermal spraying, sputtering, sol-gel deposition, micro arc oxidation, electrolytic techniques and electron

beam deposition. Thermal spray techniques are the most widely documented and used. Despite benefits such as high deposition efficiency, thermal spraying techniques are associated with a number of shortcomings. For instance, these techniques involve high processing temperatures which could lead to the decomposition of HA in to highly resorbable oxyapatite (OHA), tricalcium phosphate (TCP) and tetracalcium phosphate (TTCP). Secondly, thermal spray techniques offer limited control over coating thickness and produce films in the 50-200 μm range and yet such a film thickness has been associated with poor mechanical properties (Cigadas *et al*, 1993 and Wang *et al*, 1993). Thermal spraying is also a line of sight process which limits its suitability in the coating of complex geometries. Hence the exploration of alternative coating deposition methods is necessary. Electrospraying has recently attracted attention in the field of biomedical engineering owing to its easy equipment set up and low cost compared to alternative film deposition methods.

Electrospraying refers to the process whereby tiny droplets are obtained from the electrically forced break up of a moving liquid (Grace and Marjnissen, 1994). During this process, a liquid is pumped through a metal nozzle which is connected to a power supply. A ground electrode is placed below the nozzle exit. The electric field created between the capillary exit and the ground electrode deforms the liquid at the nozzle exit into a jet or cone that subsequently disintegrates in to droplets (Jaworek and Krupa, 1999). The electrospray process is influenced by the physical properties of the liquid such as surface tension, viscosity, density, and electrical conductivity as well as the nozzle diameter, applied voltage and liquid volume flow rate. Electrospraying has been classified into a number of modes depending on the geometrical form of the liquid at the nozzle exit and the mechanism of jet disintegration (Cloupeau and Prunet-Foch, 1990 and Grace and Marjnissen, 1994). These include micro dripping, spindle, stable cone jet, multi jet, oscillating jet and the precession modes. However, the stable cone jet mode is the most desirable and widely used owing to its great stability and ability to produce near mono-disperse droplets of a few micrometers to sub-micrometer in size. In addition to being a simple and low-cost film deposition technique, electrospraying is also an ambient temperature processing method. Therefore this film deposition technique has been exploited in a wide range of industrial applications including agriculture, electronics and ink jet printing.

1.2 Aims and objectives

This research primarily sought to explore the application of electrospraying in the deposition of novel bioceramic composite films with enhanced bioactivity and mechanical properties. The first objective of this research was to investigate the deposition of uniform and crack-free single-phase bioceramic films. Sol-gel synthesis and wet precipitation were used to prepare TiO_2/ZrO_2 sols and HA suspensions respectively. The stable cone-jet electrospray mode was then obtained by varying the applied voltage and flow rate. Film morphology was optimized by investigating the influence of several key deposition parameters including sol or suspension concentration, volume flow rate, needle-to-substrate distance, precursor type, solvent type, spray time as well as the effect of post deposition annealing temperature.

Although the electrospray process has been used to deposit single-phase bioceramic films in the literature, no attempts have been made to produce composite bioceramic films using this technique. Therefore, the second objective of this research was to investigate the electrospray deposition of bioceramic composite films. A series of TiO_2/HA and ZrO_2/HA composite suspensions were prepared and the influence of suspension composition on the electrospray process and film deposition was investigated. The third objective of this research was to fabricate TiO_2/HA and ZrO_2/HA bi-layer and functionally graded films to further enhance the mechanical properties of the bioceramic coatings. These films were synthesized using the one and two component sols/suspensions utilized in previous work. The biocompatibility of the bioceramic films were subsequently compared in terms of bone-like apatite nucleation and *in vitro* cellular response whereas the mechanical properties of the films were evaluated in terms of scratch resistance.

1.3 Thesis content

Chapter 1 gives an overview of the main problem which is to enhance the bioactivity and mechanical properties of coated implants. The use of bioceramic films is justified, and the various film deposition techniques briefly discussed. This chapter also introduces electrospraying and provides a brief background of this film deposition technique. The aims and objectives of this research are then outlined, and an overview of the thesis contents is given.

Chapter 2 discusses the structure and properties of bone tissue and summarizes the various methodologies utilized in the replacement of diseased or damaged bone tissue. This chapter also details the use of coated metal implants and further highlights the

factors affecting the biological and mechanical performance of implant materials. The assessment of the biological and mechanical properties of implant materials is also briefly discussed. This chapter further describes electrospraying and outlines the factors affecting this process. Alternative film deposition methods are reviewed and compared with electrospraying.

Chapter 3 describes the experimental procedures carried out. This chapter details the preparation and characterization of the sols and suspensions and also describes the electrospray deposition of the bioceramic films. The film characterization techniques such as scanning electron microscopy (SEM), X-Ray diffraction and Raman spectroscopy are described. This chapter further discusses the techniques utilized in the assessment of the surface roughness and wettability of the bioceramic films and also details the *in vitro* characterization of the bioceramic films in terms of MG63 cellular response and soaking in simulated body fluid (SBF). The scratch testing technique is also discussed.

Chapter 4 investigates the electrospray deposition and characterization of TiO_2 films. TiO_2 nano-particles were prepared using sol-gel synthesis. The chemical composition and liquid physical properties of the TiO_2 sols were characterized. The effect of the liquid physical properties on the electrospray process was investigated. TiO_2 films with varying morphology were subsequently produced by varying the process parameters such as suspension concentration, needle to substrate distance, needle internal diameter, spraying time, and solvent carrier. The effect of annealing temperature and solvent type on the *in vitro* response and scratch resistance of the TiO_2 films was then assessed.

Chapter 5 discusses the electrospray deposition of ZrO_2 films. ZrO_2 sols were synthesized and characterized. The influence of the deposition parameters on the electrospray process and film morphology was investigated. The films were subsequently compared in terms of the *in vitro* cellular response and scratch resistance.

Chapter 6 describes the electrospray synthesis of two-phase bioceramic films A range of HA suspensions were initially prepared and characterized. Optimum electrospray conditions were obtained by investigating the effect of the various deposition parameters. Two phase suspensions with a range of TiO_2:HA and ZrO_2:HA composition were then prepared and characterized. The influence of suspension composition on the electrospray process was investigated prior to film deposition. Buffer layer films and functionally graded films were subsequently prepared using the

two phase suspensions. The effect of phase composition on the *in vitro* behavior and mechanical integrity of the films was then investigated.

Chapter 7 concludes the results obtained in the investigations carried out in chapter 4-6. Based on the findings from these investigations, several recommendations are made for the future work that could be undertaken in order to further exploit this interesting area of research.

Chapter 2 Literature review

The literature review provides a comprehensive discussion of the structure and properties of the hard tissues and also outlines the key developments in the field of dental and orthopedic treatment and replacement. This section further details the use of coated prostheses and introduces the concept of bi-layer films, composite films and functionally graded films. This chapter also discusses the various techniques utilized in the deposition of such films and discusses the use of electrospraying as a deposition method for bioceramic coatings. The key factors of this processing method are discussed together with the influencing parameters.

2.1 Bone structure and composition

The basic structural foundation of vertebrates is provided by the skeleton. The bones in the skeleton serve as an attachment of the muscles for body movement and provide support and protection for the vital organs. Bone tissue also houses the hematopoietic tissue of the bone marrow and acts as a source of minerals such as calcium and phosphate. Some specialized organs such as inner ear and teeth are also composed of mineralized tissue (Myer, 2003 and Shea and Miller, 2005).

2.1.1 Composition of bone

Bone tissue is composed of both organic and inorganic phases which are distributed within an extracellular matrix or ground substance. The organic phase constitutes about 30% by weight of bone and consists of 90-96% type I collagen fibers which impart high flexibility and toughness to the bone tissue. The bone mineral phase constitutes about 60 wt% of bone tissue and can be described as a calcium phosphate with an apatitic structure and a composition similar to hydroxyapatite (HA, $Ca_{10}(PO_4)_6(OH)_2$, Ca/P=1.67). However, biological apatites are calcium-deficient with a Ca/P ratios of 1.5-1.65, depending on their location within the body, and also contain carbonate (bone tissue) or fluoride (dental enamel). The bone mineral phase provides rigidity and strength to the bone tissue.

The bone matrix primarily consists of glycoproteins and proteoglycans which are highly anionic complexes with considerable ion binding capability and assist in various cellular support functions.The non-collagenous proteins in the bone matrix include osteocalcin,

osteonectin, osteopontin, plasma proteins and lipids. These play a critical role in skeletal growth, metabolism and turn-over.

Around 10 wt% of bone consists of water phase which fills the bone porosity such as the Haversian canals, lacunae, canaliculi and resorption cavities (enlargements of the Haversian canals). The water phase facilitates the diffusion of nutrients and contributes to the viscoelastic properties of the bone tissue (Simske *et al,* 1997).

2.1.2 Structure of bone

The structure of bone has been classified into a number of hierarchical levels as illustrated in **Figure 2.1** (Park, 1979). These include the ultrastructure, microstructure and macrostructure of bone. At the ultrastructural level, bone tissue is composed of apatite crystals in the form of slender needles with a length of 20-40 nm and a thickness of 1.5-3 nm. The needles are enmeshed within the collagen fibre matrix. This assembly forms structures referred to as fibrils.

The microstructure of bone comprises of fibrils arranged as stacked thin sheets called lamellae (3-7 μm thick) which contain unidirectional fibrils in alternating angles between layers (lamellar bone) or as a block of randomly oriented woven fibrils (woven bone). Lamellar bone is commonly found in adults whereas woven bone can be found in young children where rapid growth is required to occur as well as during the initial stages of fracture healing (Myer, 2003). The structure of cortical bone is mainly osteonal or haversian such that there are about 4 to 20 lamellae arranged concentrically around a central haversian canal. The haversian canal is a vascular channel about 50 μm in diameter that contains blood capillaries, nerves and bone cells. Its purpose is to provide the elements required for bone remodelling. Thus the structure containing the lamellae and the haversian canal is referred to as an osteon (Myer, 2003 and Teoh, 2004). Osteons typically have a diameter of about 200 μm and are 1-3 mm long. Cortical bone also contains Volkmann's canals which provide a radial flow path for the blood in the bone. These have the same diameter as the haversian canals.

Osteons are the main discrete unit of adult cortical bone and are constantly being broken down and replaced during bone remodelling. The outermost concentric lamella of the osteon is surrounded by a narrow zone called the cement line. The cement line is composed of calcified mucopolysaccharides with very little collagen. This region is 1-2 μm thick and is the weakest part of the bone, facilitating the dissipation of energy during crack propagation.

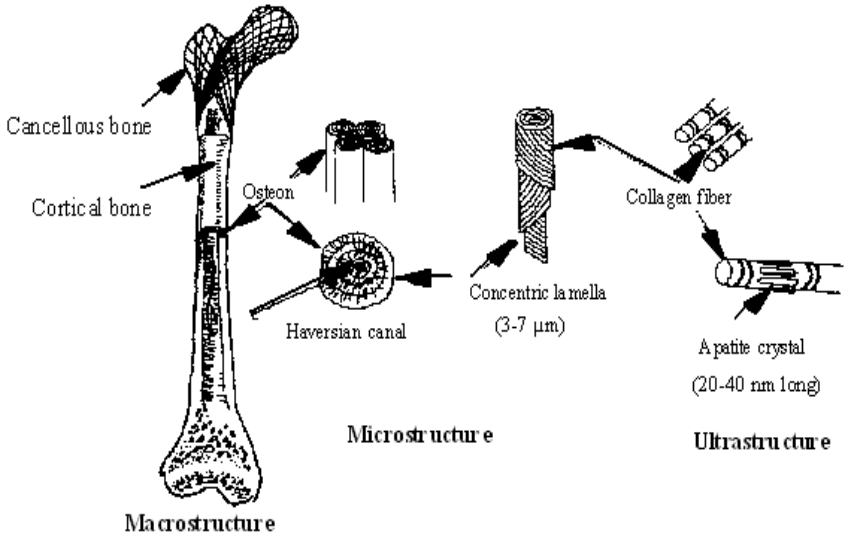

Figure 2.1 Organizational levels of bone showing the macro-, micro- and ultra structure (Park, 1979)

At the macroscopic level, 80-85% of bone tissue is composed of cortical bone with the rest being cancellous (trabecular) bone. Cortical (or compact) bone is a hard outer shell that forms a shaft around the marrow cavity of the cortex. It also surrounds the cancellous bone which it thereby supports and protects. Cortical bone is composed of tightly packed lamellar haversian or woven bone. Cancellous bone is located at the ends of the long bones and is a highly porous cellular solid. Cancellous bone is composed of lamellae arranged in less organised packets which form a network of rods and plates about 100-300 μm thick interspersed with large marrow spaces. The cancellous bone gradually changes into the cortical bone toward the middle of the bone. The epiphysis is located at the end of the bones and is covered with cartilage which provides a low friction surface for joint movement. The cartilage is continuous with the periosteum which is a fibrous sheath that covers the external surface of the bone.

Bone tissue contains four types of cells. These include the osteogenic cells, osteoblasts, osteocytes and osteoclasts. Osteogenic cells proliferate and develop into osteoblasts. Osteoblasts form a monolayer on the bone surfaces and are cuboid in morphology and mononuclear in nature. They are responsible for the deposition of new bone. They become osteocytes as they are gradually buried in the extracellular matrix they secrete. Bone formation occurs when the matrix secreted by the osteoblasts

becomes densely fibrous (osteoid). Calcium phosphate crystals are deposited in the osteoid turning it into bone matrix.

Osteocytes are mature bone cells and are embedded in an extracellular matrix. These cells are located within small ellipsoidal holes known as lacunae. The lacunae are found along the interfaces between the lamellae. Each individual osteocyte also has dendritic processes that extend from the cell through tiny channels known as canaliculi. These meet at cellular gap functions with the processes of neighbouring cells (Myer, 2003). Osteocytes maintain the bone matrix extracellular ion transport and maintain homeostasis via the release of calcium ions from the bone matrix when required. The density, patterning and size of the osteocytes vary according to the location and loading requirements of the bone.

Osteoclasts have great mobility over bone structures and their function is the resorption of extracellular matrix (Shea and Miller, 2005). Bone also consists of bone lining cells, fibrolasts and fibrocytes. The bone lining cells control the movement of ions between the bone tissue and the surrounding tissue whereas the fibroblasts and fibrocytes produce collagen.

2.1.3 Mechanical properties of bone

The compressive modulus of cortical bone is 17 GPa whereas that of cancellous bone is in the range 100-200 MPa (Cullinane and Salisbury, 2004). The tensile strength of cortical bone is estimated to be 130 MPa whereas that of cancellous bone is about 50 MPa. The Young's modulii of cortical and cancellous bone are 7-30 GPa and 7-25 GPa, respectively (Bonfield, 1988 and Rho *et al*, 1997). Bone is a highly anisotropic material whose mechanical properties vary depending on the direction of loading. For instance, the tensile strength of cortical bone in the longitudinal direction is about 133 MPa whereas it is 52 MPa for tangential loading. Similarly, the compressive stress is 200 MPa in the longitudinal direction and 130 MPa and 67 MPa for tangential and shear loading respectively (Black and Hastings, 1998). In general, bone is a relatively tough material and therefore has the ability to support the body.

2.1.4 Bone defects and injuries

At present there exists a large demand for biomedical implants for the correction and healing of skeletal defects and diseases. Globally, there is a growing number of patients requiring load-bearing hip, knee and dental implants as well as bone

replacement parts in the maxillar-mandibular area, the ossicular chain of the inner ear and alveolar ridge, and iliac crest augmentation. According to the UK National Health Service, 50,000 hip and 70,000 knee arthroplasties are carried out in Great Britain alone per annum. Hence total joint replacement is one of the most widely performed surgical procedures.

The great demand for biomedical prostheses has been attributed to a number of factors. Firstly, it is well known that hip and knee joints are subjected to a great amount of wear and tear during the average human lifetime. Moreover, recent years have seen an increase in life expectancy and obesity. This results in the eventual wear of the protective tissue lining of the acetabular cup of the hip joint which increases friction and subsequently gives rise to inflammation, pain and ultimately immobilisation (Heimann, 2006). It is also well established that the hard tissues tend to undergo a reduction in density and hence strength with a corresponding increase in age. This effect is more pronounced in females (Dattani, 2007). The loss in bone density has been ascribed to a combination of factors which include poor calcium dietary intake, ethnicity, excessive cigarette and alcohol consumption as well as premature menopause and low oestrogen levels in females (Kates *et al,* 2007). Furthermore, age related conditions of the hard tissues such as arthritis have also been found to cause joint pain and immobility. Equally, the number of younger patients requiring biomedical prostheses is rapidly rising owing to active lifestyles which involve damaging sporting activities that promote premature joint wear. Furthermore, these patients have been found to outlive the implant lifetime thereby necessitating revision surgery.

2.1.5 Current hard tissue treatment approaches

Currently, there are two approaches available for the treatment of diseased or damaged hard tissues and joints. These include transplantation and implantation (Sopyan *et al*, 2007). Transplantation involves the harvest of bone-grafts from either the patient (autografts) or from a donor (allografts) which are then transported to the host site. The use of bone-grafts offers a number of benefits; For example, they induce the formation of new bone and produce no adverse immunological response. However, there are several complications associated with the use of bone-grafts. For instance, autografts do not precisely duplicate the mechanical properties and shape of the bone to be replaced and require additional surgery for harvesting which causes more pain to the patient. Autografts are also associated with the risk of fracture, long lasting pain, nerve damage, possible infection and even morbidity at the donor site. Furthermore,

autografts are limited in availability. Allografts on the other hand carry the risk of exposing patients to the infection with diseases such as Hepatits B and HIV and are also the subject of ethical and religious concerns. Moreover, their storage is expensive and can result in the alteration of the mechanical properties and biological response of the implants (Suchanek and Yoshimura, 1998).

Implantation involves the replacement of the hard tissues using man-made materials (biomaterials). Biomaterials are defined as “systematically, pharmacologically inert substances designed for implantation within or incorporation with living systems” (Park, 2007). According to Hench (1991, 1998) no material implanted in living tissue remains inert. All materials elicit a response from living tissue. Therefore there are four types of tissue-implant response as summarized in **Table 2.1**.

Table 2.1 Types of tissue-implant response (Hench, 1998)

If the material is toxic, the surrounding tissue dies
If the material is non-toxic and biologically inactive (bioinert) a fibrous tissue of variable thickness forms
If the material is non-toxic and biologically active (bioactive), an interfacial bond forms
If the material is non-toxic and dissolves (resorbable), the surrounding material replaces it

Hence biomaterials can be classified as bioinert, bioactive or bioresorbable. Bioinert materials display minimal interaction with the surrounding host tissue and elicit the formation of fibrous tissue upon implantation. Bioactive materials have been described as materials that induce specific biological activity upon implantation in the human body. Bioactive materials are capable of inducing the formation of bone tissue around the implant and strongly integrate with the bone tissue (osseointegration). In orthopaedic and dental application bioactive materials induce bone-like apatite formation both *in vitro* and *in vivo (*Kokubo and Takadama, 2006). Bioresorbable materials are dissolved *in vivo* and replaced by the surrounding tissue. Compared to bone grafts, biomaterials offer a lower risk of disease transmission and infection. There is also a vast array of materials available for use as implant materials.

2.1.6 Implant selection criteria

In general, biomaterials are required to be biocompatible, bioactive, non-toxic and should not cause any inflammatory or allergic reactions. Biomaterials also need to be corrosion and wear resistant. Biocompatibilty is described as the “acceptance of an artificial implant by surrounding tissues and by the body as a whole” (Park and Lakes, 2007). For load-bearing orthopaedic and dental implants adequate mechanical properties are also an important prerequisite.

There are two prerequisites for successful implantation. These include rapid osseointegration and long term stability. Both processes are affected by the biocompatibility and bioactivity which are in turn dependent on the implant surface characteristics. The surface characteristics such as surface roughness, wettability, surface chemistry and surface charge affect the initial cellular response. The implant-tissue interfacial response is also affected by the tissue characteristics: age, type and health, blood circulation in the tissue and at the interface, motion at the interface, closeness of fit, as well as mechanical loading.

2.1.6.1 *In vitro* characterization using bone cells

The cell adhesion process involves a series of biochemical and mechanical interactions. It is well known that most cells in the human body are surrounded by and grow on a complex mixture of non-living material known as the extracellular matrix (ECM). In the case of the bone-derived cells, adherence and growth occur on an ECM comprised of protoglycans filled with calcium phosphate and proteins (90% collagen and elastin fibres and 10% adhesive glycoproteins including glue cells, fibronectin, vitronectin, laminin et cetera). Bone cells are classified as anchorage dependent cells inasmuch as they can only survive *in vitro* upon attaching to a surface. Thus cell proliferation and differentiation can only be attained if cell adhesion is achieved. Consequently, the initial cell-substrate interactions play a critical role during implant osseointegration.

Cell adhesion is initiated by the wetting of the substrate surface by the fluid (cell culture medium *in vitro* or interstitial fluids or blood *in vivo*). This results in the immediate adsorption of water and proteins onto the substrate surface. Consequently, the cells are able to sense the features of the ECM through this conditioning film. The cells initially attach to the conditioning film through physicochemical interactions such as ionic forces and Van Der Waal’s forces, and subsequently through the adsorbed cell

mediation proteins. The adsorbed proteins interact with the cell surface molecules known as the integrins.

Basically, the integrins are the cells surface receptors and are transmembrane molecules which act as an interface between the intracellular and extracellular compartments. On the intracellular side, the integrins interact with the molecules of the cytoskeleton and with the signalling molecules referred to as focal adhesions (**Figure 2.2**).

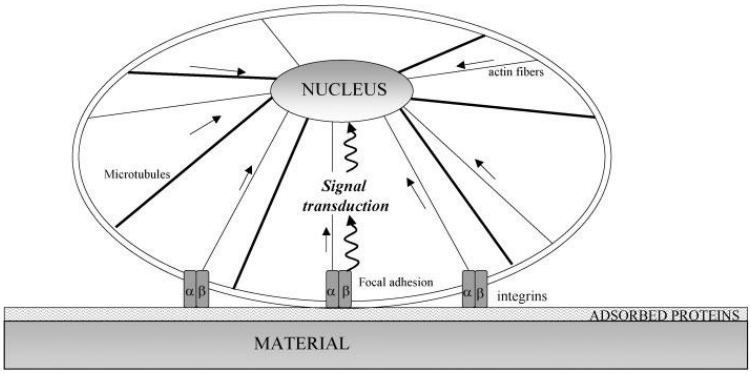

Figure 2.2 Schematic of proteins involved in the attachment of bone-derived cells (Anselme *et al,* 2010)

On the extracellular side, they interact with the ariginine-glycine-aspartic acid (RGD) peptide sequence present on a number of ECM proteins such as fibronectin, vitronectin, osteopontin, bone sialoprotein and collagen. However, fibronectin (FN) and vitronectin (VN) have been identified as the primary proteins that promote the adhesion of bone-derived cells (Rupp *et al,* 2004 and Cimpean *et al*, 2010). The formation of the protypic integrin-ligand pair results in the transmission of signals from the ECM to the nucleus via a biochemical signal transduction pathway. The signal transduction involves the accumulation and phsphorylation of several proteins including FAK, Rho, ERK et cetera (Anselme *et al*, 2010). The signals can also be transmitted mechanically through the physical link that exists between focal adhesion sites and the nuclear membrane created by the cytoskeleton. The integrins are also physically hardwired to the nucleus through the cytoskeleton. When the integrin receptors interact with the ECM adsorbed biomolecules they cluster to form focal adhesions. At this point the cytoskeleton is reorgzanised to allow the spreading of the cells on the substrate. The cytoskeleton comprises three different molecules namely the actin fibers, tubulin microfilaments and the vimentin, desmin or keratin microfilaments. In the focal adhesion the cytoskeletal molecules interact with signalling molecules such as talin,

vinculin, paxillin, tensin and protein kinases. Focal adhesions are closed junctions where the distance between the substrate surface and the cell membrane is 10-15 nm.

Cell attachment, spreading, division and migration are also affected by myosins which are actin-based motor proteins that translocate along the actin fibres and facilitate their contraction. After adhesion and spreading the cells secure their shape stability through a prestress state maintained by actin fibres throughout the cell body and balanced by microtubules. The cells are also able to migrate and orientate themselves along the surface topography eg grooves. This phenomenon is referred to as contact guidance. Cell migration is driven by the cell filopodia. It has been shown that the cells use the filopodia to explore their immediate vicinity before migrating. The biochemical and mechanical interactions allow signal transduction to the cell nucleus that may either induce cell death through apoptosis or cell growth and differentiation if the converse is true. Successful cell adhesion and migration are followed by cell division and proliferation. The cells also start to synthesize the molecules they normally synthesize in their tissue of origin. This is known as differentiation. In the case of bone-derived cells, collagen and other proteins normally found in bone are synthesized.

2.1.7 Titanium and titanium alloy implants

Metals such as stainless steel, cobalt-chromium (Co-Cr) alloys and titanium (Ti) and titanium alloys have been successfully utilized as biomaterials for several decades. Compared to other biomaterials such as ceramics and polymers, metallic biomaterials are able to endure significant loads and withstand fatigue loading which makes them suitable as load- bearing implants in the body (e.g. dental implants, implants for hip, knee, ankle, shoulder, wrist, and finger or toe joints). The mechanical properties of metal implant materials in comparison to bone have been summarized in **Table 2.2**.

Table 2.2 The mechanical properties of metal implants and hard tissue (Black and Hastings, 1998 and Hench, 2005)

Material	Elastic modulus GPa	Compressive Strength (MPa)	Tensile strength (MPa)	Fracture toughness ($MPa\sqrt{m}$)
Stainless steel (316L)	200	505-860	200-1100	100
Co-Cr	200	655	450-1000	100
Ti6Al4V	110	860	750-1050	80
Cortical bone	7–30	100–230	50–150	2–12
Cancellous bone	0.05–0.5	2–12	10–20	

As shown, the elastic modulus of Ti and Ti alloys is more compatibile with that of cortical bone with respect to alternative metals which reduces the likelihood of stress-shielding whereby the implant bears most of the load, shielding the bone tissue from its normal physiological load, thereby resulting in irregular bone growth or bone loss (Teoh, 2004, Myer, 2003, and Liu *et al*, 2004). Hence, Ti and Ti alloys are widely used as hard tissue replacements. Ti and Ti alloys also have a high strength to weight ratio which gives rise to high strength, light–weight implants and have superior machinability and formability compared to stainless steels and the Co-based alloys. Furthermore, Ti and Ti alloys have exhibited superior biocompatibility and corrosion resistance owing to the presence of a chemically stable, amorphous or nanocrystalline native oxide film (approximately 3-8 nm thick) which grows on the metal surface upon exposure to air (Liu *et al*, 2004). However, Mu *et al* (2000) and Browne and Gregson (2000) reported that Ti accumulated in the tissues adjacent to the metal implant. This was attributed to metal ion leakage and was an indication that Ti-based implants tend to undergo some degree of corrosion *in vivo* irrespective of the native oxide layer. Corrosion can result in degradation of the metal surface to oxides and hydroxides which could cause inflammation and subsequently inhibit bone formation accompanied by implant loosening or failure due to embrittlement.

Ti-based implants also have poor tribological properties such as low surface hardness, high friction coefficient and poor wear resistance. Thus wear particles may easily form if the implant surface rubs against bone or another implant surface, resulting in an inflammatory response within the surrounding tissues (Goodman *et al*, 2006). Moreover, corrosion and wear have been cited as the main causes of implant degradation which typically occurs after 10-15 years in service (Willmann, 1999). Furthermore, Ti-based implants do not form a direct bond with bone tissue but instead cause the formation of fibrous tissue which results in poor fixation at the bone-implant interface, and subsequently implant failure. Therefore, in order to improve the surface properties and biocompatibility of Ti and Ti alloys, the metal implant surface can be modified physically via machining, grinding, polishing and grit blasting using Al_2O_3, SiO_2 or SiC (Jeffcoat, *et al*, 2003, Gaske *et al*, 2004 and Wang *et al*, 2006).

Ti substrates can also be chemically roughened by treatment in hydrogen peroxide (H_2O_2) or etching in hydrochloric acid (HCl), Hydrofluoric acid (HF), Sulfuric acid (H_2SO_4) or nitric acid (HNO_3) (Pan *et al*, 1998, Klokkevold *et al*, 2001 and Liu *et al*, 2004). Alkaline treatment can also be used to roughen Ti substrates by immersion in sodium hydroxide (NaOH) followed by heat treatment (Kim *et al*, 1999 and Liu *et al*,

2004). However, superior surface properties have been obtained as a result of depositing a variety of bioceramics onto the Ti metal surface.

2.2 Bioceramics

Bioceramics are basically ceramic materials that are specially developed for the repair and reconstruction of diseased or damaged parts of the musculo-skeletal (Hench, 1991). Bioceramics may be bioinert (alumina), resorbable (tricalcium phosphate), and bioactive (bioactive glasses and glass ceramics) or porous for tissue in-growth (alumina, hydroxyapatite-coated metals). Bioceramics may be used in bulk as implants or as bone fillers after surgery. Bioceramics can also be used as a second phase in a composite and also as a film on a substrate (Hench, 1991). The most commonly used bioceramic film materials for load-bearing metallic include hydroxyapatite (HA), titanium dioxide (TiO_2) and zirconium dioxide (ZrO_2).

2.2.1 Hydroxyapatite (HA)

Hydroxyapatite (HA) is a member of the calcium phosphate family which includes alpha tricacium phosphate (α-TCP), beta tricalcium phosphate (β-TCP), tetracalcium phosphate (TTCP), oxyhydroxyapatite (OHA) and amorphous calcium phosphate (ACP). The calcium phosphate phases are distinguished by the molar Ca:P ratio, basicity/acidity, and solubility. The lower the Ca:P ratio, the more acidic and water soluble the calcium phosphate. In general HA is a highly stable phase compared with other calcium phosphate phases at physiological pH. The dissolution rates of the calcium phosphate phases decrease in the order ACP>>TTCP>α-TCP>OHA>β-TCP>>HA. Additionally, β-TCP cannot be precipitated from aqueous solutions whereas α-TCP is only obtained after heating at 1125°C. Hence, HA is the most promising member of the calcium phosphate family.

The ideal relative composition of hydroxyapatite (HA) is given as follows 39.9% Ca, 18.5% P and 3.3.8% OH (Myer, 2003). The ratio of calcium to phosphorous is typically 1.67. (Myer, 2003 and de Groot *et al*, 1998) HA molecules are normally composed of atoms arranged in a hexagonal crystal lattice (**Figure 2.3**).

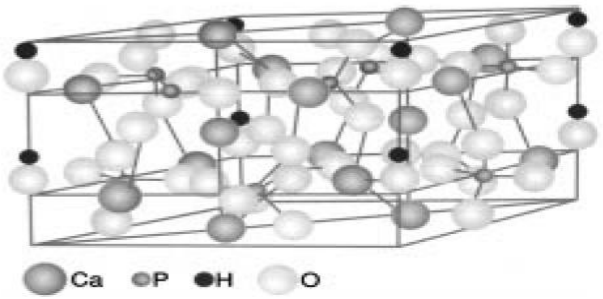

Figure 2.3 Unit cell of apatite crystal (de Groot et al, 1998)

However, it has also been found that this hexagonal structure is lost if alternating hydroxyl columns are oriented in opposite directions, resulting in a monoclinic structure (de Groot *et al*, 1998).

The widespread use of HA films can be attributed to its similarity with the naturally occurring calcium phosphate found in the mineral phase of bone, which renders HA biocompatible and therefore a suitable material for the repair and reconstruction of bone tissue (Jarcho, 1981).

The use of this bioceramic material further stems from the fact that HA is bioactive. Jarcho and co-workers (1979) showed there was intimate contact between HA and bone after implantation in a bone defect. Crystallites of biologic apatite were observed at the implant surface which gradually blended into the bonelike mineralized tissue. Tracey and Doremus (1984) used transmission electron microscopy (TEM) to demonstrate that there was a direct chemical bond at the bone-hydroxyapatite interface.

It has been suggested that the bone-bonding process is initiated by partial dissolution of the HA film with the release of calcium (Ca^{2+}) and phosphate (PO_4^{3-}) ions which increases the ion concentration in the local environment around the HA surface. This results in reprecipitation of crystals on the HA surface and ion exchange with the surrounding tissues. A carbonated calcium phosphate layer is subsequently formed and is incorporated with a collagenous matrix, followed by bone growth towards the implant surface. Bone remodeling then takes place in the area of stress transfer. Osteoclasts resorb the normal bone by actively secreting hydrogen ions in the extracellular space which creates a local pH of approximately 4.8, and leads to fast resorption of fast resorption off the HA in the mineral phase and the implanted HA. The

bone-implant surface is subjected to further bone ingrowth and remodeling. Biological fixation is attained via the bidirectional growth of the bonding layer (Sun *et al*, 2001).

HA is also osteoconductive, and hence can direct bone tissue to conform to its surface. The presence of HA can lead to bone formation and successful fixation at a gap distance of 1 mm between the HA surface and the surrounding bone tissue (Sun *et al*, 2001). However, Jarcho *et al* (1979) observed that there was no evidence of bone formation around intramuscular implants which implies that HA is not osteoinductive and can not stimulate undifferentiated cells to transform into preosteoblasts.

On the other hand, HA has poor mechanical properties (De With *et al*, 1981). The fracture toughness of HA (1 $\mathrm{MPa}\sqrt{\mathrm{m}}$) is approximately half the minimum fracture toughness reported for cortical bone (2-12 $\mathrm{MPa}\sqrt{\mathrm{m}}$) whereas the tensile strength (40-100 MPa) is significantly lower than that of cortical bone (50-150 MPa) (Hench and Wilson, 1993 and Ratner *et al*, 2012). Therefore, HA cannot be utilized as a bulk implant in load-bearing applications. In order to circumvent this problem, HA has been deposited as a film onto the Ti and Ti alloys which combines the excellent bioactivity of HA with the superior mechanical properties of the metal.

HA coated implants have been observed to bring about accelerated, firm and long-lasting fixation of implants both in animal and human clinical studies (Geesink, *et al* 1987, and Furlong and Osborn, 1991). Ducheyne and Healy (1988) and later Sousa and Barbosa (1995 and 1996) also successfully demonstrated that such coatings prevent the leakage of metal ions into the bodily environment. However, Yang *et al* (1996) and Yang *et al* (2003) reported that implant failure consistently occurred at the HA-Ti interface *in vitro*. Similarly, Yang *et al* (2001) and Kweh *et al* (2002) demonstrated that HA films separated from the underlying metal substrate after immersion in physiological fluid. Moreover animal studies also revealed the HA-metal delamination to be the most common failure mode (Geesink *et al*, 1988, Cook *et al*, 1988 and Ong *et al*, 2004).

The stability of the HA-metal interface is typically assessed in terms of adhesion between HA and the metal substrate. Experimentally, film-substrate adhesion can be evaluated qualitatively in terms of the adhesion strength which takes into account the maximum force per unit area required to separate the coating from the substrate. This is typically accomplished by the tensile adhesion test, shear test and scratch test. Several theories have been proposed to explain the mechanism of adhesion of films to metallic substrates. Diffusion, mechanical interlocking, electrostatic attraction, physical

adsorption, chemical bonding and weak boundary layers are all believed to be responsible for bonding between coatings and metal substrates (Berndt and Lin, 1993). However, in the case of HA coatings the adhesion has mainly been attributed mechanical interlocking between the HA material and the asperities on the metal implant surface as well as chemical diffusion and bonding between HA and the metal substrate in the interfacial region. The chemical bonding or diffusion results in the formation of calcium titanate phase (perovskite) and/or Ti-P compounds which are believed to further enhance bonding strength of HA coatings on the metal substrate (Filliagi *et al*, 1991, Ji *et al*, 1992, Tsui *et al*, 1998, and Liu *et al*, 2002).

The Food and Drug Administration (FDA) and the International Organisation for Standardisation (ISO) propose a shear strength of 22-29 MPa and a minimum tensile bond strength of 51 MPa for HA films on metal substrates. However, the bond and shear strengths of HA films typically fall short of these values. For example Han *et al* (2000) reported a tensile bond strength in the range 4-14 MPa whereas Blalock *et al* (2007) reported a tensile bond strength in the range 0.9-10 MPa. In a different study, Rohandizeh and co-workers (2005) were only able to obtain a tensile bond strength of approximately 5 MPa. Therefore the use of HA-coated implants is greatly hindered by a lack of adequate film cohesion as well as HA-Ti interfacial bonding.

The poor interfacial strength at the HA-metal interface is attributed to the abrupt change in materials properties such as fracture toughness and young's modulus at the film-metal interface. The coefficient of thermal expansivity of HA ($\alpha_{HA}=15\times10^{-6}K^{-1}$) is approximately twice that of Ti or Ti alloy ($\alpha_{Ti}=8.8\text{-}9\times10^{-6}K^{-1}$) (Bauer, 1990 and Ravaglioli, 1992). Therefore residual stresses and subsequently microcracks can be set up within the film since most film deposition techniques require thermal energy during film deposition or for post deposition treatment. The micocracks act as stress concentrators which facilitate crack propagation (Yang and Chang, 2001). HA films also typically contain porosity which may vary in the range of 10-90%. Pores act as stress concentrators and also increase film dissolution in physiological fluids (Mohammadi *et al*, 2007 and Sun *et al*, 2001). It has been suggested that pores may be connected three dimensionally forming channels extending to the surface thus increasing the area exposed to the solution. This could lead to increased film instability (Park *et al*, 1998).

Commercial HA films are also relatively thick (approximately 50-75 μm) and yet thicker films have higher accumulated stresses and porosity (Sun *et al*, 2001). Furthermore,

HA films typically contain amorphous phase, which is formed due to rapid cooling of HA following deposition or heat treatment. Amorphous phase is highly necessary in order to initiate bone apposition. Weng and co-workers (1997) and later Sun and co-workers (2002) noted that bone-like apatite formation was quickly initiated on amorphous films compared to highly crystalline ones since the first step in the formation of the HA-bone bond involves dissolution of the film surface. However, Whitehead *et al* (1993) and Kweh *et al* (2002) reported a decline in bond strength due to dissolution of the amorphous phase. This was attributed to cause a loss in film integrity which promotes delamination of the film.

Poor HA-metal interfacial bonding can lead to cracking, shearing off and chipping of the HA coating during implantation of the prosthesis, resulting in the formation of a gap between the prosthesis and the coating. The presence of such a gap promotes the invasion of fibrous non-adherent tissue leading to aseptic loosening of the implant. Furthermore, Lahiri *et al* (2010) reported that an HA film gave a larger wear track volume (approximately 1.23 mm^3) compared to HA-Carbon nanotube films (0.24 mm^3). However, Morscher *et al* (1998) and Røkkum *et al* (2002) demonstrated that loose HA particles can cause third-body wear in articulating joint replacements. Therefore, the poor wear resistance of HA is another limiting factor for its successful application as a surface coating in dental and orthopaedic applications. Hence there is an urgent need to enhance the mechanical properties of HA films as well as stability at the HA-metal interface.

2.2.2 Titania

Titania (TiO_2), also known as titanium dioxide or titanium IV oxide, is the naturally occurring oxide of titanium. A transitional metal oxide, titania occurs in three main polymorphs namely, rutile, anatase and brookite of which rutile and anatase are the most common polymorphs (Cromer and Herrington, 1955, and Baur, 1961). Rutile is the most stable polymorh whereas anatase and brookite are metastable at room temperature and are irreversibly converted to the former upon being heated at temperatures between 400-1200ºC. The transformation temperature is determined by grain size, impurities, dopants, precursor materials and synthesis technique.

The major distinction between these three polymorphs is the crystal structure. Rutile and anatase are tetragonal with 6 and 12 atoms per unit cell respectively whereas brookite is orthorhombic with eight formular units in the unit cell. The basic unit cell

structures and crystallographic properties of the three polymorphs of TiO_2 are illustrated in **Figure 2.4** and **Table 2.3**.

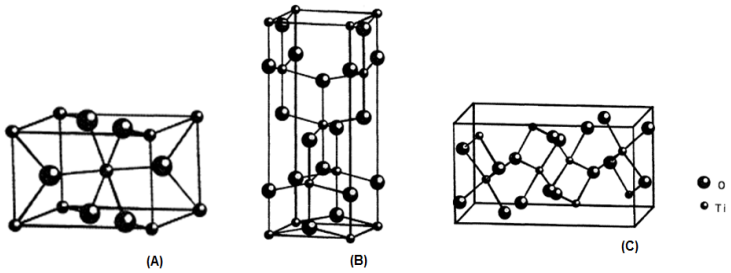

Figure 2.4 TiO_2 polymorphs (A) Rutile, (B) Anatase and (C) Brookite

Table 2.3 Crystal structure of TiO_2 (Bauer, 1961 and Herrington, 1965)

Polymorph	Density (kgm^{-3})	Crystal structure	Lattice constants ($\times10^{-10}m$)	Ti-O bond length ($\times10^{-10}m$)	O-Ti-O bond angle
Rutile	4130	Tetragonal	a=4.4936 c=2.9587	1.949 (4) 1.980 (2)	81.2° 90.0°
Anatase	3790	Tetragonal	a=3.784 b=9.515	1.937 (4) 1.965 (2)	77.7° 92.6°
Brookite	3990	Orthorhombic	a=9.184 b=5.447 c=5.145	1.87~2.04	77.0°~105.0°

The use of TiO_2 is based on its similarity with the native oxide layer that is formed spontaneously on the surfaces of Ti and Ti alloys. The favourable properties of Ti and Ti alloys namely, chemical inertness, corrosion resistance, repassivation ability and biocompatibility are attributed to the chemical stability and structure of the oxide layer (Liu *et al*, 2004). On the other hand, the native oxide layer on as-received implants is non-uniform and poorly defined with poor mechanical properties and is easily fractured due to fretting and sliding wear (Guleryuz and Cimenoglu, 2003). Therefore the surface layer needs to be extended by film deposition.

In studies conducted by Liu *et al* (2003) TiO_2 films displayed lower electrochemical corrosion measurements compared to uncoated nickel titanium (NiTi) whereas Kim *et al* (2004) reported that TiO_2 film caused a reduction of the corrosion current in physiological saline solution at 37 °C with respect to the uncoated Ti alloy substrate. From these findings it is therefore evident that TiO_2 films enhance the corrosion resistance of Ti substrates. Furthermore, Guleryuz and Cimenoglu (2003) reported an enhancement in surface properties due to the presence of TiO_2. The surface hardness

was increased from 3500 to 9000 HV accompanied by a 25-fold increase in wear resistance after immersion of test samples in 0.9 NaCl solution. Subsequent studies by Krishna *et al* (2007) also showed that the surface hardness of a Ti substrate was increased from 200 to 600-800 HV due to the presence of a TiO_2 film. Additionally, the coated surface had a lower coefficient of friction and displayed minimal wear in comparison with the uncoated implant. These findings highlight the advantages of depositing TiO_2 films onto the Ti and Ti alloy surface. Moreover, the TiO_2-Ti bonding strengths (approximately 24-43 MPa) are significantly higher than the reported bond strengths at the HA-Ti interface (Patsi *et al*, 1998 and Han and Xu, 2004).

.

TiO_2 films are able to induce the formation of bone-like apatite which is a prerequisite for bone formation on the implant surface *in vivo* (Kokubo and Takadama, 2006). For example, Li *et al* (1994) demonstrated that TiO_2 films induced the formation of bone-like apatite after immersion in simulated body fluid (SBF) for up to 21 days. Similarly, Zhao *et al* (2010) reported that TiO_2 films induced the formation of calcium-deficient carbonate substituted apatite on their surface after 7 days in SBF. Moreover, the apatite layer can grow to a thickness of 10 μm after an immersion period of 2 weeks (Li *et al*, 1994). On the other hand, Han *et al* (2003) did not observe the presence of apatite on the plasma sprayed TiO_2 surface even after 50 days. Similarly, Liu *et al* (2005 and 2008) reported a lack of bone-like apatite formation on as-sprayed micro- and nano-structured TiO_2 films after 2 and 4 weeks. Therefore, not all types of TiO_2 films can induce the formation of apatite. However, Liu *et al* (2008) observed that post deposition UV irradiation of the nanostructured films rendered them bioactive by creating surface Ti-OH functional groups whereas the microstructured films remained bioinert. These findings suggest that there are two major criteria for the bioactivity of TiO_2 films. Hence TiO_2 films need to have Ti-OH functional groups which have been suggested as ion adsorption sites for the formation of apatite, and should also have a nanostructure which enhances ion adsorption.

Furthermore, the apatite formation ability of TiO_2 is affected by the crystal structure. Uchida *et al* (2003) reported that the fit of the (0 0 0 1) plane in apatite to the (1 1 0) plane in anatase or the (1 0 1) plane in rutile shows a close superposition of hydrogen bonding groups in these crystals. These epitaxial relationships lead to favourable apatite formation. However, there is a smaller mismatch in the crystal lattice parameters of apatite and anatase compared to that between apatite and rutile. Additionally, the hydroxyl groups of apatite are better superimposed on oxygen atoms in anatase than in rutile. Hence the anatase crystal structure is more favourable for

apatite formation as it provides more effective epitaxial nucleation sites for apatite crystals

TiO_2 films are also compatible with bone cells. Vondrovcova *et al* (2012) and Zhang *et al* (2012) reported that TiO_2 films promoted the proliferation and differentiation of osteoblast-like cells over 7 days. However, He *et al* (2008) have indicated that anatase phase gives enhanced cell adhesion, spreading, proliferation and differentiation compared to the rutile phase. These findings suggest that the anatase phase induces a more favourable cellular response in comparison to the rutile phase.

In vivo studies have further shown that TiO_2 films also display favourable bone apposition. Yamamoto *et al* (2011) found that TiO_2 coated implants exhibited a similar bone-implant contact ratio to uncoated Ti implants after implantation in rat tibia for 14 days. In contrast, Chung *et al* (2013) reported that TiO_2 coated implants integrated well with the host tissue after implantation in rabbit femurs over 12 weeks in comparison with the uncoated Ti implants. However, the TiO_2 coated implants displayed lower push-out strengths for implant retrieval with respect to the HA coated implants. Similar findings were reported by Kuroda *et al* (2007) who found that the TiO_2 coated implants inserted in rat tibia gave a lower bone-to implant contact ratio with respect to HA coated implants after 14 days. These findings imply that the TiO_2/bone interfacial bond is weaker than the HA/bone interfacial bond, suggesting a lower degree of bioactivity for TiO_2. These findings suggest that there is no biological advantage in depositing TiO_2 films onto Ti based implants since there was no significant difference in the osteoconductivity of the TiO_2 coated and uncoated implants Therefore it is necessary to enhance the bioactivity of the TiO_2 films.

2.2.3 Zirconia

Zirconia (ZrO_2), which has the synonym zirconium dioxide is the crystalline oxide of the metal zirconium. Zirconia crystallizes in three common polymorphs; monoclinic (M), tetragonal (T) and cubic (C) which are distinguished by their crystal structure, as shown in **Figure 2.5**. Pure zirconia is monoclinic (M) at room temperature and pressure. An increase in temperature causes a transformation from monoclinic to Tetragonal (T) by 1170 °C. This is followed by a transformation to a cubic fluorite structure starting at about 2370 °C with melting taking place at 2716 °C (Subbaroo, 1981, and Picconi and Maccaurro, 1999).

The phase transformations are characterized by being diffusionless, involving only coordinated shifts in lattice positions as opposed to atom transport, occur over a temperature range instead of at a fixed temperature and involve shape deformation (Kelly and Denry, 2007).

As the material cools, the phase transition from cubic to tetragonal to monoclinic is accompanied by a substantial increase in volume which results in cracking and subsequently renders pure zirconia useless for industrial and medical applications. In order to improve the mechanical reliability of zirconia, it is necessary to stabilize the tetragonal and (or) cubic phases. This is typically achieved by doping the zirconia crystal lattice with molecules such as Yttria (Y_2O_3), magnesium oxide (MgO) and calcium oxide (CaO) in proportions ranging from 2-8 mol% depending on whether full or partial stability is required (Picone and Maccaurro, 1999 and Manicone *et al*, 2007).

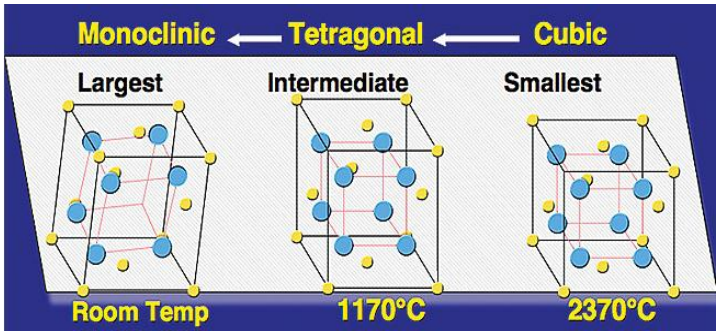

Figure 2.5 Crystal structure of ZrO_2 polymorphs
(http://www.dentalaegis.com/idt/2012/03/machinable zirconia assessed on 27/07/2012)

The use of zirconia and in particular, partially stabilized zirconia can be explained by the superior toughness of this material which is directly linked to the transformation toughening phenomenon, whereby, the application of a stress on a zirconia surface causes a transition from metastable tetragonal phase to monoclinic phase. This is accompanied by a volume expansion which in turn closes up an existing crack and as such inhibits crack propagation. Hence ZrO_2 has been used extensively in femoral heads in total hip replacement and also in the fabrication of bridges and abutments for dental applications (Derbyshire *et al*, 1994, Clarke and Allen, 2000, and Oliva *et al*, 2010).

ZrO_2 also offers several benefits as a coating material. Branzoi *et al* (2010) reported that ZrO_2 coated Z3Ta implants gave a low corrosion current in fetal bovine serum at

37 °C compared to the uncoated implants. Similarly Zykova *et al* (2012) reported that ZrO_2 coated Ti implants gave a lower current density than the Ti controls. Therefore, ZrO_2 films are highly effective as a protective layer against corrosion.

The surface properties of Ti and Ti alloy substrates have also been enhanced by ZrO_2 films. For example, Kanbara *et al* (2011) observed that the hardness at the surface of Ti and Ti alloys was increased from 125-256 HV to 1356 HV due to the presence of the ZrO_2 film, which also reduced the cross sectional area of the wear tracks from 20-40 μm^2 to ~0 μm^2 and 120-170 μm^2 to ~10 μm^2 respectively after 5000 wear cycles. Additionally, ZrO_2 films also display superior bonding strength to Ti substrates as reported by Wang *et al* (2010). These authors observed that monoclinic ZrO_2 films gave a bond strength of approximately 48 Mpa. This is a positive indication of the superior adherence of the ZrO_2 films compared to TiO_2 and HA films,

Similarly to TiO_2, ZrO_2 films can induce the formation of bone-like apatite in SBF due to the presence of surface hydroxyl groups (Zr-OH) (Uchida *et al,* 2002A and Liu *et al,* 2006). However, ZrO_2 films do not form apatite unless they assume the tetragonal and (or) monoclinic structure which provide effective epitaxial nucleation sites for apatite crystals (Uchida *et al*, 2002B).

Cell culturing studies have also indicated that ZrO_2 films are non-cytotoxic and promote the attachment and subsequent proliferation and differentitation of osteoblasts (Wang *et al*, 2010 and Watanabe *et al,* 2012). Hence, ZrO_2 coated implants have also been able to induce the formation of new bone with minimal inflammation in vivo. However, despite their osteoconductivity, ZrO_2 coated implants are generally comparable to Ti implants. For example, although Gahlert *et al* (2009) reported the existence of new bone adjacent to implants inserted in the mandibles of adult pigs, there was no significant difference in the the bone density and bone-implant contact ratio between the coated and uncoated implants at 4, 8 and 12 weeks. Similarly, Depprich *et al* (2008) found that there was no significant difference in the bone contact between coated and uncoated implants after 1, 4, and 12 weeks of implantation in minipig tibia. In contrast, Stadlinger *et al* (2011) reported that the ZrO_2 films displayed lower bone-implant contact compared to the uncoated Ti implants. From these findings, it is evident that ZrO_2 does not enhance implant osseointegration which suggests the need to enhance the bioactivity of this material.

The mechanical properties of bioceramic materials have been summarized in **Table 2.4.** As shown, the metal oxides are mechanically superior to hydroxyapatite. Hence TiO_2 and ZrO_2 films display superior hardness and wear resistance.

Table 2.4 Comparison of mechanical properties of common bioceramics (Reidel and Chen, 2010 and Buddy et al ,2012)

Material	Elastic modulus (GPa)	Compressive strength (MPa)	Tensile strength (MPa)	Fracture toughness ($MPa\sqrt{m}$)
HA	70-120	100-900	40-100	1
TiO_2	230	680		2.8-6.1
ZrO_2	140-200	2000-2500	245-700	5.5-11

2.2.4 Two phase bioceramic films

In order to enhance the surface properties of coated implants, several attempts have been made to deposit multiple component films onto the Ti and Ti alloy surface. Such films improve the surface properties by combining the excellent bioactivity of HA with the superior mechanical integrity and corrosion resistance of TiO_2 or ZrO_2. Multiple component films are typically synthesized by applying the oxide material either in conjunction with HA as composite or functionally graded coating or as a bond coat.

2.2.4.1 Bond coats

Basically, a bond coat or buffer layer is an intermediate layer between the HA coating and the metal substrate as illustrated in **Figure 2.6**.

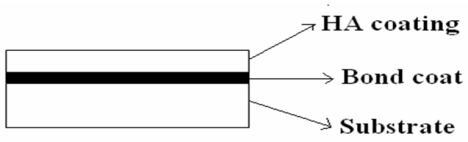

Figure 2.6 Illustration of HA-metal substrate with bond coat

Compared to the overlying HA coatings, bond coats are relatively thin with a coating thickness of upto 20µm. This helps in the prevention of excessive residual stresses due to the introduction of an additional layer within the HA-metal substrate system (Kim *et al*, 2004).

The use of buffer layers was first reported in the 1990s by Lamy and co-workers (1996) who used atmospheric plasma spraying to deposit 15-20 μm dicalcium silicate (Ca_2SiO_4) films on Ti alloy substrates followed by 200μm HA coatings. But while a 25% increase in tensile bond strength was observed for the HA-buffer layer system compared to the HA only system, a sharp decline in bond strength was obtained following immersion of coating samples in SBF. This was attributed to the hydration of hydraulic β- Ca_2SiO_4 formed from non hydraulic γ-Ca_2SiO_4 during plasma spraying. However, improved performance in terms of adhesion strength and resorption resistance has also been reported following the utilization of buffer layers based on TiO_2 and ZrO_2.

In a study by Kim *et al* (2004) the tensile bond strength was increased from approximately 35 MPa to 55 MPa owing to the presence of a TiO_2 buffer layer. Similarly, Lin and Yen (2004) observed a bond enhancement from 11.3 MPa to 46.7 MPa, whereas Lee and co workers (2007) attained a bond strength increase from 20 MPa to 90 MPa. Similar findings have also been obtained in studies based on ZrO_2 whereby the presence of the ZrO_2 buffer layer increased the bond strength of the HA films from 28.6 MPa to 36.2 MPa (Chou and Chang, 2002). As expected, TiO_2 and ZrO_2 act as a reinforcing phase in the HA-Ti system. However, the difference in bond strength of the different films is a direct consequence of the difference in film deposition and post deposition methods.

The bond enhancing effect of an oxide buffer layer has been further confirmed by Xu *et al* (2006). These authors reported that there was minimal delamination and cracking at either interface in the HA-TiO_2-Ti system. Moreover, TiO_2 buffer layers were also seen to initiate apatite formation in physiological fluid and encourage human osteoblast cell growth in a manner similar to HA single layer coatings (Kim *et al*, 2004, Lin and Yen, 2004, and Lee *et al*, 2007). Heimann *et al* (2004) reported on the behaviour of the HA-TiO_2 buffer layer coatings *in vivo*. These authors found that extracted implants from adult sheep femurs exhibited a continuous and tight succession of bonding between the metal implant and HA+TiO_2 coating as well as between the bone and coating, whereas the HA coating without a buffer layer bore frequent gap formation between the metal implant and the coating. This is consistent with the earlier work of Itiravivong and coworkers (2003) where implants removed from the femurs of adult dogs showed a significant increase in bone coverage in the presence of a buffer layer (approximately 94 %) compared to implants without (approximately 81 %). These findings indicate that the two-layer films are also highly bioactive and osteoconductive, which is advantageous from a biological point of view.

The bond enhancing effects of buffer layers have been attributed to three major mechanisms: Firstly, buffer layers present a rougher morphology to the overlying HA coating compared to the bare Ti or Ti alloy substrate. This is evident in the work of Chou and Chang (2002), where a ZrO_2 buffer layer bore an average surface roughness of 5.73 µm compared to 3.55 µm for the Ti substrate. Secondly, a number of authors have observed that elemental diffusion and (or) chemical reaction occur at the HA-buffer layer interface yielding an extremely thin layer of calcium titanates or zirconates (Chou and Chang, 2001 and Kurzweg *et al*, 1998a). This gives rise to chemical bonding which augments the mechanical bonding already in effect at the coating-metal interface. Another strengthening mechanism is believed to be the reduction in coefficient of thermal expansivity mismatch that is obtained by inserting a buffer layer. For example the coefficient of thermal expansivity of TiO_2 is 9.0×10-6/K, whereas Ti and HA have CTEs of 8.9×10^{-6} and 13.4×10^{-6} /K respectively (Heimann 1999 and Kim *et al*, 2004). The intermediate properties of the buffer layer result in a reduction in residual stress along the HA-metal substrate interface following thermal treatment, which in turn enhances bonding. Also, TiO_2 is said to enhance interfacial bonding simply because it acts as an extension of the already existing native surface oxide (Heimann *et al*, 2004 and Kim *et al*, 2004).

In addition to enhancing HA-substrate interfacial bonding, buffer layers have also been shown to have other uses with regards to orthopedic and dental implants:

Bond coats reduce the steep temperature gradients that occur during plasma spraying and lead to the formation of amorphous calcium phosphate which is easily dissolved *in vivo* (Heimann, 1999, Kurzweg *et al*, 1998B, Heiman *et al*, 1998, Heimann and Wirth, 2006 and Lee *et al*, 2007).

Bond coats also increase the overall corrosion resistance of the metal implant and as such prevent the release of potentially cytotoxic heavy metal ions into the bodily environment (Heimann *et al*, 1998, Nie *et al*, 2000, Kim *et al*, 2004 and Lin and Yen, 2004).

Weng *et al* (1994) and later Wen *et al* (2000) demonstrated that the Ti metal catalyzed the thermal decomposition of HA. Hence another function of bond coats is to prevent direct contact between Ti metal and HA.

2.2.4.2 Composite coatings

In composite films, the HA and secondary phase starting materials are mixed together mechanically while in powder form or by ceramic slurry mixing in the presence of a binder prior to film deposition. The resulting film thus contains the toughening phase either as a continuous or dispersed phase.

The advantages of using composite films were reported by Kim *et al* (2005) who observed that the presence of TiO_2 enhanced the tensile bond strength. The tensile bond strength was increased from 37 MPa to 56 MPa on increasing the TiO_2 content from 10 to 30 mol%. Later, Xiao and co-workers (2006) reported a two fold increase in bond strength from approximately 11 MPa to approximately 23 MPa due to the addition of 25wt% TiO_2. Similarly, Im *et al* (2007) obtained an increase in critical load during scratch testing from 2 N to 5.39 N upon increasing the amount of TiO_2 from 0 mol% to 70 mol%.

Bond enhancement following the addition of ZrO_2 has also been documented; Chang *et al* (2001) found that the presence of 10 wt% ZrO_2 gave rise to an increase in bond strength from 28.24±3.68 MPa to 32.49±4.24 MPa. A similar trend was observed by Fu *et al* (2001a and 2001b) due to the addition of 30wt% YSZ such that the bond strength was increased from 19.2 MPa to 26.3-43.42 MPa. Research by Xiao *et al* (2006) also documented an increase in bond strength with a corresponding increase in ZrO_2 wt%. More recently, De-Jun et al (2012) also reported that the critical scratch load increased from 17.5 N to 30 N on increasing the ZrO_2 content from 25 wt% to 50 wt%.

Further increases in bond strength have been attained by using three component films with ZrO_2, Ti and Ti6Al4V as reinforcing phases. For instance, Gu *et al* (2004) showed that an HA(35wt%)/YSZ(15wt%)/Ti6Al4V(50wt%) had a bond strength of approximately 32MPa whereas an HA(50wt%)/Ti6Al4V(50wt%) coating had a bond strength of approximately 28MPa. Zhao *et al* (2006) achieved a bond strength of approximately 59.6 MPa for the HA/Ti6Al4V/YSZ coating compared to 55.9MPa obtained using an HA/Ti6Al4V coating. Furthermore, Qiu *et al* (2010) observed that HA/ZrO_2 composite films increased the corrosion resistance of a Ti substrate in SBF by 60 times.

Composite coatings have also been observed to display higher stability in physiological fluid and also promote HOB cell proliferation and differentiation with respect to monolithic TiO_2 and ZrO_2 films (Ding *et al*, 1999, Zheng *et al*, 2000, Ramires *et al*, 2001, Wen *et al*, 2007 and Sato *et al*, 2008). Additionally, Kuroda *et al* (2007) reported that implants with HA/TiO_2 composite films gave a higher bone-implant contact ratio compared to the monolithic TiO_2 and HA films after 14 days in rat tibia., whereas

Nathanael *et al* (2012) reported that the HA/TiO_2 composites exhibited enhanced antimicrobial properties which improved with the proportion of TiO_2. On the other hand, the enhancement in bioactivity is at the expense of the mechanical integrity. Therefore, while the composition of composite films should be selected to give a good combination of bioactivity and mechanical integrity, the "ideal" composite film composition has not yet been defined.

The bond strength enhancement obtained using composite coatings has been ascribed to dispersion strengthening such that the tough secondary phase particles act as impediments to crack growth via crack deflection. HA also forms a solid solution with the toughening secondary phases, which together with the mutual chemical reaction between the two augments the mechanical interlocking at the interface. However, in the case of ZrO_2 the presence of calcium zirconate ($CaZrO_3$) causes the decomposition of HA in to α-TCP and the undesirable calcium oxide (CaO) (Chou and Chang, 1999 and Li *et al*, 2004).

Another strengthening mechanism is due to the reduction of the coefficient of thermal expansivity owing to the presence of the toughening secondary phase which has intermediate coefficient of thermal expansivity and thus reduces the level of post deposition residual stress within the coating. Additionally ZrO_2 undergoes stress induced phase transformation from tetragonal to monoclinic (Chang and Chou, 2002 and Liu *et al*, 2004).

2.2.4.3 Functionally graded films

Functionally graded films are based on principles from both composite films and buffer layers. Basically, a functionally graded film is composed of a buffer layer at the substrate which gives maximum bonding whilst the outermost top coat layer provides good bioactive properties to accelerate bone healing. In between the two there lies a transition layer with intermediate properties (**Figure 2.7**).

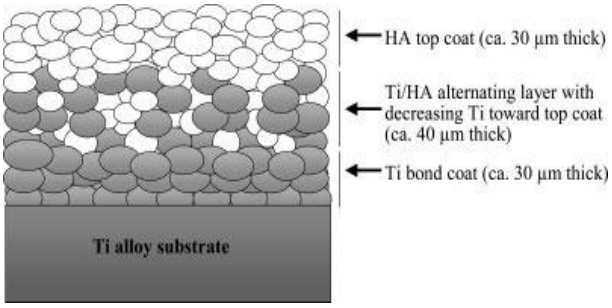

Figure 2.7 Functionally graded coating (Chen *et al*, 2006)

In a study by Ning *et al* (2005), a bond strength of 53.6 MPa was achieved using HA/ZrO_2/Ti FGC while a monolithic HA film gave a bond strength of 22.9 MPa. A similar enhancement in bond strength has also been obtained using Ti and Ti6Al4V particles as a reinforcing phase. For example, Ozeki *et al* (2002) obtained a bond strength of 15.2 MPa for an HA/Ti functionally graded coating compared to 8.0 MPa for an HA single coating while Lu *et al* (2003). achieved a bond strength improvement from 16.6MPa (HA) to 30.6 MPa (HA/Ti FGC). Equally, Khor *et al* (2003) reported that an HA/Ti6Al4V FGC gave a bond strength of 38Mpa while a pure HA coating gave a bond strength of 18 MPa. Inagaki *et al* (2003) achieved a bond strength of 50.2 MPa for a functionally graded coating containing Ti and a bond strength of under 5 MPa for the pure HA coating. Chen *et al* (2006) further obtained a bond strength of 23.1 ±3.4 MPa with an HA/Ti functionally graded coating compared to 14.2 ± 3.1 MPa with pure HA. Moreover, these authors demonstrated a decrease of HA bond strength to 10.9 MPa after cyclic fatigue in air for 1 million cycles whereas the functionally graded coating's bond strength remained relatively unaffected at approximately 22 MPa. These findings suggest that the film-metal interfacial strength can be enhanced by using TiO_2 or ZrO_2 as a reinforcing phase due to their superior mechanical properties.

As in the case of bond coats and composite coatings, FGCs have also been seen to have a high stability in SBF and promote the attachment and proliferation of osteoblasts (Ding *et al*, 2003 and Ren-Fu *et al,* 2012). *In vivo* studies by Ozeki *et al* (2002) also showed that there was no significant difference in the push-out strength of HA- coated implants and Ti-HA coated implants after 12 weeks in dog femora. This is an indication of the high conductivity of functionally graded films.

This significant difference can be explained by the fact that the transition layer possesses intermediate mechanical properties hence there is a gradual change in properties through the coating thickness such that the occurrence of residual stress

following coating deposition is more readily suppressed. Also, the presence of the tougher strengthening phases in the FGC leads to crack deflection or pinning, which in turn strengthens the coating.

The representative bond strengths of the different type of coating systems are summarized in **Table 2.5.** However, these values are not directly comparable as the coatings under consideration were deposited using different methods and therefore had varying characteristics such as thickness and microstructure. Thus it is necessary to systematically characterize the various coating systems under similar conditions.

Table 2.5 Comparison of bond strengths of different coating systems

Coating composition	Bond strength (MPa)	References
HA single layer	8-35	Ozeki *et al*, (2002), Lu *et al*, (2003)
HA/TiO_2 buffer layer system	36-90	Kim *et al*, (2004), Lin and Yen, (2004), Lee *et al*, (2007)
HA/ZrO_2 buffer layer system	36-40	Chou and Chang (2002) and Hsu et al (2009B)
HA/TiO_2 Composite coatings	26-60	Zheng *et al* (2000), Kim *et al*, (2005), Xiao *et al*, (2006) and Zhao *et al*,(2006)
HA/ZrO_2 Composite coatings	26-62	Chang *et al* (2001), Fu *et al* (2001A), Xiao *et al* (2006), Morks and Kobayashi (2007)
Functionally graded coatings	30-54	Inagaki *et al*, (2003), Khor *et al, (*2003), Chen *et al*, (2006) and Ning *et al*, (2005)

2.3 Coatings deposition methods

There is a wide range of methods available for the deposition of coatings onto metal substrates in industry. However, for the purposes of two component HA/TiO_2 and HA/ZrO_2 films for biomedical applications, researchers have reported on the use of thermal spraying techniques such as plasma spraying and high velocity oxy fuel spraying and evaporative techniques, such as magnetron sputtering and E-beam deposition (Heimann *et al*, 1999, Ding *et al*, 2003, 2004, Inagaki *et al*, 2006, Heimann and Wirth, 2006, Gaona *et al*, 2007 and Rakngarm and Mutoh, 2008). The use of wet methods which encompass sol-gel processing, electrochemical deposition and micro

arc oxidation has also been documented (Lin and Yen, 2004, Kim *et al*, 2006, Xiao *et al*, 2006, Im *et al*, 2007, and, Wen *et al*, 2007).

2.3.1 Plasma spraying

Plasma spraying belongs to a family of processes in which the coating material is thermally melted into liquid droplets and introduced energetically to the metal surface on which the individual particles stick and condense. The film is formed by continuous build up of successive layers of liquid droplets, softened material domains and hard particles (Zhang *et al*, 1997). Plasma spraying includes atmospheric plasma spraying and vacuum plasma spraying which are distinguished by the fact that VPS is carried out under a very low oxygen surrounding or vacuum atmosphere.

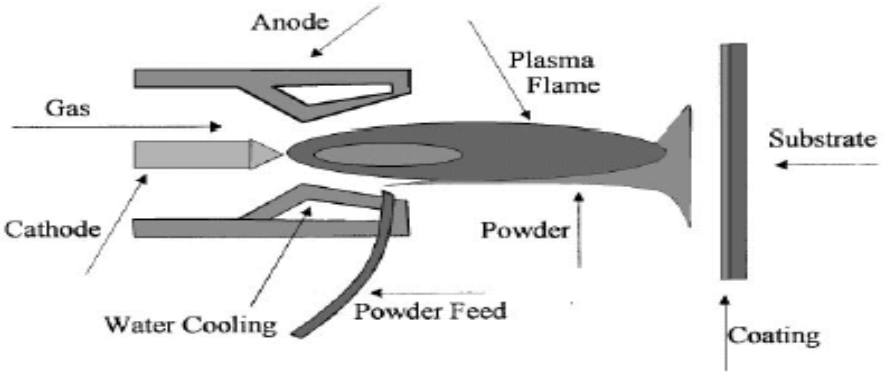

Figure 2.8 Illustration of plasma spraying (Gledhill *et al*, 1999)

During plasma spraying (**Figure 2.8**), the plasma gas, typically an inert gas, such as nitrogen, argon or helium is passed between two electrodes. A high voltage discharge occurs causing ionization in the region between the cathode and anode. A dc arc is then formed between the two diodes due to resistance heating from the arc. This causes the heating and partial ionization of the plasma gas. The gas is then forced through a convergent-divergent nozzle. At temperatures in excess of 20,000 °C, the volume of the gas increases considerably which causes the gas to exit the nozzle at very high velocities of up to 400m/s.

After leaving the nozzle, the gas returns to its natural state, liberating large amounts of heat in the process. The coating material in the form of a powder is injected in to the stream of hot gas, which causes the powder to be fully or partially melted and projected at high velocity to the substrate. The metal substrate reaches a maximum temperature

of about 300 °C which could have a significant effect the metal substrate properties (de Groot *et al*, 1998, Yankee *et al*, 1991 and Lewis, 2000).

The plasma spray process is affected by the degree of ionization which is determined by the plasma gas, as well as the parameters of the plasma torch such as spray current, spray distance and spray torch traverse speed.

2.3.2 High velocity oxy fuel spraying

Basically, HVOF spraying is a combustion flame spraying method. The first step of coating deposition involves the injection of oxygen and a fuel gas which may be kerosene, propylene, acetylene or hydrogen into the combustion chamber. Combustion of the two results in a hot, high pressure flame, which is forced down a nozzle increasing its velocity. The coating material in powder form is injected axially in to the jet as a suspension in a carrier gas. The exhaust flow has been known to reach velocities of about 1700 m/s which are effectively supersonic speeds.

However, the molten particles are accelerated to velocities in the range of 100-800 m/s before impacting on the substrate to form the coating. The maximum temperature achieved during this technique is 3000 ◦C which is low compared to conventional plasma spraying. (Haman *et al*, 1995, Haman, 1999 and Li *et al*, 2002). The film characteristics are determined by plasma gas composition, spray current, spray distance and spray gun traverse speed

Generally speaking, thermal spraying has a high deposition efficiency and is a low cost deposition technique. However, the high temperatures involved during processing lead to degradation of the coating material. Moreover thermal sprayed coatings tend to be highly porous and also possess microcracks which can affect the mechanical integrity of the coatings. The fact that thermal spray processes are line of sight operations makes these processes inadequate for coating deposition on complex geometries.

2.3.3 Sputtering

Sputtering is one of a number of physical vapour deposition processes in which atoms, molecules, or ions are produced from target materials and transported to the substrate on which condensation and (or) chemical reaction with the substrate surface occur resulting in film growth.

During sputtering, a target material is bombarded with particles which are usually positive ions or atoms of a heavy neutral gas such as argon (**Figure 2.9**). This results in the ejection of atoms from the surface of the target. The ejected atoms impact on the metallic substrate placed in the path of the sputtered material where they condense forming a thin film. Bombardment is facilitated by the fact that the surface of the target is made the cathode by the electrical circuit. The sputtering process is affected by the process parameters which include particle energy, substrate temperature, and the reactive gas properties (Ding *et a*l, 1999a, Ding *et al*, 1999b, and Ramires *et al*, 2001). However, although, sputtering results in the deposition of uniform and highly dense films, it is also a line of sight process with a low deposition rate and high operational costs.

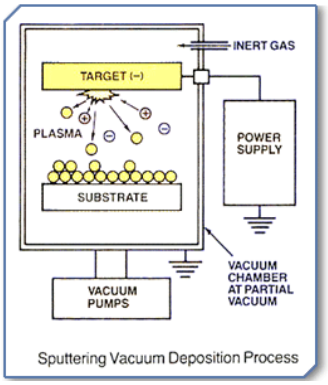

Figure 2.9 Illustration of sputtering (http://www.tcbonding.com/images/sput_diagram.gif assessed 06/04/2013)

2.3.4 Electron beam deposition

Electron beam deposition (E beam deposition) is also a physical vapour deposition technique. This method involves the use of a deposition chamber which is evacuated to pressures of about 10^{-7} prior to deposition. Electron Beam systems also consist of a cathode and an anode (**Figure 2.10)**. The cathode emits electrons usually by thermionic emission, field electron emission or anodic arc method. These are accelerated to a high kinetic energy due to the high voltage potential and are focused onto the target which is the coating material in compressed powder form.

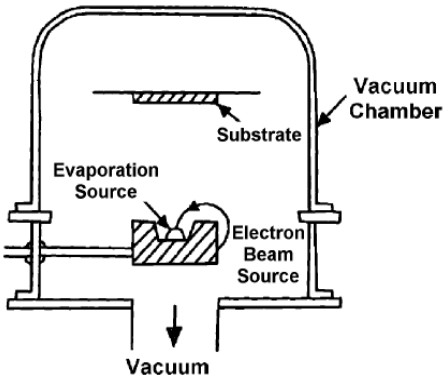

Figure 2.10 Illustration of electron beam deposition (Wasa *et al*, 2004)

The kinetic energy of the electrons is then converted into thermal energy as the beam strikes the target surface. The result of this is that the target is evaporated onto the substrate which has been placed in the path of the generated vapor. Uniform coating morphology is usually obtained by rotating the substrate holder.

The coating process is influenced by the substrate holder speed as well as the applied voltage and current. The target density also plays a role in determining the coating structure and morphology. This process is characterized by having a high deposition efficiency and offers a high level of control over the coating structure and morphology. On the other hand, coatings produced in this way tend to be amorphous and require post deposition to crystallize them which could result in the presence of residual stress and the degradation of the metal substrate mechanical properties. There are also some difficulties with maintaining a uniform evaporation rate during deposition (Hamdi and Ektessabi, 2001, Kim *et al*, 2003, Lee *et al*, 2005, and Lee *et al*, 2007).

2.3.5 Thermal oxidation

This technique involves the modification of Ti and Ti alloy surfaces with the aid of thermal treatment. Prior to treatment, the metal substrate is polished to a mirror shine and cleaned thoroughly to facilitate the process and subsequently heated in air at elevated temperatures in the range 200-600 °C for 1-60 hours (Guleryez and Lu, 2004 and Hsu *et al*, 2009a). This treatment enables the growth of a TiO_2 layer on the metal surface.

The nature of the coatings obtained using this method is time and temperature dependent. But while this process requires a relatively simple and low cost equipment set up, it also presents some challenges as it offers no control over the composition and structure of the coating obtained. Also, heat treatment at higher temperatures (>882°C) could cause a significant decline in the bulk mechanical properties of the metal such as fatigue resistance (Yue *et al* ,1984 and Lynn and DuQuesnay, 2002b).

2.3.6 Electrochemical deposition

During electrochemical deposition, a thin coating is obtained by passing an electric current through an electrolyte contained between two electrodes. The electrolyte is usually an aqueous solution of a metal salt such as zirconyl nitrate ($ZrO(NO_3)_2$ or titanium tetrachloride($TiCl_4$) (Hsu *et al*, 2009a, Lin and Yen, 2005 and Yen *et al*, 2006)

The metal substrate usually serves as the cathode in the system whereas the anode is a non reactive material such as graphite or platinum. Coating deposition is then followed by heat treatment in order to facilitate crystallization.

One major advantage of this coating synthesis method is the fact that it occurs at room temperature. The chemical composition of the coating obtained using this method can also be controlled to a great degree. However, the requirement for post deposition annealing is a drawback.

2.3.7 Micro arc deposition

In this technique, the metal substrate to be treated is immersed in an electrolyte as an anode and a positive voltage applied (**Figure 2.11**).

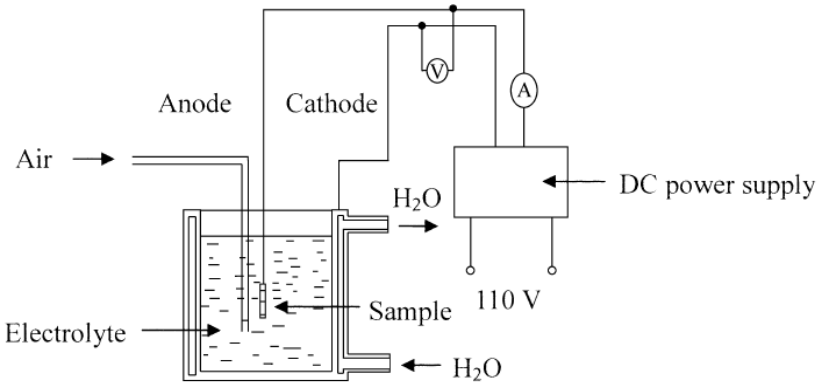

Figure 2.11 Illustration of micro arc oxidation (Liu *et al,* 2005)

When the voltage exceeds a certain value, dielectric break down of the surface oxide layer occurs, accompanied by visible micro-arcs. Simultaneously, Ti ions from the metal and OH ions from the electrolyte quickly migrate in opposite directions to form TiO_2 again. At present, sulphuric acid, nitric acid, phosphoric acid, sodium hydroxide, calcium acetate monohydrate, calcium glycerophosphate and natrium glycerophosphate are among the electrolytes that have been used for the fabrication of titania on titanium and titanium alloy substrates. However, Yao *et al* (2008) have also reported obtaining zirconia containing films on a Ti alloy substrate using a Zirconate electrolyte K_2ZrF_6.

Initially, a smooth film is obtained. However, some regions soon develop cracks and become porous. Upon increasing the voltage the film breaks down locally and regions of original and modified film develop simultaneously with the latter occupying more space, which gives rise to a coating with a combination of flat and porous regions. The characteristics of the coatings obtained are determined by the deposition parameters with, pore size and porosity increasing with the applied voltage (Song *et al*, 2004, Abdullah and Sorrell, 2007, Huang *et al*, 2005, and Kim *et al*, 2009). Frauchiger *et al* (2004) further demonstrated an increase in porosity with a corresponding increase in electrolyte, concentration whereas Song *et al* (2004) and Abdullah and Sorrell (2007) reported an increase in coating thickness with applied voltage and treatment time.

2.3.8 Sol-gel processing

The sol-gel process is a wet chemical technique (chemical solution deposition) for the synthesis of ceramic materials and films. This process involves the evolution of inorganic networks through the formation of colloidal suspension (sol) and the gelation of the sol to form a network in a continuous liquid phase (gel).

The initial step in the sol-gel process involves the formation of an inorganic polymer by hydrolysis and condensation of the precursor solution, resulting in the formation of a highly cross-linked sol. The precursor materials are typically aqueous solutions of inorganic salts or metal alkoxides $M(OR)_n$, where M is usually a transition metal atom and (OR) an alkyl group such as C_2H_5O. The latter have been more widely used owing to benefits such as greater process control and higher phase purity of the final product. These materials tend to be highly reactive. This is a direct consequence of the low electronegativity of the transition metals, such that their oxidation state is frequently lower than their coordination number in an oxide network. Therefore, coordination expansion occurs spontaneously upon reaction with water or other nucleophilic species

to achieve desired coordination. Metal alkoxides are also rendered highly susceptible to nucleophilic attack by the presence of the highly electronegative OR groups which stabilize the metal atom in its highest oxidation state.

Hydrolysis leads to a sol which is a dispersion of colloidal particles in a liquid. Hydrolysis is typically attained in the presence of water (aqueous route) or in the presence of an organic solvent under the exclusion of water (non-aqueous route). The latter is considered to be more desirable as the moderate reactivity of the oxygen-carbon bond in the organic solvent results in a slow and steady rate of reaction compared to water.

Condensation results in a gel, which is an interconnected, rigid and porous network enclosing a continuous liquid phase. This is called the sol-gel transition. Gel formation is followed by aging, drying and crystallization. The various processes involved in the sol-gel synthesis are illustrated in **Figure 2.12**.

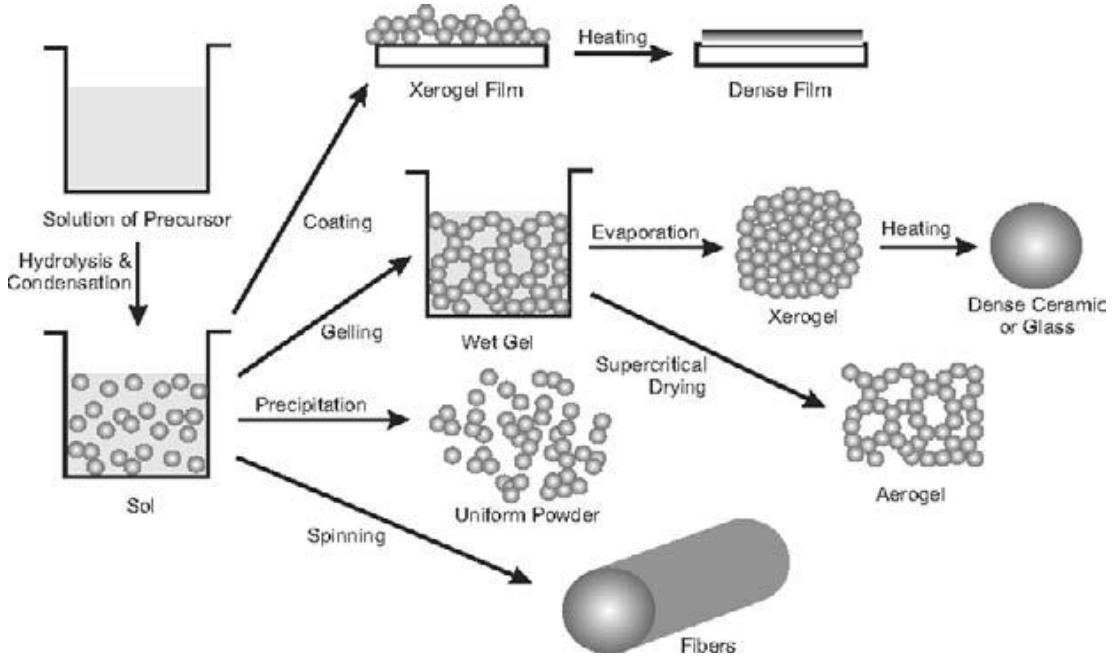

Figure 2.12 Various processes involved in the control of the morphology of the sol-gel product (Niederberger and Pinna, 2009)

The hydrolysis and condensation reactions are affected by the electropholicity of the metal, the strength of the entering nucleophilic and the stability of the group. The sol-gel process is also affected by the complexity of the alkoxy groups which in turn causes stearic hinderance. The molecular structure of the metal alkoxide (monomeric or oligomeric) is also critical inasmuch as it affects the reactivity of the terminal OR groups

which renders monomeric alkoxides more advantageous than their oligomeric counterparts. Other factors affecting the sol-gel process include the amount of water added and the rate of addition as well as the polarity, dipole moment and acidity of the solvent.

However while Sol-gel synthesis offers a great level of control of the chemical and microstructural composition of the coatings obtained and is a low cost process with simple equipment; it is also associated with residual stresses within the coating owing to the requirement for post deposition heat treatment.

Table 2.6 summarizes the salient characteristics of the various film deposition methods**.**

Table 2.6 Comparison of film deposition techniques

Method	Thickness	Advantages	Disadvantages
Thermal spraying	30-200 µm	-High deposition rate -Low cost	-Line of sight -Amorphous films -Impurity phases -Microcracking -
Sputtering	0.05-0.5 µm	-Produces uniform coatings on flat surfaces -Produces dense coatings	-Line of sight process -Low deposition rate -High cost -Gives amorphous films
Sol-gel processing	<1 µm	-Thin coatings -Enables coating of complex shapes -Low process temperatures - Forms crystalline coating	-Requires precise control over process conditions -Expensive raw materials
Electrochemical deposition	≈80µm	-Uniform coating structure -No impurity phases -Ambient processing temperatures	-Complicated equipment set up
Electron beam deposition	<200nm	-High deposition efficiency -Offers a high level of control over film morphology	-Produces amorphous films hence heat treatment is required -Requires precise control over processing
Microarc oxidation	<1 µm	-Allows coating of complex geometries -Allows easy fabrication of composite coatings	-Involves high processing temperatures -Complicated equipment set up -Produces amorphous films
Thermal oxidation	<10nm	-Versatile -Easy set up	-Offers no control over coating thickness and morphology -Degradation of metal properties

As shown, each of the methods produce films that are several micrometers to millimeters thick. Currently, thermal spray methods and in particular plasma spraying is the most widely documented and commercially utilized method. However, this complex and expensive method has several drawbacks as summarized whereas the alternative methods are largely in the research stage. To overcome these challenges, alternative film deposition methods are being investigated.

Electrohydrodynamic atomization has recently been developed for the synthesis of thin ceramic films for semiconductors, solid electrolytes and lithium battery materials. Using this method, various types of ceramic materials can be deposited as thin films. Compared to alternative film deposition methods, this ambient temperature film deposition method requires the use of a simple equipment set up and is cost effective with a high deposition efficiency. Moreover, this method enables film deposition on complex geometries and also enables the tailoring of the film morphology depending on the process parameters.

2.4 Electrohydrodynamic atomisation

Electrostatic atomisation describes the process whereby a liquid jet disintegrates into an aerosol due to the influence of an electric field (Grace and Marjnissen, 1994). This process has been classified into different modes according to two major criteria namely; the geometrical form of the liquid at the nozzle outlet and the mechanism of disintegration of the jet into droplets (Jaworek and Krupa, 1999). These two criteria are also responsible for the geometrical shape of the aerosol and to a lesser degree the size of the droplets obtained.

The geometric form of the different modes differs vastly when observed in continuous light. This arises from the microstructure of the jet, its formation and disintegration into drops. Typically each mode occurs suddenly at a certain flow rate and voltage and is maintained within a given range of values before abruptly changing into a different mode upon changing either the voltage or the flow rate.

The spray modes are further divided into two categories. The first category encompasses those modes in which only fragments of liquid are emitted from the nozzle directly and comprises the dripping, micro-dripping, spindle, multi spindle and ramified meniscus jet modes.

The second category includes the modes in which the liquid is ejected from the nozzle exit in the form of a long continuous jet which disintegrates into droplets some distance,

usually a few mm, from the nozzle outlet. The jet can either be stable, oscillating or rotating around the nozzle rim. The cone jet, precession, oscillating jet, multijet and ramified jet modes all fall in to this category.

The various spray modes and their salient features have been summarized in **Tables 2.7 and 2.8,** respectively.

Table 2.7 Forms of liquid emmision (Jaworek and Kruppa, 1999)

Category 1		**Category 2**	
Dripping		Oscillating	
Microdripping		Precision	
Spindle		Cone jet	
Multispindle		Multi jet	
Ramified meniscus		Ramified jet	

Table 2.8 Features of electrospray modes (Jaworek and Krupa, 1999)

Spraying mode	Form of the meniscus and jet	Dynamics of the meniscus/jet	Forms of liquid emitted	Sprayed aerosol
		Fragments of liquid		
1. Dripping mode	Semi-spherical meniscus	Axially vibrating	Simple regular drop (with trailing thread or sibling)	Single drop (with siblings)
2. Microdripping mode	Cone meniscus (linear or convex)	Axially stable	Simple drop (with trailing/leading thread)	Series of droplets (accompanied with fine mist)
3. Spindle mode	Cone/semispherical meniscus	Axially vibrating	Elongated fragment of liquid (spindle) (with trailing thread)	Spindles (accompanied with fine mist)
4. Multispindle mode	Flat/multi-cone	Stable/Laterally vibrating	Multiple spindles (with leading/trailing thread)	Spindles generated around the axis (accompanied with fine mist)
		Liquid jets		
5. Cone-jet mode	Cone meniscus (linear, concave, convex, skewed)	Axially stable	Simple straight linear jet with varicose or kink instabilities	Fine nearly monodisperse aerosol
6. Oscillating-jet mode	Skewed cone	Oscillating in a plane	Oscillating in a plane with kink/oscillating instabilities	Fine aerosol sprayed in ellipsoidal-base cone
7. Precession mode	Skewed cone	Rotating around the capillary axis	Rotating around the capillary axis with centrifugal (spiral) instabilities	Fine aerosol sprayed in a regular cone
8. Multijet mode	Flat, with small cones on the rim	Stable	Multiple jets (usually with kink instabilities)	Fine aerosol
9. Ramified-jet mode	Irregular	Randomly changed	Irregular fragments	Irregular droplets sprayed in unpredictable directions

2.4.1 The stable cone jet mode

The widespread interest in the stable cone jet mode stems from its ability to produce near monodisperse liquid droplets. Electrostatic atomisation in the cone jet mode has been the subject of many works of research for many years. Since the pioneering work of Zeleny (1917), several researchers have added to the body of knowledge regarding this process. During this process, the electrical stresses are able to overcome the surface tension forces which results in the transformation of the droplet into a cone shape. At the cone apex, a liquid jet with a high charge density occurs. This jet is usually 100 micrometers in diameter (Hartman, 1999). In some instances the jet disintegrates into highly charged main droplets with a narrow size distribution and number of smaller secondary and satellite droplets (Cloupeau and Prunet-Foch, 1989, Tang and Gomez, 1994 and Chen *et al*, 1995). However, the total volume of the secondary and satellite droplets is relatively low compared to that of the main droplets.

2.4.1.1 Mechanism of cone jet formation

Electrostatic atomisation in the stable cone jet mode occurs in three stages (Hartman, 1999). The first stage involves the acceleration of the liquid in the liquid cone. The cone shape is known as a Taylor cone after the man who first analytically calculated it and is the result of the balance of the outward stress due to the applied electric field and the

inward stress due to the surface tension. Gravitational, inertial and viscous forces also play a role in determining the shape of the cone.

The balance of the various forces is also critical in the acceleration of the liquid in the cone. It has been established that liquids generally transport charge in the form of ions, with free charges mainly existing at the liquid surface. At the onset of cone jet formation, the electric field lines penetrate the liquid and cause the ions in the liquid to move to the surface of the solution at a rate that is determined by the electrical relaxation time constant. This property is dependent on the electrical conductivity and the absolute permittivity. The presence of the surface charge results in a minimal normal electric field inside the liquid compared to outside the liquid. The surface charge shields the bulk of the liquid from the influence of the electric field hence there are no free charges inside the liquid. At the same time, the tangential electric field accelerates the ions at the liquid surface towards the cone apex. Thus there is a high charge density within this region. A thin jet subsequently emerges from the cone apex. The forces acting on the Taylor cone are shown in **Figure 2.13.**

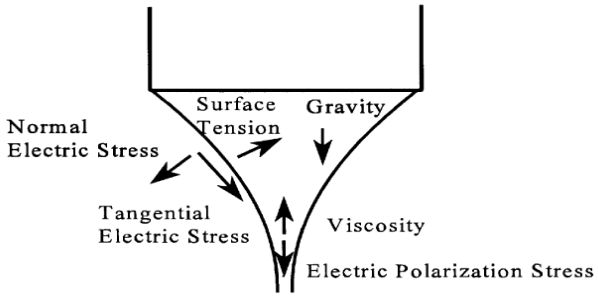

Figure 2.13 Forces acting in the liquid cone (Hartmann *et al*, 1999)

The second stage is the breakup of the jet into droplets. The size distribution of the droplets generated in this mode is highly dependent on the jet diameter and on the breakup of this jet into droplets. For every liquid, there is a minimum flow rate below which a stable cone jet cannot be obtained. At this minimum flow rate, the jet breaks up due to axissymetric instabilities. These instabilities are also known as varicose instabilities. Upon increasing the flow rate, the current through the liquid cone increases which in turn increases the surface charge on the jet. Above a certain surface charge, the jet break up will also be influenced by lateral or azimuthal instabilities (kink instabilities) When the influence of these instabilities increases then the size distribution of the main droplets becomes larger (Cloupeau and Prunet-Foch,

1989, Hartman, 1999 and Hartman, 2000). The two types of instabilities are illustrated in **Figure 2.14**.

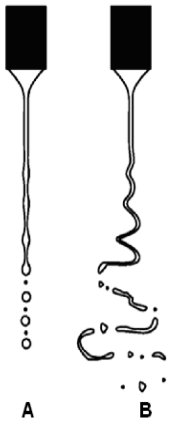

Figure 2.14 Jet break-up (A) Axissymetric (varicose) instabilities and (B) Azimuthal (kink) instabilities (Hartmann, 2000)

The third stage is the development of the aerosol after the droplets have been formed. Since the droplets are highly charged and bear different sizes and thus different inertia, size segregation occurs such that the smaller droplets are found at the edge of the spray whilst the large droplets are at the spray centre (Ganan-Calvo *et al*, 1994). If the highly charged droplets evaporate, then the Rayleigh limit for droplet charge is reached causing the droplet to split up (droplet fission)

This phenomenon was first reported by Rayliegh in 1882 (Miao *et al*, 1999). He calculated the electric charge beyond which a droplet is no longer stable. This critical charge Q_R will be reached if the electrostatic pressure directed outward is equal to the capillary pressure directed inward as is given as as follows;

$$Q_R=2\pi\ (2\varepsilon\gamma D_d^3)^{1/2} \qquad (2.1)$$

Where ε is dielectric constant, γ is liquid surface tension, and D_d is Droplet diameter.

Droplet fission changes the produced size distribution. Droplet size and charge vary according to the liquid flow rate and liquid properties, namely, density, viscosity, conductivity, electrical permittivity, and surface tension. Therefore, the main droplet size produced ranges from nanometers with production frequencies in the order of 10^9 Hz to hundreds of micrometers with production frequencies of about 10^4 Hz. (Meesters *et al*, 1992 and Hartman, 1998).

2.4.1.2 Stable cone jet criteria

Ganan-Calvo *et al* (1997) postulated that electrostatic atomisation in the cone jet mode can only occur if the hydrodynamic time (t_h) is much greater than the electrical relaxation time (t_e). The hydrodynamic time is the time required for fluid particles with a characteristic velocity U to move across a zone of characteristic length L. This condition is given as follows;

$$t_h >>> t_e \tag{2.2}$$

$$\frac{LD^2}{Q} >>> \frac{\beta\varepsilon_O}{\kappa} \tag{2.3}$$

Where Q is Flow rate, K is Electrical conductivity, β isRelative permittivity, ε_O is Permitivity of a vacuum

Therefore, liquids with an electrical relaxation time higher than the hydrodynamic time cannot be sprayed using electrostatic atomization.

2.4.2 Film production using the electrostatic atomization

Film formation using electrostatic atomization involves several steps many of which occur sequentially or concurrently after droplet formation and include droplet transport, evaporation, disruption; preferential landing of droplets, discharge, droplet spreading, penetration of droplet solution, drying, surface and diffusion all of which have some bearing on the morphology of the films produced.

2.4.2.1 Droplet transport

This occurs due to the interaction between the highly charged droplets and the grounded substrate. It is well known that a charged droplet is attracted towards a grounded substrate by a coulomb force. Hence, the charged droplets are directed towards the substrate by the electric field. The flight time is mainly affected by the viscous forces due to the surrounding atmosphere, although gravitational forces may be ignored as the droplet sizes are usually very small.

2.4.2.2 Solvent evaporation and droplet disruption

Evaporation comes into play during droplet transport and is greatly dependent on the volatility of the fluid as well as external factors such as the nozzle to substrate distance, humidity and the processing temperature (Wilhelm *et al*, 2003).

In the case of highly volatile liquids and or long nozzle to substrate distances, high processing temperatures or low humidity, shrinkage of droplets may occur although the total charge remains constant (Abbas and Latham, 1967). An excessive drop in droplet diameter could lead to droplet disruption once the maximum charge density has been reached. This is known as the Rayleigh limit. The disruption of a droplet due to this phenomenon yields a number of highly charged, very tiny droplets hence the size distribution is no longer near mono disperse.

For non volatile solvents, the droplet size remains fairly constant thus the droplet size distribution is more or less mono disperse. This also occurs for low processing temperatures and short nozzle to substrate distances.

2.4.2.3 Preferential landing of droplets on the substrate

The electric field also induces charges on the substrate surface. These charges bear a sign opposite to that of the droplets or nozzle. The charge distribution is generally non uniform and depends on the position of the substrate relative to the nozzle as well as the local curvature at the substrate surface. The surface charge is usually more concentrated in regions of higher local curvature; hence droplets approaching the substrate tend to be more attracted towards these regions where they lose their charge almost instantaneously upon landing. This is known as preferential landing and causes agglomeration of particles (Chen *et al*, 1996). This occurrence also causes the replication of the substrate surface profile by the coating.

2.4.2.4 Droplet spreading

Droplets arriving at the substrate surface spread rapidly at a rate determined by the viscosity of the liquid. Ideally, the spreading rate should be inversely proportional to viscosity. The spreading rate is also determined by the surface tension at the interface at the interface between the droplet and the substrate surface. However, spreading occurs simultaneously with solvent evaporation (Davies and Rideal, 1961).

2.4.3 Factors affecting electrostatic atomization

The electrostatic atomization process is governed by liquid properties such as density, surface tension, viscosity and electrical conductivity. Applied voltage, liquid flow rate, nozzle characteristics an, nozzle-to-substrate distance also govern the atomisation process.

2.4.3.1 Applied voltage

Applied voltage is a fundamental parameter during the electrostatic atomisation process since atomisation is due to the electrical field produced by this parameter. The electric field can be controlled by varying the applied voltage V. Thus a higher voltage can be expected to produce a stronger atomisation effect.

In investigations carried out by Cloupeau and Prunet-Foch (1990) and later Tang and Gomez (1996), applied voltage affected the spray mode obtained. At lower flow rates, the dripping and microdripping modes are seen to occur whereas the cone-jet and multi-jet modes are manifested when the applied voltage is increased further.

Applied voltage also affects the shape of the cone as reported by Hayati *et al* (1987a) and Jayasinghe and Edirisinghe (2004). Upon increasing the applied voltage to the fluid the cone depth decreases with an accompanying decrease in jet diameter. Hayati and colleagues (1987b) further observed that the point at jet break up occurs during atomisation shifts closer to the nozzle exit when the applied voltage is increased. Moreover, these authors further reported that the cone angle became larger when the applied voltage was increased.

The applied voltage also influences the droplet sizes. Jayasinghe and Edirisinghe (2002 and 2004) showed that relic size and hence droplet size became increasingly smaller with an increase in voltage. This trend had earlier been reported by Tang and Gomez (1996) in whose work the droplet size decreased monotonically when the voltage applied to low conductivity solution is increased. In the case of Hartman *et al* (2000) higher applied voltages also brought about an increase in the number of secondary droplets and satellites as a result of increase current through the spray cone. But, where the aforementioned researchers documented a correlation between applied voltage and droplet size, De La Mora and Loscartales (1994) observed no correlation between droplet size and applied voltage for high conductivity liquids. However, high voltages generally yield a more atomising effect.

2.4.3.2 Flow rate

Flow rate is another critical parameter in determining both the droplet size and the stable cone jet regime. Flow rate is generally varied by the nozzle cross sectional area or the pump output (Tang and Gomez, 1996). Grace and Marjnissen (1994) have classified the possible flow rate ranges into two, namely, high (> 10^{-5}ml/s) and low (<10^{-5}ml/s). Meesters and co-workers (1992) demonstrated that high flow rates were only able to produce a taylor-like cone but no visible jet, whereas Balachandran *et al* (1992) were able to obtain a stable cone jet when spraying highly conducting liquids at high flow rates. However, Jayasinghe and Edirisinghe (2004) reported that liquids with high flow rates possess high kinetic energies which cannot be compensated by surface tension thus the liquid simply becomes a jet and breaks into droplets.

The effect of the flow rate is evident in the work of De La Mora (1992) where low flow rate conditions typically generated monodisperse droplets in the submicron range. Furthermore, Chen *et al* (1995), Tang and Gomez (1996) and Balachandran *et al* (2001) further showed that droplet size increased with liquid flow rate. Similarly, Jayasinghe and Edirisinghe (2004) observed that relic size and as such droplet diameter increases as the flow rate is increased. The increase in droplet size with flow rate has been attributed to an increase in production frequency as well as an increase in jet diameter.

The flow rate also has a major role in determining the deposition area. According Chen and colleagues (1999) the spray area can be determined as follows;

$$A_{spray} = \pi [H \tan \frac{\alpha}{2}]^2 \qquad (2.4)$$

Where H is Nozzle to substrate distance, α is spray angle which is the angle between the spray cone and the nozzle to substrate distance.

These researchers noted that a larger flow rate yielded a larger spray angle. Consequently, the spray area can be expected to increase with the flow rate. It has also been reported that an increase in flow rate encourages stability of the spray jet (Hayati *et al*, 1987a and Balachandran *et al*, 2001). On the other hand this is at the expense of an increase in droplet size. Moreover, Rosell-Lampart and De La Mora (1994) reported that droplet modality increases with flow rate while Hartman *et al* (2000) found that the production of secondary droplets and satellites increased when the flow rate increased due to an increase in current through the spray cone. Hence monodispersity is attained at lower flow rates.

2.4.3.3 Nozzle to substrate distance

The nozzle to substrate distance also influences the electrostatic atomization process. Firstly, Tang and Gomez (1996) demonstrated this parameter affects the onset voltage for cone jet formation such that the onset voltage is increased with an increase in the nozzle to substrate distance. Noymer and Garel (2000) further reported that the voltage range under which a stable cone jet can be maintained increases non linearly with the nozzle to substrate distance. The influence of this parameter arises from the fact that the strength of the electric field is determined by the ratio of the applied voltage to the distance between the electrodes which in this case is the nozzle to substrate distance. The non linearity of the relationship between the nozzle to substrate distance and the voltage can be explained as follows; The intensity of the electric field near the nozzle tip is the main controlling factor in the nature of the emitted droplets of which the dominant dimension for intensity of the field near the tip is the nozzle exit and not the distance from the substrate.

From a film deposition perspective, the nozzle to substrate distance affects the spray distance. This is evident from equation 2.4 which implies that the spray area is directly proportional to the nozzle-to-substrate distance.

2.4.3.4 Nozzle characteristics

Tang and Gomez (1996) reported that the nozzle diameter has little or no effect on the droplet size and confirmed that the nozzle diameter affects the electrostatic atomisation in terms of the applied voltage and flow rate regime. It was seen that the maximum flow rate for stable cone jet formation underwent a significant reduction once the nozzle diameter was increased, accompanied by an corresponding increase in minimum flow rate. A similar trend was found by Cloupeau and Prunet-Foch (1989). In contrast, Chen *et al* (1999) observed that maximum flow rate achievable for cone jet formation increased with an increase in nozzle diameter. Moreover, they reported a definite shift to higher applied voltage ranges with the use of larger nozzle diameters. An increase in nozzle diameter further influences the liquid velocity. Hayati *et al* (1986a) reported that a reduction in the nozzle diameter increased the fluid velocity which subsequently made the jet more stable.

Smith (1986) reported that the applied voltage for jetting in the stable cone jet mode bears a positive correlation to the needle internal diameter. He proposed that the applied voltage is related to the needle internal diameter according to equation 2.5

$$V_o = A_1(2\cos\theta_o)^{\frac{1}{2}}(\kappa R_a/\varepsilon_o)^{\frac{1}{2}}\ln(4H/R_a) = \kappa R_a^{\frac{1}{2}}\ln(4H/R_a) \quad (2.5)$$

Where V_o is applied voltage for electrospraying in the steady cone-jet mode, A_1 is an empirical parameter ranging from 0.5 and 0.707, θ_o is 49.29^o (Taylor's angle), R_a is needle internal diameter, ε_0 is permittivity of vacuum, κ is electrical conductivity, and H is needle to ground electrode spacing.

The variation of V_O with respect to the variation of R_a can be obtained from

$$dV_o/dR_a = (\kappa/2)\ln(4H/R_a)/R_a^{\frac{1}{2}} + \kappa R_a^{\frac{3}{2}}/(4H) \quad (2.6)$$

When H> R_a, then dV_O/dR_a >0.

Aside from nozzle diameter, nozzle geometry also plays a major role in determining the conditions under which a stable cone jet can be attained. This is evidenced in Chen and colleague's (1999) work whereby a nozzle with an angular exit extended the upper flow rate limit for stable cone jet formation as compared to a nozzle with a flat ended exit.

Equally important is the wettability of the nozzle material. For highly wettable nozzles are thought to lead to liquid accumulation over all or a small part of the nozzle exit periphery, which in turn lowers the overall flow rate and electric field on the meniscus and thus destabilises the electrostatic atomisation process (Cloupeau and Prunet-Foch,1989). Hence a vertical nozzle arrangement is preferred over a horizontal arrangement, as it prevents excessive wetting effects at low voltage. Non wettable surfaces are also said to facilitate lower minimum flow rates for stable cone jet formation (Cloupeau and Prunet- Foch, 1994).

2.4.3.5 The influence of liquid physical properties

2.4.3.5.1 Electrical conductivity

This is the most important liquid physical property in the determination of both jet stability and droplet size. For liquids of low conductivity, there are insufficient free charges in the bulk of the liquid to create a surface charge hence the relaxation time is too long. Therefore the liquid undergoes a low electric force and is unable to be atomised. Instead the liquid is subjected to a dielectrophoretic force which causes the

liquid to migrate to the region of highest field intensity which in this case is the nozzle tip.

In the case of high conductivity liquids, the relaxation time is too short and can be smaller than the time for droplet formation. In this instance, the surface charge may build up in excess of the Rayleigh limit before a drop is completely formed and break away from the surface. This surface charge creates a normal stress on the drop which on its own is unable to produce stable jets. Thus sparking may be observed at the nozzle tip (De La Mora and Loscartales, 1992).

Several attempts have been made to identify the limiting values of electrical conductivity that permit atomization in the stable cone jet mode. For example Jones and Thong (1971) reported a maximum electric conductivity of 10^{-5} Sm^{-1} while Mutoh *et al* (1979) indicated a minimum electric conductivity of 10^{-7} Sm^{-1}. However, Smith (1986) has since pointed out that no such limit exists. For the sprayable liquids, an increase in electrical conductivity causes a shift of the maximum flow rate and voltage limits to the lower ranges (Cloupeau and Prunet-Foch, 1989, Chen *et al*, 1995, and Tang and Gomez, 1996). The relationship between electrical conductivity and the liquid flow rate during electrospraying in the cone-jet mode was qualitatively determined by Smith (1986). This author demonstrated that the liquid flow rate is related to the electrical conductivity according to the equation;

$$F=\frac{4\pi\varepsilon_o Sin\theta_o Cos\theta_o}{(1-\cos\theta_o)}\frac{\kappa T}{\rho\delta} \qquad (2.7)$$

Where ε_o is permittivity of a vacuum, κ is thickness of a thin layer of liquid in the cone, Θ_o is cone half angle, T is surface tension, ρ isdensity and σ is electrical conductivity.

A fall in average droplet diameter also occurs due to an increase in conductivity which is a direct consequence of the reduction in jet diameter and length (Chen *et al*, 1995, Tang and Gomez, 1996 and Chen *et al*, 1999).

2.4.3.5.2 Viscosity

Liquid viscosity plays a significant role in the jet break up process. It has been shown experimentally that the jet break up process of the electrospray is controlled by a natural surface wave instability. The size of the droplet therefore depends on the wavelength with the maximum growth rate along the liquid ligament which, in turn is determined by the liquid viscosity.

Rossel-Lompart and De La Mora (1994) introduced a dimensional parameter π_n to determine the influence of viscosity on the electrospray process.

$$\pi_n = \frac{\sqrt[3]{\frac{\gamma^2 \rho \beta \varepsilon_o}{\kappa}}}{\eta} \tag{2.8}$$

Where ρ is Density, ε_o is Permittivity of a vacuum, γ is Surface tension, κ is Electrical conductivity, η is Viscosity.

If π_n >>>1, the viscosity has no effect. However, if π_n <<1, then viscosity has an effect on the jet break up process. Jaworek and Krupa (1999) and Jayasinghe and Edirisinghe (2002) noted that viscosity affected the cone shape with cone depth and diameter decreasing with an increase in viscosity. Also viscosity affects the droplet size such that an increase in this property increases with the average droplet diameter and size distribution as was reported by Smith (1986) and Jayasinghe and Edirisinghe (2002).

2.4.3.5.3 Surface tension

Since atomization only occurs once the electric force overcomes the surface tension, this property is of paramount importance as well. Smith (1986) demonstrated that the onset voltage for stable cone jet formation increased with a concurrent increase in surface tension. However, if the surface tension is too high then a stable cone jet may not be established, as the field required could exceed the dielectric break down of the surrounding gas leading to corona discharge (Cloupeau and Prunet-Foch, 1990 and Tang and Gomez, 1996). An increase in surface tension also increases the polydispersity of the droplets obtained and increases the maximum flow rate for stable cone jet formation as shown in Equation 2.8.

2.4.3.5.4 Density

Density plays a major role in the acceleration processes of the liquid near the cone apex. Studies by Hartmann *et al* (2000) indicated that an increase in liquid density reduces the minimum flow rate required to give the cone-jet mode as well as the droplet size.

2.4.4 Scaling laws

The relationship between the liquid physical properties and the droplet size and spray current have been experimentally and dimensionally determined by Ganan-Calvo *et al* (1997).

For liquids of high viscosity and conductivity the current and droplet diameter are governed by the $Q^{1/2}$ law such that

$$I \sim \frac{(QK\gamma)^{1/2}}{(\beta-1)^{1/4}} \tag{2.9}$$

$$d \sim \left[\frac{(\beta-1)^{1/2} Q\varepsilon_o}{K}\right]^{1/3} \tag{2.10}$$

Liquids of low viscosity and conductivity on the other hand are governed by the $Q^{1/4}$ law giving

$$I \sim \left[\frac{\gamma^3 \varepsilon_o K Q}{\rho}\right]^{1/4} \tag{2.11}$$

$$d \sim \left[\frac{\rho\varepsilon_o Q^3}{\gamma K}\right]^{1/6} \tag{2.12}$$

Where I is spray current d is droplet diameter, ρ is liquid density, ε_o is Permittivity of a vacuum, γ is Surface tension, κ is Electrical conductivity, η is Viscosity.

2.4.5 Deposition of ceramic films by electrospraying

As in the case of alternative film deposition, the morphology of electrosprayed films is strongly dependent on the film deposition parameters. Therefore, four types of film morphology have been reported. These include Type (I) dense film morphology, Type (II) dense film morphology with incorporated particles, Type (III) porous top layer with dense bottom layer and Type (IV) fractal-like porous morphology. The various morphologies are illustrated in **Figure 2.15**. These morphologies may be manifested depending on the processing parameters utilised.

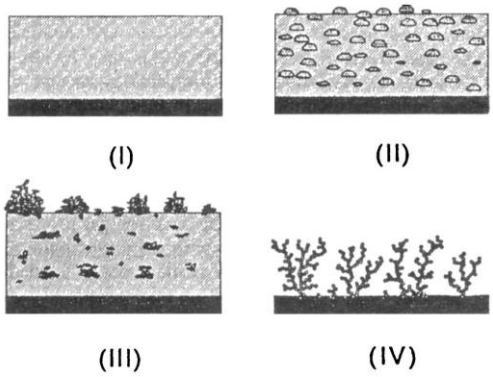

Figure 2.15 Types of morphology obtained during electrospraying (Chen *et al*, 1996a)

2.4.5.1 Effect of substrate temperature

Coating formation in the electrospraying process results from the evaporation of the solvent in the droplet and precipitation of salts contained in the precursor solution when it reaches the substrate. Consequently, the temperature of the substrate is important as it controls the evaporation rate of the solvent and precursor decomposition. Chen *at al* (1996a) found that a substrate temperature of 240°C resulted in the deposition of dense (Type I) Lithium films whereas a substrate temperature of 450°C gave a porous fractal-like film morphology (Type IV). However, Nguyen and Djurado (2001) reported that a substrate temperature of 300°C caused the deposition of dense but highly cracked tetragonal ZrO_2 films whilst highly porous films were obtained at a substrate temperature of 360°C. Neagu *et al* (2006) also reported that severely cracked ZrO_2 coatings were reported at the lowest deposition temperature of 480°C. However, a porous, fractal-like coating was obtained at the highest deposition temperature.

Similarly, Ghimbeu *et al* (2007) showed that dense but severely cracked SnO_2 films were obtained at a substrate temperature of 150°C whereas porous films were obtained at a substrate temperature of 400°C. Subsequent studies by Hwang *et al* (2007) also showed a strong dependence of NiO/CGO films on the substrate temperature. The lowest deposition temperature of 200 ºC yielded a severely cracked morphology. However, the highest deposition temperature of 450 ºC yielded a porous fractal-like morphology (Type IV). Consequently, it has been established that a low substrate temperature leads to a low evaporation rate of the solvent during droplet transport. Therefore, the fast evaporation of the solvent leads to a large volume change and as such mechanical stresses in the drying layer. The stresses are proportional to the amount of evaporated solvent which results in cracked coating morphology.

Increased substrate temperature reduces solvent evaporation, which in turn reduces cracking.

2.4.5.2 Effect of deposition time

It has been shown that an increase in deposition time results in the evolution of the film morphology from type I and type IV. This is particularly evident in the studies of Hwang *et al* (2007). A spray time of 10s gave a continuous flat NiO/CGO film. When the spray time was increased to 1 min, a scattering of particles was observed on a continuous flat bottom layer (Type II). At a spray time of 10 min, a cauliflower-like porous fractal morphology was observed (Type IV). Similarly, Chen *et al* (1996) reported that $LiCoO_2$ coatings exhibited a relatively dense morphology with incorporated particles after a deposition time of 1 h. Upon increasing the spray time to 6 h, a highly porous morphology was obtained. In other studies, Nguyen and Djurado (2001) showed that a deposition time of 0.1 h gave thin and dense ZrO_2 films whereas porous films were obtained after a spray duration of 2 h. This has been attributed to particle agglomeration. At a short deposition time, aerosol droplets land on the substrate. The rather wet droplets readily wet the substrate forming a continuous flat coating. Upon increasing the spray time, limited wetting occurs due to the reduced surface energy of the film. Consequently, agglomeration occurs giving rise to a highly porous morphology.

2.4.5.3 Effect of solvent concentration

The concentration of the precursor solution is another important process variable. Neagu *et al* (2005) reported that increasing the concentration of the zirconia precursor salt from 0.04 to 0.16 M increased coating thickness. However, the films became more non-homogeneous. Hwang *et al* (2007) also reported an increase in porosity with precursor concentration. Both research groups found that increasing precursor concentration also increased the conductivity. These findings concurred with the results of Taniguchi and Hozokawa (2008). The latter observed increasing the concentration of the SnO precursor solution from 0.005 to 0.05 mol/dm^3 increased the conductivity and thereby reduced the droplet diameter. Conversely, a lower concentration and hence a smaller conductivity increases the droplet size. Consequently, more droplet wetting occurs. Therefore a more uniform coating is obtained at a lower concentration.

2.4.5.4 Effect of precursor flow rate

Precursor flow rate also influences the coating morphology. Princivalle *et al* (2004) observed that a low flow rate yielded a dense and continuous La (S_r) $M_nO_{3-\delta}$ coating. However, a highly porous layer was obtained at higher flow rates. In contrast, Hwang *et al* (2007) reported a fractal-like coating at a low flow rate. However, dense uniform films were obtained at a higher flow rate. Similarly, Ghimbeu *et al* (2007) found that a low flow rate (1ml/hr) gave porous SnO_2 films whilst a flow rate of 4ml/hr gave a dense film morphology. The discrepancy in coating morphology can be explained by a difference in coating material and deposition parameters such as flow rate and substrate temperature. However, flow rate affects the droplet size which in turn affects the wettability of the droplets at the substrate.

2.4.5.5 Effect of needle to substrate distance

Changing the distance between the needle and the substrate affects the flux of matter that reaches the substrate, while the same quantity of solution is sprayed over a larger area of the substrate if the needle to substrate distance is increased and vice versa. Leeuwenburgh *et al* (2005) demonstrated that a uniform and reticular calcium phosphate film morphology could be attained at a nozzle to substrate distance of 10 mm whereas a porous film morphology was obtained at a needle to substrate distance of 30 mm. Consequently the film surface roughness was increased from 0.3-0.4 μm to 0.6-1.0 μm. Neagu *et al* (2006) reported that a short spray distance of 37 mm gave a severely cracked coating morphology. However, a dense and uniform coating was obtained upon increasing the distance to 57 mm. This was attributed to an increase in solvent evaporation as droplets travelled to the substrate which in turn reduces the amount of evaporation at the substrate and reduces material shrinkage and hence cracking.

2.4.5.6 Effect of solvent type

The morphology of the coating is determined by the droplet size and physical properties such as boiling point and spreading behaviour of the incoming droplets on the substrate. The latter properties can be modified by the solvent type. The influence of solvent type is clear in the studies carried out by Chen *et al* (1996). These authors reported that the morphology of $LiCoO_2$ films could be changed from highly porous and fractal-like to dense by utilising a 50 vol% ethanol +50 vol % butyl carbitol mixture as a solvent instead of 100% ethanol. Leeuwenburgh et al (2003) also obtained a fractal like

porous CaP morphology upon using ethanol as a solvent whereas butyl carbitol gave a dense, reticular film morphology. Similarly, Neagu *et al* (2005) reported that the homogeneity of zirconia films was drastically improved by the use of a butyl carbitol-water-ethanol mixture. These results have been attributed to a reduction in solvent evaporation due to the high boiling point of butyl carbitol (230 ºC) compared to ethanol (78 ºC).The presence of butyl carbitol also improves viscosity of the droplets which further improves coating uniformity.

2.4.5.7 Effect of substrate type and roughness

The substrate type also affects the spreading of the droplets. Chen and colleague (1996) compared the formation of $LiCoO_2$ coatings on alumina and aluminium substrates. The film obtained on the metal was fairly dense whereas a highly agglomerated coating was obtained on the oxide layer. Hwang *et al* (2007) also found that NiO/CGO coatings were dense and continuous on a silicon wafer substrate compared to stainless steel and glass substrates. This was attributed to the low water contact angle of this material (5.3º) compared to stainless steel (17.3º) and glass (25.2º). Substrate roughness also increases the occurrence of rough and highly porous coating morphology due to preferential landing of aerosol droplets.

Chapter 3 Experimental methods

This chapter provides a detailed description of the experimental methods that were carried out in this research. The materials used as well as their corresponding suppliers and details are introduced. The methods used in the preparation of the titania (TiO_2), zirconia (ZrO_2), hydroxyapatite (HA), and composite bioceramic suspensions and films are discussed in detail together with their subsequent characterization techniques. This chapter further presents the experimental set up that was utilized in the electrospraying of the bioceramic films. The equipment used in this research was calibrated against reference data. Reproducibility of the results was ensured by repeating the experiments at least thrice.

3.1 Materials

3.1.1 Solvents for bioceramic suspensions

Pure ethanol (etOH) (99.7 wt%, BDH laboratory supplies, Poole, UK) and 1-propanol (prOH) (Sigma-Aldrich, Gillingham, UK) and ethylene glycol (EG) (Sigma-Aldrich, Gillingham, UK) were used as liquid carriers for TiO_2, ZrO_2 and HA. Pure etOH was used as the standard material in the calibration of the characterization devices. The solvents were mainly distinguished by their boiling points. At ambient temperature, the evaporability of the solvents is in the order etOH>prOH>EG. The properties of the alcohols at ambient temperature are given in **Table 3.1**.

Table 3.1 Physical properties of the liquid carriers, stabilizing agent and dispersants

Liquid	Density (kgm^{-3})	Electrical conductivity $\times10^{-4}(Sm^{-1})$	Viscosity (mPa.s)	Surface tension (mN/m)	Boiling point (°C)
prOH	804	2.0	2.41	29.5	97
etOH	790	3.4	1.3	23.0	78
EG	1113	1.9	19.0	46.0	197.1

3.1.2 Bioceramic preparation

Nano-particles were considered to be more beneficial for use owing to their large surface area to volume ratio which could enhance ion and protein adsorption *in vivo* and *in vitro* as well as their larger number of grain boundaries which result in superior mechanical properties such as fracture toughness and hardness compared to micron-

sized particles. Nano-particles also require lower calcination temperatures. Furthermore, nano-sized HA closely resembles the naturally existing CaP phase in the body.

3.1.2.1 Metal oxide preparation

The metal-organic sol-gel route was selected for TiO_2 and ZrO_2 nano-particle synthesis due to its flexibility in terms of process control and its ability to produce phase pure materials. However, metal alkoxides are highly reactive and hydrolyzed instantly leading to the uncontrolled precipitation of polydisperse powders on addition of water. To circumvent this problem, the alkoxide molecules were chemically modified using alcohol molecules as shown below;

$$M(OR)_4 + mROH \longrightarrow [M(OR)_{n-m}(OX)_m] + mROH \quad (3.1)$$

Where M=metal atom and R=organic solvent (Livage and Sanchez, 1992).

3.1.2.1.1 Titania preparation

Titanium (IV) Isopropoxide, $Ti[OCH(CH_3)_2]_4$ (99.999% metals basis,Sigma-Aldrich, Poole, UK) was used as a precursor in the experiments. The TiO_2 suspensions were prepared by using 99.7% ethanol (etOH) (VWR international, Lutterworth, UK) and 99.5% Isopropanol (prOH) (Sigma- Aldrich, Poole, UK) as solvents. 2-8wt% TiO_2 suspensions were prepared by transferring TTIP to air tight bottles containing etOH and prOH, respectively. The resulting solutions were stirred for 3 hours at ambient conditions. The measurements for the precursors and solvent were carried out in a AND HF-1200G balance (A&D Instruments Ltd, Japan).

3.1.2.1.2 Zirconia preparation

Zirconium (IV) propoxide and zirconium propoxide complex (Sigma-Aldrich, Gillingham, UK) were used as precursors during the sol-gel synthesis of zirconia. 2wt% ZrO_2 sols were prepared transferring the ZrO_2 precursors to air tight bottles containing etOH. The resulting solutions were stirred for 3 hours at ambient conditions. The sol-gel process is summarized in **Figure 3.1**.

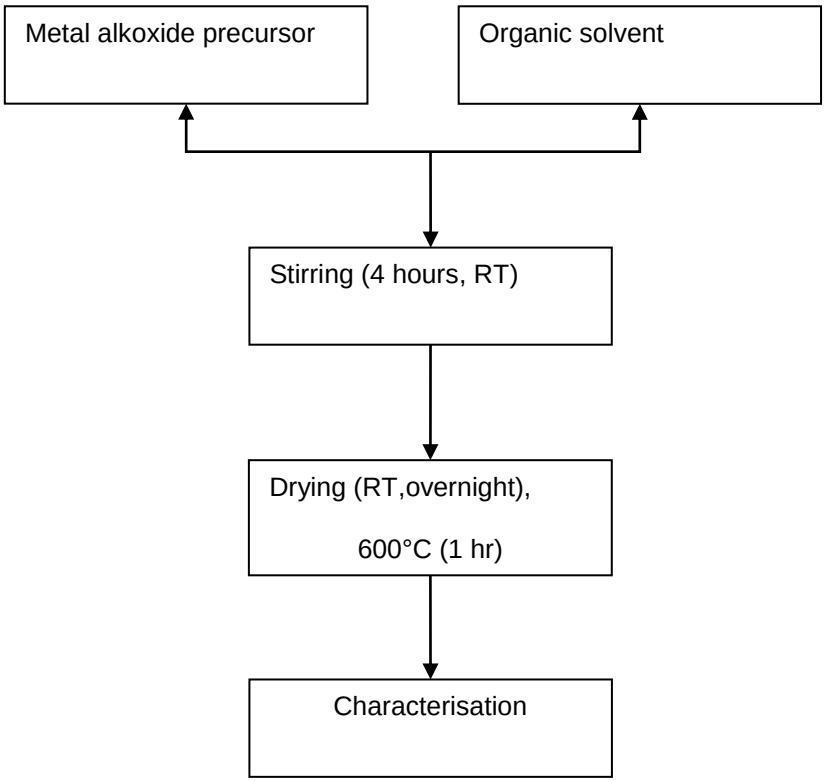

Figure 3.1 Flow chart showing sol-gel preparation of oxide nano-particles

3.1.2.2 Hydroxyapatite preparation

Nano-sized hydroxyapatite (HA) was synthesized by a precipitation reaction between calcium hydroxide (Sigma-Aldrich, Gillingham, UK) and orthophosphoric acid (Sigma-Aldrich, Gillingham, UK). Orthophosphoric acid was added dropwise to calcium hydroxide solution at a Ca/P molar ratio of 1.67, and the resultant solution maintained under continuous stirring at room temperature. The pH was kept above 10.5 by the addition of ammonium hydroxide solution (Sigma-Aldrich, Gillingham, UK). Stirring was carried out for a further 16h after addition of the reactants. The precipitate was allowed to settle for a week and washed with boiling water. The original water-based 25wt% HA suspension was then heated at 60 °C with constant stirring to evaporate the water content and then added to the solvent carrier at specific weight. HA suspensions were prepared by adding 2 wt% HA to etOH containing 0 to 10 wt% EG. The resultant suspensions were then subjected to ultrasonic agitation in a water bath for 15 mins at 200 W input power (Branson, USA). This was followed by stirring for 6-8 hours.

3.1.2.3 Composite suspension preparation

A series of HA/TiO_2 and HA/ZrO_2 composite suspensions were prepared by varying the proportion of the 2wt% HA, 2wt% TiO_2 and 2wt% ZrO_2 in the weight ratios of 75:25, 50:50 and 25:75 respectively. The suspensions and their corresponding labeling have been summarized in **Table 3.2.**

Table 3.2 Bioceramic sol and suspension labeling

Sol	Label
2wt% TiO_2 (prOH)	TP2
4wt% TiO_2 (prOH)	TP4
6wt% TiO_2 (prOH)	TP6
8wt% TiO_2 (prOH)	TP8
2wt% TiO_2 (etOH)	TE2
4wt% TiO_2 (etOH)	TE4
6wt% TiO_2 (etOH)	TE6
8wt% TiO_2 (etOH)	TE8
2wt% ZrO_2 (etOH/prOH)	ZEP2
2wt% ZrO_2 (etOH)	ZE2
2wt% HA (etOH)	HA
2wt% HA (2 wt% EG/etOH)	HA-2EG
2wt% HA (6 wt% EG/etOH)	HA-6EG (H100)
2wt% HA (10 wt% EG/etOH)	HA-10EG
2wt% TiO_2 (6 wt% EG/etOH)	T100 (TiO_2)
75wt% TiO_2:25wt%HA (6 wt% EG/etOH)	T75H25
50wt% TiO_2:50wt%HA (6 wt% EG/etOH)	T50H50
25wt% TiO_2:75wt%HA (6 wt% EG/etOH)	T25H75
2wt% ZrO_2 (6 wt% EG/etOH)	Z100 (ZrO_2)
75wt% ZrO_2:25wt%HA (6 wt% EG/etOH)	Z75H25
50wt% ZrO_2:50wt%HA (6 wt% EG/etOH)	Z50H50
25wt% ZrO_2:75wt%HA (6 wt% EG/etOH)	Z25H75

3.1.3 Suspension characterization

Liquid physical properties play a major role in the establishment of the stable cone-jet mode. The liquid flow rate regime is affected by the density and electrical conductivity whereas the atomisation voltage is influenced by the surface tension. The liquid viscosity has an impact on the cone-shape and jet break up process. Hence the liquid physical properties were characeterized. The equipment used for the characterization

was cleaned thoroughly using ethanol and distilled water and dried before each measurement. Characterization was carried out at ambient temperature.

3.1.3.1 Density

The densities of the suspensions were determined using a standard density bottle with a capacity of 25ml. The bottle was supplied by VWR international, Lutterworth,UK. The mass of the empty bottle and that filled with the suspension was measured and recorded using a weighing balance (AND HF-1200G, A&D Instruments Ltd, Japan). The density was thus obtained by obtaining the difference of the two masses and dividing the result by the capacity of the density bottle. Six consecutive measurements were taken and the average obtained which was then reported in this thesis. The measurements were carried out under ambient conditions and the density bottle calibrated using ethanol.

3.1.3.2 Surface tension

Surface tension was measured using the Wilhelmy plate method. A Kruss Tensiometer K9 was used to take the surface tension measurements. Approximately 30ml of suspension was placed in a beaker and placed on a stage under a Wilhelm plate which was hanging from a hook. The stage was raised so that the plate was fully submerged within the suspension. The stage was then slowly lowered and the reading recorded at the point that the bottom edge of the plate was approximately parallel to the liquid surface. Six consecutive readings were taken. The instrument was calibrated using ethanol and the plate cleaned thoroughly and dried before each reading was made.

3.1.3.3 Viscosity

Viscosity measurements were carried out using a U-tube viscometer BS/U type C in a water bath at 20°C. In order to obtain the kinematic viscosity, the samples were suctioned up the the u-tube. The time taken (t) for samples to travel between two marked regions in the viscometer after removal of suction was measured using a stop-watch with millisecond accuracy. The kinematic viscosity was obtained as follows;

$$\nu = Ct \tag{3.2}$$

Where ν = kinematic viscosity, C= Tube constant, t= Time

The dynamic viscosity (η) was then calculated by multiplying the kinematic viscosity with the relative density (ρ) of the suspension.

$$\eta = \nu\rho \tag{3.3}$$

Six time measurements were made for each suspension and the average reported in this thesis.

3.1.3.4 Electrical conductivity

Electrical conductivity was measured using a HI-8733 conductivity probe (Hanna instruments, Romania). Approximately 30mls were used for electrical conductivity measurements. The electrode was then submerged in to the suspension until the specified mark was covered by the suspension and held for up to 30 s while the suspension was slowly agitated in order to dislodge any air bubbles. A reading was then taken six readings were taken and then averaged.

3.1.4 Substrate preparation

The substrate utilized in this research for the deposition of bioceramic coatings was Ti alloy Ti6Al4V (Timex, UK) of 1 mm thickness. The Ti alloy plate was cut into square shaped plates measuring 10mm by 10mm. The Ti alloy plates were ground using silicon carbide papers grades 800, 1200 and 2500. The plates were then ultrasonically cleaned in distilled water for 10 minutes. This procedure was repeated using acetone and ethanol. The samples were subsequently dried at room temperature.

3.2 Electrospray equipment

The equipment set-up utilized for electrospraying is illustrated in **Figure 3.2**. The equipment set-up comprised of a stainless needle (Stanley engineering LTD, Birmingham) held in epoxy for insulation and rigidity. Three needles with internal diameter of 0.30mm, 0.50mm and 0.70mm were utilized. The external diameters were 0.635mm, 0.510 mm and 1.10 mm respectively. The needle in-let was connected via silicone tubing to a 1 ml syringe (Becton D plastic, Swindon, UK) mounted on a Harvard Apparatus PHD 4400 programmable infusion pump. The pump was calibrated for long and short periods of time prior to each new experiment. The needle was also connected via an electric cable to a FC30 P4 120W regulated high voltage DC power

supply (Glassman Europe Ltd, Hampshire, UK). The output voltage and output current range of this unit were 0-30kV and 0-4mA respectively. The operating temperature of the unit was in the range -20-50 °C. However, experiments were conducted at ambient temperature in this research. The needle outlet was illuminated by a fibre optic lamp and observed using a speedCam motionBLITZ high speed camera with a microscopic lens (Weinberger AG, Dietikon, Switzerland). The camera was connected to a PC.

3.2.1 Mode map selection

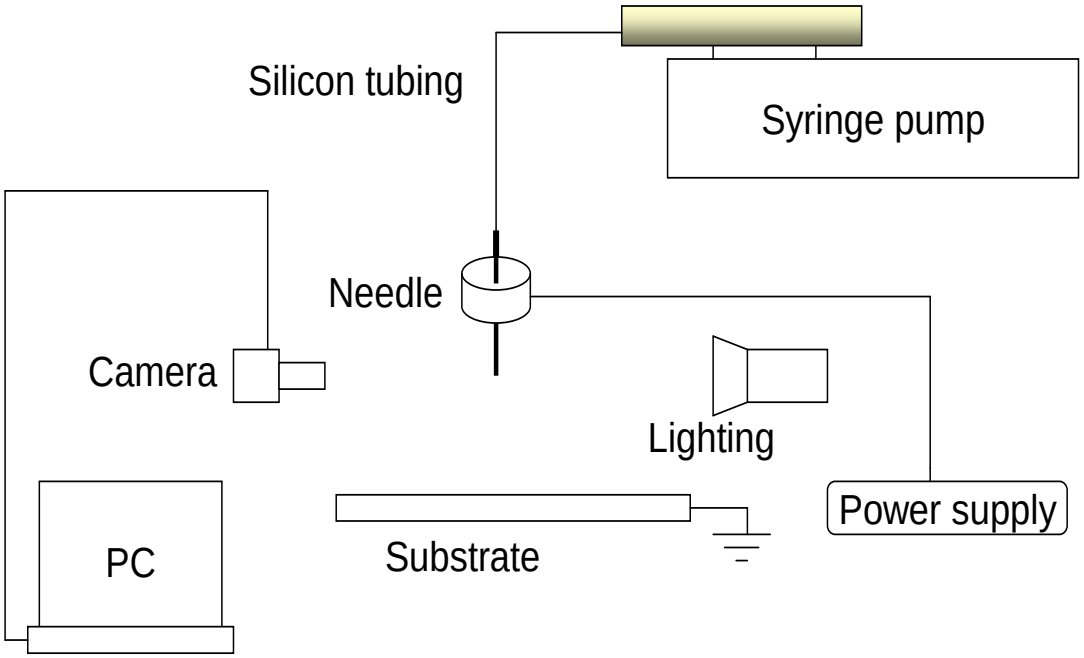

Figure 3.2 Schematic of electrospray equipment set-up

Prior to film deposition, stable cone-jet mode maps were established by varying the flow rate and applied voltage. For a given flow rate, there are two voltage limits beyond which a stable cone-jet mode cannot be attained. When these limiting voltages for the different liquid flow rates are connected, two limiting curves can be obtained which give the boundary of the stable-cone jet domain in the voltage-flow rate plane. The determination of the stable cone-jet domain is a key step in the achievement of optimum electrospray conditions for film deposition.

3.2.2 Film deposition

In film technology, a homogeneous and crack-free morphology is critical in order to prolong component service life. Therefore, film morphology was optimized by varying

several key parameters. Deposition time plays a critical role in determining film coverage and thickness. The flow rate is an important parameter inasmuch as it affects the stability of the cone jet. This deposition parameter also bears a significant effect on the droplet production frequency and droplet size (Ganan-Calvo *et al*, 1997). The needle to substrate distance has a significant role in determining the in-flight droplet size and ultimately film morphology (Princivalle *et al*, 2005, Leeuwenburgh *et al*, 2006, and Marinha *et al*, 2009). The needle to substrate distance also affects the deposition area (Chen *et al*, 1999). The needle internal diameter has two major effects. Firstly, it affects the maximum flow rate that can be attained during stable cone-jet formation. Secondly, it also has a major role in determining the jet diameter and therefore, the droplet size obtained at the needle exit. Sol concentration affects the liquid physical properties which in turn affects the droplet diameter and film thickness. Since film formation is due to the spreading of droplets at the substrate, the influence of the deposition parameters on the relic diameter was investigated firstly. The relics obtained from electrostatic atomization were collected by placing a microscopic glass slide directly below the needle exit.

3.2.3 Measurement of spray area

The bioceramic sols and suspensions were electrosprayed onto a Ti plate at a distance of 20 mm below the needle exit for a duration of 180 s. The diameter of the sprayed area was measured using vernier calipers. A large spray diameter is essential for a high deposition efficiency on large implants in industrial applications.

3.3 Optical microscopy

The relics obtained from electrostatic atomization were assessed using an optical microscope (Nikon Eclipse ME 600). The relics were then measured using ACQUIS digital imaging software (Synoptics Ltd, Cambridge, UK) and Image Pro plus software.

3.4 Heat treatment

It is well known that the mechanical properties and *in vitro* response of bioceramic films is significantly improved by thermal treatment. Hence the electrospray films were subjected to post deposition annealing (Olofinjana *et al* (2000). A laboratory furnace (Lenton thermal design, Ltd, Leicestershire, UK) was used to sinter the electrosprayed

films. The maximum temperature and output power of the furnace was 1600 °C and 5kW respectively. The furnace is equipped with a temperature program controller (Eurotherm 2216) by which the sintering temperature, dwell time and heating and cooling rates can be programmed. The heating programmes utilised in this research are illustrated in **Figure 3.3**.

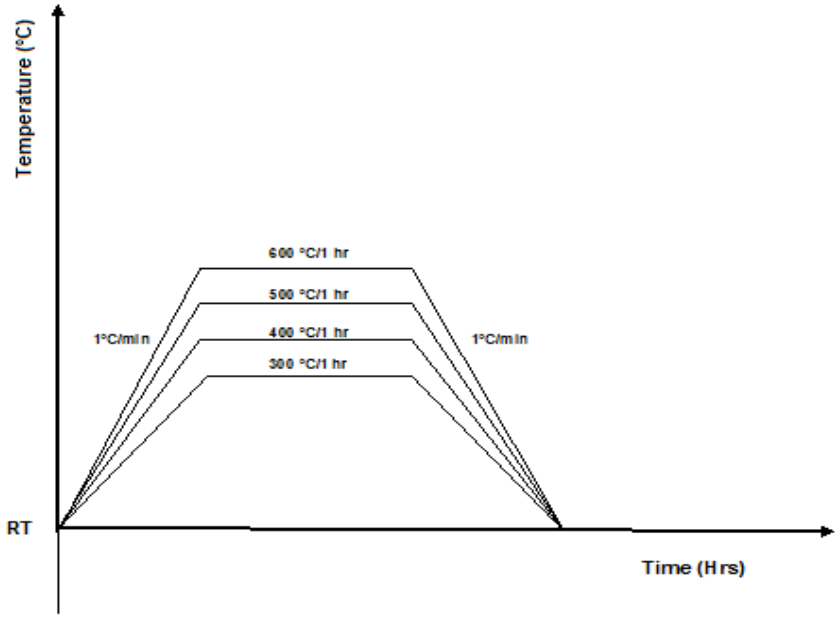

Figure 3.3 Programmes used in the annealing of the bioceramic films (RT represents room temperature)

3.5 Scanning electron microscopy

The morphological characteristics of the bioceramic films were observed using scanning electron microscopy. Two microscopes were used as per availability. The majority of the samples utilized in this research were observed using a Hitachi S-3400 N scanning electron microscope operating at an accelerating voltage of 20 kV and a working distance of 20 mm. A JEOL JSM 6300F field emission SEM was also used. This microscope requires very high vacuum conditions and the films became susceptible to charging at high accelerating voltage. Hence the voltage was reduced to 3-5 kV. A working distance of 15 mm was utilised. Prior to observation, the samples were mounted on top of cylindrical steel stub (25 mm x 37.5 mm) supplied by Agar Scientific, Essex, UK) and sputter coated with gold for 1-2 minute (Edwards sputter coater S150 B). For elemental analysis, the samples were mounted onto the aluminium stubs using LEIT adhesive carbon tabs supplied by Agar Scientific. The samples were

then carbon coated (CED 030 Carbon Evaporator, Balzers Ltd., Liechtenstein) using high purity carbon tread (TAAB Company, Aldermaston, UK). The elemental distribution map was plotted using INCA software (INCA Instruments, Oxford, UK).

3.6 Estimation of film thickness

The thickness (t) of the electrosprayed films was estimated from;

$$\Phi V = \Pi R^2 t \qquad (3.4)$$

Where Φ is the volume fraction of the nano particles, V is the Total volume of sol/suspension sprayed within a given time, R is the radius of the sprayed deposit, and t is the film thickness.

Assumptions; All of solvent evaporated upon reaching the ground substrate and the deposited films contained minimal porosity.

This calculation was used to estimate the thickness of the bioceramic films obtained in chapters **4, 5, 6** and **7**.

3.7 Film characterization

The successful fixation of implant materials is based on the existence of structural and functional bonding between the living bone tissue and the implant surface without the presence of intervening soft or fibrous tissue. The first step in the process of tissue-implant integration involves the attachment of the bone cells to the implant surface. This affects the subsequent cellular and tissue responses.

The interactions between biomaterials and cells are mainly affected by the surface characteristics which include surface roughness, surface energy and surface composition. It is widely accepted that rough and textured surfaces enhance cell attachment and stimulate cell differentiation and the formation of extracellular matrix as do hydrophilic surfaces. Cell attachment and metabolism are further affected by the surface chemistry and composition. Therefore, the surface characteristics of the electrosprayed films were analyzed since the interactions between the cells and the film surfaces occurred at their interface.

3.7.1 Raman spectroscopy

Raman spectroscopy is used for chemical identification, characterization of molecular structures, effects of bonding, environment and stress on samples. Raman spectroscopy is a light scattering technique whereby a photon of light interacts with a

sample to produce scattered radiation of different wavelengths which are characteristic of the bonds (vibrations) present and can be used to identify the material.

Raman scattering measurements were carried out using a Raman microscope (Horiba Instruments, Kyoto, Japan). The samples were in turn mounted on microscope slides and focused using the objective lens. Three different areas of the samples were selected and illuminated with the laser. The Ar^+ laser with 514.5 nm incident wavelength was used to illuminate the as-deposited and annealed films. Scanning was carried out over a range of 100-1400 cm^{-1} over an 8 hr period.

3.7.2 Fourier transform infrared spectroscopy (FTIR)

Fourier transform infrared spectroscopy (FTIR) is a qualitative analysis technique for the identification of compounds. This method relies on the use of infrared light which occurs between 0.7 and 500 µm in the electromagnetic spectrum between the visible and microwave regions. When IR radiation interacts with a molecule, the latter is excited to a higher vibrational state due to energy absorption. The wavelength of the light absorbed by a particular molecule is a function of the energy difference between the at rest and excited vibrational states. The wavelengths that are absorbed by a given sample are characteristic of its molecular structure. This technique provides the user with the same information as traditional infrared. In order to characterize the molecular structure of the bioceramics, powder samples were thoroughly mixed with KBr and compressed into pellets under a load of approximately 10 kg. Infrared spectra obtained from 4000 to 370 cm^{-1} by transmission Fourier-Transform Infrared Spectrometry (Spectrum One, Perkin-Elmer).

3.7.3 X-Ray diffraction

X-ray diffraction (XRD) is a versatile, non-destructive technique that can be utilized for the determination of the chemical composition and crystallographic nature of a material. X-rays are emitted due to the bombardment of a metal with high energy electrons. The high energy electrons undergo a deceleration as they collide with the inner shell electrons from the inner shell electrons from the metal atoms. Consequently, the excess energy is emitted in the form of electromagnetic radiation with a continuous range of wavelengths. Thus a few sharp high intensity peaks are superimposed on the continuum and correspond to the x-ray photons.

The phase composition of the films was characterised using an X-Ray diffractometer (Bruker D8 discover, AXS LTD, Germany) with a CuKα radiation source of wavelength (λ=0.1540nm). The diffracted intensity was measured in the 2θ range 15-70º with a step of 0.02º. A voltage of 40kV and a current of 30mA were used for X-ray excitation.

3.7.4 Contact angle measurement

The contact angle is defined as the angle made by the intersection of the liquid /solid interface and the liquid/air interface. A high contact angle indicates a low solid surface energy (low degree of wetting/hydrophobicity) whereas a low contact angle indicates a high surface energy (high degree of wetting/hydrophilicity).

Contact angle measurement is typically undertaken using the sessile drop technique as illustrated in **Figure 3.4.**

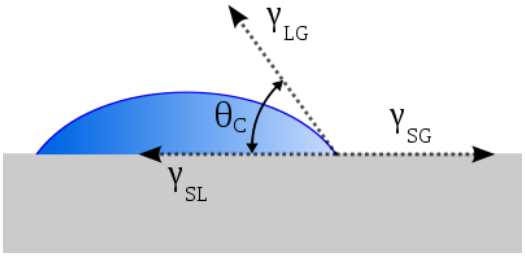

Figure 3.4 Contact angle of a drop on a surface

θ_c is the contact ange, γ_{LG} is the liquid vapour interfacial energy, γ_{SG} is the solid-vapour interfacial energy and γ_{SL} is the liquid-solid interfacial energy.

The wetting characteristics for a given liquid and solid can be generalized as follows;

$\theta_c=0$ (complete wetting/ superhydrohpilic) (3.5)

$0< \theta_c< 90º$ (partial wetting/hydrophilic) (3.6)

$\theta_c>90º$(non-wetting/hydrophobic) (3.7)

The contact angle of the coating samples in this research were measured using a contact angle meter (KSV instruments, Coventry, UK) equipped with a high speed camera. Then 2 µl sessile distilled water drops were placed on the surface at ambient temperature and images recorded over 20 s. The contact angle values were calculated by analyzing the drop shape using CAM2008 software.

3.7.5 Surface roughness measurement

Surface roughness is a measure of the texture of a material and is formed by fluctuations in the surface of short wavelengths and characterised by hills (asperities) (local maxima) and valleys (local minima) of varying amplitudes and spacings which are large compared to molecular dimentions. Surface roughness is typically quantified in terms of the vertical deviations from its ideal form and is usually represented by a number of parameters. However, R_t, R_{max} and R_a are the most common.

Surface roughness was characterised by laser proflilometry. This technique is an accurate and non-contact procedure for the assessment of surface topographies. A scantron proscan 1000 laser surface profilometer (Scantron Industrial Ltd) was utilized for the roughness measurements in this research. The KL131A displacement probe (Z range 400µm) was used together with a semiconductor laser beam (ʎ=780nm) with a beam diameter of 12-35µm and resolution of 0.2µm. The surface to be analyzed was placed on the device stage and held in place using “blue tack”. The laser beam was then focused on the surface. Fast scanning measurements were then carried out as the stage was moving. At each measurement point, the reflected beam was analyzed by a spectrometer which recorded a specific colour frequency. Changes in beam displacement due to variations in surface shape were recorded as a colour frequency change.

A maximum of five random areas of $5\times5mm^2$ were measured on each sample with a step size of 5µm in both the X and Y direction. A 3D image of the surface was generated via the combination of data from the various measured points. Each point recorded was averaged from 10 readings at that point. To estimate the surface roughness (R_a), R_a values were calculated across 5mm in both the x and y direction for each of the random areas scanned and the average obtained. The average of the 10 recorded values and their standard deviations were then calculated. The experiment was carried out in triplicate for each test condition.

3.8 Simulated body fluid preparation

According to Kokubo and co-workers (2003 and 2006), bone-bonding *in vivo* is mediated through an apatite layer that is formed on the implant surface early in the implantation period and thereafter, the bone matrix integrates into the apatite. The apatite layer consists of nano-crystals of carbonate ion containing apatite that has a defective structure and low crystallization. These features bear strong similarity to the mineral phase in bone and hence the osteoblasts preferentially proliferate on the

apatite and differentiate to form an extracellular matrix composed of biological apatite and collagen. Hence, the surrounding bone is able to come into direct contact with the surface apatite layer. When this process occurs, a chemical bond is formed between the bone mineral and the surface apatite to decrease the interfacial energy between them. Therefore, the formation of bone-like apatite is considered to be an essential requirement for the chemical bonding of an artificial material to bone tissue. The formation of bone-like apatite on the surface of biomaterials can be reproduced by immersing the test surfaces in protein free and acellular simulated body fluid which has an ionic concentration nearly equivalent to that of human blood plasma as summarized in **Table 3.4**.

Table 3.3 Ionic concentration of SBF and blood plasma

	Na^+	K^+	Mg^{2+}	Ca^{2+}	Cl^-	HCO_3^-	HPO_4^{2-}	SO_4^{2-}
Blood plasma	142	5	1.5	2.5	103.0	27	1.0	0.5
SBF	142	5	1.5	2.5	148.0	42	1.0	0.5

SBF was prepared according to the recipe suggested by Kokubo *et al* (2006). The recipe is summarized in **Table 3.4**.

.

Table 3.4 Order and amount of reagents used in the preparation of SBF

Order	Reagent	Amount	Provider
1	NaCl	8.035g	Sigma-Aldrich, Gillingham
2	$NaHCO_3$	0.355 g	Sigma-Aldrich, Gillingham
3	KCl	0.225 g	Sigma-Aldrich, Gillingham
4	$K_2HPO_4.3H_2O$	0.231 g	Sigma-Aldrich, Gillingham
5	$MgCl_2.6H2O$	0.311 g	Sigma-Aldrich, Gillingham
6	1.0M-HCl	39 ml	Sigma-Aldrich, Gillingham
7	$CaCl_2$	0.292 g	Sigma-Aldrich, Gillingham
8	Na_2SO_4	0.072 g	Sigma-Aldrich, Gillingham
9	Tris-buffer	6.118 g	Sigma-Aldrich, Gillingham
10	1.0M-HCl	0-5 ml	Sigma-Aldrich, Gillingham

Prior to SBF preparation, a 1000ml plastic beaker was thoroughly cleaned using diluted HCl and distilled and deionised water. 700ml of distilled and deionised water was then poured into the bottle which was placed in a water bath maintained at a constant temperature of 36.5±0.5 °C. The water was stirred constantly using an overhead stirrer.

The chemicals in **Table 3.4** were dissolved in the water one by one in the order given until reagent 8. Water was then added to the solution to increase the total volume to 900 ml. A pH was calibrated with fresh buffer solution and then placed inside the temperature was 36.5±1.5°C. Tris was then added little by little to prevent local pH increase. With the temperature maintained at 36.5±0.5°C the pH was adjusted to 7.45. 1.0M-HCl was then added drop by drop the pH. Tris and 1.0M-HCl were added alternately until the pH was exactly 7.40 at 36.5°C.

The solution was poured in to a 1000 ml volumetric flask. Distilled water was added to adjust the total volume to the 1000 ml mark after the solution was cooled to room temperature (20°C. The prepared SBF was either used immediately or stored in an air tight plastic bottle and refrigerated at 5°C to be used within 30 days.

3.9 Cell culture studies

Analysis of cell behavior carried out under well-controlled conditions provides information about the biocompatibility of the materials. Variations from the normal cell morphology are observed using SEM whereas the cell number provides an indication of the influence of the substrate and cell medium. Consequently, in addition to cellular morphology, cell proliferation is one of the most important parameters in biocompatibility tests.

MG63 osteoblast-like cells were used to study the biological response of the electrosprayed coatings. The suitability of MG63 cells as a model for the assessment of the biocompatibility of various materials is well documented (Francheschi, *et al*, 1985, Boyan *et al*, 1989, and La Jeuness *et al*, 1991). The MG63 cell line has been widely utilised in several *in vitro* studies involving titanium surface topographies, potential bone grafting materials and implant coating materials. In spite of being a tumor cell line with a more rapid proliferation rate compared to HOBs, MG63 cells display several osteoblastic traits which are associated with bone forming cells (Bachle and Kohal, 2003). For example, MG63 cells display an increase in alkaline phosphatise activity due to 1, 25 dihydroxyvitamin D_3 (1, 25 $(OH)_2$ D_3) administration similarly to bone-derived cells (Clover and Gowen, 1994). Furthermore, MG63 cells exhibit a number of osteoblast-like phenotypic markers including response to parathyroid hormone (Aisa *et al*, 1996) and the inhibition of cell proliferation with 1, 25 $(OH)_2$ D_3 (Boyan *et al*, 1989). Thus, MG63 cells are considered to be relatively immature osteoblasts.

3.9.1 Maintenance of primary MG63 cells

MG63 cells were obtained from the Eastman dental institute archives after cryogenic storage at -196°C in 10% dimethyl sulphoxide (DMSO) (Sigma-Aldrich, UK), and 90% Dublecco's modified eagle's medium (DMEM) (Gibco's life technologies, UK). In order to commence experimental work, the vials of MG63 cells were removed from storage and thawed by immersion in a 37ºC water bath for 90 s. The exterior of the vials were sterilised by spraying with 70% ethanol. DMSO was rinsed away by asceptically adding 10ml of standard growth medium (DMEM supplemented with 10% fetal bovine serum (FBS) and 1% penicillin and streptomycin). All reagents used were obtained from Gibco's life technologies, UK. The cell suspension was then transferred to a sterile 50ml graduated centrifuge tube followed by centrigugation at 1000 RPM for 5 minutes at room temperature. The supernatant was discarded and the cell pellet resuspended in 10ml of standard growth medium. The MG63 cells were then transferred to a 75 cm^3 tissue culture flask (T_{75}) (BD Biosciences, UK) and incubated at 37ºC, 95% relative humidity and 5% CO_2. The growth medium was changed every 2 days.

3.9.2 Cell subculture

Upon reaching near confluence (~80%), the cells were detached first by rinsing twice with 10ml of Phosphate buffered saline (PBS) (Sigma-Aldrich, UK) warmed to 37ºC. 2ml of trypsin/EDTA (Gibco's life technologies, UK) at 37ºC were then piptted into the flask which was then incubated for 5 minutes resulting in the detachment and rounding up of the cells. 8ml of standard growth medium was gently added to the flask in order to inhibit the action of the trypsin. The cell suspension was then transferred to a sterile 50ml centrifuge tube. The cells were then collected by centrifugation at 1000 RPM for 5 minutes at room temperature. The supernatant was then removed and the cell pellet resuspended in 4 ml of standard growth medium and redistributed into 4 tissue culture flasks (T_{75}). 9ml of growth medium was gently added to each of the flasks and was changed every 2 days. The cells used for the experiments were collected from the 15^{th}-18^{th} passages.

3.9.3 Cell counting

MG63 cells were detached from the flasks as described in the previous section and resuspended in 3ml of standard growth medium. The cell number was determined using a haemocytometer which is a thick glass slide with central grids to facilitate cell

counting. Prior to cell counting, the haemocytometer was cleaned with 70% ethanol and a coverslip gently but firmly affixed. The cell pellet was dispersed by gently agitating with a pipette. 100µl of cell suspension was transferred to a 1.5ml eppendorf tube followed by 100µl of 0.4% trypan blue solution. Homogeneous mixing was achieved by gentle agitation. Trypan blue is metabolised by live cells and hence they are not stained by the dye whereas the dead cells absorb the dye and are as such stained by the dye. 10µl of stained cell suspension was transferred to the edge of each of the two counting chambers. An optical microscope was used to observe the cells during counting. Upon obtaining the cell number, the required cell number per ml was obtained by diluting with standard growth medium. Surplus cells were cryopreserved as described in the preceeding sections until needed.

3.9.4 Cell culture

Prior to cell culture, test samples were placed in 24 well plates and sterilised in a Steristrom ultraviolet cabinet. Each sample face was illuminated at a frequency of 254nm for 30 minutes. Cells were then seeded onto each sample at a density of 1×10^4 cells per well and incubated for 1 hour to allow the cells to attach to the sample surfaces. 1ml of standard growth medium was then carefully pipette into each well followed by incubation. The growth medium was changed every 2 days. Uncoated Ti alloy and tissue culture plastic (tcp) were used as controls.

3.9.5 AlamarBlue™ cytotoxicity assay

AlamarBlue™ (Serotec, UK) enables the non-destructive and continuous assessment of cell proliferation over prolonged periods of time by virtue of being non-toxic to cells (Ahmed, *et al*, 1994). The assay is an indicator dye which incorporates an oxidation-reduction (REDOX) indicator that both fluoresces and changes colour in response to the chemical reduction of growth medium resulting from cell growth. Reduction related to cell growth causes the redox indicator to change from oxidized non-fluorescent blue to reduced fluorescent red. Cell proliferation is therefore quantified from the intensity of the colour produced which is directly correlated to the number of metabolically active cells.

At 1, 4 and 7 days of cell culture, 100µl of AlamarBlue™ assay was added to each well and incubated for 4 hours. After the incubation period, the medium from each well was aspirated and 100µl aliquots placed in a 96 well plate. The medium in the 24 well

plates was then replenished and the plates further incubated. The 96 well plates were subsequently read using an Ascent Fluoroscan plate reader (Labsystems, UK) at a wavelength of 530nm with a reference wavelength of 590nm. Samples were tested in triplicate and 3 readings were taken from each of the samples giving a total of 9 readings for each group. The experiments were repeated to ensure reproducibility.

3.9.6 Protein secretion assay

The Qubit® assay is composed of an advanced dye that fluoresces due to the presence of proteins. The dye has a low fluorescence. However, when the dye comes into contact with protein, the dye binds on to the protein molecules which causes it to become intensely fluorescent. The amount of fluorescence is read by a Qubit® 2.0 fluorometer and is converted to the amount of protein present per µl by the device. The degree of fluorescence is directly proportional to the amount of protein present.

At 1, 7, 14 and 21 days of cell culture, 500µl aliquots of growth medium were removed from each well and transferred to 1ml eppendorf tubes. These were subsequently stored at -80ºC until measurement. The remaining growth medium was aspirated and replaced with 1ml of fresh growth medium and the cells incubated as discussed in previous sections.

Prior to testing, the assay reagents and frozen growth medium were warmed to room temperature. The working solution was prepared by mixing the Qubit® protein reagent with the protein buffer at a 1:200 ratio. 190µl of Qubit® working solution was pipetted into 0.5ml PCR tubes followed by 10µl of standard solutions. Mixing was attained by vortexing for 2-3 seconds, whilst taking care not to create bubbles. 180µl of working solution was added to the 0.5ml tubes followed by 20µl of thawed medium and mixing carried out as previously discussed. All tubes were allowed to incubate at room temperature for 15 minutes. The Qubit® 2.0 fluorometer was calibrated using the standards. The protein content of the samples was read in turn. 3 aliquots were tested for each sample, giving a total of 9 readings for each test condition.

3.9.7 Cellular morphology on coating samples

The cell morphology of the HOS cells on the films substrates was observed by scanning electron microscopy (SEM). Prior to microscopic observation, the cells were initially fixed in 3% gluteraldehyde in 0.1M cocadylate buffer at 4°C (Agar scientific, UK) for a minimum of 24 hours. The cells were then dehydrated using a series of graded

ethyl alcohol (20-90%), at time intervals of 10 minutes, followed by dehydration in 100% ethyl alcohol at three 10 minute intervals. The cells were subsequently dehydrated using Hexamethyldisalazane (HMDS) (TAAB Ltd, UK) for 5 minutes and air dried in a fume cupboard.

3.10 Scratch testing

In general, the *in vivo* performance of coated orthopaedic prostheses is dependent on the existence of firm adhesion between the bioceramic film and underlying metal prosthesis as well as the implant and surrounding bone tissue. Interfacial bonding with metallic implant materials is a prerequisite in the prevention of cracking, shearing off and chipping of the film during implantation of the prosthesis. Thus the integrity of the film-implant interface plays a major role in the determination of implant longevity. Film-substrate interfacial bonding was assessed by means of the scratch technique

Scratch testing involves the use of a stylus or diamond tip which is drawn across the surface of the coating. The test is a combination of two operations namely, the normal indentation process and horizontal tip motion. A stepwise vertical increasing load was applied to the tip during scratching until the coating separates from the substrate.

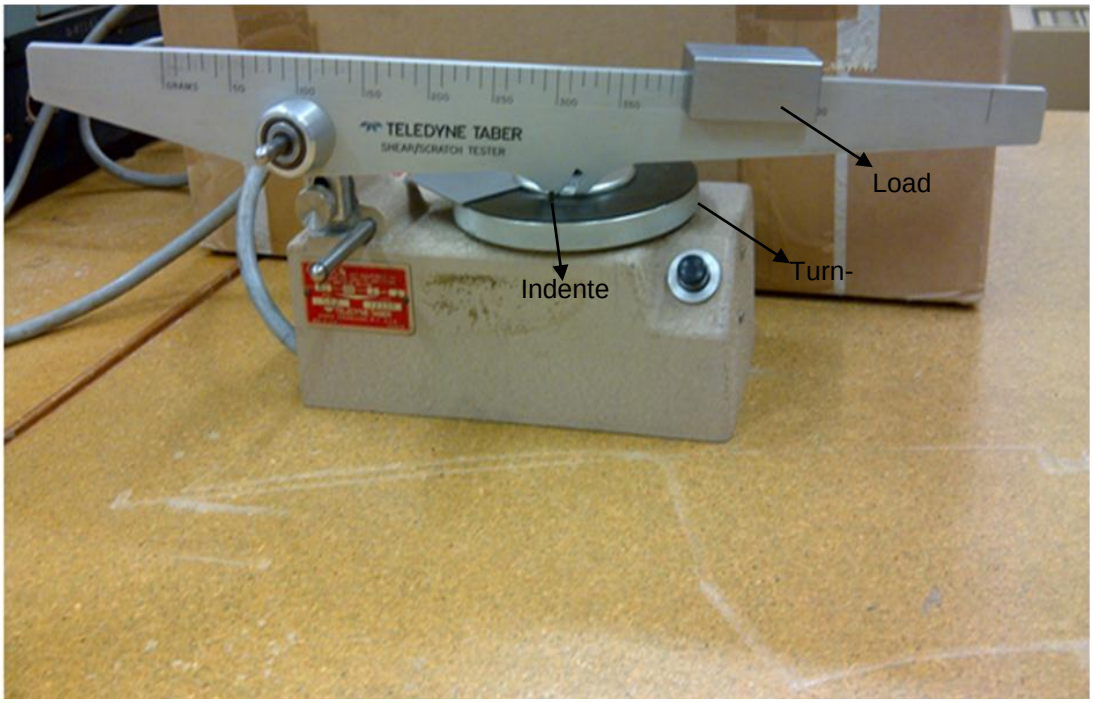

Figure 3.5 Scratch testing procedure

A Taber© shear/scratch tester (Taber industries, UK) (**Figure 3.5**) was used to determine the scratch resistance of the film samples. Prior to experimentation, the coated Ti alloy plates were firmly fastened on to the sample holder with the aid of a screw. Sliding weights of 500 or 1000g were then fastened onto the precision scale beam and the diamond stylus rested against the film surface. A constant speed motor operating at a speed of 0.5 rpm was used to rotate the turn table on which the sample to be tested was fixed for 30s. Consequently, scratch tracks were obtained on the film surface. These were subsequently observed using SEM and EDS (SN3800, Hitachi) at an operating voltage of 20kV and a working distance of 20mm. The scratch width was measured using imaging analysis software (LAS EZ software (Leica, Microsystems, Milton Keynes, UK).

The scratch hardness (Pa) was then estimated from equation 3.8 according to the specification of ASTM G171-03;

$$H_S = \frac{8L}{\pi d^2} \tag{3.8}$$

where L (N) is the applied normal force and d (m) is the corresponding scratch width. the critical load was defined at the onset of the film loss associated with a beginning of visibility of metallic substrate inside the scratch track. The scratch hardness is an indicator of film cohesion and adhesion.

3.11 Statistical analysis

The experimental data were expressed as mean ± standard deviation. The experimental data was analyzed using spss v.21 statistical software. Sample means were compared using Student's T-test. A difference of $p<0.05$ was considered to be statistically significant.

Chapter 4 Preparation and characterization of electrosprayed TiO_2 films

This chapter investigates the preparation of bioactive electrospray TiO_2 films. Titanium isopropoxide (TTIP) was chosen as a precursor material owing to its monomeric nature which results in less stearic hinderance and hence eases interchange between the alkoxide and organic solvent compared to titanium ethoxide and titanium butoxide (Hu *et al*, 1992). TTIP was also selected due to the moderate bulkiness of its alkyl groups which render this precursor relatively stable as the ease of interchange functional groups decreases with an increase in the complexity of the alkyl groups which in turn increases the steric hinderance. The reactivity of the alkyl groups decreases in the order MeO>EtO>prO>Bu^{t}O (Mehrotra, 1988 and Sanchez *et al*, 1988).

Currently, there is a wide range solvents available for the hydrolysis of TTIP. PrOH and etOH were selected as organic solvents as a result of their well established ability to hydrolyse metal alkoxides. It is also well known that, both molecular weight and polarity of the organic solvent affect the rate of hydrolysis and condensation and also influence the crystallisation, porosity and microstructure of the final product (Behnajady et al, 2011). This provided the basis for the comparison of prOH and etOH during sol-gel synthesis. The organic solvents were also utilized based on their well-established ability to undergo electrospray atomization. It was expected that the difference in sol properties could affect the electrospray process and subsequently the bioactivity and mechanical integrity of the TiO_2 films. **Table 4.1**.summarizes the parameters utilized in the electrospray processing of the TiO_2 films.

Table 4.1 Deposition parameters for the electrospray deposition of TiO_2 and ZrO_2 sols

Study	**Fixed parameters** (Unless stated otherwise)	**Variable parameters**
I Mode map selection sol concentration (2-8%)	D=20mm d_{needle}=300µm	F=1-60 µl/min V = 0-4.6 kV sols=TP2-TP8 TE2-TE8
Needle internal diameter (d_{needle}=300-700 µm)	D= 20mm sols= TP2 and TE2	F=1-40 µl/min v=0-4.6 kV d_{needle}=300-700 µm
Precursor type	D=20mm d_{needle}=300µm	sols= ZE2, ZEP2 F=1-25 µl/min v=0-4.6 kV
III Relic diameter and film morphology		
Spray time	D= 20 mm d_{needle}=300 µm F=5 µl/min V=3.3-4.2 kV Sol=TE2, TP2, ZE2, ZEP2	T=30-600 s
Needle to substrate distance	T=180 s d_{needle}=300 µm sol= TP2, TE2, ZE2, ZEP2 ,F=5 µl/min V=3.3-4.2 kV	D=10-50 mm
Flow rate	T=180s d_{needle}=300µm, sol= TP2, TE2, ZE2, ZEP2 V=3.3-4.2 kV, D=20 mm	F=2-20 µl/min
Needle size	T=180 s sol =TP2, TE2 V=3.3-4.2 kV, D=20 mm,F=5 µl/min	d_{needle}=300-700 µm
Sol concentration	T=180 s, V=3.3-4.2 kV D=20 mm, F=5 µl/min d_{needle}=300 µm	TE2, TP2

D=needle to substrate distance, d= needle internal diameter, F= flow rate, V=voltage, T=deposition time

4.1 Sol-gel synthesis and characterisation of TiO_2 sols

The sol-gel reaction between the precursor and organic solvents took place according to equations;

$$Ti(OR)_4 + 4R'OH \longrightarrow Ti(OR')_4 + 4ROH \quad (4.1)$$

$$2Ti(OR')_4 \longrightarrow Ti(OR')_3\text{-}O\text{-}Ti(OR')_3 \quad (4.2)$$

Where M=Ti, R=C_3H_7, and R'=C_2H_4 or C_3H_7.

The sols obtained using prOH (TP) were transparent; there was no visible change in appearance when the concentration of the TiO_2-complex increased from 2-8wt%. In contrast, the TE sols were turbid in appearance due to the precipitation of nano-particles. The turbidity of TE sols increased with the concentration of TiO_2 -complex. The outcomes of the sol gel process are summarized in **Figure 4.1**.

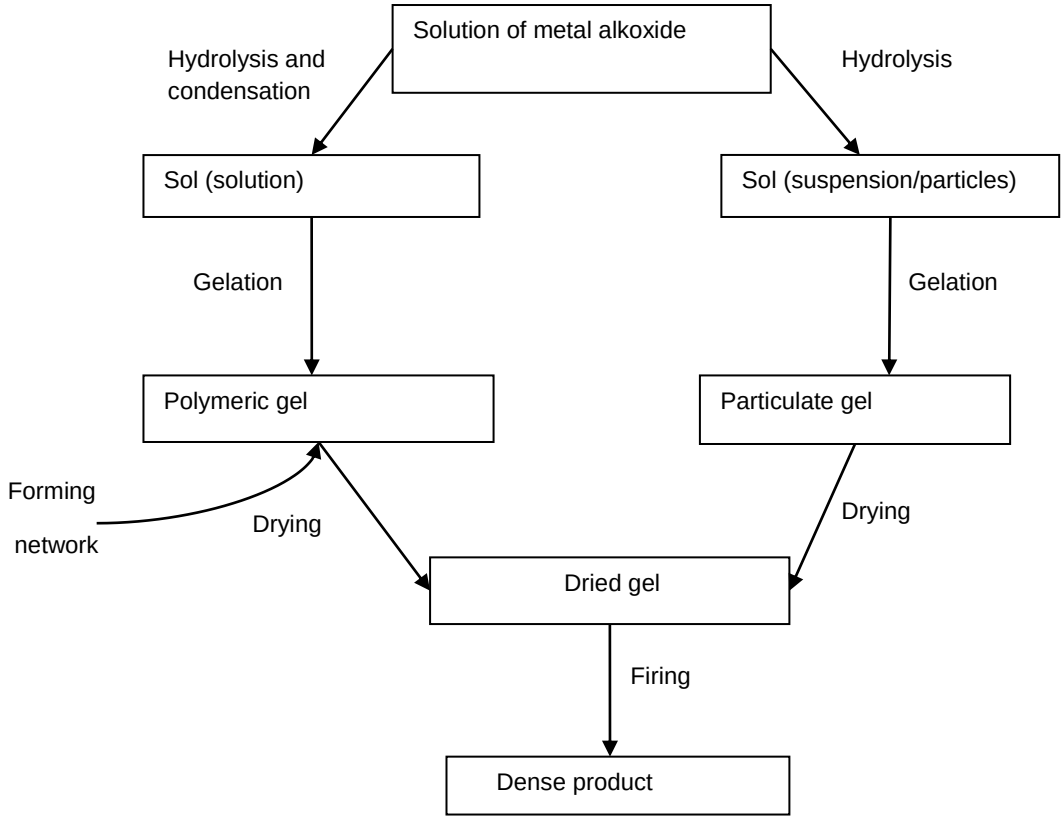

Figure 4.1 Schematic depicting outcome of sol-gel synthesis of TiO_2

4.1.1 Phase composition analysis of TiO_2 sols

Figure 4.2 shows the FTIR spectra of the TiO_2-complex powders after drying under ambient conditions. Both the TP2 and TE2 powders exhibited characteristic peaks owing to the TiO_2 phase in the wave range between 400-900 cm^{-1}. The weak peaks around 500 cm^{-1} and 615 cm^{-1} were assigned to the stretching vibrations of the Ti-O-Ti bond. The powders further displayed weak peaks around 815 and 825 cm^{-1} due to the stretching vibrations of the Ti-O bond. The powders also displayed poorly defined

peaks around 1045 cm^{-1} due to the deformation vibrations of the Ti-OH groups whereas the small peaks around 1378 cm^{-1} and 1445 cm^{-1} where attributed to the symmetric and asymmetric deformations of the CH_3 groups, respectively. The symmetric and asymmetric vibrations of the CH_2 groups were also evident around 2860 cm^{-1} and 2920 cm^{-1}. The powders further displayed fairly sharp peaks around 1610 cm^{-1} due to the flexural vibrations of the H-O-H groups and a broad band at 3200-3500 cm^{-1} due to the stretching vibrations of the –OH groups.

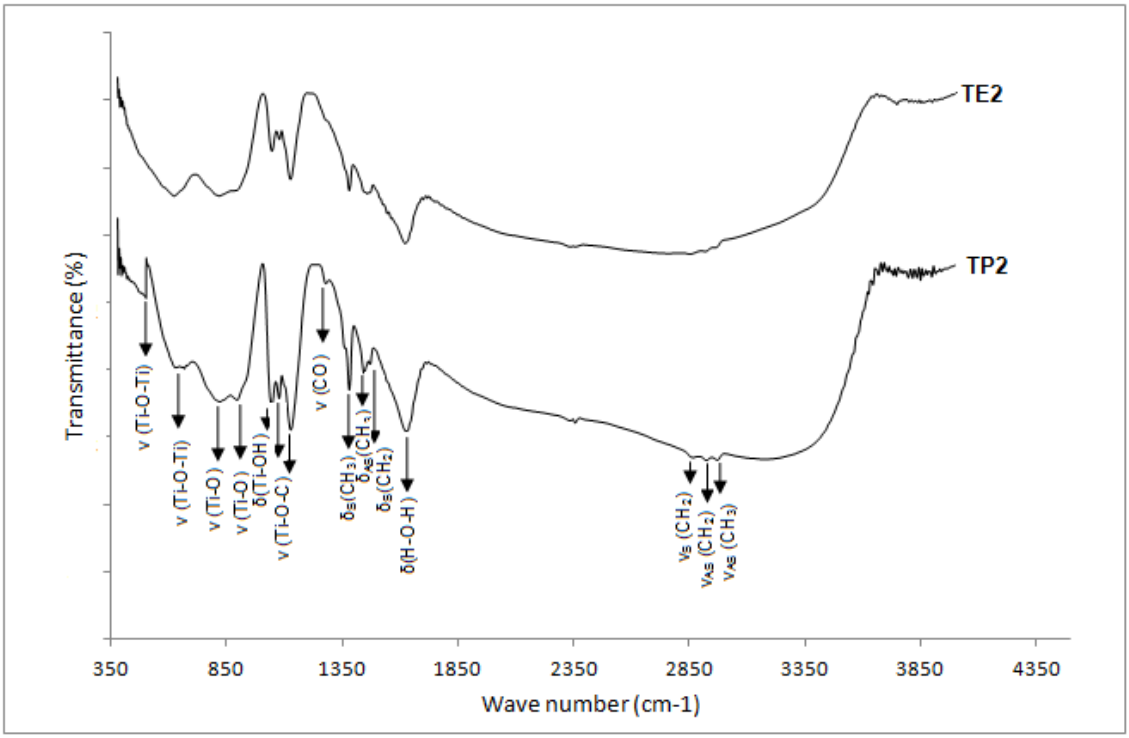

Figure 4.2 FTIR spectra of TiO_2-complex obtained using prOH and etOH as organic solvents. The powders were dried overnight under ambient conditions

The TP2, powders further displayed weak peaks around 930 cm^{-1}, 1070 cm^{-1} and 1119 cm^{-1} owing to the stretching vibrations of the Ti-O-C terminal bonds. The presence of the isopropoxy residual groups in these powders was signified by the weak peaks around 1000 cm^{-1} and 1264 cm^{-1}. These were assigned to the deformation vibrations of the CO bonds in the isopropoxide structure. The TP2 powders further displayed weak peaks around 1489 cm^{-1} and 2960 cm^{-1}. These were attributed to the symmetric vibration of the CH_2 groups and the asymmetric vibrations of the CH_3 groups, respectively. The TP4-TP8 and TE4-TE8 powders gave similar spectra (results not

shown here. The wave numbers and their corresponding assignments are summarized in **Table 4.2.**

Table 4.2 Assignment of peaks of FTIR spectra of TiO_2 powders

Wave number (cm^{-1})				Assignment
TP2	TE2	TP2D	TE2D	
-	-	481	489	ν (Ti-O-Ti)
500	505			ν (Ti-O-Ti)
616	611	-	-	ν (Ti-O-Ti)
-	-	667	654	ν (Ti-O-Ti)
810	815	813	815	ν (Ti-O)
825	830	-	-	ν (Ti-O)
930	-	925	930	ν (Ti-O-C)
-	-	1011	997	ν (Ti-O-C)
1047	1048	1048	1050	δ (Ti-O-H)
1075	-	1090	1092	ν (Ti-O-C)
1126	-	1117	1119	ν (Ti-O-C)
-	1140	-	-	δ (Ti-O-H)
		1216	1204	δ (C-O)
		1244	1238	δ (C-N)
1263	-	1264	1260	δ (C-O)
1378	1372	1378	1369	$\nu_S(CH_3)$
1443	1439	1445	1439	$\nu_{AS}(CH_3)$
1489	-	-	-	$\nu_S(CH_2)$
1624	1610	1648	1647	δ (H-O-H)
2862	2853	2872	2875	$\nu_S(CH_2)$
2925	2924	2921	2924	$\nu_{AS}(CH_2)$
2960	-	-	-	$\nu_{AS}(CH_3)$
-	-	3218	3259	$\nu_{AS}(NH_2)$
-	-	3397	3413	$\nu_S(NH_2)$
3200-3500	3200-3500	3200-3500	3200-3500	$\nu_{AS,S}(OH)$

4.1.2 Characterization of liquid physical properties of TiO_2 sols/suspensions

The liquid physical properties of the TiO_2 sols are summarized in **Table 4.2**. As shown, the density of the TP sols was higher than that of the TE sols. The density and viscosity of the TiO_2 sols were slightly higher than that of the solvent used. An increase in the

TiO_2-complex concentration increased the density of the TP sols from 805 to 811 kgm^{-3} whereas that of the TE sols increased from 790-807 kgm^{-3}. The viscosity of the TP sols increased from 2.44 to 2.54 mPaS as the sol concentration was increased from 0 to 8 wt%. The viscosity of the TE sols was also increased from 1.33 to 1.55 mPaS as the sol concentration was increased from 0 to 8 wt%.

Furthermore, the surface tension of the TiO_2 sols was higher than that of the pure solvents. The surface tension of the TP sols was marginally increased from 33.65 to 34.55 mN/m as the concentration was increased from 2 to 8 wt%. The surface tension of the TE sols was also slightly increased from 28.78 to 33.90 mN/m due to an increase in TiO_2 concentration.

On the other hand, the electrical conductivity of the TiO_2 sols was lower than that of the pure organic solvent carriers. The electrical conductivity of the TP sols was reduced from 1.85 to 0.1 Sm^{-1} upon increasing the concentration from 2 to 8 wt%. The electrical conductivity of the TE sols was reduced from 3.10 to 0.6 Sm^{-1} as a result of increasing the TiO_2 concentration from 2 to 8 wt%. In general, the liquid physical properties of the TiO_2 sols exhibited a similar trend irrespective of the organic solvent used.

Table 4.3 Comparison of liquid physical properties of TiO_2 sols

Suspension	Boiling point (°C)	Density (kgm^{-3})	Viscosity (mPa S)	Surface tension (mNm^{-1})	Electrical conductivity $\times 10^{-4}$ (Sm^{-1})
1-prOH	97	804	2.48	29.5	2.0
TP2		808	2.51	33.7	1.9
TP4		811	2.53	34.2	1.4
TP6		813	2.55	34.3	0.6
TP8		819	2.62	34.6	0.1
etOH	78	790	1.3	23.3	3.4
TE2		794	1.31	28.8	2.9
TE4		796	1.33	30.1	1.9
TE6		800	1.39	31.9	0.9
TE8		807	1.55	33.9	0.6

4.2 Electrospraying of TiO_2 sols

4.2.1 Operating mode of electrospraying

Prior to film deposition, the feasibility of electrospraying of the bioceramic sols was investigated by determining the effect of the applied voltage on the liquid jet at the needle exit. **Figure 4.3** shows the evolution of the liquid jet with applied voltage for the TP2 sol at a flow rate of 5 µl/min.

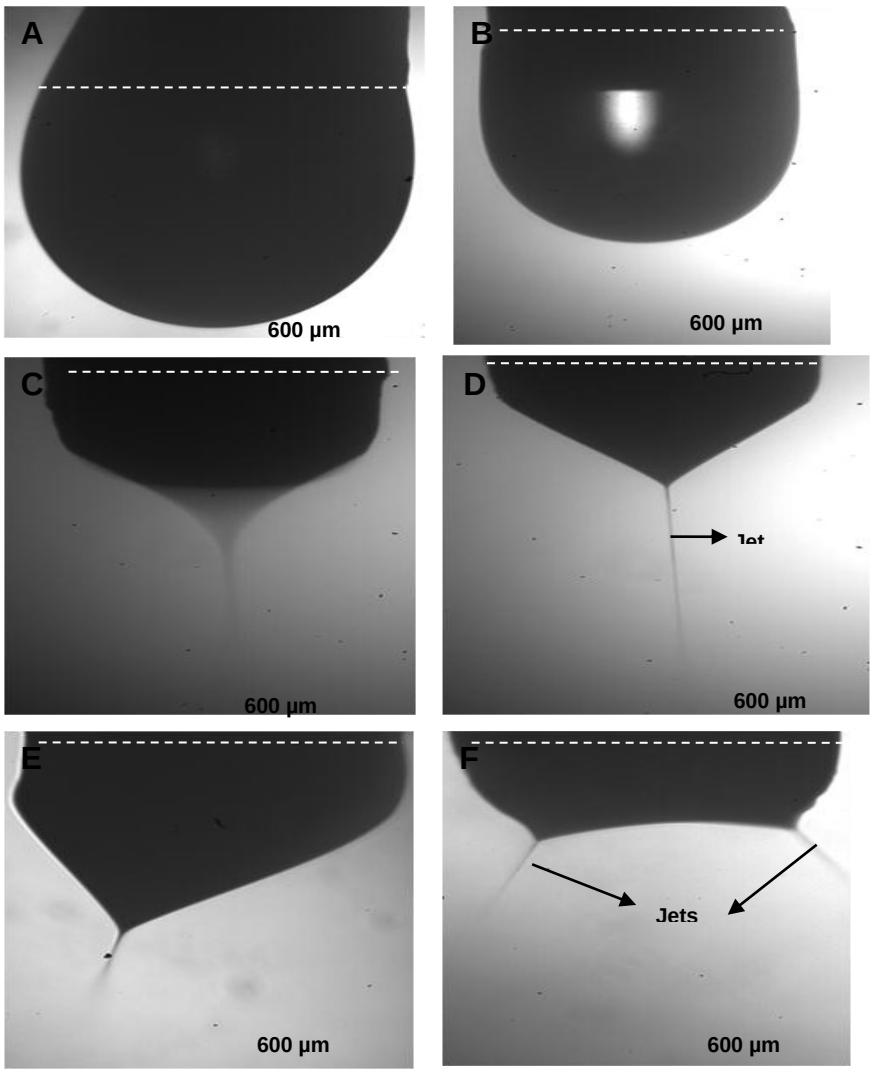

Figure 4.3 Evolution of TP2 droplet at needle exit with applied voltage at a flow rate of 5 ul/min; (A) dripping mode, (B) micro-dripping mode , (C) unstable cone-jet mode, (D and E) stable cone-jet mode and (F) multi-jet mode. The applied voltage was varied from 1 to 6 kV.

At an applied voltage of 0 kV, a large spherical droplet was observed at the needle exit (**Figure 4.3 A**). Upon gradually increasing the applied voltage (0 to 2.9 kV), the droplet shrunk and became hemispherical in shape (**Figure 4.3 B**). This was the micro-dripping mode. With further increase in the applied voltage (2.9 to 3.5 kV), the droplet shape varied between semi-spherical and cone-shaped (**Figure 4.3 C**). This was the unstable cone-jet mode. At an applied voltage of 3.5 kV, the liquid at the needle exit suddenly assumed the geometry of a fine cone, and a thin jet was emitted from the cone apex (**Figure 4.3 D**). This was the stable cone-jet mode. When the applied voltage was further increased gradually, the cone-depth was reduced and the cone jet became axissymetric with respect to the needle exit (**Figure 4.3 E**). This was still classified as the stable-cone jet mode. At an applied voltage of 4.0 kV, two cone jets

were suddenly observed at the rim of the needle exit (**Figure 4.3 F**). This was the multi – jet mode. From these results it was evident that the applied voltage played a critical role in the acquisition of a stable cone-jet.

Similar electrospray jetting modes were also obtained using the TP4-TP8 and TE2-TE8 sols, although the onset voltages for each mode were different among the various TiO_2 sols. Thus it was confirmed that the presence of the bioceramic nano-particles in the organic solvent did not affect the basic process of electrospraying.

4.2.2 Mode map selection

To understand the effect of various processing parameters on the electrospraying of TiO_2, a series of investigations were carried out by fixing and varying different processing parameters as shown in **Table 4.1**.

4.2.2.1 The influence of TiO_2 sol concentration on the applied voltage-flow rate regime

The stable cone-jet mode maps obtained using the TP sols are shown in **Figure 4.4**. For the TP2 sol, the onset voltage for stable-cone jet formation was at approximately 3.6 kV at the lowest achievable flow rate of 1 µl/min (minimum pump flow rate). This mode was maintained as the applied voltage was further increased before abruptly changing to the multi jet mode at approximately 3.9 kV. Upon increasing the flow rate, the minimum voltage at which a stable cone-jet could be attained was reduced whereas the maximum voltage was increased. However, the largest operating voltage range (3.5-4.0 kV) was found to occur at approximately 5µl/min. Beyond this flow rate, two significant phenomena were observed to take place. Firstly, both the minimum and maximum voltage limits were gradually increased. Secondly, the operating voltage range gradually became narrower and the onset and maximum operating voltages eventually converged at a flow rate of 28 µl/min. Stable cone jet formation did not occur when the flow rate was increased any further. The TP4-TP8 sols displayed a similar trend. However, an increase in the sol concentration increased the maximum sol flow rate from 28 to 54 µl/min and also shifted the overall operating voltage from 3.4-4.2 kV to 3.7-4.7 kV. The flow rates at which the maximum operating voltage range was attained for each sol was also shifted

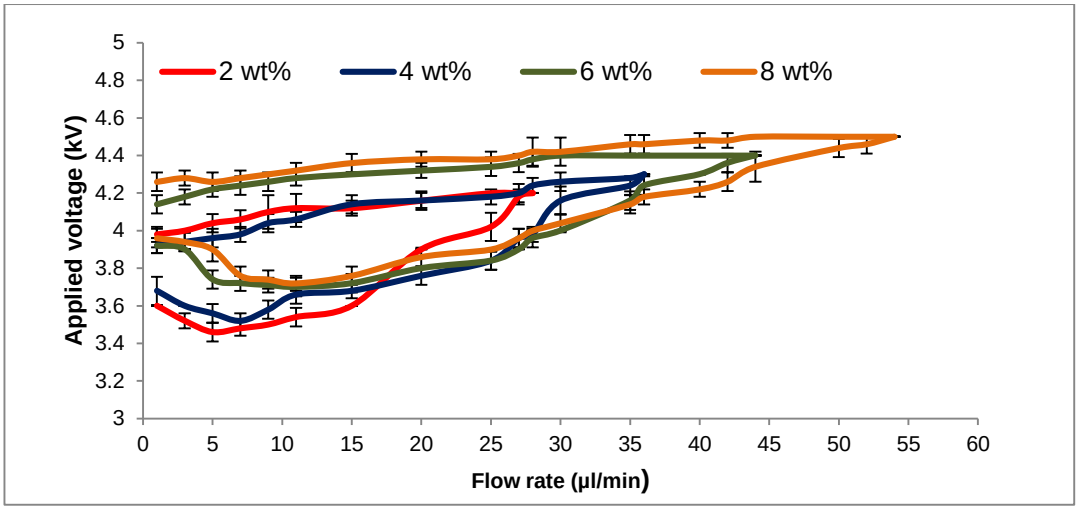

Figure 4.4 Effect of sol concentration on the stable cone-jet mode maps of TP sols electrosprayed using a needle internal diameter of 300 µm and a needle to ground distance of 20 mm

Similarly to the TP sols, an increase in the TE sol concentration caused an increase in the flow rate and applied voltage during electrospraying. The maximum sol flow rate was increased from 13 µl/min to 32 µl//min whereas the overall operating voltage range was increased from 3.2-4.0 kV to 3.6-4.3 kV (results not shown here). The increase in sol concentration also increased the flow rate at which the maximum operating voltage range could be achieved. **Table 4.3** compares the electrospray parameters of the TiO_2 sols obtained using different solvent carriers. As shown, the maximum sol flow rate of the TP sols was significantly higher than that of the TE sols. However, there was no significant difference in the operating voltage of the various TiO_2 sols. Hence, an increase in sol concentration had a similar effect on the stable cone jet mode maps of the TiO_2 films irrespective of the solvent carrier utilized.

Table 4.4 Comparison of electrospray characteristics of TiO_2 sols

Conc	F_{max} (µl/min)		Δv_{max} (kV)		$F_{\Delta vmax}$ (µl/min)	
	prOH	etOH	prOH	etOH	prOH	etOH
2	28	13	3.4-4.2	3.2-4.0	5	5
4	36	23	3.5-4.3	3.4-4.1	6	7
6	44	25	3.7-4.4	3.5-4.2	11	9
8	54	32	3.7-4.5	3.6-4.3	13	11

F_{max}(µl/min)=Maximum flow rate, Δv_{max}=maximum voltage range, $F_{\Delta vmax}$=Flow rate at maximum voltage range

4.2.2.2 The influence of needle diameter on the applied voltage-flow rate regime

The effect of the needle internal diameter on the stable cone-jet mode map was studied using the TP2 and TE2 sols. As shown in **Table 4.5**, the maximum TP2 sol flow rate was increased from 28 µl/min to 40 µl/min on increasing the needle internal diameter from 300 µm to 700 µm. The overall operating voltage range was also increased from 3.5-4.2 kV to 3.8-4.6 kV. There was also an increase in the flow rate at which the maximum operating voltage range could be achieved.

Table 4.5 Comparison of electrospray parameters of TiO_2 sols electrosprayed using different needle internal diameters

D_{needle}	F_{max}(µl/min)		Min V (kV)		Max V (kV)		Δv_{max} (kV)		$F_{\Delta vmax}$(µl/min)	
(µm)	TP2	TE2	TP2	TE2	TP2	TE2	TP2	TE2	TP2	TE2
330	28	13	3.4	3.2	4.2	4.0	3.4-4.2	3.2-4.0	5	5
510	35	15	3.6	3.5	4.4	4.2	3.6-4.0	3.6-4.0	7	7
700	40	19	3.8	3.8	4.6	4.3	3.8-4.2	3.8-4.3	15	9

Similarly, an increase in the needle internal diameter caused an increase in the maximum TE2 sol flow rate. The maximum sol flow rate was increased from 13 µl/min to 19 µl/min as the needle internal diameter was increased from 330 µm to 700 µm. The onset and maximal operating voltage were also shifted towards higher values and the overall operating voltage range was increased from 3.2-4.0 kV to 3.8-4.3 kV. Furthermore, there was also a slight positive shift in the flow rate at which the maximum operating voltage range was obtained. The maximum sol flow rate of the stable cone-jet mode of the TP2 sol was approximately twice that of the TE2 sol for the range of needle diameter investigated. However, there was no significant difference in the operating voltage for both TiO_2 sols.

4.3 Deposition of electrosprayed TiO_2 films

4.3.1 The influence of spray time

Prior to film deposition, the effect of solvent type on the droplet relic diameter was investigated using the TP2 and TE2 sols as summarized in **Table 4.1**. The flow rate of 5 µl/min produced sufficiently fine droplet relics (< 15 µm) which appeared to be monodisperse (**Figure 4.5).** Fine and monodisperse droplets result in a more homogeneous film morphology (Grace and Marijnisen, 1994).

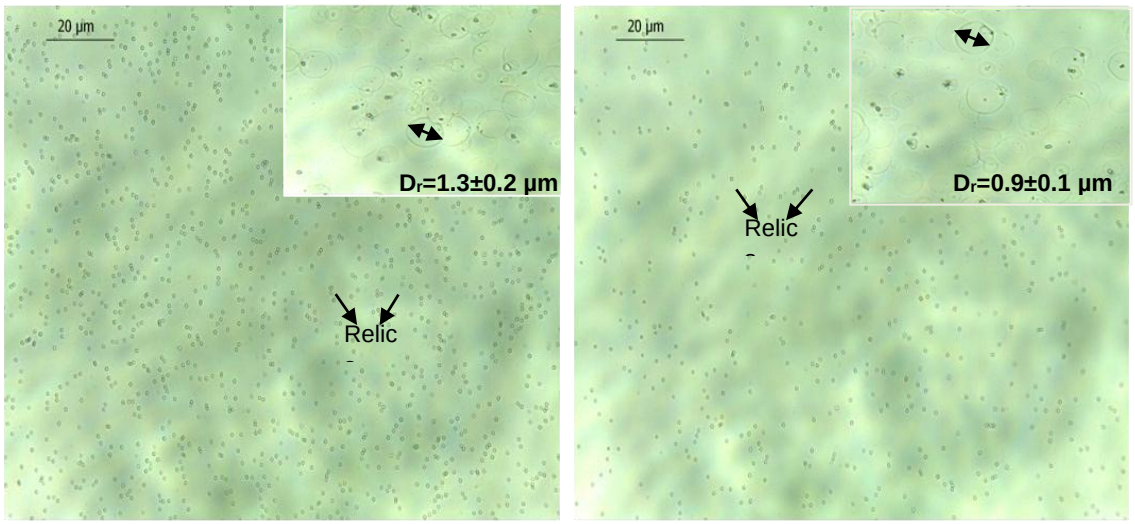

Figure 4.5 Monodisperse TiO_2 droplet relics obtained using (A) TP2 sol and (B) TE2 sol electro-sprayed at a flow rate of 5 µl/min and a needle to substrate distance of 20 mm (n=50).

The TP2 and TE2 sols both gave a droplet relic diameter of approximately 1 µm. However, the average droplet relic diameter obtained using the TP2 sol was statistically higher than that obtained using the TE2 sol ($p<0.05$). The TP2 sol gave a droplet relic diameter of 1.3 µm whereas the TE2 sol gave a droplet relic diameter of approximately 0.9 µm, indicating that under identical electrospray conditions, the diameter of the electrospray droplets and relics displayed a marginal dependence on the solvent carrier utilized. Furthermore, the TP2 sol gave a spray diameter of approximately 34 mm whereas a spray diameter of approximately 38 mm was obtained on electrospraying the TE2 sol. Hence, the diameter of the spray area was affected by the solvent type.

Figure 4.6 compares the influence of spray time on the morphology of TiO_2 films obtained using the TP2 and TE2 sols. For the TP2 sol, short spray duration of 60s gave a continuous but inhomogeneous film. When the deposition time was increased to 180s, the TiO_2 film surface exhibited a uniform and dense topography (Type 1 morphology). No cracks were evident and the film had a relatively smooth surface compared to that deposited using a shorter spray duration. At a spray time of 300s, overall film uniformity still prevailed and the films produced were relatively dense. However, when the spray time was further increased to 600s, the deposited films were continuous and featureless with microcracks.

For the TiO_2 films obtained using the TE2 sol, a spray duration of 60s yielded an inhomogeneous film. The film was composed of a continuous sub-layer with a top layer

of flake-like structures (Type 2 morphology). The film appeared to have a rough topography. Increasing the spray duration to 180s resulted in the deposition of rough films with a fractal morphology due to the presence of a network of irregular particles. The underlying continuous sub-layer was no longer visible (Type 3 morphology). A further increase in the spray duration to 300s also resulted in the deposition of rough and highly dense films with a fractal morphology. The relative density of the particle layer was appreciably increased by prolonging the spray duration to 600s resulting in increased film roughness and homogeneity (Type 4 morphology).

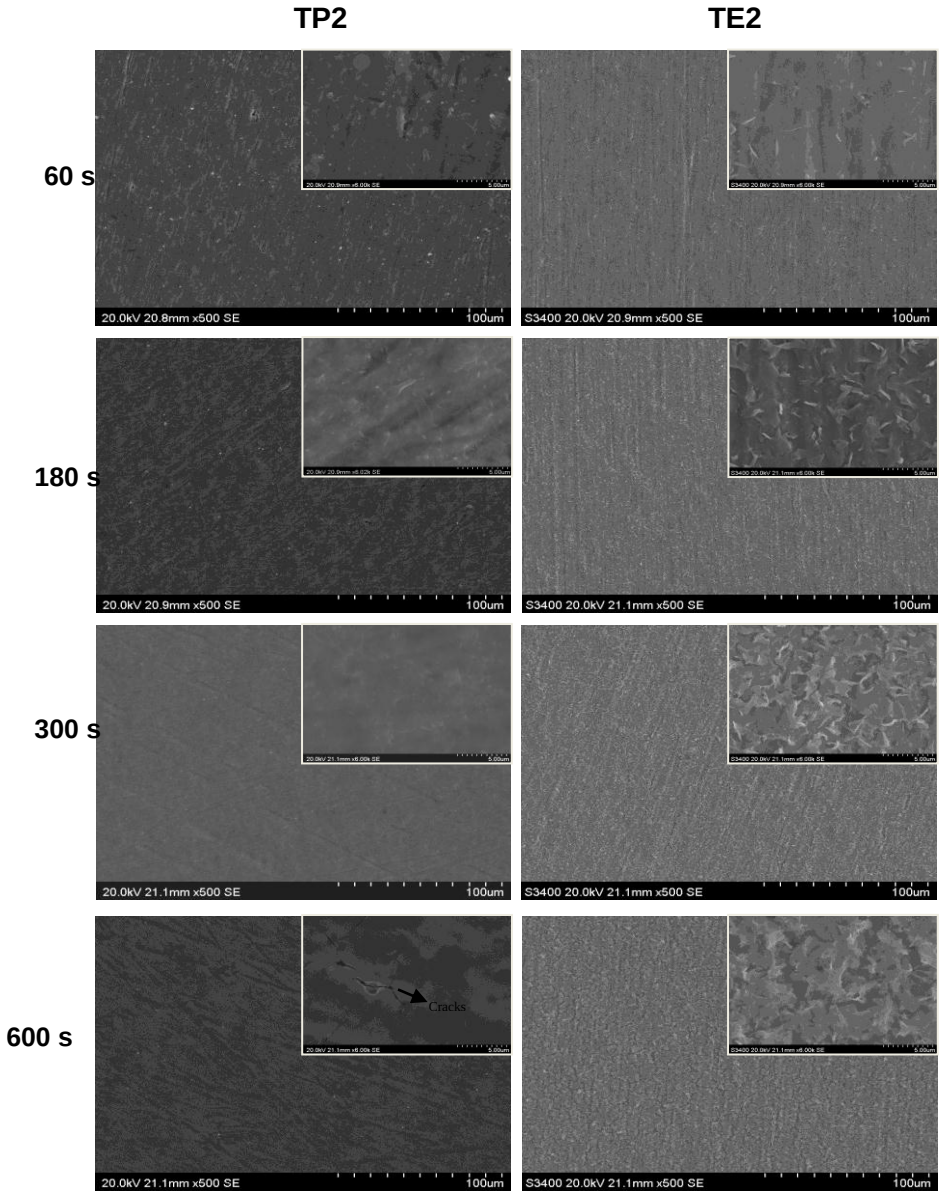

Figure 4.6 Influence of deposition time on TiO_2 films deposited using TP2 and TE2 sols with a needle internal diameter of 300 um at a flow rate of 5 ul/min and needle to substrate distance of 20mm.

The relationship between the deposition time and film thickness was estimated from equation 3.3. When the spraying time was 60 s, the estimated thickness of the TP2 films was approximately 80 nm. On increasing the spray time to 600 s, the estimated film thickness was increased to 820 nm as shown in **Table 4.6**. Similarly, the TE2 film thickness was increased from approximately 65 nm to approximately 660 nm on increasing the spray time from 60 s to 600 s. Therefore, as expected, the film thickness was directly proportional to the deposition time.

Table 4.6 Estimated thickness of TiO_2 films with varying deposition time (n=5)

Spray time (s)	Estimated thickness (nm)	
	TP2	TE2
60	81.8±0.5	65.4±0.5
180	245.3±1.6	196.3±1.1
300	408.9±2.6	327.0±3.2
600	823.6±5.3	659.6±5.9

The morphology of TiO_2 films deposited under similar conditions was affected by the solvent type. The prOH solvent carrier gave TiO_2 films with a predominantly Type 1 morphology whereas the etOH solvent carrier gave a Type 2 film morphology at short deposition times which became Type 4 morphology at long deposition times. Also, the films produced using prOH were estimated to be thicker than those produced using the etOH solvent. For both solvent carriers, uniform and crack free films could be obtained at deposition time <180s. Thus 180s was used for further investigations in this work.

4.3.2 Influence of sol flow rate

The effect of flow rate on the size of the TiO_2 droplets was investigated using the TP2 sol. As shown in **Table 4.7,** the droplet relic diameter was directly proportional to the sol flow rate. The average droplet relic diameter increased from 1.08±0.12 µm to 6.20±3.53 µm when the sol flow rate was increased from 2 to 20 µl/min. There was no significant difference in the average relic diameter of the droplets obtained at a flow rate of 2-10 µl/min. However, the average droplet relic diameter obtained at 15-20 µl/min was significantly higher than that obtained at 2-10 µl/min.

Table 4.7 Electrospray characteristics obtained at different sol flow rates (n=5).

Flow rate (µl/min)	Average droplet relic diameter (µm)	Spray diameter (mm)	Estimated thickness (nm)
2	1.1±0.1	30.6±0.2	122.8±1.7
5	1.4±0.2	34.4±0.3	245.3±1.6
10	1.4±0.7	44.4±0.9	291.5±11.5
15	2.9±1.1	49.4±1.1	353.2±14.4
20	6.2±1.1	53.6±0.2	401.0±3.4

The morphologies of the TiO_2 films deposited at different flow rates were similar to those observed in **Figure 4.5** (results not shown). For the TP2 sol, a flow rate of 2 µl/min resulted in the deposition of dense and continuous films (Type 1 morphology). On increasing the flow rate to 5 µl/min, film homogeneity was still maintained. A similar morphology was observed for the films deposited at 10 µl/min although occasional microcracks were present. On the other hand, a small number of microcracks were present in the films deposited at 15 µl/min although the films were generally dense and continuous whereas the films deposited at a flow rate of 20 µl/min were severely cracked.

For the TE2 sol, a flow rate of 2 µl/min gave uniform coverage. The deposited films consisted of a dense layer with an overlying layer of flake-like structures (Type 3 morphology). Increasing the sol flow rate to 5 µl/min resulted in an increment in film roughness. The films bore a fractal morphology and were composed of a uniform layer with a network of particle agglomerates. Upon increasing the flow rate to 10 µl/min a marginal decrease in film roughness was evident, although the films still bore a Type 3 morphology. The films consisted of a uniform sub-layer with a reduced number of flake-like structures. Increasing the flow rate to 15 µl/min resulted in a further reduction in roughness.

Using the TP2 sol, it was also found that the sol flow rate also affected the spray area and the subsequent film thickness. As summarized in **Table 4.7**, an increase in TP2 sol flow rate from 2 to 20 µl/min caused the spray diameter to increase from approximately 30mm to 54 mm as predicated in the literature (Chen *et al*, 1999). As expected, the increase in sol flow rate also increased the film thickness from approximately 120 nm to approximately 400 nm. Hence the film morphology could also be optimized by varying the flow rate. For the TP2 sol the variation in flow rate resulted in Type 1 morphology whereas the TE2 sol gave Type 3 morphology with a reduced level of agglomeration as

the flow rate was increased. Low flow rates (<10 μl/min) produced uniform and crack free films for both the TP2 and TE2 sols. However, the spray area was smaller for the lower sol flow rates. Therefore, the flow rate was selected to give a compromise between the spray area and film morphology. A flow rate of 5μl/min was used in further investigations as it gave adequate film coverage and also a reasonable spray coverage area.

4.3.3 Effect of sol concentration

Table 4.8 summarises the variation in droplet relic diameter with sol concentration. The droplet diameter appeared to increase proportionally with the sol concentration. There was no statistical difference in the average droplet relic diameter obtained from the electrostatic atomisation of the TP2 and TP4 sols. Similarly, there was no significant difference in the average droplet relic diameter obtained using the TP6 and TP8 sols. However, the results showed that there was a slight increase in diameter as the sol concentration was increased from 2 to 8 wt%. On the other hand, the spray diameter was reduced from approximately 34 mm to 29 mm on increasing the sol concentration from 2 to 8 wt% as summarized in **Table 4.8**.

Table 4.8 Electropray characteristics obtained different sol concentration (n=5).

Sol concentration (wt%)	Average droplet relic diameter (μm)	Spray diameter (mm)	Estimated thickness (nm)
2	1.4±0.2	34.4±0.6	245.3±1.6
4	1.4±0.3	33.0±0.5	562.9±19.3
6	1.5±0.3	31.0±0.4	997.7±17.6
8	1.1±0.3	29.9±0.3	1344.0±11.8

The morphology of TiO_2 films deposited using the TP and TE sols is shown in **Figure 4.7**. The TP2 sol resulted in the deposition of dense and continuous films with a relatively smooth and continuous morphology (Type 1) as observed in the preceding sections. The TP4 sol produced relatively dense and uniform films with occasional cracking. The TP6 sol led to the deposition of highly cracked films with occasional particle agglomerates. The severity of the cracking and agglomeration was appreciably increased for the TP8 sol.

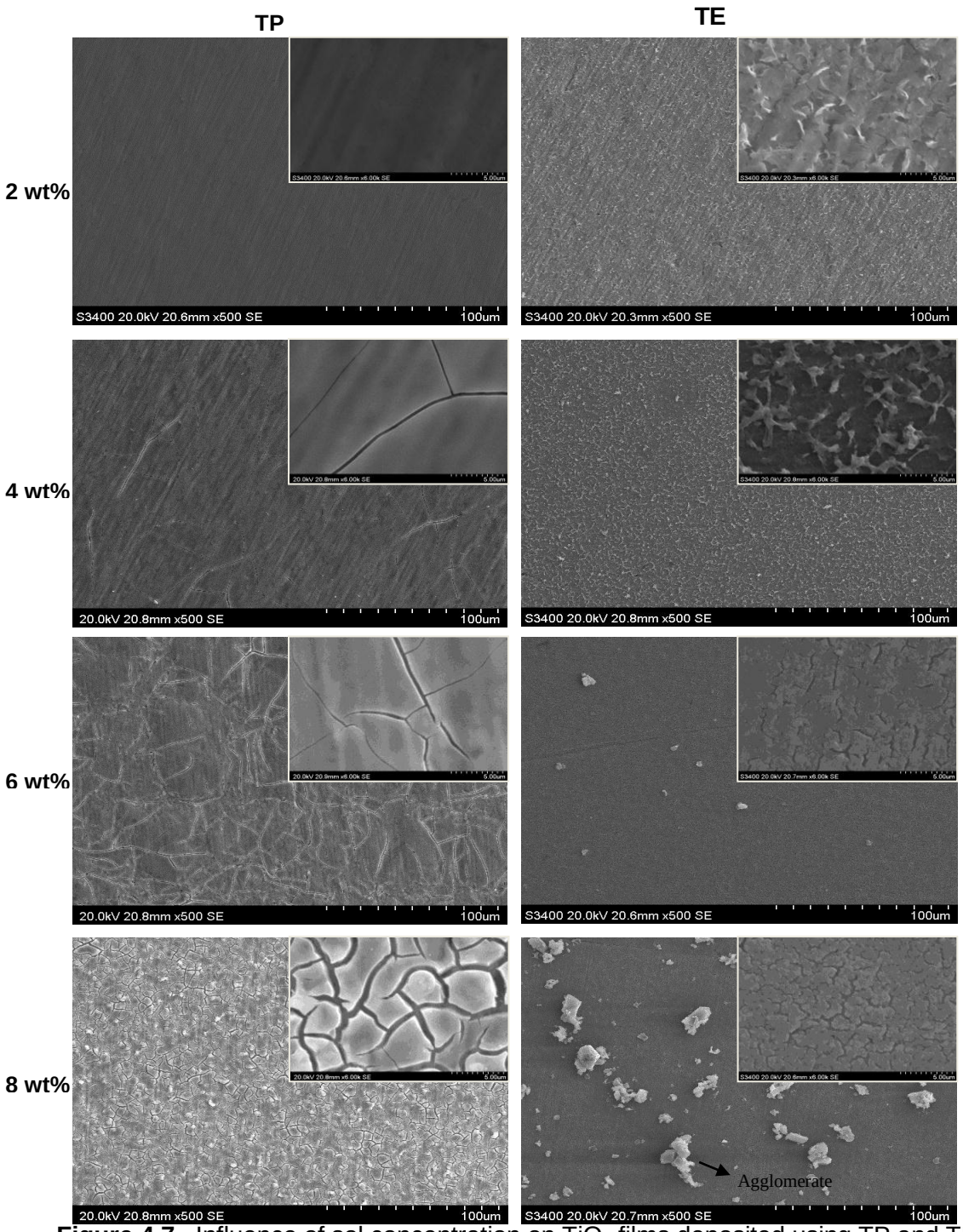

Figure 4.7 Influence of sol concentration on TiO_2 films deposited using TP and TE sols electrosprayed with a needle internal diameter of 300 um with a needle to substrate distance of 20 mm and a spray duration of 180 s

For the TE sols, the TE2 sol resulted in the deposition of a dense underlying layer with a network of flake-like structures. The morphology of the films deposited from the TE4 sol was similar to that produced from the TE2 sol. However, there was a reduction in the number of the flake-like structures which resulted in a more homogeneous film topography. The TE6 sol produced dense and uniform films with occasional particle

agglomerates. However, numerous small cracks were present in the film. For the TE8 sol the deposited films were generally dense and uniform with a high number of microcracks. Additionally, large particle agglomerates were present. The variation of the film thickness was studied using the TP sols. The estimated thickness was increased from approximately 240 nm to 1340 nm due to the increase in sol concentration. Furthermore, the TP sols gave a Type 1 morphology which became defective as the sol concentration was increased whereas the morphology of the TE films changed from Type 3 to Type 2 as the sol concentration was increased.

Clearly, the sol concentration is a critical parameter for the electrospraying of the TiO_2 films. A high sol concentration resulted in a higher film growth rate with respect to a lower sol concentration under similar spray conditions. However the films produced were highly defective, which necessitated a shorter deposition time and hence limits the versatility of the electrospray process. Also, despite extending the electrospray flow rate regime to higher values, a higher sol concentration reduced the spray diameter which further reduced the efficiency of the electrospray process for large implants. A low concentration was considered to be more economical which can minimize the cost of raw materials for industrial applications. Hence a sol concentration of 2 wt% was selected for use in further investigations.

4.3.4 Influence of needle to substrate distance

The influence of needle to substrate distance on the average relic diameter was investigated using the TP2 sol and the average relic measurements are compared in **Table 4.8**.

Table 4.9 Average relic diameter obtained using different needle to substrate distance

Needle to substrate distance (mm)	Average droplet relic diameter (μm)	Spray diameter (mm)	Estimated film thickness (nm)
10	2.7±0.2	10.5±0.5	2419.3±6.3
20	1.4±0.1	34.4±0.6	245.3±1.6
30	1.2±0.1	51.6±0.4	86.4±1.0
40	0.9±0.1	81.3±0.1	46.7±0.8
50	0.8±0.2	93.1±0.4	34.5±0.4

The average relic diameter was significantly reduced by an increase in the needle to substrate distance. The average relic diameter was reduced by approximately ¼ on increasing the needle to substrate distance from 10 mm to 50 mm. In contrast, there was a nine fold increase in spray diameter as the needle to substrate distance was increased from 10 to 50 mm.

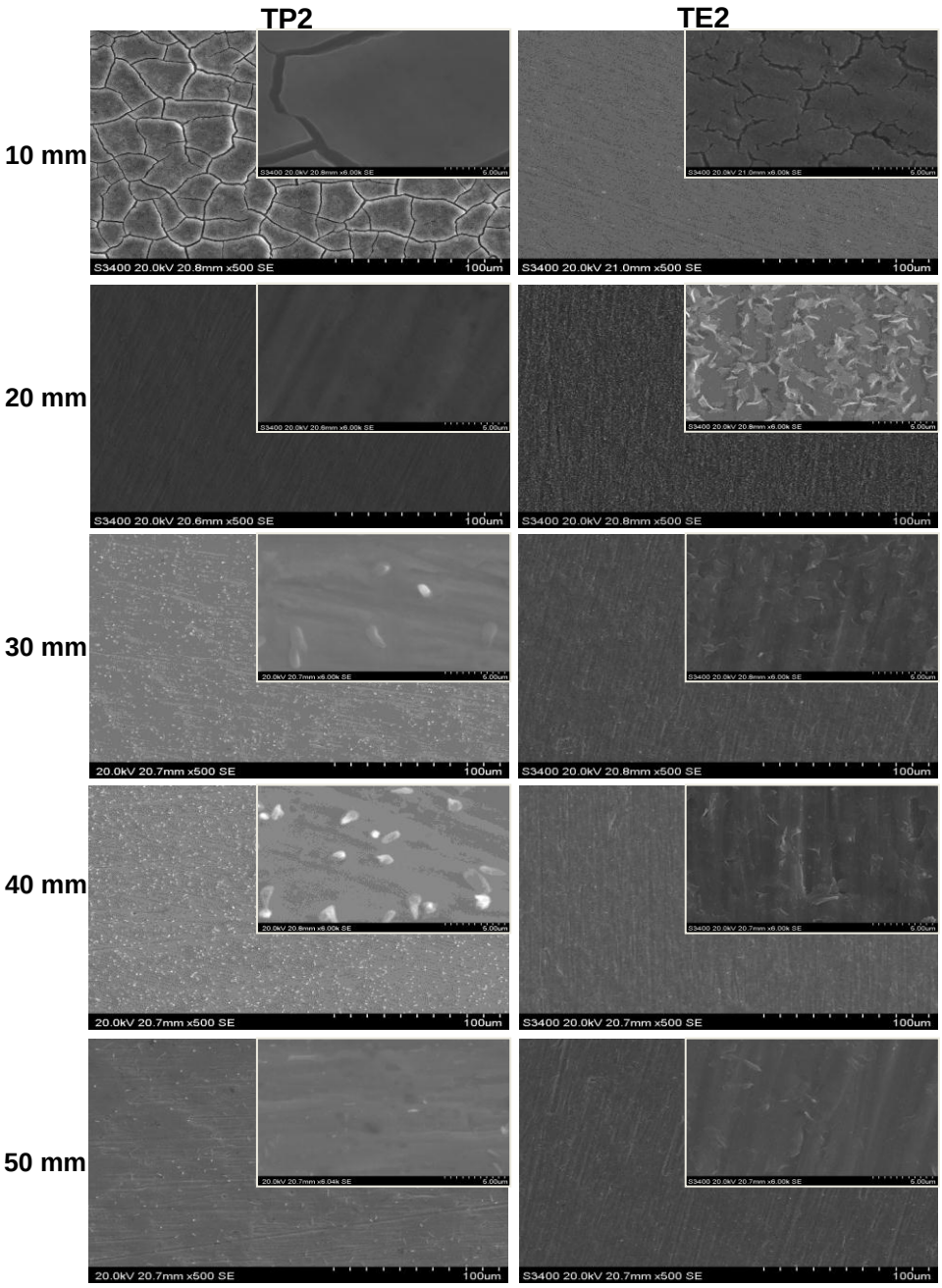

Figure 4.8 Effect of needle to substrate distance on TiO_2 films deposited using TP2 and TE2 sols using a needle of internal diameter 300 um and a flow rate of 5 ul/min at a spray duration of 180 s

The effect of the needle to substrate distance on the morphology of the TiO_2 films deposited from theTP2 and TE2 sols is compared in **Figure 4.8**. For the TP2 sol, a short deposition distance of 10mm resulted in the deposition of severely cracked films. Upon increasing the spray distance to 20mm, the films deposited were fairly dense and continuous. No cracks were evident (Type 2 morphology).

At 30mm, the film morphology was composed of a dense layer with incorporated spherical particles (Type 2 morphology). A similar film morphology was evident for a needle to substrate distance of 40mm. However, there was an overall reduction in the number of the incorporated particles. For a needle to substrate distance of 50mm the films produced also consisted of a dense layer with occasional spherical particle agglomerates. These films appeared to be smoother than those deposited at a needle to substrate distance of 40 mm.

For the TE2 sol, a needle to substrate distance of 10 mm also resulted in the deposition of highly cracked films. Increasing the needle to substrate distance to 20 mm led to the deposition of rough films with a fractal morphology. For a needle to substrate distance of 30 mm the deposited films comprised of a continuous bottom layer with occasional flake-like structures. A further increase in needle to substrate diameter to 40 mm also yielded continuous films although there was a marked reduction in the density of the particle agglomerates. The films deposited at a needle to substrate distance of 50mm appeared to be smoother than those deposited at shorter needle to substrate distances and consisted of a dense layer.

The variation of film thickness with needle to substrate distance was predicted using the TP2 sol. The estimated film thickness was significantly reduced from approximately 2460 nm to approximately 35 nm as a result of increasing the needle to substrate distance from 10 mm to 50 mm. Clearly, the needle to substrate distance plays a critical role during the electrospray deposition of the TiO_2 films. For the TP2 films, an increase in the needle to substrate distance changed the film morphology from Type 1 to Type 2 whereas the TE2 film morphology was changed from Type 3 to Type 1 on increasing the needle to substrate distance. This suggested that the needle to substrate distance should be a compromise between desirable film uniformity and an adequate spray area while minimizing the deposition time for higher processing efficiency. Thus intermediate spray distances were considered to be suitable. In the case of the TP2 sol, an intermediate spray distance of 20mm was selected as it gave a uniform and dense film morphology as well as a reasonable coverage area. On the

other hand, the TiO_2 films obtained using the TE2 sol displayed a more homogeneous morphology at a needle to substrate distance of 30mm.

4.3.5 Influence of needle diameter

The effect of the needle internal diameter on the relic diameter was firstly investigated using the TP2 sol and the results are compared in **Table 4.10.** The average relic diameter underwent a five-fold increment with an increase in the needle internal diameter ($p<0.05$).

Table 4.10 Influence of needle internal diameter on average relic diameter (n=5)

Needle internal diameter (μm)	Average droplet relic diameter (μm)	Spray diameter (mm)	Estimated thickness (nm)
300	1.4±0.2	34.4±0.3	245.3±1.7
500	3.5±1.3	32.1±0.7	278.5±1.6
700	5.3±1.6	30.8±0.1	303.0±1.2

Figure 4.9 shows the morphology of the TiO_2 films obtained from electrospraying the TP2 and TE2 sols with needles with internal diameter of 300-700 μm. For the TP2 sol, the TiO_2 films deposited using the 300 μm internal diameter needle were dense and relatively featureless. Increasing the needle internal diameter 510 μm resulted in a slight increase in surface roughness. The films produced were fairly dense with incorporated spherical particles (Type 2 morphology). A further increase in needle internal diameter to 700 μm also led to the deposition of a dense layer with incorporated particles.

For the TiO_2 films deposited from the TE2 sol, the 330 μm internal diameter needle resulted in the deposition of a dense sub-layer with a network of reticular particle agglomerates. Film deposition with a needle internal diameter of 510 μm yielded a more homogeneous film morphology. The films consisted of a uniform sub-layer with occasional flake-like features. A similar morphology was produced on increasing the needle internal diameter to 700 μm and the films appeared to be smoother than those obtained using the smaller needles.

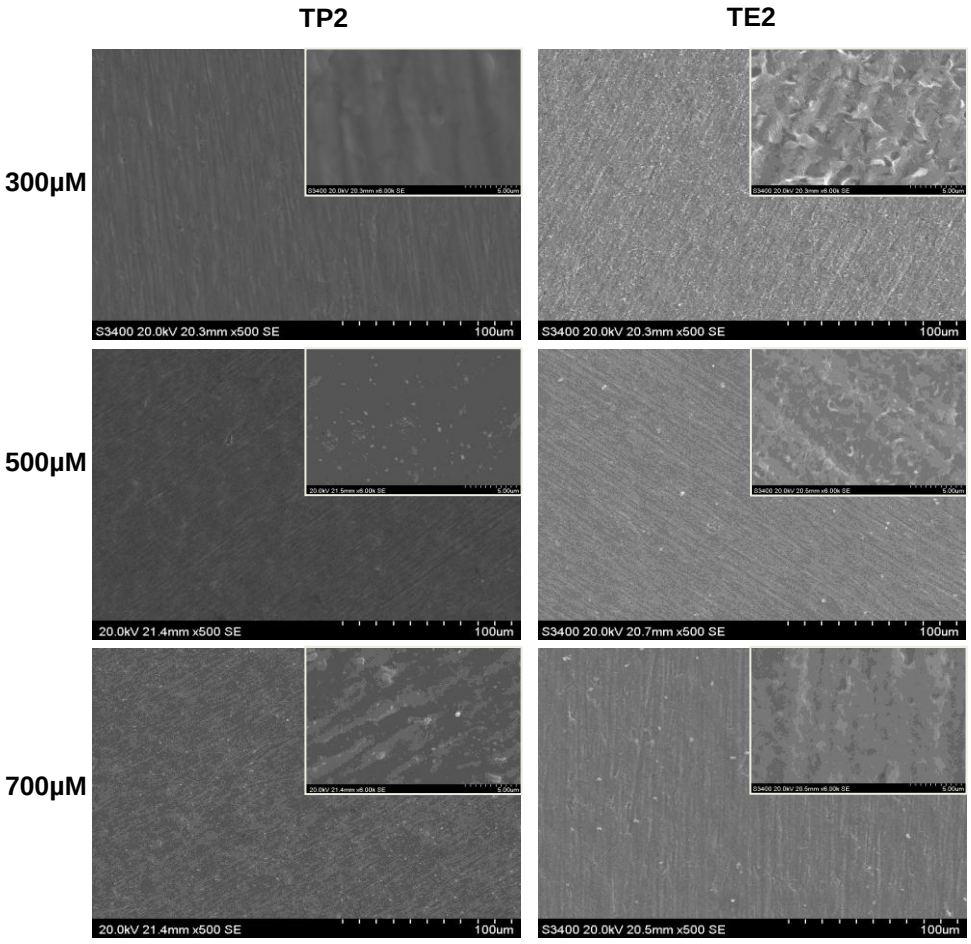

Figure 4.9 Influence of needle internal diameter on TiO_2 films deposited using TP2 and TE2 sols at a flow rate of 5 ul/min and a spray duration of 180 s and needle to substrate distance of 20 mm

Therefore, this study showed that an increase in needle internal diameter caused the evolution of the TP2 film morphology from Type 1 to Type 2 whereas the TE2 film morphology evolved from Type 3 to Type 1. On the other hand, an increase in needle internal diameter had a marginal effect on the spray diameter and film thickness as shown in **Table 4.10**. Based on the TP2 sol it was found that the spray diameter was reduced from approximately 34 mm to 30 mm whereas the estimated film thickness was increased from 240 nm to approximately 300 nm. However, finer droplets are considered to be more desirable for a more compact film structure. Hence, a needle internal diameter of 330 µm was selected for use in further experimental investigations as it also gave the largest spray diameter.

In summary, the film morphology was a function of the deposition parameters. The films were compared and ranked in terms of homogeneity and coverage. The results indicated that the sol concentration, sol flow rate, needle to substrate distance and deposition time had a major influence on the film morphology. However, needle internal diameter had a marginal effect on the film morphology. Therefore, for the 2 wt%

TiO_2sols, optimum uniformity was achieved using a needle of internal diameter 300 µm set at a distance of 20mm from the ground substrate. The applied voltage was varied between 3.4 to 4.0 kV at the optimum flow rate of 5 µl/min. Additionally, the morphology of the TiO_2 films deposited from the TE2 sol could be changed from reticular to dense by increasing the needle to substrate distance from 20 to 40 mm.

4.4 Influence post deposition treatment

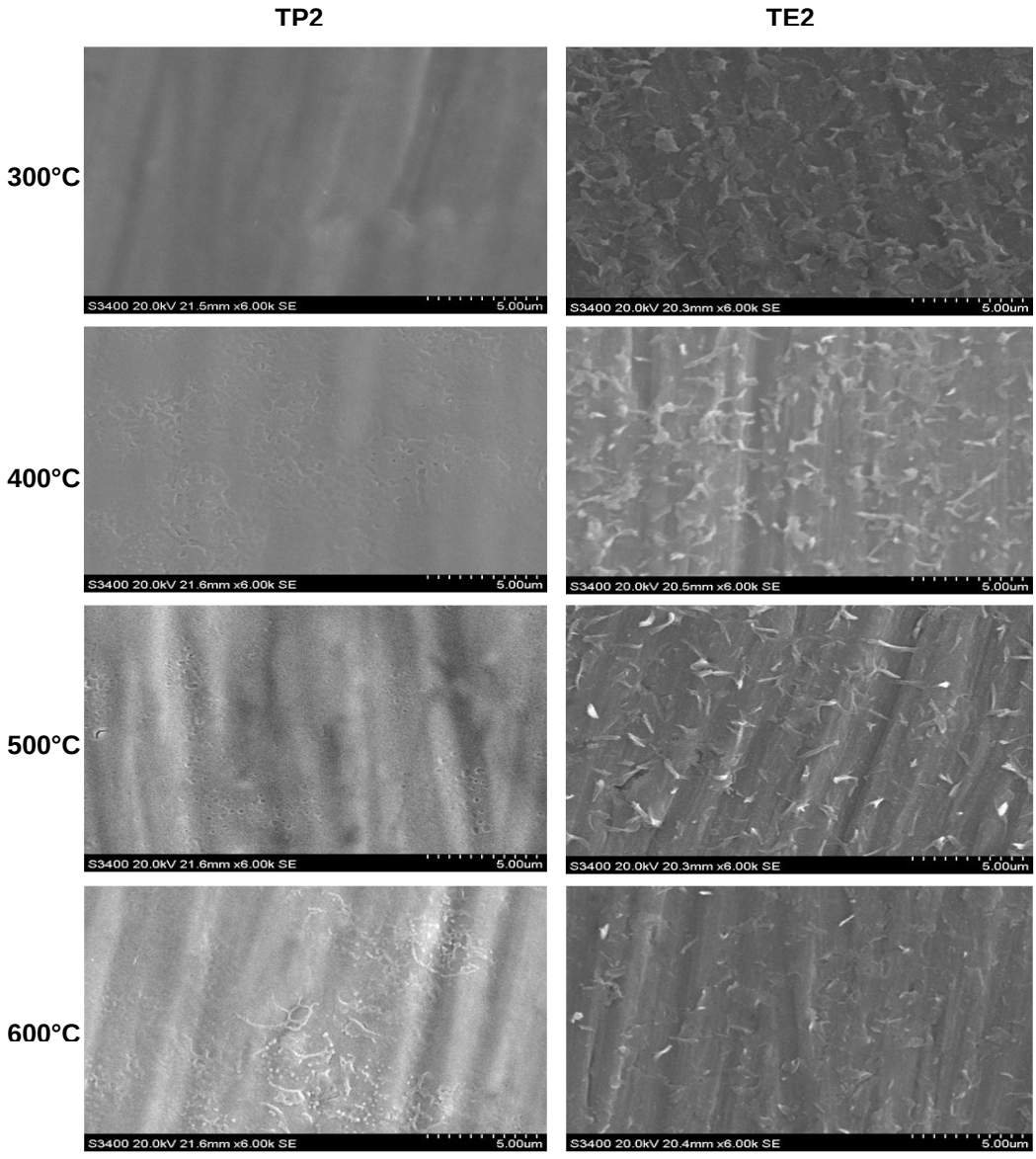

Figure 4.10 Scanning electron micrographs depicting the effect of post deposition annealing temperature on the morphology of TiO_2 films deposited using prOH and etOH as solvent. The films were deposited at a flow rate of 5 ul/min and a spray duration of 180 s and needle to substrate distance of 20 mm

The films produced by room temperature electrospraying of the sol-gel derived TiO_2 particles were amorphous as evidenced by the initial FTIR studies of the TiO_2 powders (**Figure 4.1**). However, Olofinjana *et al* (2000) clearly demonstrated that the mechanical properties of TiO_2 films were enhanced by thermal treatment. Therefore, the films deposited using the optimised process parameters were subjected to annealing at a range of temperatures. The morphologies of the annealed films are shown in **Figure 4.10.** For the TiO_2 films obtained using the TP2 sol, the films annealed at 300 °C were relatively uniform and dense, similarly to the as deposited film. However, annealing at 400-600 ºC caused the appearance of some rough spots on the film surface although the film morphology remained largely uniform.

In contrast, the TiO_2 films obtained using the TE2 sol underwent a reduction in film roughness due to annealing. The films annealed at 300 ºC displayed a similar morphology to that of the as deposited films and consisted of a dense sub-layer with a flake-like features. Upon increasing the annealing temperature to 400 ºC, a slight reduction in film roughness was observed as the dimensions of the flake-like structures were reduced. A further increase of annealing temperature to 600 ºC led to the disappearance of the flake-like structures and the films were relatively dense and homogeneous. Therefore, for the TP2 films, annealing resulted in a slight increase in surface roughness whereas the converse was true for the TE2 films. Generally, the initial fixation of coated implants *in vivo* relies on the existence of a dense and uniform film morphology. Hence, based on the morphological studies, the TP2 films were used in further investigations.

4.5 Surface characterization of TiO_2 films

4.5.1 Phase composition of TiO_2 films

4.5.1.1 Influence of annealing temperature on TiO_2 films

Figure 4.11 shows the XRD spectra of the electrospray TP2 films annealed at various temperatures. It can be seen that all the samples show a dominant reflection at the 2Θ value of 40.17°. This corresponded to the Ti alloy substrate with (101) orientation. Additionally, there were two smaller peaks at 2Θ values of 35.09° and 38.42° which were attributed to the Ti phase with (100) and (002) orientation respectively. The samples also showed two distinct peaks at 2Θ values of 53.89° and 62.69°. These were related to the anatase phase of TiO_2 with (105) and (204) orientation due to the closeness of their relative intensities to the standard data (JCPDS-ICDD 21-1272).

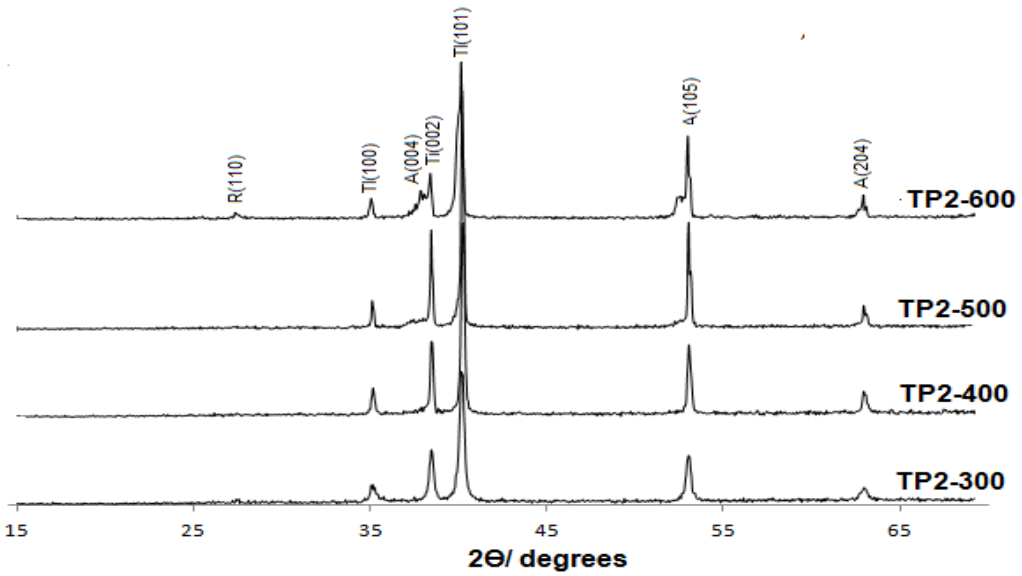

Figure 4.11 XRD spectra of TP2 films annealed at 300-600 °C. The films were deposited at a flow rate of 5 ul/min and a spray duration of 180 s and needle to substrate distance of 20 mm

The films annealed in the range 400-600°C showed stronger and sharper peaks compared to the film annealed at 300°C. The film annealed at 600°C also showed two more orientations at (004) and (110). The former was related to the anatase phase whereas the latter was attributed to the rutile phase. This suggested that an increase in annealing temperature led to an improvement in the film crystallinity and also caused the evolution of the rutile phase.

The TiO_2 films were further characterized by Raman spectroscopy. The Raman spectra are shown in **Figure 4.12**. All the films displayed a strong characteristic peak at 147 cm^{-1} due to the anatase film. The films also showed well-defined peaks at 447 cm^{-1} and 612 cm^{-1} which were attributed to the rutile phase. The films annealed at 400-600°C also showed peaks at 235 cm^{-1} and 320 cm^{-1} due to the rutile phase, and at 520 cm^{-1} due to the anatase phase. The film annealed at 600°C also showed an additional weak peak at 810 cm^{-1} due to the rutile phase. As the annealing temperature was increased, there was a progressive increase in peak intensity accompanied by sharpening of the peaks observed which further indicated an increase in crystallinity of the TiO_2 films as suggested by the XRD study.

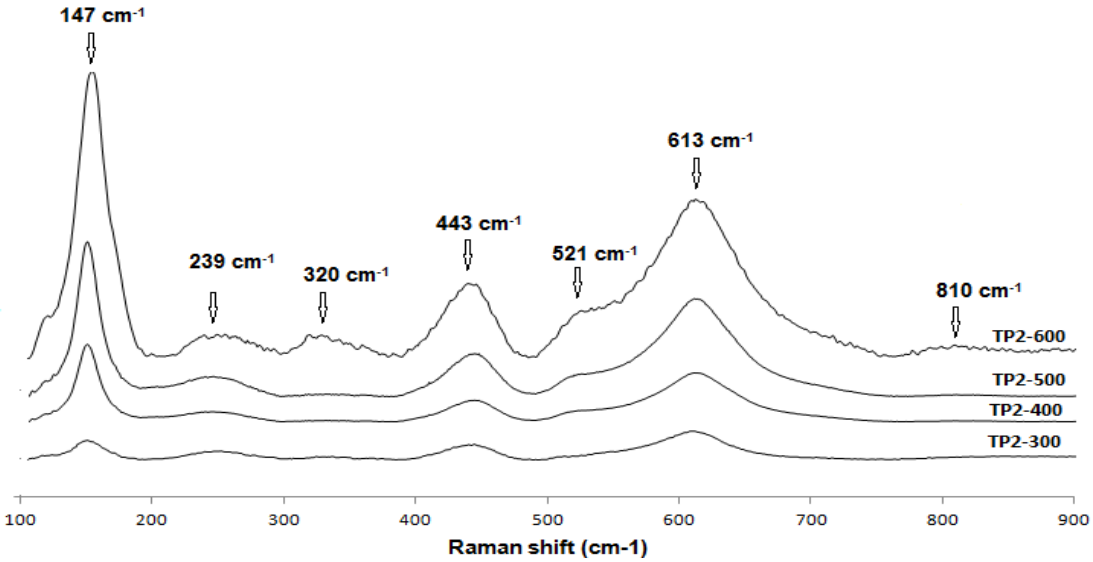

Figure 4.12 Raman spectrum of TiO_2 films annealed at various temperatures. The films were deposited at a flow rate of 5 ul/min and a spray duration of 180 s and needle to substrate distance of 20 mm

4.5.1.2 Influence of solvent type

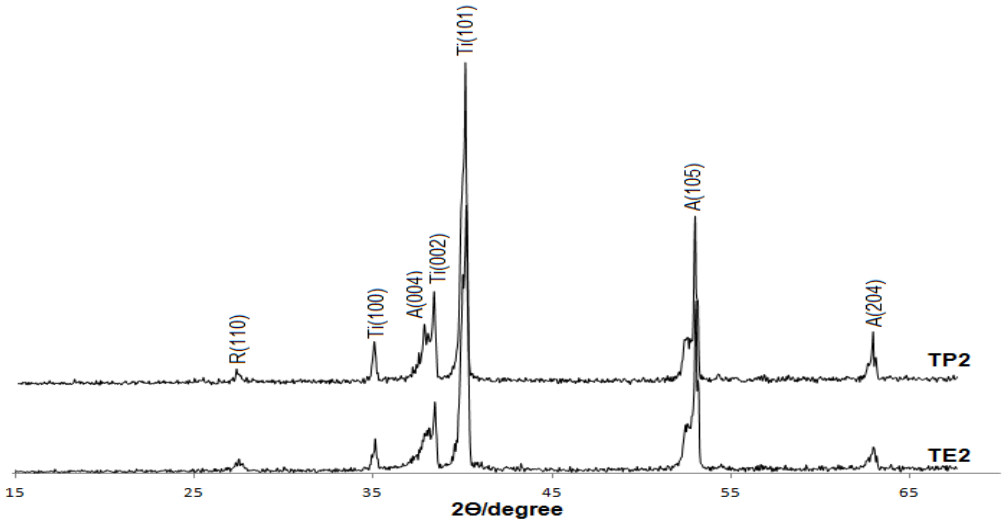

Figure 4.13 XRD spectra of TiO_2 films deposited using different organic solvents. The films were deposited at a flow rate of 5 ul/min and a spray duration of 180 s and needle to substrate distance of 20 mm

Figure 4.13 compares the phase composition of the TP2 and TE2 films annealed at 600°C. Similarly to the TP2 films, the TE2 films showed characteristic peaks owing to the rutile and anatase phases. However, the XRD spectra of the TP2 films was slightly

stronger than that of the TE2 films, suggesting that the TP2 films were more crystalline with respect to the TE2 films.

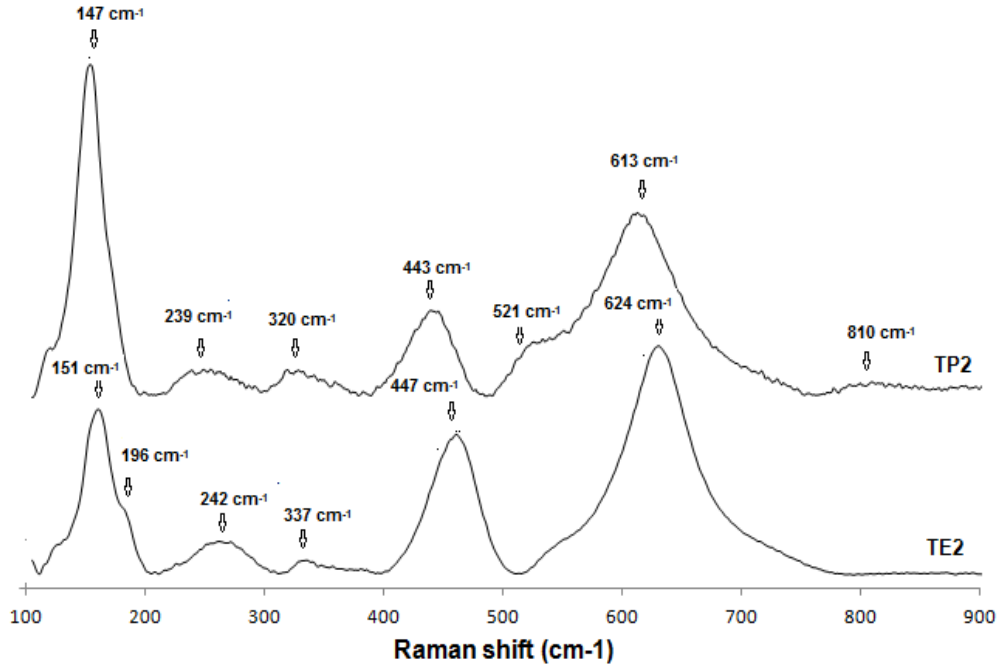

Figure 4.14 Raman spectra of TiO_2 films deposited using different sols. The films were deposited at a flow rate of 5 ul/min and a spray duration of 180 s and needle to substrate distance of 20 mm

The phase composition of the TE2 and TP2 films was also compared using Raman spectroscopy. As shown in **Figure 4.14** the TE2 films displayed a dominant peak at 151 cm^{-1} due to the anatase phase. The formation of the rutile phase was evident from the characteristic peaks at 144 cm^{-1}, 235 cm^{-1}, 320 cm^{-1} and 447 cm^{-1}. This was similar to the findings obtained from the TP2 films. However, the TE2 films also displayed an additional weak peak at 196 cm^{-1} which was attributed to the anatase phase. Furthermore, the intensity of the dominant peaks owing to the rutile phase were stronger for the TE2 films compared to the TP2 films which suggested that the former had a higher composition of the rutile phase compared to the latter.

4.5.2 Surface roughness of TiO_2 films

4.5.2.1 Effect of annealing temperature on surface roughness

The average surface roughness (R_a) of the TiO_2 (TP2 sol) films annealed at 300-600 ºC and the uncoated Ti alloy is shown in **Table 4.11**.

Table 4.11 Surface properties of TiO_2 films (n=12)

Surface	Average surface roughness (μm)	Contact angle °
TP2-300	0.77±0.03	17.58±0.21
TP2-400	0.82±0.04	13.92±0.65
TP2-500	0.90±0.03	11.88±0.25
TP2-600	0.93±0.03	8.70±0.19
TE2-600	1.02±0.07	6.61±0.52
Ti alloy	1.36±0.18	71.27±0.42

The results obtained clearly show that the annealing temperature affected the film roughness. The surface roughness of the uncoated Ti alloy was significantly higher than that of the films ($p<0.05$). However the film roughness displayed a marginal increase with annealing temperature although there was no significant difference in the surface roughness of the films annealed at 400-600 °C. The uncoated Ti alloy surface displayed an average surface roughness of 1.36 μm whereas the surface roughness of the annealed films varied between 0.7 and 0.9 μm as summarized in **Table 4.11**. The slight increase in average surface roughness with heat treatment temperature demonstrated that annealing had a marginal effect on the average surface roughness of the TiO_2 films. Moreover, these results were in agreement with the observations made using SEM.

4.5.2.2 Effect of solvent type

Table 4.11 compares the average surface roughness of the TiO_2 films deposited using prOH and etOH as solvent carriers and annealed at 600°C. As shown, the average surface roughness of the TE2 films was slightly higher than that of the TP2 films ($P<0.05$). Furthermore, the average surface roughness of the films was statistically lower than that of the uncoated Ti surface ($P<0.05$).

4.5.3 Film hydrophilicity

4.5.3.1 Effect of annealing temperature

The overall mean contact angles of the annealed films are shown in **Table 4.11**. The TP2-300 film had a contact angle of approximately 17.58±0.21°. However, the water contact angle was gradually reduced to 8.70±0.19° with an increase in annealing temperature. This indicated that the wettability of the TiO_2 films was enhanced by

increasing the annealing temperature. On the other hand, the contact angle of the uncoated alloy was significantly higher than that of the TiO_2 films (approximately 4 times that of the TP2-300 film). Therefore, the wettability of the Ti alloy could be increased by the deposition of a TiO_2 film.

4.5.3.2 Effect of solvent type

The water contact angles of the TiO_2 films obtained using prOH and etOH as organic solvent carriers are compared in **Table 4.13.** The contact of the TE2 films was statistically lower than that of the TP2 films ($p<0.05$), which suggested that the former was more hydrophilic than the latter. The contact of the TE2 films was also significantly lower than that of the uncoated Ti surface. Thus the wettability of the Ti alloy was also enhanced by the presence of the TE2 film. Moreover, the wettability of the TiO_2 films was affected by solvent type during film deposition.

4.6 *In vitro* characterization

From earlier studies, it was demonstrated that TiO_2 films with varying morphology could be produced via electrospraying. Furthermore, it was found that post deposition treatment such as high temperature annealing affected the crystallinity and phase composition of the films, in addition to the physical properties such as wettability and surface roughness. Therefore, it was hypothesized that the variation in the physical and chemical properties might be critical in the enhancement of the initial cell response and as such the biocompatibility of the TiO_2 films.

4.6.1 Effect of annealing temperature of TiO_2 films

The reduction of alamarBlue™ by MG63 cells on the annealed TiO_2 films over a 7 day period is shown in **Figure 4.15**. The study showed that all the surfaces enabled cell growth over the 7 day test period. On day 1, there was no significant difference in cell proliferation on the TiO_2 films annealed at 300-500 °C. However, these samples exhibited statistically lower proliferation compared to the film annealed at 600°C and the uncoated Ti alloy ($P<0.05$). Cell proliferation on the TiO_2 film annealed at 600°C was statistically higher than on the uncoated Ti alloy. This implied that the initial cell attachment was enhanced by an increase in annealing temperature.

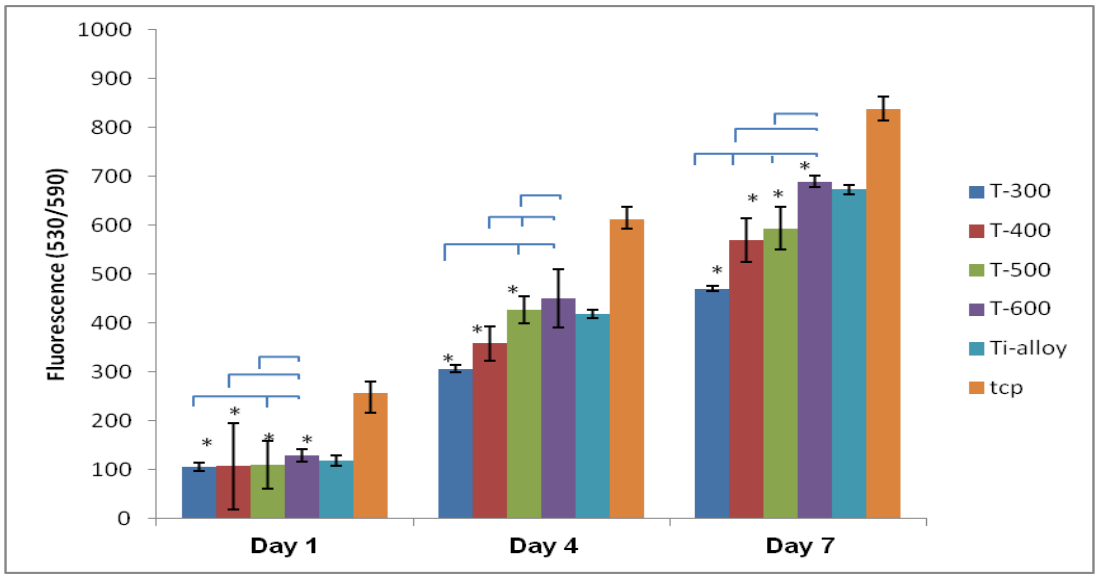

Figure 4.15 Proliferation of osteoblast-like cells on TP2 films annealed at 300-600 °C. Ti alloy was used as a control. Results represent mean±s.d of triplicates obtained from 3 different experiments (n=12). Horizontal brackets indicate a statistical difference between groups ($p<0.05$). Asteriks (*) indicate a statistical difference compared with the uncoated Ti alloy control ($p<0.05$)

On day 4, there was no significant difference in cell proliferation on the films annealed at 300-400°C. However, this was statistically lower than on the films annealed at 500-600 °C and the uncoated Ti alloy. There was no significant difference in cell proliferation on the latter test surfaces.

On day 7, the film annealed at 300 °C exhibited the lowest proliferation compared to the films annealed at the higher temperature and the uncoated Ti alloy. There was no significant difference in cell proliferation on the films annealed at 400-500 °C although these samples exhibited lower proliferation compared to the films annealed at 600 °C and the uncoated Ti alloy. However, cell proliferation on the film annealed at 600 °C was statistically higher than on the uncoated Ti alloy. Therefore cell attachment and proliferation were enhanced by an increase in annealing temperature.

The cell morphology on TiO_2 films annealed at different temperatures is shown in **Figure 4.16**. After an incubation period of 1 day, the cells exhibited a flattened and polygonal morphology on the TP2-300°C films. However, the cells on the films annealed at 400-600°C adopted a more flattened and spread out morphology which was an indication of normal cell growth. Cell filopodial processes were also observed anchoring the cells to the film surfaces and were also observed attaching the cells to each other.

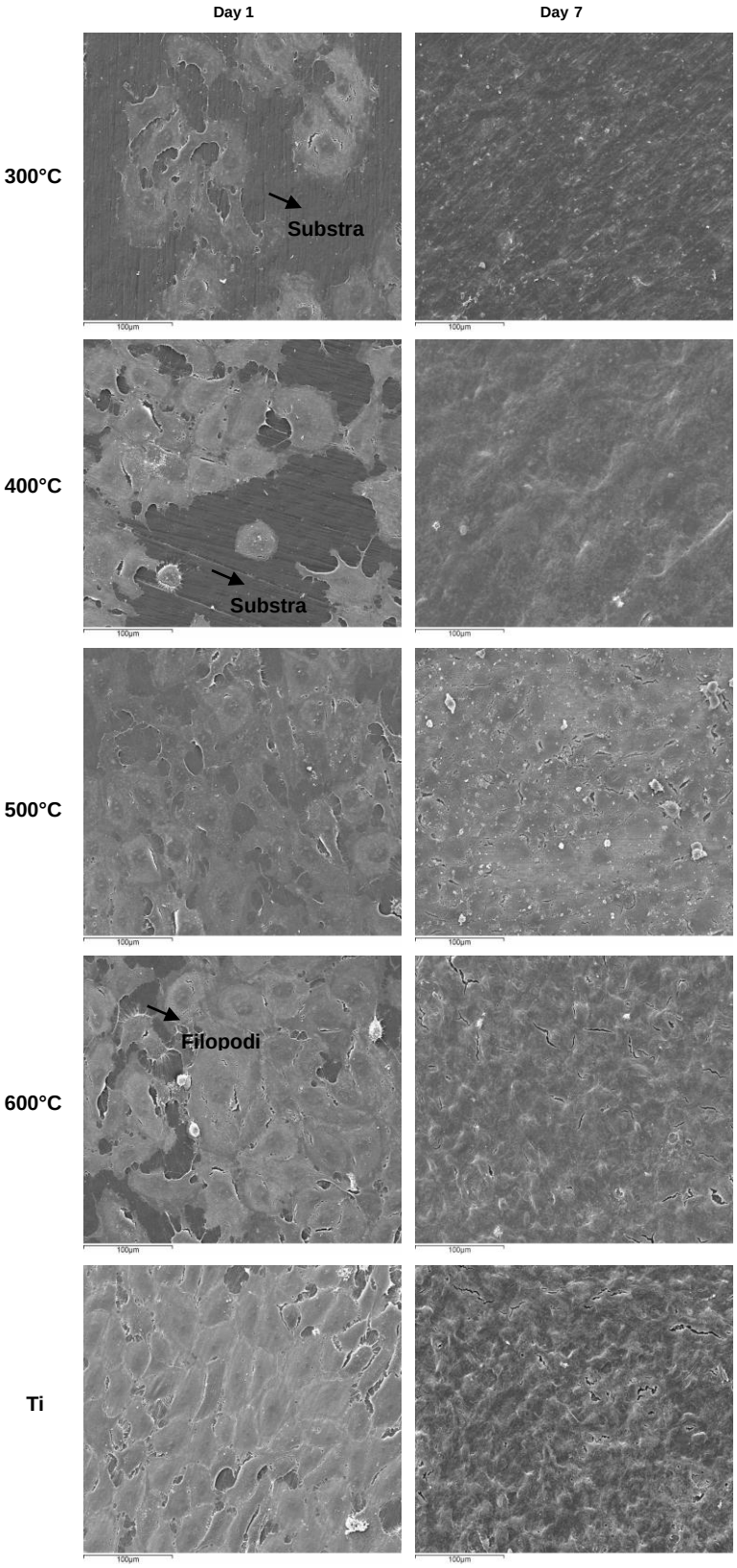

Figure 4.16 Scanning electron micrographs of MG63 cell morphology on TiO_2 films annealed at 300-600°C. at a flow rate of 5μl/min and needle of internal diameter 300 μm set at a needle to substrate distance of 20mm. Cells were cultured for 1-7 days

Furthermore, the degree of cell spreading appeared to increase with annealing temperature and there was an increase in the cell density observed on the TiO_2 film surfaces due to an increase in the annealing temperature. The film surface was also evident beneath the cells. In contrast, the cells on the uncoated Ti substrate were densely packed with a less spread out and polygonal morphology.

After an incubation period of 7 days, the individual cellular morphology was indistinguishable and cell multilayers with occasional cracking were present on all the test surfaces. This further confirmed that the cells were able to grow on all the test surfaces and also confirmed the non-cytotoxic nature of the TiO_2 films annealed at different temperatures.

4.6.2 Effect of solvent type

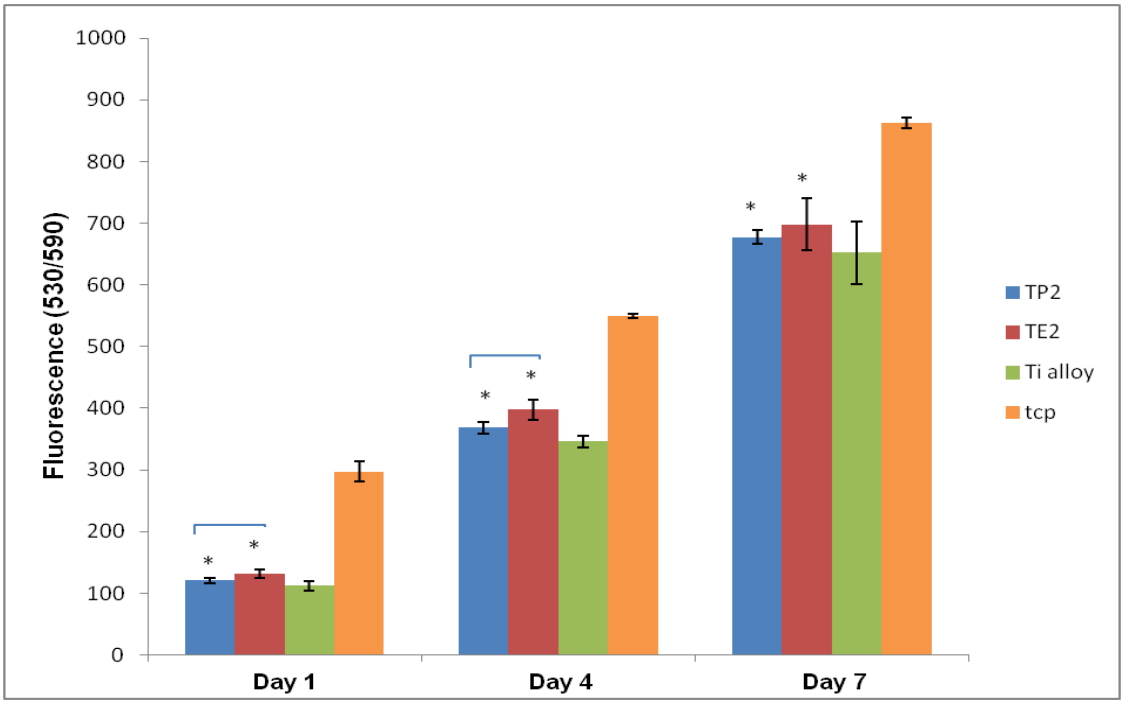

Figure 4.17 Proliferation of MG63 cells on TiO_2 films deposited using stabilized and non-stabilized sols over a 1-7 day incubation period (n=12). Results represent mean±s.d of triplicates obtaine from 3 different experiments. Horizontal brackets indicate a statistical difference between groups ($p<0.05$). Asteriks (*) indicate a statistical difference compared with the uncoated Ti alloy control ($p<0.05$)

The proliferation of MG63 cells on TiO_2 films deposited using different solvent carriers is shown in **Figure 4.17**. On day 1, the MG63 cell proliferation on the TiO_2 films was significantly higher than on the uncoated Ti alloy, which indicated that the initial cell

attachment was higher on the former with respect to the latter. However, the cell proliferation on the TE2 films was significantly higher than on the TP2 films, suggesting that the initial cell attachment was higher on the TE2 films. By day 4, an increase in cellular metabolism was evident, with the cell proliferation on the TiO_2 films being significantly higher than on the uncoated Ti surface. Furthermore, the cell proliferation on the TE2 films was significantly higher than that on the TP2 films ($p<0.05$). However, by day 7, there was no significant difference in the cellular metabolic activity on the TiO_2 films. Moreover, the cell proliferation on the TiO_2 film surfaces was statistically higher than on the uncoated Ti alloy. This showed that the TiO_2 films deposited using etOH as a solvent carrier promoted MG63 cell attachment and growth over the 7 day test period and also enhanced the *in vitro* biocompatibility of Ti and Ti alloys.

Figure 4.18 shows the MG63 cellular morphology on TiO_2 films deposited using different solvent carriers.

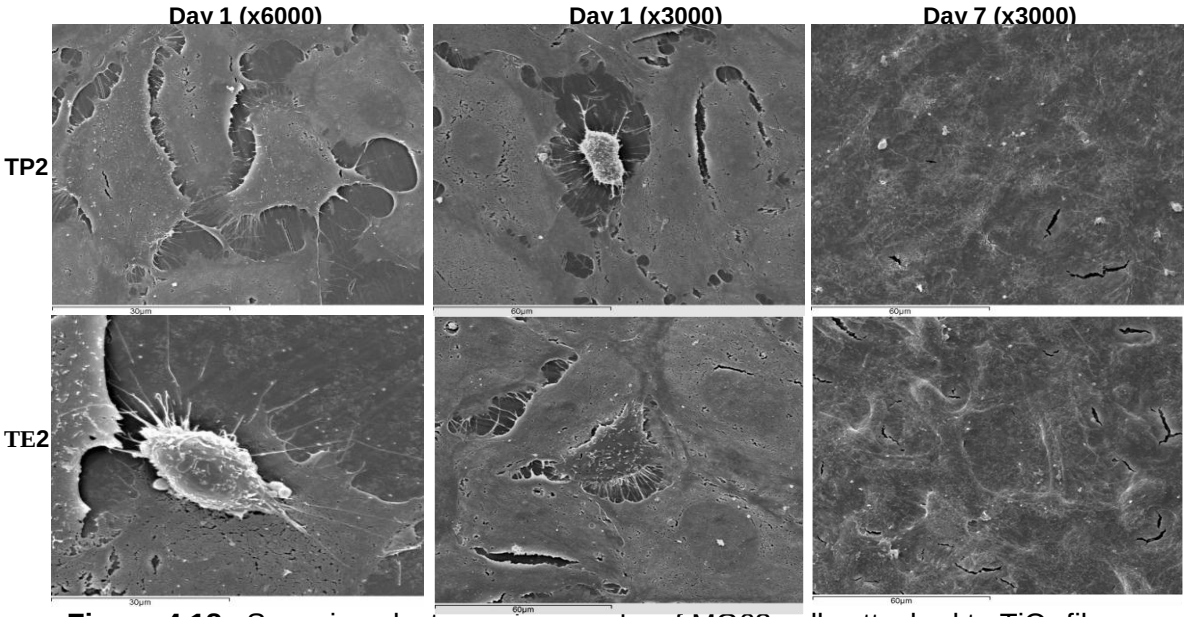

Figure 4.18 Scanning electron micrographs of MG63 cells attached to TiO_2 films deposited using the TP2 and TE2 sols at a flow rate of 5µl/min and needle of internal diameter 300 µm set at a needle to substrate distance of 20mm. The films were subjected to heat treatment at 600°C. The cells were cultured for 1-7 days

There was no significant difference in the cellular structure on the different TiO_2 surfaces. The cells displayed a flattened and spread out morphology. Filopodial processes were also observed to be extending from the cells towards the surface asperities for anchorage. In particular, the filopodia of the cells on the TE2 films preferentially attached to the rougher regions on the film surface. After 7 days of cell culture multilayers of cells were evident on all the surfaces. The individual cell

morphology was no longer distinguishable and the film surfaces were no longer visible. The morphology of the cells on the uncoated Ti substrate was as shown in **Figure 4.16**. These findings were a positive indication that cell proliferation had occurred on the TiO_2 films and correlated well with the results obtained using the cytotoxicity assay. Thus the electrosprayed TiO_2 films promoted cellular activity irrespective of the variation in the organic solvent carrier utilized during deposition.

4.7 Scratch resistance

4.7.1 Effect of annealing temperature scratch resistance of TiO_2 films

4.7.1.1 Scratch morphology

Figure 4.19 shows the scratches obtained on the annealed TiO_2 films due to scratch loads of 0.5-5 kg.

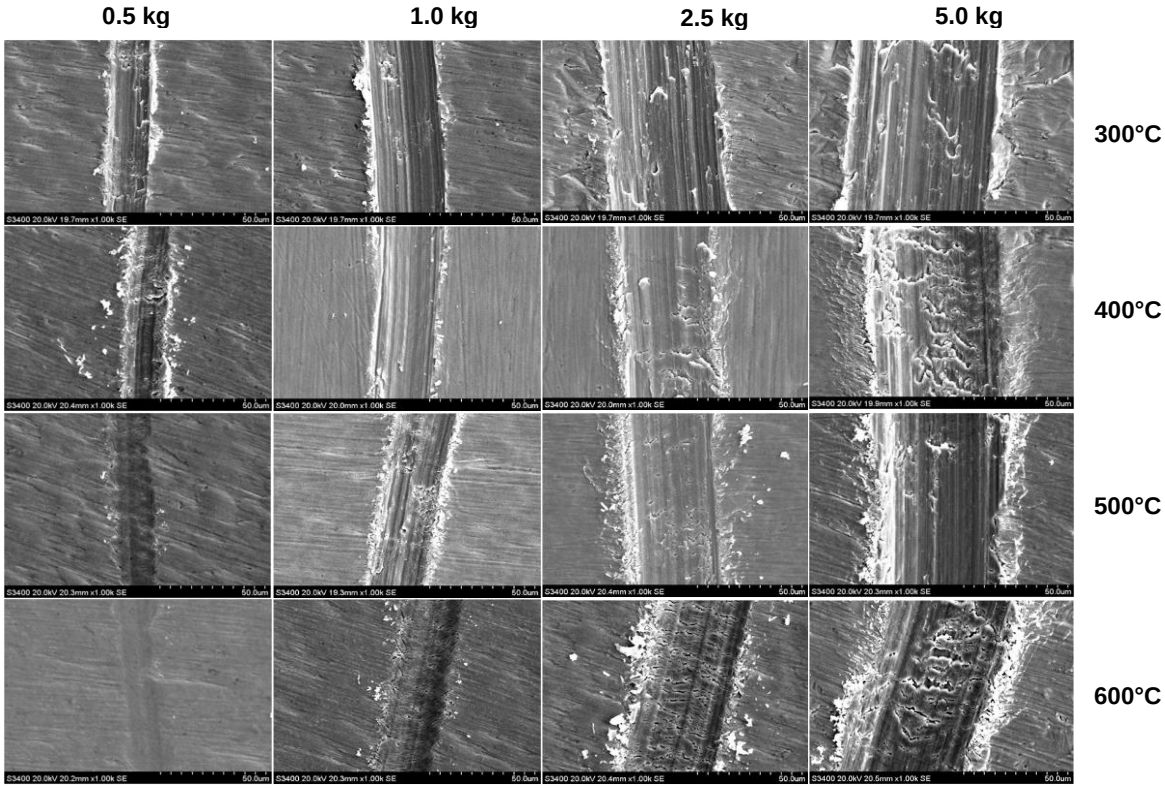

Figure 4.19 Scanning electron micrographs depicting scratch morphology on TiO_2 films deposited at a flow rate of 5µl/min and needle of internal diameter 300 µm set at a needle to substrate distance of 20mm. The films were subjected to heat treatment at 300-600°C.

For the TiO_2 film annealed at 300 °C, a scratch load of 0.5kg left a well-defined scratch track. There was evidence of film detachment due to the presence of several cracks

within the scratch track. The debris created was present along the edges of the scratch track. In the case of the TiO_2 films annealed at 400 °C, a scratch load of 0.5kg also left a well-defined scratch track. There appeared to be less film detachment as evidenced by the reduced level of film damage due to the indenter. However, a small number of cracks were present. These were oriented parallel to each other and transverse to the direction of movement of the indenter. Similarly, the application of a 0.5 kg scratch load on the surface of the TiO_2 films annealed at 500 °C resulted in the formation of a well-defined scratch track. However, there was minimal damage to the film surface in terms of cracking (or) material removal which indicated that the film material was pressed into the scratch track by the diamond indenter. On the other hand, an applied scratch load of 0.5 kg on the surface of the TiO_2 film annealed at 600 °C left a poorly defined scratch track whose edges were indistinguishable from the adjacent film. The film displayed minimal damage within the scratch track. Furthermore the width of the scratch tracks left by the diamond indenter appeared to be narrower in the case of the TiO_2 films annealed at 500-600 °C in comparison to the films annealed at lower temperatures.

For a scratch load of 1 kg, the film annealed at 300 °C displayed a well defined scratch track with large cracks and debris as described before, which was an indication of material removal by the diamond indenter. A similar phenomenon was also observed for the film annealed at 400 °C although the scratch track seemed to be narrower. For the film annealed at 500 °C, the scratch load of 1kg caused a well-defined scratch track with occasional large cracks which was an indication of film detachment. In the case of the TiO_2 film annealed at 600 °C, the 1 kg scratch load left a well defined scratch track with a high density of small transverse cracks. The former also appeared to be narrower than the scratch tracks present on the films annealed at lower temperatures, and there was minimal debris present along the edges of the scratch track. A further increase in the scratch load to 5 kg resulted in a similar trend. The films annealed at 300-500 °C displayed well-defined scratch tracks with severe cracking. In particular, the loads of 2.5-5 kg led to the removal of large sections of the film material along the scratch tracks on these TiO_2 films. The films annealed at 600 °C also exhibited well-defined scratch tracks as a result of the application of the 2.5-5kg scratch loads.However, there appeared to be less damage on the film material within the scratch tracks in terms of film material removal as evidenced by the presence of the transverse cracks in the scratch tracks on this film. The degree of cracking became more severe as the scratch load was increased from 2.5 to 5 kg.

In conclusion, an increase in the scratch load resulted in an increase in film removal. But the degree of film removal was reduced by an increase in the annealing temperature. These results indicated that the as deposited TiO_2 films were weakly bound to the underlying Ti substrate and that it was beneficial to subject the films to post deposition thermal treatment. The results further demonstrated that the annealing affected the scratch resistance of the electrosprayed TiO_2 films. The lack of severe damage on the surface of the films annealed at 600 °C was a clear indication that the mechanical properties of the films were enhanced by high temperature annealing.

4.7.1.2 Phase composition of scratch morphology

The phase composition within the scratch tracks made on the annealed TiO_2 films due to a scratch load of 0.5 kg was assessed using EDX. The scratch tracks on all the films displayed characteristic Ti peaks which were attributed to both the TiO_2 film and the underlying metal substrate. The scratch tracks also displayed a characteristic O peak. This was due to the presence of the TiO_2 films since the characteristic peak owing to the aforementioned element were absent in the EDX spectra of the uncoated Ti alloy (results not shown here). Furthermore, the O peaks appeared to display an increase in intensity for the TiO_2 films annealed at higher temperature. **Table 4.12** presents the elemental composition of the scratch tracks on TiO_2 films annealed at different temperatures.

Table 4.12 Average elemental composition within scratch tracks on TiO_2 films annealed at different temperatures and subjected to a scratch load of 0.5 Kg. The EDX spectra also exhibited Si and C peaks due to particle embedment from the initial Ti alloy grinding operation. C atoms were also present owing to the carbon coating operation prior to SEM analysis (results not shown) (n=3)

Sample	Elemental composition (wt%)		O/Ti
	O	Ti	
TP2-300	8.08±0.47	91.72±2.03	0.09
TP2-400	16.81±3.19	81.75±3.11	0.23
TP2-500	29.67±1.20	69.31±1.45	0.42
TP2-600	32.47±0.93	65.74±0.90	0.49

The scratch tracks on the TiO_2 films annealed at 300 °C had an O and Ti composition of approximately 6.5 and 91.7 wt%, respectively. However, the scratch tracks on the

TiO_2 films annealed at 600 °C exhibited O and Ti elemental compositions of approximately 33 and 65 wt% respectively. Since the detected Ti composition was affected by both the film and the substrate, this element could not be used as a quantitative measure of the amount of film material within the scratch track. Therefore, the elemental composition of O was considered to be more suitable for the indirect quantification of the TiO_2 film material within the scratch tracks. A high O content indicated the existence of the TiO_2 film as a result of less damage during indentation.

The relative oxygen proportion in the scratch tracks on the annealed TiO_2 films subjected to scratch loads of 0-2.5 kg is summarized **Table 4.13**. The unscratched annealed TiO_2 films were used as controls.

Table 4.13 Relative oxygen composition (wt%) of scratch tracks on TiO_2 films annealed at different temperatures (n=3).

Sample	Scratch load (kg)			
	0	**0.5**	**1.0**	**2.5**
TP2-300	35.16±2.82	8.08±0.47	6.47±0.72	3.41±0.38
TP2-400	37.17±0.11	12.84±0.86	7.73±1.47	7.31±0.42
TP2-500	38.09±1.34	29.67±1.20	24.17±1.76	20.83±0.55
TP2-600	38.26±1.38	32.47±0.93	26.87±1.12	21.57±1.18
TE2-600	37.19±0.13	33.19±0.93	29.26±0.82	21.39±0.31

There was no significant difference in the elemental composition of unscratched TiO_2 films annealed at 300-600 °C. The O content of the films was similar (approximately35-38 wt%). However, the relative composition of O was reduced within the scratch tracks on applying a scratch load of 0.5 Kg. The composition of O detected varied from approximately 8wt% to 32wt% as the annealing temperature varied from 300 to 600 °C. An increase in the scratch load from 0.5 to 2.5 Kg resulted in a further reduction in the amount of O detected. The proportion of O present was higher in the scratch tracks on the TiO_2 films annealed at the higher temperatures of 500-600 °C.

4.7.1.3 Average scratch width

The variation of scratch width with annealing temperature is summarized in **Table 4.14.** For each film there was an increase in scratch width on increasing the scratch load. However, the scratch load was reduced with increasing annealing temperature for each load. For example, for a load of 0.5 kg, the scratch width was reduced by approximately 15% when increasing the annealing temperature from 300 to 600 °C.

Table 4.14 Comparison of scratch width obtained on TiO_2 films annealed at different temperatures (n=15)

Sample	Scratch width (µm)			
	0.5 kg	**1 kg**	**2.5 kg**	**5 kg**
TP2-300	103.5±4.5	138.3±5.2	258.7±12.1	356.9±13.6
TP2-400	98.4±4.9	132.6±6.3	230.7±6.1	328.9±7.6
TP2-500	96.3±4.5	129.3±5.1	228.4±6.2	323.9±11.5
TP2-600	87.3±5.2	126.5±3.2	221.1±5.0	314.9±11.4
TE2-600	79.0±5.4	106.6±5.3	186.6±6.01	303.1±10.7

4.7.1.4 Scratch hardness

The variation of scratch hardness with annealing temperature is presented in **Table 4.15**. A scratch load of 1 Kg was selected as it caused transverse cracking and (or) material removal on all the films under investigation.

Table 4.15 Comparison of scratch hardness obtained on TiO_2 films annealed at different temperatures

Sample	Scratch hardness (GPa)
TP2-300	1.2±0.2
TP2-400	1.2±0.1
TP2-500	1.4±0.1
TP2-600	1.7±0.1
TE2	2.2±0.2

These results were in agreement with the findings made from SEM observations of the scratch track morphology and further confirmed that the annealing temperature had a significant impact on the scratch resistance of the TiO_2 films. The higher O elemental content showed that the film material was less susceptible to removal after annealing at higher temperatures. Annealing of the TiO_2 films at higher temperatures also facilitated less penetration of the diamond indenter within the film depth as evidenced by the lower scratch width obtained on the films annealed at 500 to 600 °C.

4.7.2 Effect of solvent type on the scratch resistance of TiO_2 films

4.7.2.1 Scratch morphology

The morphology of the scratch tracks on the TiO_2 films deposited using different solvent carriers is shown in **Figure 4.20**.

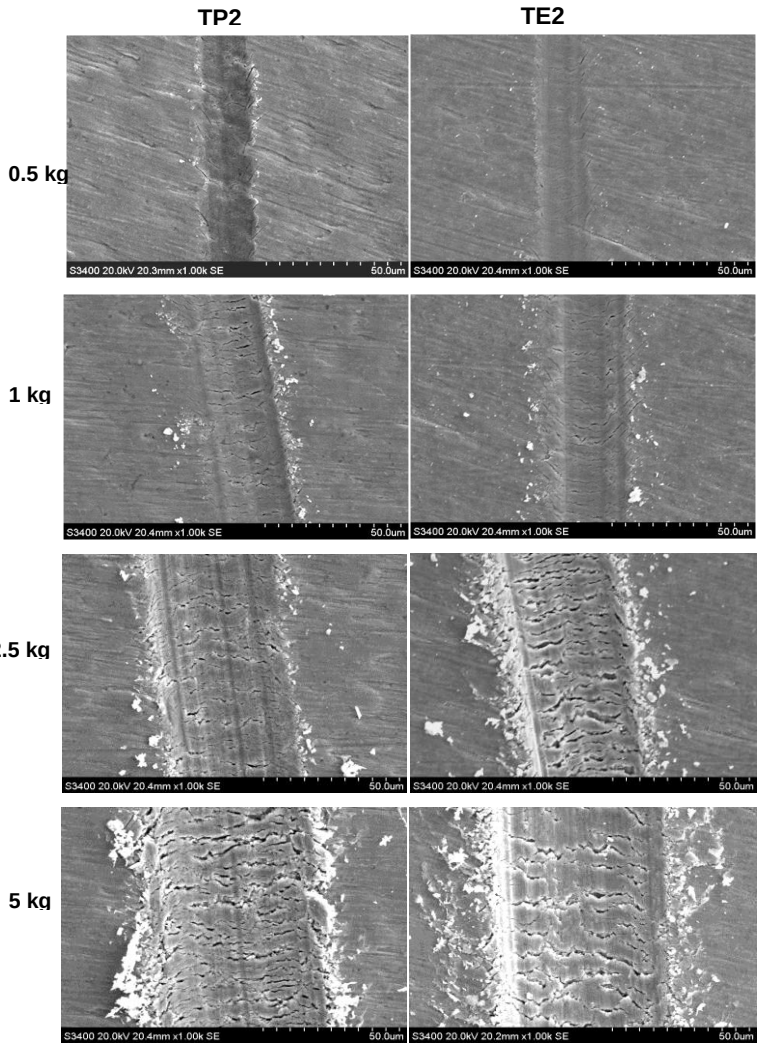

Figure 4.20 Scanning electron micrographs depicting scratch morphology on TiO_2 deposited using the TP2 and TE2 sols at a flow rate of 5µl/min and needle of internal diameter 300 µm set at a needle to substrate distance of 20mm. The films were subjected to heat treatment at 600°C.

For a scratch load of 0.5 kg, there was no significant difference in the morphology of the scratch tracks on the TiO_2 films. The scratch tracks were fairly well defined with little transverse cracking. Similarly for a scratch load of 1 kg, the scratch tracks were well-defined and bore several transverse cracks. Debris was present along the scratch tracks. However, the TP2 films also displayed a higher density of transverse cracks with respect to the TE2 films. A further increase in the scratch load resulted in an increase in the scratch width and transverse cracking as expected. However, the scratch width obtained on the TP2 films appeared to be slightly higher than that on the TE2 films.

4.7.2.2 Phase composition of scratch tracks

Elemental analysis of the unscratched films showed that there was no significant difference in the O content for the unscratched TP2 and TE2 films. The O elemental content was approximately 37 wt% for both films. However, the application of scratch loads of 0.5-2.5 kg led to a slight reduction in the amount of O detected as shown in **Table 4.14**. The O elemental content of the TP2 films was slightly lower than that of the TE2 films, although there was no significant difference among the TiO_2 films, which suggested that more TP2 film material had been stripped from the Ti-alloy substrate compared to the TE2 film.

4.7.2.3 Average scratch width

The average scratch width on the TiO_2 films obtained using the different organic solvents is presented in **Table 4.14**. For a scratch load of 0.5 kg, the average width of the scratches on the TE2 films was significantly lower than that on the TP2 films ($p<0.05$). A similar trend was obtained on increasing the scratch load to 5 kg. This was in agreement with the observations made using SEM and the elemental analysis of the scratch tracks inasmuch as an increase in scratch width could be indirectly related to a reduction in film material as evidenced by the corresponding reduction in the elemental composition of O.

4.7.2.4 Scratch hardness

The scratch hardness of the TiO_2 films deposited using different solvent carriers has been compared in **Table 4.14**. As shown, the scratch hardness generally declined on increasing the scratch load from 0.5 kg to 5 kg. Furthermore, the scratch hardness of the TE2 films was statistically higher than that of the TP2 films ($P<0.05$). These findings suggested that the solvent type could affect the mechanical properties in terms of cohesive and adhesive strength. Thus etOH was considered to be a more suitable solvent carrier for the deposition of TiO_2 films.

4.8 Discussion

The main aim of this study was to investigate the applicability of combining sol-gel synthesis and electrospraying for the deposition of TiO_2 films. The electrospray process and film morphology were primarily affected by the solvent type. By varying parameters such as the needle to substrate distance, flow rate and time, uniform and crack-free

films were obtained. The bioactivity and mechanical integrity of the films were influenced by solvent type and post deposition heat treatment.

4.8.1 Chemical and physical characteristics of TiO_2 sols

From visual observation of the TiO_2 sols, it was evident that the solvent type affected the sol properties. This was attributed to a difference in solvent polarity. EtOH was highly polar and reactive compared to prOH due to its shorter and less complex chain length which implied weaker bonding and also less stearic hinderance during alcoholysis (alcohol exchange process). This resulted in an accelerated rate of alcoholysis leading to the precipitation of TiO_2-complex.

It is proposed that the particle formation occurred according to the following mechanism; the precursor reacted with the alcohol to form low molecular weight oligomers which were soluble in the etOH solvent. As the monomeric precursor was consumed, the molecular weight of the oligomers was increased and the solubility of the oligomers decreased up to the point where they became insoluble, thus the TiO_2-complex particles nucleated. The primary particles absorbed the free monomers and grew over time to achieve a stable and final size. Therefore, precipitates were observed for the etOH solvent. The prOH solvent resulted in a slower alcoholysis reaction which gave a polymeric gel.

The FTIR spectra showed that the as-prepared sols contained metal oxide complexes, contrary to findings by (Davies *et al*, 1995) and Kaewwiset *et al* (2008) where metal oxide particles were obtained. This was expected since a non-aqueous sol-gel route was selected for use and requires thermal decomposition for metal oxide formation which fundamentally differs from the aqueous route which relies on the hydrolysis of the metal precursor by water molecules to produce oxide nano-particles. The presence of organic residues was also reported by Bezrodna *et al* (2004) and Su and Wang (2011) and could attributed to the adsorption of solvent molecules on the the powder surface whereas the isopropoxy residues could be attributed to realkoylation due to the reversible nature of the alcoholysis.

The FTIR spectra also indicated that water from the atmosphere adsorbed onto the powder surface via physisorption and chemisorption and reacted with the oxide complex according to the equation;

$$H_2O+M\text{-}O\text{-}M \longrightarrow 2M\text{-}OH \qquad (4.2)$$

Where M=Ti

The slight difference in the spectral intensity of the TP and TE powders could be attributed to the difference in the final particle size. In studies by Calleja *et al* (2004) and Behnajady *et al* (2011), it was observed that the TiO_2 particle size increased with the alcohol chain length. This was associated with a reduction polarity and reactivity such that a slower rate of reaction enhanced growth of the TiO_2 particle nuclei. Consequently it could be suggested that the prOH solvent yielded larger particles compared to the etOH solvent. This explained the overall weakness of the FTIR spectrum of the TE powders with respect to the TP powders.

The insulating bioceramic nanoparticles also acted as impurities in the solvent carrier and as such increased the surface tension, density and viscosity whereas the electrical conductivity was reduced. These findings concurred with those of Mahalingham and Edirisinghe (2007) and Li *et al*, (2008). The higher density, viscosity and surface tension of the TP sols sols with respect to the TE sols was due to the larger molecular mass of prOH with respect to etOH. PrOH also gave a polymeric gel whereas the etOH gave a particulate gel which affected the liquid physical properties.

4.8.2 Electrospraying of the TiO_2 sols

The TiO_2 sols were successfully atomised in the stable cone-jet mode of electrospraying which indicated that the electrical relaxation time was much less than the hydrodynamic time as postulated by Ganan-Calvo *et al* (2007). An increase in flow rate however, reduced the hydrodynamic time. Thus the stable cone-jet mode could not be attained at higher flow rate. Moreover, at higher flow rates the surface tension forces were unable to support the large mass of liquid at the needle exit resulting in the emission a simple jet at the needle exit.

From the investigations conducted using the TP and TE it was shown that solvent carrier primarily influenced the flow rate regime. The results demonstrated that sol concentration strongly affected the maximum flow rate regime during electrospraying in the stable cone jet mode but had a marginal effect on the operating voltage irrespective of the solvent carrier utilized. These phenomena can be understood from the relationship derived by Smith (1986) (Equation 2.5) which suggests that the maximum flow rate is directly proportional to the surface tension and inversely proportional to the electrical conductivity and density.

Generally, an increase in sol concentration caused an increase in the maximum flow rate since the surface tension was increased whereas the electrical conductivity was reduced. These findings also clearly indicated that the influence of the density on the flow rate regime was outweighed by that of the electrical conductivity and surface tension as the maximum flow rate was increased irrespective of the corresponding increase in density. These findings correlated well with research documented by Smith (1986) and subsequently Cloupeau and Prunet-Foch (1989) as well as Tang and Gomez (1996).

The electrical conductivity was considered to be the most critical parameter affecting the electrospray process as this parameter changed dramatically in comparison with the density and surface tension on increasing the sol concentration. For higher sol concentration, there were fewer free ions in the liquid. An increase in the flow rate reduced the hydrodynamic time and also increased the current through the liquid cone. Therefore, the electrical relaxation time was much lower than the hydrodynamic time at higher flow rates. For lower sol concentration, the increase in flow rate also reduced the hydrodynamic time but increased the current through the cone. This drastically reduced the relaxation time which became too short. Hence a stable cone-jet could not be attained at higher flow rates. This further explains the lower maximum flow rate obtained using the TE in comparison with TP sols. The results also showed that there was a slight increase in the minimal and maximal operating voltage due to increasing the sol concentration. This could be explained by the increase in surface tension since the operating voltage range scales with the square root of the surface tension (Smith, 1986).

The results showed that electrospray atomization of the bioceramic sols and suspensions was influenced by needle internal diameter. Using the TP2 and TE2 sols it was shown that there was a positive correlation between the needle internal diameter and the maximum flow rate for atomisation in the stable cone-jet mode which was in contrast to the findings of of Cloupeau and Prunet-Foch (1998) and Tang and Gomez (1996) who reported a reduction in the maximum flow rate as the needle internal diameter was increased. On the other hand, Chen *et al* (1999) found that the maximum flow rate was increased due to a corresponding increment in needle internal diameter. A possible reason for this discrepancy in results could be the difference in the spray media. Cloupeau and Prunet-Foch (1989) and Tang and Gomez (1996) reported on the electrospraying of pure liquid media. However, Chen *et al* (1999) reported on the electrospraying of ceramic nanoparticles namely, ZnO, ZrO_2 and Al_2O_3 suspended in etOH, similarly to this work.

The positive relationship between needle diameter and maximum flow rate can be explained in terms of the stable cone-jet criteria (equation 2.3). A larger needle diameter increased the jet diameter which in turn increased the hydrodynamic time. Hence the stable cone-jet mode could be achieved at higher flow rates. Furthermore, this study demonstrated that the applied voltage was increased by the needle internal diameter. This can be explained by relationship presented by Smith (1986) (Equations 2.5 and 2.6). The needle to substrate distance was much greater than the needle internal diameter. Hence, dV_O / dR_a >0. This means that a larger needle required a higher voltage in order to obtain a stable cone-jet.

4.8.3 Optimization of TiO_2 film morphology

The results clearly demonstrated that the relic diameter and subsequently the film morphology could be controlled by varying the liquid physical properties and deposition parameters. It has been reported that the primary droplet diameter and hence the average relic diameter, scales directly with the flow rate and density and inversely with the surface tension and electrical conductivity (Ganan-Calvo *et al*, 1997 and Ganan-Calvo, 1999). Therefore, under similar electrospray conditions (flow rate and applied voltage), the TE2 sol gave a lower average relic diameter with respect to the TP2 sol as the TE2 sol had a higher electrical conductivity and lower density than the TP2 sol although the surface tension was lower. The results also indicated that the electrical conductivity and density had a predominant effect on the droplet characteristics in comparison with the surface tension as the average relic diameter of the TE2 sol was smaller than that of the TP2 sol despite the lower surface tension of the TE2 sol. The viscosity of the sols was very low compared to that reported in the literature. For example, Rosell-Lompart and Fernandez de La Mora (1994) reported on viscosities of upto 140 mPaS whereas Hartman *et al* (2000) reported on viscosities of up to 100 mPaS. Therefore the influence of this property on the droplet characteristics was considered to be negligible.

The lower average relic diameter of the TE2 sol was also attributed to the effects of solvent evaporation. Small droplets have a larger specific area (surface area/ volume ratio) (Leeuwenburg *et al*, 2006). Thus the micron-sized droplets obtained during the electrostatic atomisation of the TiO_2 sols had a large specific area and underwent evaporation during transportation to the ground substrate due to the thermal energy provided by the surrounding atmosphere. On the other hand, etOH is highly volatile in comparison with prOH. Hence the droplets produced using the TE2 sol underwent a

higher degree of evaporation resulting in smaller droplet relics in comparison with the TP2 sol. The electric field also induced a charge on the spray droplets with a similar sign to that at the needle. Consequently, the droplets experienced repulsive forces which in turn caused droplet divergence. Since the TE sols were more conductive than the TP sols, it can be suggested that a charge of larger magnitude was induced on the droplets obtained from the TE sol in comparison with TP sols. Therefore, the TE yielded a larger electrospray diameter as a result of higher repulsive forces.

Film deposition from the droplet relics occurred according to the following mechanism; the droplets leaving the cone tip contained TiO_2-complex particles. These were directed towards the grounded substrate due to their surface charge and the electric field. Upon striking the substrate, the droplets lost their charge and also started to spread at a rate determined by the surface tension and the sol viscosity. The film material was deposited on the substrate surface as the droplets spread. Full film coverage was obtained via the coalescence of adjacent spreading droplets. The film formation process was accompanied by solvent evaporation. However, the solvent loss at the surface was higher than the solvent loss through the film depth by diffusion which induced tensile stresses within the films accompanied by differential shrinkage.

For both solvent types, a short deposition time led to the arrival of a small number of droplets onto the substrate surface which were unable to coalesce with each other before complete solvent evaporation, resulting in inhomogeneous films. On increasing the spray duration the incoming drops were able to occupy the voids created due to insufficient spreading of the initially deposited film materials which improved the film homogeneity. The difference in film morphology due to solvent type was attributed to the difference in volatility. For the less volatile prOH solvent, the droplets arriving at the substrate underwent a lower rate of evaporation as they spread on the substrate hence they were able to spread over larger distances prior to complete evaporation resulting in full droplet coalescence and hence, dense films. In the case of the more volatile etOH solvent, the droplets arriving at the substrate underwent rapid solvent evaporation during spreading which reduced the spreading ability of the droplets. Therefore, full droplet coalescence did not occur resulting in the rougher film morphology observed.

On the other hand, it is also well known that the surface tension of a metal surface is much greater than that of an oxide layer (Nguyen and Djurado, 2001 and Ghimbeau *et al*, 2007). Initially, the arriving droplets struck the metal substrate and readily wet the

surface due to the high surface tension, resulting in a dense film layer. At a longer spray time, the charged droplets were no longer spreading on the metallic substrate but instead spread on the oxide layer. This resulted in a reduction in wettability and subsequently, the deposition of discrete particles. Equally, it is also well known that the strong electrostatic field produced during electrospraying also induces surface charges on the ground electrode with a sign opposite to that of the droplets and needle (Hwang *et al*, 2007). However, the surface charge varies along the surface owing to the local curvature and is more concentrated in regions with higher surface curvature, resulting in a stronger electric field strength within this region. Thus charged droplets are attracted towards the more curved regions (preferential landing).

Based on this phenomenon, it can also be suggested that the TP films had a higher surface tension than the TE films. Thus droplets spread more readily on the TP2 surface whereas the presence of the protusions formed on the TE2 films due to insufficient droplet spreading acted as preferential landing sites. Solvent evaporation during film deposition resulted in film shrinkage due to the departure of the solvent at the film surface. However, there also existed a gradient in cohesion within the film layer owing to a difference in wettability due to the metal substrate and the deposited oxide layers. This also caused differential shrinkage through the film depth which in turn generated residual tensile stresses within the film. For the TP2 films, longer deposition time led to an accumulation of the solvent at the substrate. Solvent evaporation and higher film thickness induced intense tensile stress within the film which caused crack propagation as residual stress has a positive correlation to film thickness. These findings were similar to literature reports by Nguyen and Djurado (2001) and Neagu *et al* (2006). On the other hand, longer spray times led to the growth of the protusions for the TE2 films.

An increase in sol flow rate increased the primary droplet diameter as indicated by equation 2.9. At a lower sol flow rate, the velocity of the sol arriving at the needle exit was reduced which affected the cone and jet formation. A smaller jet diameter was formed at the cone apex. Therefore, smaller droplet diameter was obtained as demonstrated by Tang and Gomez (1996) and Balachandran *et al* (2001), since there reportedly exists a ratio of 1.89 between the jet diameter and the primary droplet diameter. At the lower flow rates, the droplets arriving at the substrate were relatively “dry” due to excessive evaporation during droplet transport which affected droplet spreading and coalescence. An increase in flow rate caused a corresponding increase in droplet diameter both in terms of solvent and TiO_2 particle content. The droplets

arriving at the substrate were considerably “wet” due to a reduced rate of evaporation during droplet transport. Thicker films were also deposited as a result.

For the TP films, incoming droplets were able to spread easily and could also penetrate into any cracks formed due to solvent evaporation at intermediate flow rates (5-10 μl/min). However higher flow rates resulted in severe volume shrinkage due to evaporation of a large quantity of solvent from the thicker deposited layers. For the TE2 films, an increase in the flow rate improved droplet spreading due to a larger proportion of liquid phase. Also, the larger droplets were not significantly deflected by the electric field. Thus preferential landing was reduced, resulting in the deposition of flatter and more uniform films. For both solvent types, even higher flow rates increased the current through the spray cone which in turn increased the incidence of secondary droplets and satellites in addition to the primary droplets. The presence of the former affected the droplet monodispersity and film homogeneity. At higher flow rates, larger spray angles (α) were attained which in turn increased the droplet divergence and spray area.

The effect of the sol concentration primarily manifested in the jet characteristics. Smith (1986) and Tang and Gomez (1996) reported that an increase in electrical conductivity caused a reduction in jet diameter, which in turn reduced the primary droplet diameter since the jet diameter is approximately twice that of the primary droplets (Tang and Gomez, 1996). Therefore, the average relic diameter increased with sol concentration. Additionally, the droplets arriving at the substrate surface had a higher TiO_2 content due to an increase in the sol concentration from 2 to 8 wt%. At the same flow rate, a higher sol concentration led to the deposition of a thicker films. Consequently, the TP films displayed severe cracking as a result of solvent evaporation from the thicker films obtained at a higher sol concentration. For the TE sols an increase in sol concentration and hence liquid phase, initially caused the flake-like structures to merge together which enhanced the film homogeneity. However, a further increment in sol concentration resulted in cracking. The presence of particle aggregates at higher sol concentration could be explained by the poor wettability of the film surface since a sol concentration led to higher viscosity which in turn reduced the wetting ability of the incoming droplets at the film surface. Hence, the etOH solvent evaporated before droplet spreading could occur. On the other hand, higher concentration reduced the charge to mass ratio which reduced the droplet divergence and spray diameter.

The needle internal diameter also affected the jet diameter since the jet diameter is typically two orders of a magnitude smaller than the latter. Hence the droplet diameter was marginally increased due to an increase in needle internal diameter. A larger needle internal diameter also reduced the electric field intensity which reduced the charge to mass ratio of the droplets and hence the droplet divergence during transport to the ground substrate. This reduced the spray area. For the same volume flow rate, an increase in needle internal diameter reduced the jet velocity and therefore, the droplet velocity in accordance with the law of conservation of energy. The low velocity conferred upon the droplets resulted in a lower kinetic energy. Thus the droplet energy at the moment of impact with the substrate was reduced and the subsequent droplets were unable to spread sufficiently due to the low surface tension of the oxide layers. The droplets therefore retained their original shape, causing a rougher film morphology for the TP2 films. For the TE2 films, the higher amount of liquid phase enhanced the spreading ability and subsequently improved droplet coalescence in spite of preferential landing. On the other hand, there was no significant difference in the voltage range considered. Hence, there was no significant difference in the droplet relic diameter and as such, film morphology.

The needle to substrate diameter mainly affected solvent evaporation during droplet transport. A larger needle to substrate distance caused severe evaporation of the solvent from the electropsray droplets which reduced the droplet diameter. At shorter needle to substrate distances the droplets striking the substrate contained a large amount of liquid phase which resulted in cracking due to solvent evaporation. Additionally, thicker films were produced due to lower droplet divergence during film deposition. An increase in the needle to substrate distance reduced the droplet spreading ability at the substrate due to insufficient liquid phase, hence discrete particles were observed on the film surface at higher needle to substrate distance. For the same flow rate, the droplet divergence increased with the needle to substrate distance. Hence, the spray area was significantly larger at a longer needle to susbtrate distance whereas the film thickness was lower.

From FTIR investigations, it was evident that the air dried powders were composed of a TiO_2-complex. Consequently, the as-prepared films had a similar composition since film deposition took place under ambient conditions. TiO_2 was obtained according to the equation;

$$2[Ti(OR')_3O] \xrightarrow{\text{air, } >300^\circ C} TiO_2 + 3CO_2 + H_2O \qquad (4.3)$$

$R'=C_2H_4$ or C_3H_7.

The SEM studies revealed that the post deposition heat treatment affected the TiO_2 film morphology, although the morphological evolution was dependent on the solvent type. The increased roughness of the TP film was attributed to thermally induced grain growth which led to agglomeration (Mathews *et al*, 2009). For the TE2 films, grain growth and agglomeration caused the flake-like features to grow towards each other. The coalescence of these features caused the film morphology to become more homogeneous. It is also possible that the thermal treatment caused the occurance of solid state diffusion as reported by Koparde and Cummings (2005). This resulted in the coalescence of the TiO_2 nano particles and could also explain the enhancement in film smoothness observed on the TE2.

4.8.4 Phase composition of electrosprayed films

XRD and Raman spectra indicated that the phase composition and crystallinity of the TiO_2 films were affected by the annealing temperature. Heat treatment facilitated the migration of solute atoms (surface diffusion) in order to form the preferred anatase crystal orientation, similarly to the findings of Verma *et al* (2005) and Qiu and Kalita (2006) for sol-gel TiO_2 films and powders, respectively. The presence of the rutile phase indicated that annealing temperature >500 °C promoted the anatase-rutile transformation in accordance to literature findings since this transformation has been found to occur at temperatures around 600 °C (Chen *et al*, 1999). The slight variation in phase composition due to solvent type was related to the difference in particle size as smaller particles with a larger surface area favour the formation of the rutile phase. Hence, stronger rutile peaks observed for the TE2 films.

4.8.5 Surface properties of electrosprayed films

From the surface roughness measurements of the TP2 films, it can be concluded that roughness parameter (R_a) was positively correlated to the annealing temperature as reported by Verma *et al* (2005) and Prabhan *et al* (2010). This was in agreement with the observations made using SEM and was attributed to grain size growth and particle agglomeration. The particle agglomerates resulted in topographical deviation in the form of hills and valleys on the film surfaces and increased the film roughness. The higher roughness of the TE2 films was a direct consequence of the occasional flattened flake-like structures. Based on these observations, it can be suggested that the topography of the TiO_2 films could be significantly altered by the shape, size and

density of the particle agglomerates which in turn affected the surface roughness. The surface roughness of the electrospray TiO_2 films was comparable to that of micro-arc oxidized films obtained by Zhu *et al* (2001) (~0.98 μm) and Gao *et al* (2013) (~1.26 μm).

The low water contact angles of the TiO_2 films (Θ<70°) were indicative of a high degree of hydrophilicity since hydrophilicity is characterised by a water contact angle less than 70° whereas hydrophobicity is associated with a water contact angle of 70° or above (Adachi *et al*, 1996). The dramatic reduction in the water contact angle measurement due to annealing correlated well with the literature findings of Kanta *et al* (2005), Zhao and Tay (2006) and Prabhan *et al* (2010). However, there was a large discrepancy in the water contact angles reported in the literature and those observed in this research. For example, Zhao and Tay obtained water contact angles of 40-90° whereas Prabhan *et al* (2010) obtained water contact angles in the range 51-87°. This was attributed to the difference in the film properties such as film morphology as dictated by the deposition technique as well as post deposition treatments and storage. The reduction of the water contact angle due to an increase in annealing temperature could be attributed to the removal of surface contamination and surface roughness.

Sol-gel TiO_2 tends to have a high surface energy owing to the presence of the highly reactive OH radicals, which are formed from the reaction between TiO_2 and surface adsorbed water since the Ti-O-Ti bond is highly polar. This can result in surface contamination due to the adsorption of hydrocarbons (Kanta et al, 2005). The surface contamination is mainly a function of factors such as temperature and humidity, recent laboratory activities, and mode of floor and bench cleaning. Hence it can be suggested that hydrocarbon contamination occurred on the surface of the TiO_2 films prior to annealing.

Hydrocarbon contamination affects the wettability of the TiO_2 by masking the hydroxyl groups which enhance wettability by bonding with water molecules via hydrogen bonding and weak Van Der Waal's forces. Consequently, water can easily spread across the TiO_2 film surface. Generally, a higher number surface hydroxyl groups results in enhanced wettability. In studies by, Kanta *et al* (2005) it was reported that the hydrocarbon layer could be pyrolysed by carrying out heat treatment at 300°C, resulting in an enhancement of wettability. Thus it is possible that annealing of the TiO_2 films at 300 °C in this research caused partial pyrolysis of the hydrocarbon layer which exposed the TiO_2 films surface. Increasing the annealing temperature led to further

pyrolysis of the hydrocarbon layer which further lowered the water contact angles and enhanced the film wettability.

The reduction of the water contact angle with annealing temperature was also related to the variation in surface roughness of the TiO_2 films. It has been reported that the surface roughness amplifies the intrinsic contact angle of a given air/solid interface (Wenzel, 1936 and Si *et al*, 2009). Hence, the hydrophilic nature of a material is increased by surface roughness whereas the hydrophobic materials will display increased hydrophobicity due to an increase in surface roughness. The increase of the hydrophilicity on a rough surface is described by Wenzel's law (Wenzel, 1936);

$$\cos \Theta_f = R\cos\Theta_w \qquad (4.4)$$

where Θ_f= water contact angle on a rough surface, Θ_w=water contact angle on a smooth surface and R=ratio of the actual area of the rough surface to the projected area.

For $\Theta_w<90°$ an increase in R results in a smaller contact angle. A rougher surface provides an additional interfacial area for the spreading of liquid and also lowers the surface tension resulting in a higher surface energy. Consequently, greater wetting is observed. In this research, elevation of the annealing temperature increased the surface roughness. This could have also affected the wettability of the films. Moreover, since a change in solvent type caused a slight increment in surface roughness, it is possible that this gave rise to a greater specific area and higher surface energy which in turn lowered the water contact angles.

4.8.6 *In vitro* cellular response

The data from the alamarBlue™ studies showed that cell attachment and growth were generally supported on all the electrospray TiO_2 films. This was possibly due to the existence of a surface charge on the films. All functional groups have isoelectric zero points at pH values much lower than 7. TiO_2 generally has an isoelectric zero point at a pH of approximately 6.5 (Yezek *et al*, 1998). Hence, TiO_2 films were negatively charged on immersion in the cell medium. This facilitated the adsorption of positively charged proteins and served as a substrate for the subsequent adsorption of FN and VN. These proteins reportedly promote adhesion and reorganisation of cellular actin microfilaments by coordinating with on the cell membranes of the negatively charged osteoblast-like cells. The results further showed that cell spreading and proliferation were enhanced by an increase in annealing temperature. This was contrary to the findings reported by Kern *et al*, (2005). These researchers observed that there was no

significant difference in the initial cell attachment of human mesenchymal cells on passivated non-heat treated Ti surfaces and those subjected to heat treatment at 750 °C, after a 3 hour incubation period. They concluded that annealing did not affect the *in vitro* cellular response despite enhancing the TiO_2 crystallinity and hydrophilicity. The discrepancy in research findings was possibly due to the difference in cell type utilised as well as the short incubation period considered in the aforementioned study.

The enhanced cellular response due to the high temperature annealing of theTiO_2 was attributed to an increase in surface roughness similarly to *et al* (1999) and Mustafa *et al* (2001). The former reported that reported that osteoblast attachment and proliferation were higher on a rough Ti surface (R_a=0.94µm) in comparison to a smooth Ti suface (R_a=0.30 µm) over a 24-48 hr incubation period whereas the latter noted that osteoblast-like cells exhibited enhanced attachment on rough grit blasted Ti discs (R_a=1.30µm) in comparison to the smooth machined Ti controls (R_a=0.2 µm) after an incubation period of 3 hours. These researchers further reported that the cells on the rough substrates exhibited a more differentiated phenotype as evidenced by the increased alkaline phosphatise (ALP) activity and osteocalcin secretion. ALP is tetrameric glycoprotein present on the surface of osteoblast and osteoblast-like cells. The secretion of this protein is enhanced during in vitro bone formation whereas osteocalcin is a calcium binding non collagenous ECM protein. Both are considered to be important markers of osteogenic differentiation. More recently, Osathanon *et al* (2011) also showed that MG63 cells attached to rougher Ti surfaces (R_a=0.2435 µm) as opposed to smooth Ti surfaces (R_a=0.0374 µm) over a 24-72 hr incubation period. Moreover, the rougher substrates enhanced cell spreading

The rougher films provided more sites for the anchorage of cellular processes which resulted in an increase in initial cell attachment and proliferation. The rougher surface topography also provided a larger superficial area which resulted films was firstly attributed to an increase in surface roughness. in enhanced adsorption of fibronectin and vitronectin from the cell culture. Additionally, higher surface roughness resulted in higher local charge densities at the film surface on immersion in the cell medium which further enhanced the adsorption of VN and FN.

The enhanced cellular response on the TiO_2 films annealed at higher temperatures was also attributed to the removal of the surface contamination which enhanced protein adsorption due to improved wetting by the water-based cell culture medium. Consequently, a higher number of cells was able to attach to the film surfaces. This mechanism is illustrated in **Figure 4.21**. Furthermore, protein molecules are adsorbed

in a more flexible, geometrical conformation on hydrophilic substrates which mimicks that in the natural ECM and are accessible by the cell adhesion receptor as opposed to hydrophobic surfaces where the adsorbed proteins are rather rigid and denatured (Vandrovcova *et al*, 2012). Furthermore, the higher crystallinity obtained at higher annealing temperatures probably resulted in a more organized cytoskeleton as reported by Ball *et al* (2001) and Eliaz *et al* (2009). This could have enhanced cell spreading. The enhancement in initial cell attachment resulted in higher cell proliferation as observed in this research.

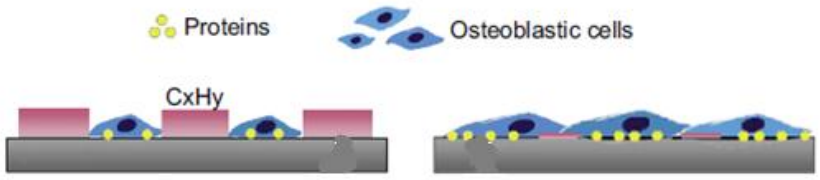

Figure 4.21 Illustration of mechanism of cell attachment due to hydrophilicity

The enhanced cellular response to the TiO_2 films deposited using the etOH solvent carrier was mainly attributed to their increased surface roughness as well as the smaller TiO_2 particle size which acted synergetically with the surface hydrophilicity to improve the conformation of the adsorbed proteins. Furthermore, the smaller particles with increased the molar free energy adsorbed more protein molecules per unit area to reduce the total free energy to become more stable.

4.8.7 Scratch resistance of TiO_2 films

Scratch hardness is considered to be a measure of film cohesion. The results showed that this parameter was affected by annealing temperature. Two major types of film failure were observed namely, cohesive failure of the film and the interfacial failure at the film-substrate interface. The former was accompanied by the presence of transverse cracks within the scratch track as well as some debris along the scratch track and was largely evident in the films annealed at 500-600 °C. The films annealed at 300-400 °C exhibited adhesive failure as evidenced by the film detachment along the scratch track. These phenomena were indirectly confirmed by phase composition analysis of the scratch tracks.

The results further showed that the scratch width was reduced by high temperature annealing which in turn enhanced the scratch hardness. This was in agreement with the findings of Hasan *et al* (2010) who reported that the scratch hardness of magnetron sputtered TiO_2 films was increased from 5.5 to 8.4 GPa by raising the substrate temperature from room temperature to 300 °C. Annealing caused particle to particle bonding as well as particle to substrate bonding. Hence the films annealed at higher temperatures exhibited an increased resistance to penetration. It is also possible that high temperature annealing facilitated the diffusion of TiO_2 solute atoms into the surface undulations which enhanced the film-substrate adhesion. However, the scratch hardness values observed in this research were much lower than those reported in the literature. This could be ascribed to a number of factors such as a difference in applied load and film microstructure.

The results also showed that scratch hardness could be affected by solvent type. The lower scratch width and higher scratch hardness of the TiO_2 films deposited using etOH displayed were related to the more compact nature and lower thickness of these films due to the smaller droplets produced during electrospraying. Lower thickness resulted in lower residual stress. These films also displayed a lower tendency for microcracking due to annealing in comparison to the films deposited using prOH. This can also explain the higher scratch resistance of the TE2 films with respect to the TP2 films. Furthermore, the presence of the higher quantity of the rutile phase in the TE2 films enhanced the mechanical integrity of these films with respect to the latter as the rutile phase superior mechanical properties, such as microhardness compared to the anatase phase. Additionally, the smaller TE2 nano-particles possibly contained a larger number of grain boundaries which acted as impediments to crack propagation.

4.9 Conclusion

The results showed that the sol-gel process and electrospray process were influenced to a great extent by the solvent carrier. Furthermore, the morphology varied from relatively dense to highly porous and reticular by chaning the solvent from prOH to etOH. The film morphology was optimized by varying deposition parameters such as sol flow rate, sol concentration, needle to substrate distance, and spray duration. Uniform and crack-free films were obtained at a concentration of 2 wt% and a 330 µm internal diameter needle at a flow rate of 5 µl/min and a needle-to-substrate distance of 20 mm at a spray time of 180 s. Post deposition annealing at 300-600 °C increased the crystallinity, wettability and surface roughness and also improved the *in vitro* cellular

response and mechanical integrity. An annealing temperature of 600°C gave the highest bioactivity and scratch resistance. However, the TiO_2 films deposited using etOH as a solvent carrier displayed displayed a superior in vitro response and mechanical integrity.

Chapter 5 Electrospray preparation and characterisation of ZrO_2 films

The primary aim of this chapter was to explore the electrospray deposition of bioactive ZrO_2 films. as an alternative to TiO_2 as a bioceramic film on Ti and Ti alloy implant surfaces. Several precursors have been utilized for the sol-gel synthesis of ZrO_2. However, zirconium (IV) propoxide was used as a ZrO_2 precursor owing to its monomeric nature which results in a fast rate of hydrolysis and condensation similarly to titanium isopropoxide. However, this precursor is highly sensitive to moisture at room temperature (Spijksma *et al*, 2009). Zirconium isopropoxide isopropanol complex is a more stable and structurally well-defined precursor (Vaarstra *et al*, 1990). Hence, the influence of precursor type on the sol properties and electrospray process and film properties was investigated. Widionak *et al* (2005) also reported that uniform and monodisperse ZrO_2 particles could be obtained using ethanol as a solvent for a variety of precursor concentrations in comparison with alternative solvents such as 1-propanol and 1-butanol. Furthermore, etOH gives the smallest nano-particles (Jaenicke *et al*, 2008). Thus etOH was utilized as a solvent in the sol-gel synthesis of ZrO_2. Film deposition was carried out using the parameters summarized in **Table 4.1**, and the films were subsequently characterized using the procedures discussed in **Chapters 3** and **4**.

5.1 Sol-gel synthesis of ZrO_2 nanoparticles

A low concentration of 2 wt% was selected for use as higher precursor concentrations typically result in larger particle sizes and sol instability (Zhao *et al*, 2000 and Widionak *et al*, 2005)

The sol-gel reaction between the metal alkoxides and the organic solvent is expressed as (Yoldas, 1982);

$$Zr(OC_3H_7)_4+4C_2H_6O \longrightarrow Zr(OC_2H_6)_4+4C_3H_7O \quad (5.1)$$

$$2Zr(OC_2H_6)_4 \longrightarrow Zr(C_2H_6O)_3\text{-}O\text{-}Zr(C_2H_6O)_3 \quad (5.2)$$

The resultant sols were referred to as ZEP2 and ZE2, respectively as shown in **Table 3.4**. The ZrO_2 sols were both slightly turbid as a result of ZrO_2 particle precipitation.

5.1.1 Phase composition of ZrO_2 sols

Figure 5.1 shows the FTIR spectra of ZrO_2 powders obtained after drying the ZrO_2 sols under ambient conditions. The powders exhibited characteristic peaks owing to the presence of ZrO_2 in the range from 350-900 cm^{-1} as reported in the literature (Duan *et al*, 2008 and Su and Wang, 2011). The ZEP2 and ZE2 powders displayed weak peaks around 613 cm^{-1} and 636 cm^{-1} which were characteristic of the stretching vibrations of the Zr-O bond. The ZE2 powders further exhibited weak peaks around 425 cm^{-1}, 497 cm^{-1} and 735 cm^{-1} which were attributed to the stretching vibrations of the Zr-O-Zr bond. The ZEP2 powder also displayed a weak peak around 813 cm^{-1} which was ascribed to the Zr-O-Zr bond.

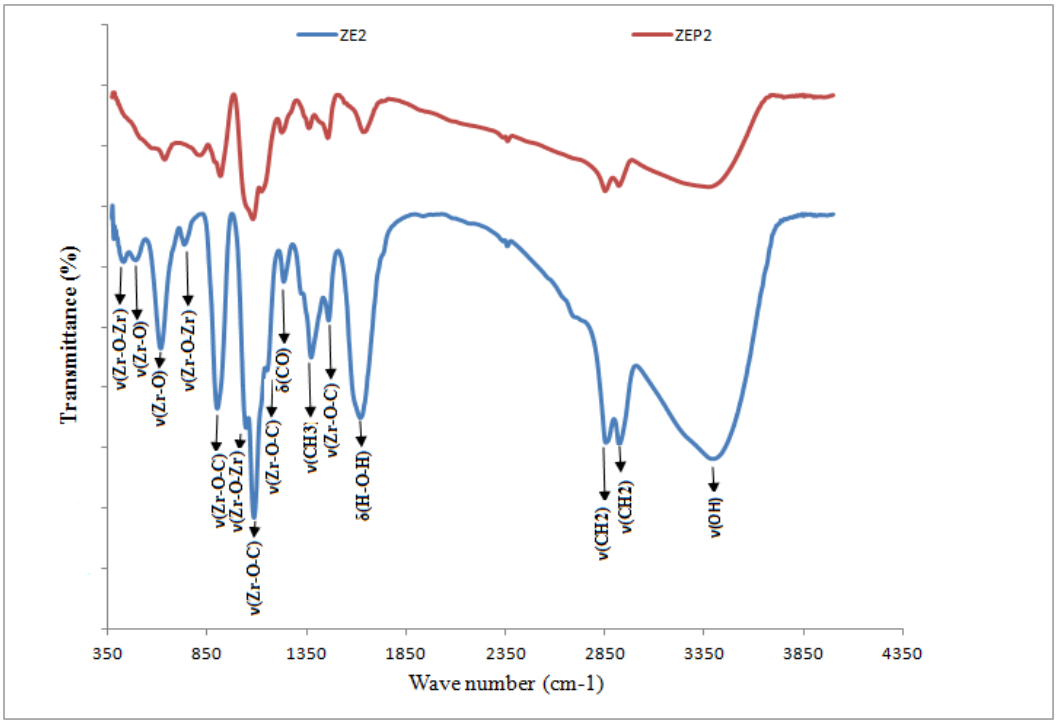

Figure 5.1 FTIR spectra of ZrO_2 powders prepared using the sol-gel method. The powders were air dried under ambient conditions for 24 hrs.

The powders also displayed weak peaks in the range 900-1160 cm^{-1} and around 1400-1570 cm^{-1} due to the stretching vibrations of the Zr-O-C terminal groups. The powders further displayed weak peaks around 1230 cm^{-1}. These were attributed to the deformation vibrations of the CO bond in the isopropoxide structures.. The powders also displayed weak peaks around 1360 cm^{-1} due to the deformation vibrations of the Zr-OH bonds. The presence of OH groups was signified by the peak around 1620 cm^{-1}. Similarly to the TiO_2-complex powders, the ZrO_2-complex powders also displayed additional peaks in the range 2800-2900 cm^{-1} and a broad band at 3200-3400 cm^{-1}

owing to the stretching vibrations of the CH_2 groups and the OH groups, respectively (results not shown here). Therefore, the sol gel powders also contained organic residues in addition to the ZrO_2-complex. Generally, the FTIR spectra of the as-prepared powders obtained from the ZE2 sol was stronger than that of the powders obtained from the ZEP2 sol.

Table 5.1 FTIR spectra of air dried zirconia powders

Wave number (cm^{-1})		Assignment
ZE2	**ZEP2**	
425	-	v(Zr-O-Zr)
497	-	v(Zr-O-Zr)
-	-	v(Zr-O-Zr)
613	636	v(Zr-O-Zr)
735	-	v(Zr-O)
-	-	v(Zr-O-Zr)
898	-	v(Zr-O)
-	921	v(Zr-O-C)
1045	1032	v(Zr-O-C)
1093	1079	v(Zr-O-C))
1121	1130	v(Zr-O-C)
1153	-	v(Zr-O-C)
1235	1225	v(Zr-O-C)
1317	-	δ(CO)
1380	1362	v(Zr-OH)
1459	1458	v(Zr-OH)
1586	-	v(Zr-O-C)
1618	1642	v(Zr-O-C)
3200-3500	3200-3500	v (O-H)

5.2 Liquid physical properties of ZrO_2 sols

The liquid physical properties of the ZrO_2 are summarized in **Table 5.2**. The density of the sols was slightly higher than that of pure etOH. There was no significant difference in the viscosity of the ZEP2 and ZE2 sols. However, the viscosity of the sols was approximately double that of pure etOH. An increase in surface tension was evident for the ZrO_2 sols in comparison to etOH and the surface tension of the ZE2 sol was slightly higher than that of the ZEP2 sol. On the other hand, the electrical conductivity of the ZrO_2 sols was lower than that of pure etOH. The electrical conductivity of the ZEP2 sol was slightly higher than that of the ZE2 sol.

Table 5.2 Liquid physical properties of zirconia sols synthesized using different precursors

Suspension	Density (kgm^{-3})	Viscosity (mPa S)	Surface tension (mN/m)	Electrical conductivity$\times10^{-4}$ (Sm^{-1})
ZEP2	802	3.14	30.9	1.60
ZE2	803	3.33	31.4	1.20
etOH	790	1.30	23.3	3.40

5.3 Electrospraying of ZrO_2 sols.

Stable cone-jet mode maps were obtained by varying the applied voltage and sol flow rate using a needle of internal diameter 300 µm and a needle to substrate distance of 20 mm. Similarly, to the TiO_2 sols, the ZrO_2 sols the stable cone-jet mode was only obtained for a given range of applied voltage and flow rate as shown in **Figure 5.2.**

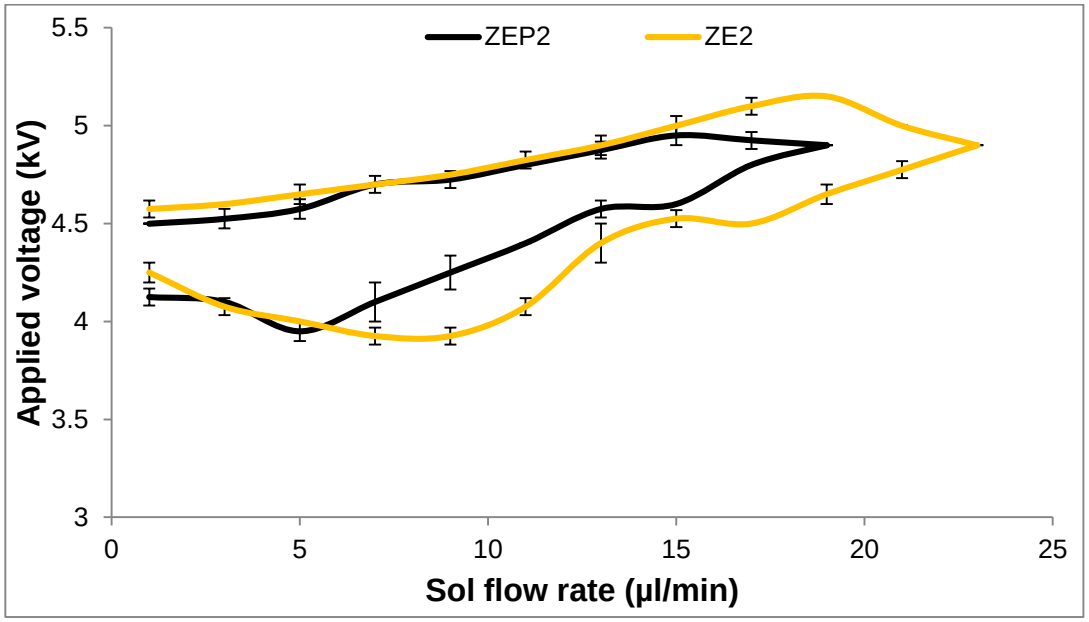

Figure 5.2 Stable cone-jet mode maps of ZrO_2 sols obtained using zirconium(IV) propoxide and zirconium isopropoxide complex. The sols were electrosprayed using a needle of internal diameter of 330 µm set at a distance of 20 mm from the ground substrate.

Table 5.3 summarizes the stable cone-jet mode parameters obtained using the ZrO_2 sols, As shown, the ZE2 sol exhibited a higher maximum sol flow rate in comparison to the ZEP2 sol. The ZE2 sol also exhibited the maximum operating voltage range at a

higher flow rate than the ZEP2 sol. There was no significant difference in the overall operating voltage range of the ZrO_2 sols. Hence, the ZrO_2 sol type as predetermined by initial precursor affected the electrospray process by influencing the flow rate regime.

Table 5.3 Comparison of electrospray characteristics of different zirconia sols obtained using the ZIP and ZIPC precursors. The sols were electrosprayed using a needle of internal diameter of 330 μm set at a distance of 20 mm from the ground substrate

Sol	F_{max} (μl/min)	Min V (kV)	Max V (kV)	Δv_{max} (kV)	$F_{\Delta vmax}$ (μl/min)
ZE2	23	4.0	5.2	3.9-4.7	9
ZEP2	19	3.9	4.9	4.1-4.7	7

5.4 Optimisation of ZrO_2 films

In order to obtain uniform substrate coverage and crack-free film morphology, the influence of three major electrospray parameters namely, spray time, needle to substrate distance and flow rate were investigated.

5.4.1 Influence of spray time

Prior to film deposition, droplet relics were collected as previously described and the results are compared in **Table 5.4**. There was no significant difference in the mean diameter of the droplet relics produced by the different ZrO_2 sols.

Table 5.4 Comparison of average droplet relic diameters obtained using different zirconia sols. The sols were electrosprayed using a needle of internal diameter of 330 μm set at a distance of 20 mm from the ground substrate

Sol	Average relic diameter (μm)
ZEP2	0.9±0.1
ZE2	1.0±0.1

Figure 5.3 shows the morphology of the ZrO_2 films deposited at 30-300s. For the ZEP2 sol and a spray duration of 30s, the films produced consisted a uniform sub-layer with occasional flake-like sturcture. The films also appeared to mimic the surface orientation of the underlying substrate. On increasing the spray time to 60s, the films produced displayed a similar morphology to those deposited at 30 s. However, the dense sub-

layer appeared to be more continuous. There was no significant variation in the film morphology obtained at a spray duration of 180-300 s.

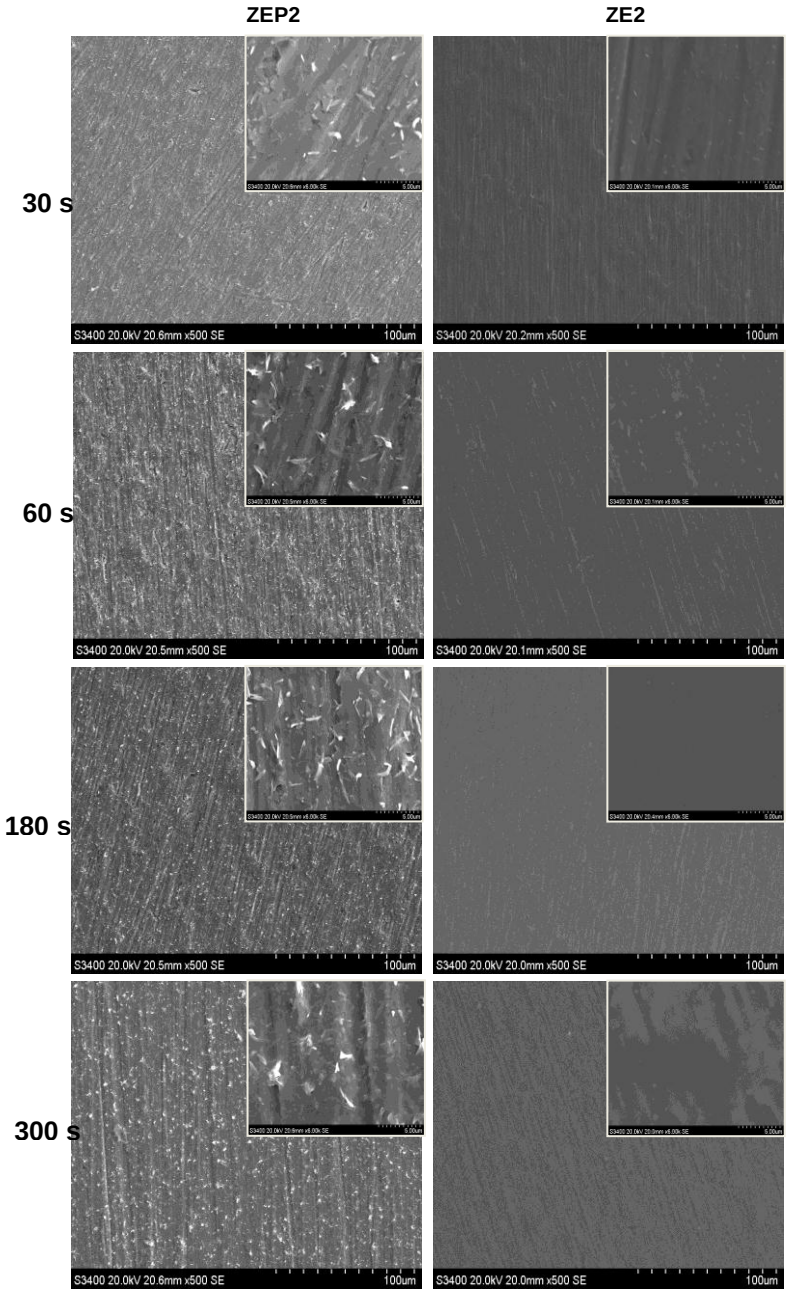

Figure 5.3 Effect of deposition time on the morphology of ZrO_2 films. The sols were electrosprayed at a flow rate of 5 μl/min using a needle of internal diameter of 330 μm set at a distance of 20 mm from the ground substrate.

For the ZE2 sol, a spray duration of 30 s resulted in a dense and featurelesss film with occasional spherical particle aglomerates. There was no significant difference in the film morphology as a result of increasing the deposition time to 300 s. The ZEP2 sol gave films with a Type 2 morphology whereas the ZE2 sol gave films with a Type 1

morphology. Thus the films produced using the ZEP2 sol appeared to be rougher than those produced using the ZE2 sol. A spray duration >60 s was considered to be adequate to produce ZrO_2 films with a uniform and crack-free morphology. However, a spray time of 180 s was selected for further investigations for comparison purposes with the TE2 films.

5.4.2 Influence of needle to substrate distance

The effect of needle to substrate distance on the ZrO_2 film morphology is shown in **Figure 5.4**. For the ZEP2 sol the films deposited at a needle to substrate distance of 10 mm were dense and continuous (Type 1 morphology) with occasional cracking. For a needle to substrate distance of 20 mm, the films produced were rough and comprised of a dense and continuous sub-layer with a top layer of a mixture elongated and flake-like agglomerates (Type 3 morphology).

An increase in the needle to substrate distance to 30 mm resulted in the deposition of smoother and more uniform films. The films produced also exhibited a Type 3 morphology and consisted of a continuous sub-layer with occasional elongated particle agglomerates. At a needle to substrate distance of 40-50 mm, the deposited films were continuous and relatively featureless (Type 1 morphology).

For the ZE2 sol, a needle to substrate distance of 10 mm gave continuous and featureless films for the ZE2 sol (Type 1 morphology). Increasing the needle to substrate distance of 20 mm also caused the deposition of uniform and continuous films. However a small number of spherical particle agglomerates was evident on the film surface resulting in a relatively rough film surface (Type 2 morphology). A further increase in the needle to substrate distance from 20 to 50 mm caused the film morphology to gradually change from Type 2 to Type 1. Therefore, the films produced at larger needle to substrate distances were relatively smooth and featureless with minimal agglomeration.

These results showed that the ZrO_2 film morphology became more homogeneous due to an increase in needle to substrate distance irrespective of the sol utilized. A needle to substrate distance of in the range 30-40 mm was adequate for the deposition of uniform and relatively smooth films. However, a needle to substrate distance of 20 mm was considered to be more desirable for the deposition of rough films for biomedical applications.

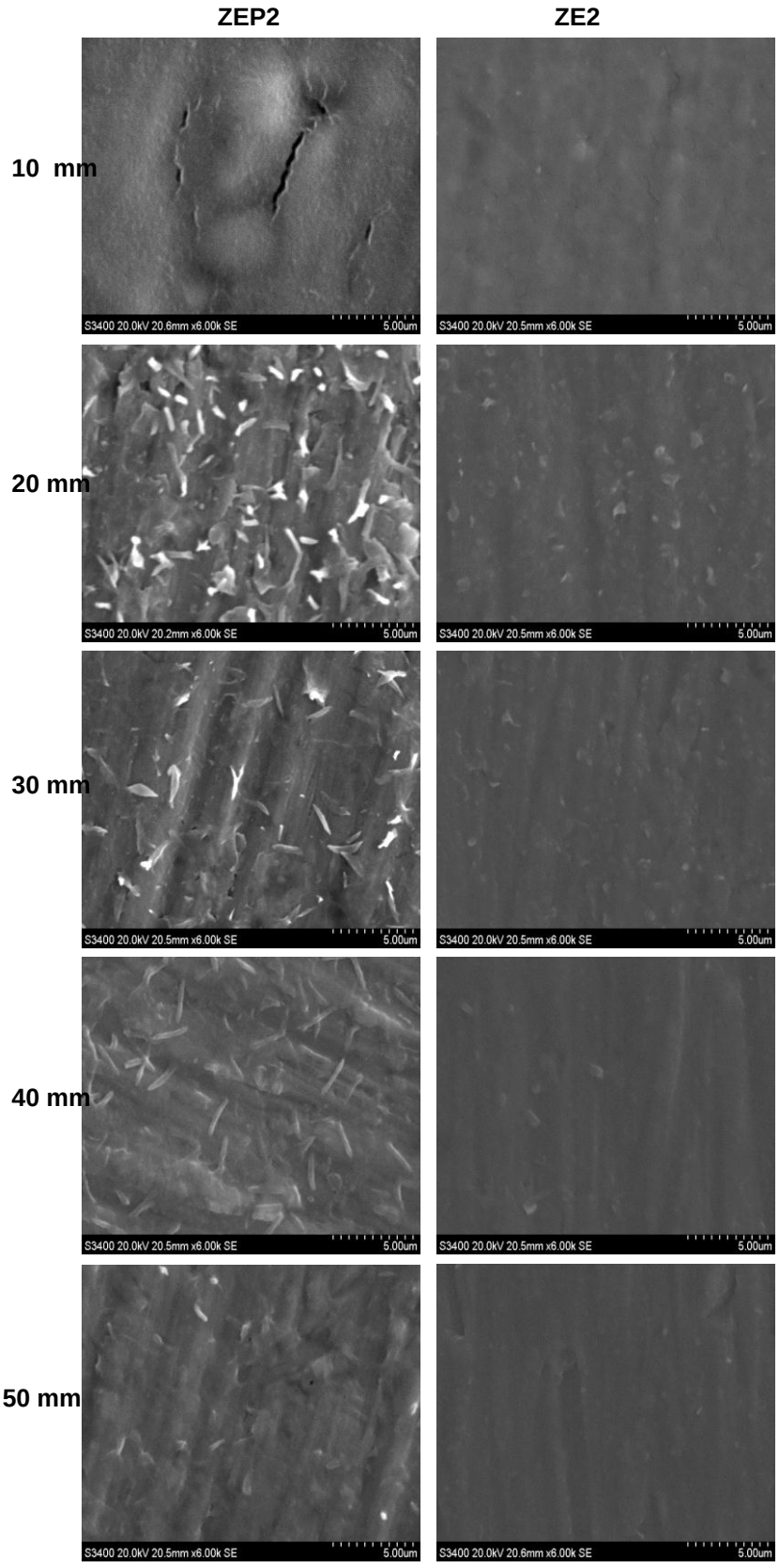

Figure 5.4 Effect of needle to substrate distance on the morphology of ZrO_2 films. The sols were electrosprayed at a flow rate of 5 μl/min using a needle of internal diameter of 330 μm

5.4.3 Influence of sol flow rate

The influence of sol flow rate on the morphology of ZrO_2 films is shown in **Figure 5.5.** For the ZEP2 sol, a flow rate of 2 µl/min yielded rough films with a dense, continuous sub-layer and a network of elongated structures (Type 3 morphology). On increasing the flow rate to 5 µl/min, the deposited films were more dense and homogeneous. The films consisted of a uniform sub-layer with occasional elongated agglomerations and flake-like structures (Type 2 morphology).

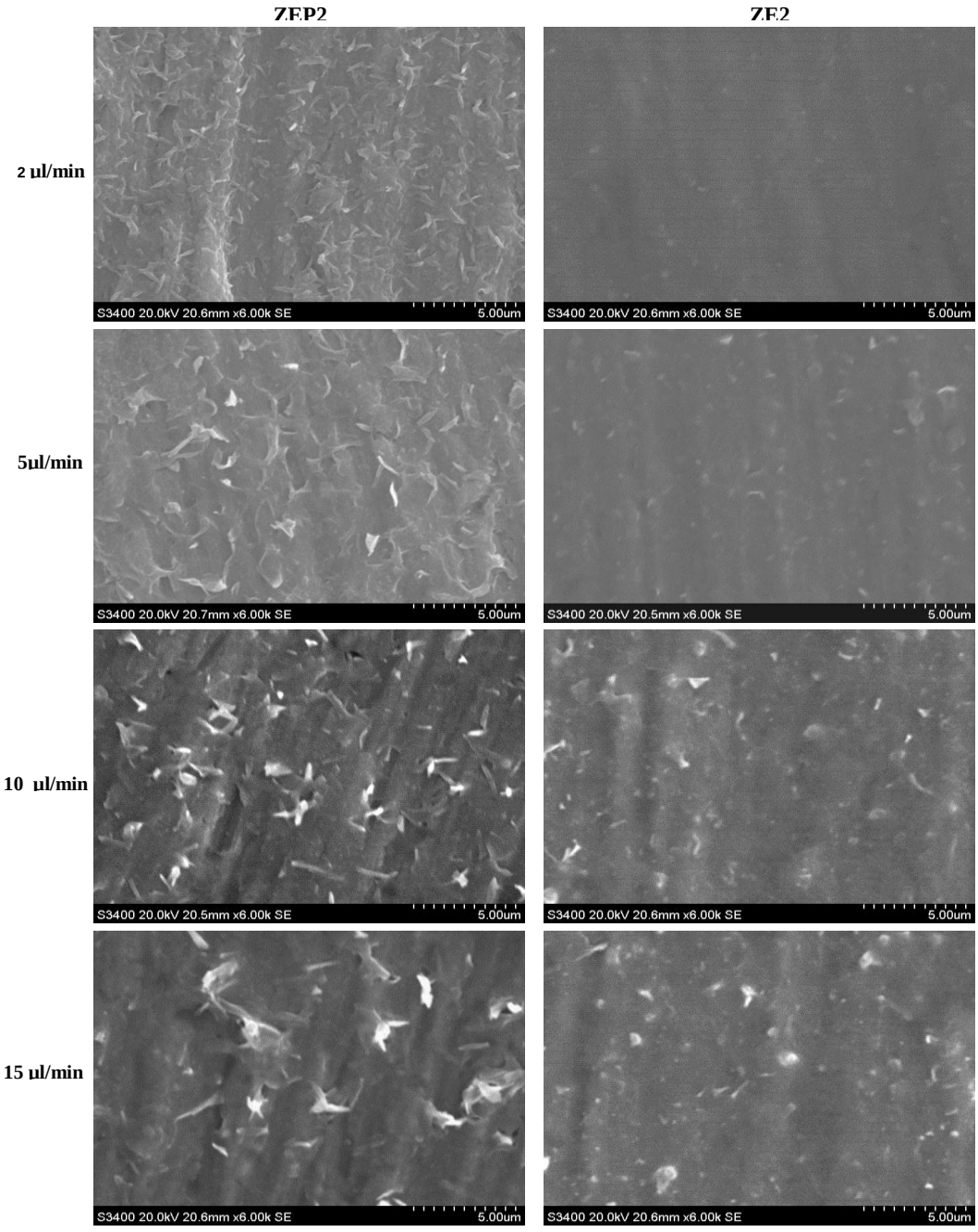

Figure 5.5 Effect of sol flow rate on the morphology of ZrO_2 films. The sols were electrosprayed using a needle of internal diameter of 330 µm. The needle to substrate distance was set at 20 mm

The films appeared to be smoother than those deposited at a lower flow rate. A further increase in the sol flow rate to 15µl/min caused the deposition of smoother and more homogeneous films with a small number of flake-like agglomerations (Type 2 morphology).

For the ZE2 sols, a flow rate of 2 µl/min resulted in the deposition of dense and continuous films (Type 1 morphology). On increasing the sol flow rate to 15µl/min, the films displayed a rougher morphology and consisted of a dense and uniform layer with incorporated particle agglomerates (Type 2 morphology). Thus for the ZEP2 sol, an increase in the flow rate changed the film morphology from Type 3 to Type 2, resulting in smoother and more homogeneous films. For the ZE2 films, an increase in flow rate changed the film morphology from Type 1 to Type 2 which reduced the film homogeneity and increased the roughness. Thus more dense and crack-free films were obtained at a flow rate of 15 µl/min for the ZEP2 whereas the ZE2 films exhibited a dense and crack-free morphology on being deposited at a flow rate of 2 µl/min.

In summary, the ZEP2 sol gave uniform and crack-free coverage at a needle to substrate distance of 20 mm, a spray time of 180 s and a flow rate of 15 µl/min whereas uniform and crack-free films were achieved at a needle to substrate distance of 20 mm, a spray duration of 180 s and a flow rate of 2 µl/min. However, in order to deposit rough films for biomedical applications, the flow rate was fixed at 5 µl/min and the spray time and needle to substrate distance were set at 180 s and 20 mm, respectively, similarly to the TiO_2 system. The spray diameter and estimated thickness of the ZrO_2 systems are shown in **Table 5.5**.

Table 5.5 Comparison of spray diameter and estimated thickness of ZrO_2 and TiO_2 systems (n=6). The sols were electrosprayed at a flow rate of 5 µl/min using a needle of internal diameter of 510 µm and a needle to substrate distance of 20 mm.

Sol	Spray diameter (µm)	Estimated thickness (nm)
ZEP2	37.07±0.69	199.58±4.91
ZE2	35.85±0.67	217.11.±6.92

The ZEP2 sol gave a larger spray diameter than the ZE2 sol. Furthermore, the ZEP2 films were estimated to be statistically thinner than the ZE2 films as summarized in **Table 5.5** ($p<0.05$).

5.4.4 Influence of annealing

The morphology of ZrO_2 films was deposited using the optimized deposition parameters is shown in **Figure 5.6**. As reported in the preceding sections, the as-deposited films obtained using the ZEP2 sol were fairly continuous with some regions of flake-like features. The films obtained using the ZE2 sol consisted of a dense and continuous sub-layer with occasional spherical particle agglomerates. On annealing the films at 600 ºC, the ZrO_2 films became more homogeneous. In particular, the films deposited using the ZEP2 sol led to the displayed a smaller number of flake-like structures. Therefore, the film homogeneity could be enhanced by high temperature annealing, as was observed in the case of the TiO_2 films deposited using the TE2 sol.

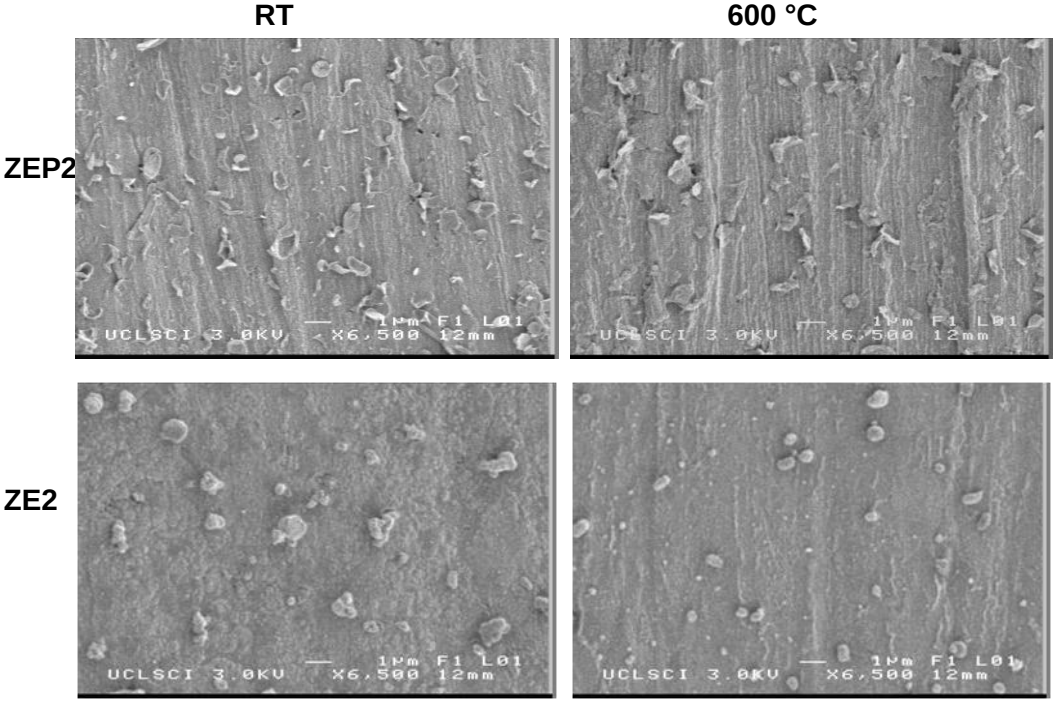

Figure 5.6 Effect of annealing on ZrO_2 film morphology. The films were deposited using a flow rate of 5µl/min and needle of internal diameter 300 µm set at a needle to substrate distance of 20mm. The films were subjected to heat treatment at 600°C

5.5 Phase composition of ZrO_2 films

The phase composition of the annealed ZrO_2 films obtained using the ZEP2 and ZE2 sol was analyzed by Raman spectroscopy as shown in **Figure 5.7**. The films were composed of a mixture of monoclinic and tetragonal phase. The sharp peaks at 189 cm-1 and 615 cm^{-1} were attributed to the tetragonal phase. The weak peaks around 148 cm^{-1}, 263 cm^{-1} and 332 cm^{-1} were also due to the presence of the tetragonal phase, whereas the peaks at 104 cm^{-1} and 476 cm^{-1} were ascribed to the tetragonal phase. However, the ZEP2 films had a higher tetragonal:monoclinic (T/M) ratio in comparison to the ZE2 film as summarized in **Table 5.6.** Thus the former contained a

higher proportion of monoclinic phase in comparison with the latter. This suggested that the ZEP2 films could be more beneficial in terms of mechanical properties since the tetragonal phase transforms in to the more stable monoclinic phase on the application of stress or a reduction in temperature.

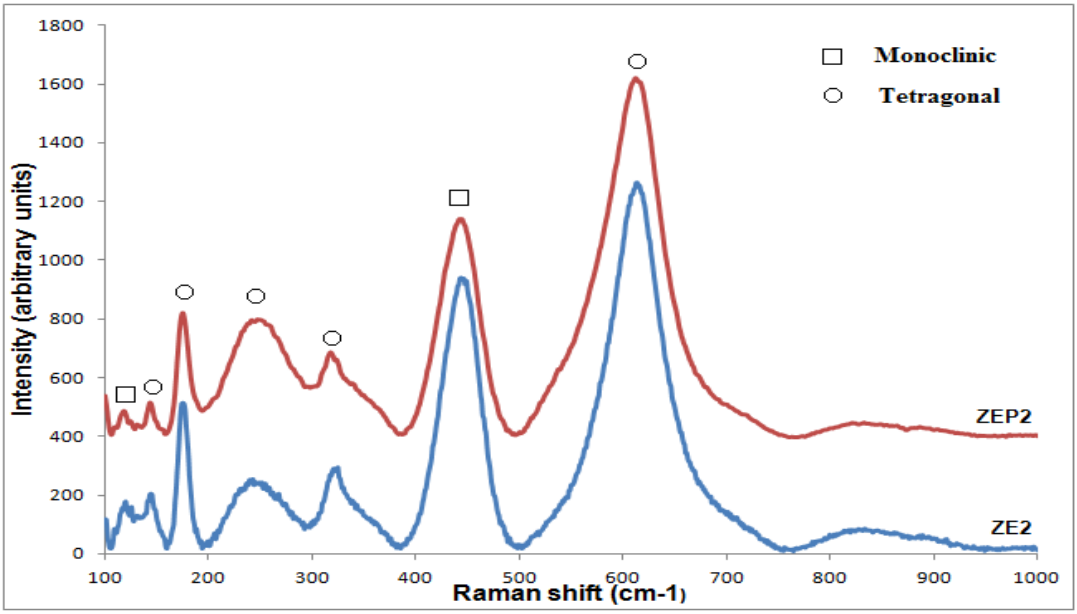

Figure 5.7 Raman spectra of annealed ZrO_2 films obtained using different precursors. The films were deposited using at a flow rate of 5µl/min and needle of internal diameter 300 µm set at a needle to substrate distance of 20mm. The films were subjected to heat treatment at 600°C

Table 5.6 Phase composition of ZrO_2 films deposited using at a flow rate of 5µl/min and needle of internal diameter 300 µm set at a needle to substrate distance of 20mm. The films were subjected to heat treatment at 600°C

Film	T/M ratio (Major)	T/M (Minor)
ZEP2	1.35	3.10
ZE2	1.66	1.69

5.6 Surface roughness of ZrO_2 films

The average surface roughness of the ZrO_2 films has been presented in **Table 5.7**. The surface roughness of the films was similar (~1µm). However, the surface roughness of the film deposited using the ZEP2 sol was slightly higher than that of the film deposited using the ZE2 film ($P<0.05$). This was an indication that the precursor type affected the surface roughness of the ZrO_2 film roughness which was in agreement with the SEM

observations. However, the uncoated Ti alloy surface was rougher than the ZrO_2 films, similarly to the observations made from the TiO_2 films.

Table 5.7 Surface properties of ZrO_2 films deposited using different precursors. films deposited using at a flow rate of 5µl/min and needle of internal diameter 300 µm set at a needle to substrate distance of 20mm. The films were subjected to heat treatment at 600°C

Surface	Surface roughness (µm)	Water contact angle °
ZEP2	0.94±0.02	15.83±0.25
ZE2	0.84±0.03	16.79±0.28
Ti alloy	1.36±0.80	71.27±0.42

5.7 Wettability of ZrO_2 films

The water contact angles of the films were significantly lower than that of the uncoated substrate (**Table 5.7**). The water contact angles were similar (~16°), which implied that the ZrO_2 film wettability was not highly sensitive to the precursor type.

5.8 *In vitro* cellular response of ZrO_2 films

5.8.1 Cell proliferation

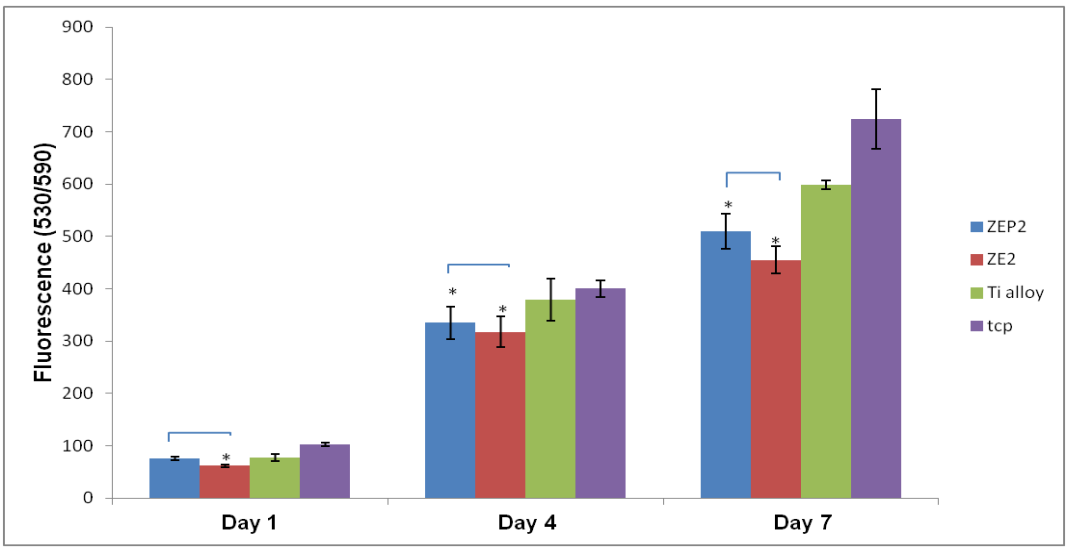

Figure 5.8 Proliferation of MG63 cells on ZrO_2 films using the ZEP2 and ZE2 sols. Results represent mean±s.d of triplicates obtained from 3 different experiments (n=12). Hotizontal brackets indicate a statistical difference between groups ($p<0.05$). Asteriks (*) indicate a statistical difference compared with the uncoated Ti alloy control ($p<0.05$)

The influence of ZrO_2 film morphology on the proliferation of MG63 cells is shown in **Figure 5.8**. On day 1, the cell proliferation on the ZEP2 film was statistically higher than on the ZE2 film ($p<0.05$). Also, the ZrO_2 films displayed lower cell proliferation compared to the uncoated Ti alloy at this time point. On day 4, MG63 cell proliferation on the ZE2 films was significantly lower than on the other test surfaces ($p<0.05$). A similar trend was evident after 7 days of cell culture. From these findings it was evident that the ZrO_2 films were non-cytotoxic inasmuch as they promoted cell attachment and proliferation. However, the ZEP2 films had a greater stimulatory effect on the osteoblast-like cells in comparison with the ZE2 films. Hence, the *in vitro* cellular response to the ZrO_2 films was indirectly affected by precursor type.

5.8.2 Cell morphology

Figure 5.9 shows the morphology of MG63 cells cultured on ZrO_2 films over a 7 day incubation period. The MG63 cells attached to the ZEP2 films bore a flattened and more spread out morphology with lamellopodia. The cells were also connected to each other forming a discontinuous layer on the film surface

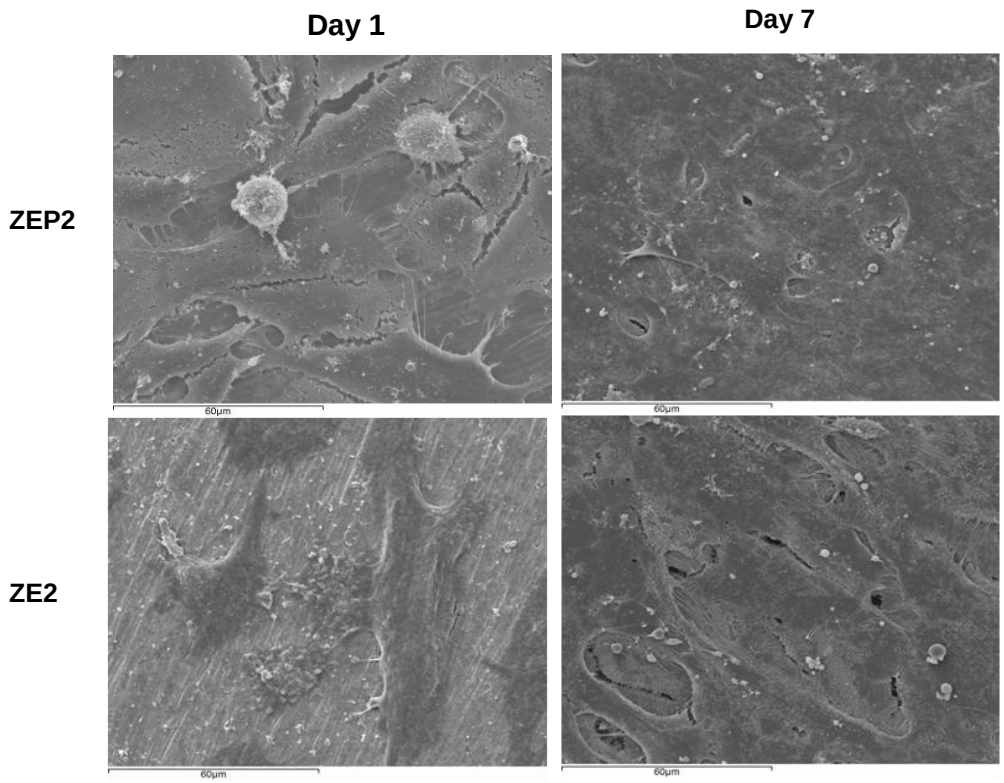

Figure 5.9 Morphology of MG63 cells cultured on ZrO_2 films after incubation for 1 and 7 days. The films were deposited using a flow rate of 5µl/min and needle of internal diameter 300 µm set at a needle to substrate distance of 20mm. The films were subjected to heat treatment at 600°C

In contrast, the cells on the ZE2 films displayed an extended polygonal morphology. This correlated well with the findings from the alamarBlue™ studies and indicated that the ZrO_2 films promoted cell attachment similarly to the TiO_2 films. However, the "rough" ZrO_2 surface promoted better cell attachment and spreading.

After an incubation period of 7 days, there was no significant difference in the cell morphology on all the film surfaces. All the surfaces were fully covered by thick cell multilayers and the individual cellular morphology was no longer distinguishable. This was a positive indication that cell proliferation had occurred on the ZrO_2 films as shown by the alamarBlue™ studies.

5.9 Scratch resistance of ZrO_2 films

5.9.1 Scratch morphology

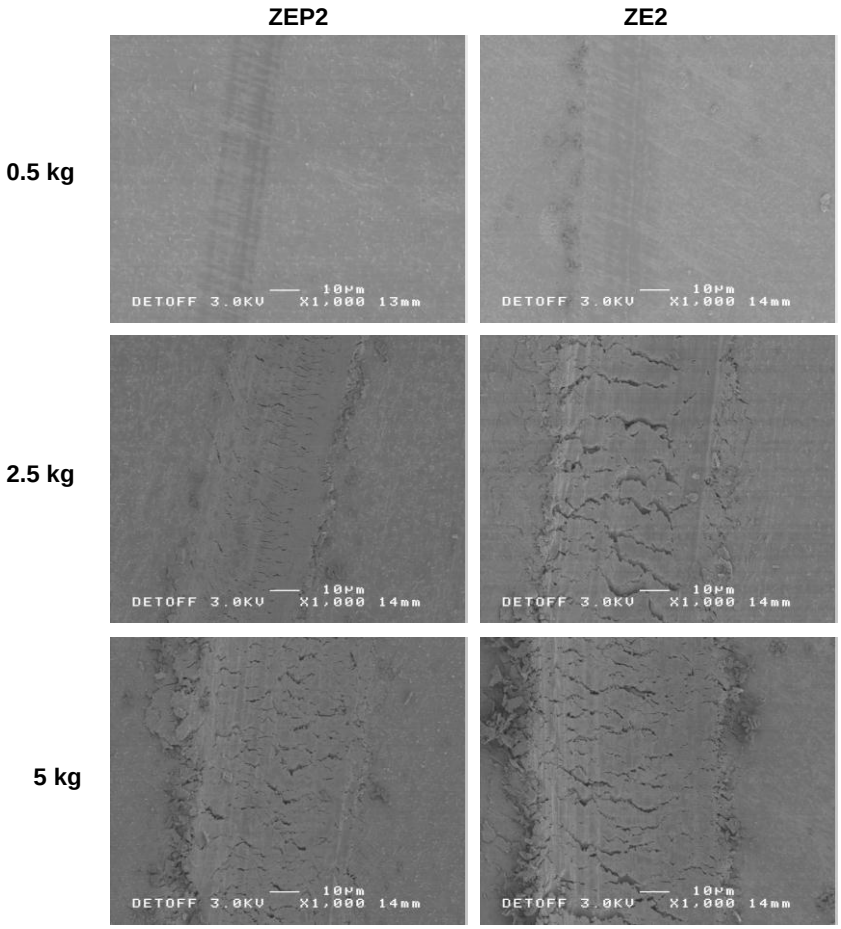

Figure 5.10 Scratch morphology on ZrO_2 films deposited using ZEP2 and ZE2 sols. The films were deposited using a flow rate of 5µl/min and needle of internal diameter 300 µm set at a needle to substrate distance of 20mm. The films were subjected to heat treatment at 600°C

The morphology of the scratches on the ZrO_2 films is shown in **Figure 5.10**. For a scratch load of 0.5 Kg, the scratch tracks on all the ZrO_2 films were poorly defined and displayed little or no damage within and along the scratch tracks. An increase in the scratch load from 0.5 to 5 Kg resulted in well defined cracks with a high number of transverse cracks. Film debris was also evident along the scratch tracks. However, the ZE2 films exhibited more damage compared to the ZEP2 films. Furthermore, the scratch widths on the ZE2 films appeared to be larger than on the ZEP2 films.

5.9.2 Scratch width

The average scratch width on the ZrO_2 films is compared in **Figure 5.11**. The scratch width on the ZEP2 films was generally smaller than that on the ZE2 films all the scratch loads considered ($p<0.05$).

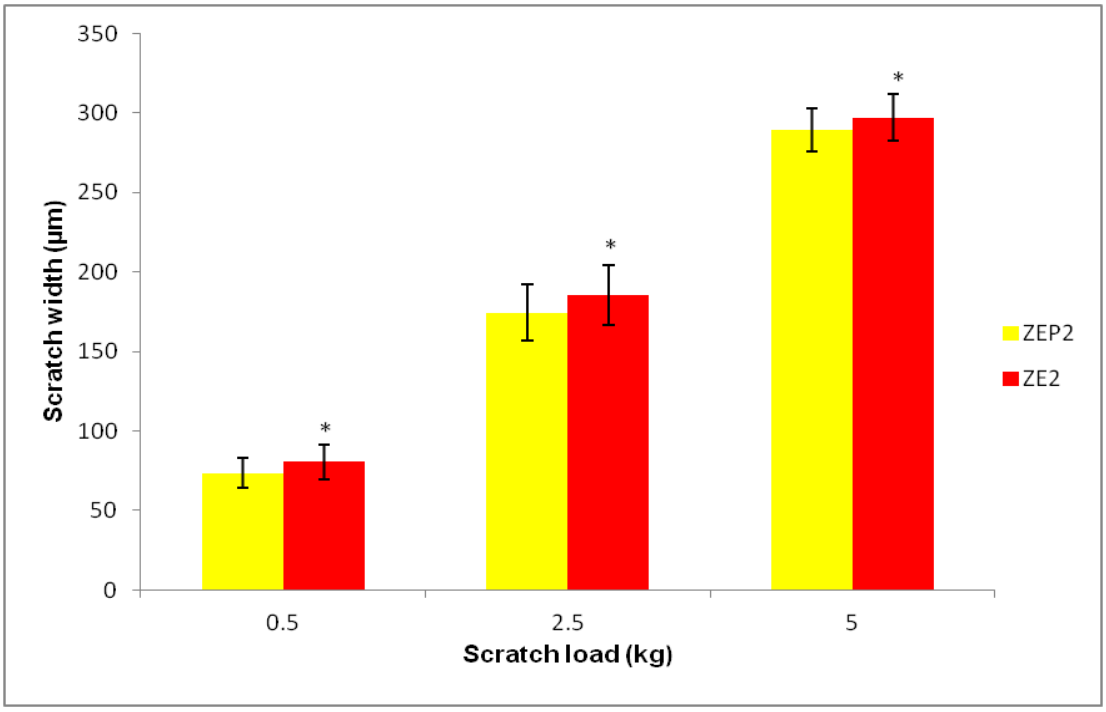

Figure 5.11 Comparison of scratch width on ZrO_2 films produced using different precursors. The films were deposited using a flow rate of 5µl/min and needle of internal diameter 300 µm set at a needle to substrate distance of 20mm. The films were subjected to heat treatment at 600°C. Results represent mean±s.d of triplicates obtained from 3 different experiments.5 measurements were made for each sample (n=15) Asteriks (*) indicate a statistical difference compared with the ZEP2 films ($p<0.05$)

The average scratch width on the ZEP2 films was approximately 74 μm, 170 μm and 290 μm for scratch loads of 0.5 Kg, 2.5 Kg and 5 Kg, respectively, whereas the scratch width on the ZE2 films was approximately 80 μm, 185 μm and 300 μm for scratch loads of 0.5 Kg, 2.5 Kg and 5 Kg, respectively.These findings suggested that the scratch resistance of the electrosprayed ZrO_2 films was indirectly affected by the precursor type

5.9.3 Scratch hardness

The scratch hardness of the ZrO_2 films was calculated for a load of 2.5 kg which caused damage on all the film surfaces. The results are summarized in Table 5.8. There was no significant difference in the scratch hardness of the ZrO_2 films deposited using different precursors ($p>0.05$), although the scratch hardness of the ZEP2 films was slightly higher than that of the ZE2 films. This was in agreement with the data obtained from the scratch width measurements and was a further indication of the effect of the precursor type on the scratch hardness of the electrosprayed ZrO_2 films.

Table 5.8 Comparison of scratch hardness of electrosprayed oxide films subjected to a load of 2.5 kg

Film	Scratch hardness (GPa)
ZEP2	2.10±0.28
ZE2	1.86±0.19

5.9.4 Scratch composition

The phase composition of the scratch tracks was evaluated in terms proportion of Ti detected from the underlying substrate and the results are compared in **Figure 5.12**. There was no significant difference in the amount of Ti detected for the unscratched films and the films subjected to a load of 0.5 kg. However, the relative proportion of Ti detected was increased upon subjected the films to a scratch load of 5 kg which indicated that film penetration had occurred on all the films resulting in the removal of film material. However, the Ti signal observed on the ZEP2 films was slightly lower than that observed on the ZE2 films, which was in agreement with the results obtained in the preceding sections.

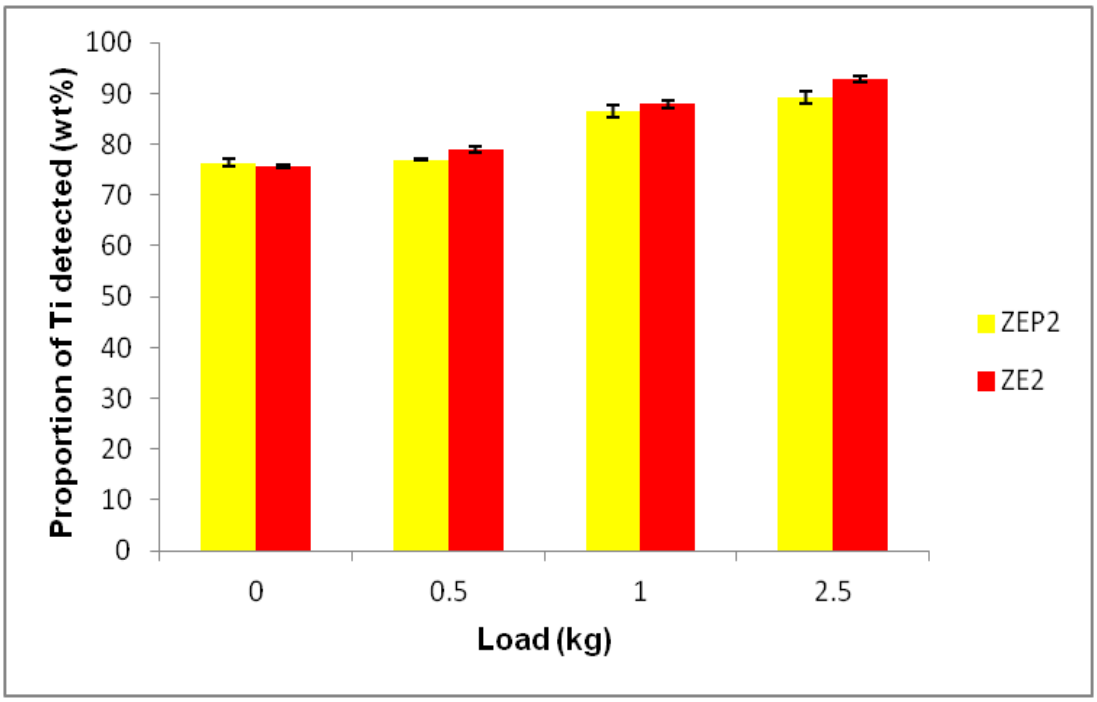

Figure 5.12 Relationship between scratch load and Ti proportion detected within scratch tracs ZrO_2 films produced using different precursors. The films were deposited using a flow rate of 5µl/min and needle of internal diameter 300 µm set at a needle to substrate distance of 20mm. The films were subjected to heat treatment at 600°C. Results represent mean±s.d of triplicates obtained from 3 different experiments (n=3).

5.10 Discussion

The main objective of the current study was to study the influence of precursor type on the deposition and properties of ZrO_2 films deposited by electrospraying different sols. The results showed that the electrospray process was affected by the precursor type. The film morphology and properties also showed a dependence on precursor type.

5.10.1 Chemical and physical properties of ZrO_2 sols

Due to the turbidity of the ZrO_2 sols, it can be concluded that the sol-gel process was not affected by precursor type. The turbidity of the sols was attributed to the high electropositivity of the Zr atom giving it a favourable partial charge for nucleophilic substitution to occur. Therefore, fast alcoholysis occurred resulting in immediate precipitation of nano-particles on the addition of the organic solvent. The formation of the nano-particles was initiated by an alcohol exchange reaction between the precursors and organic solvents which resulted in the formation of a macromolecular oxide network. The rate of alcoholysis was dependent on the molecular structure of the starting precursor. The molecular of the ZEP2 precursor was less complex and bulky than that of the ZE2 precursor which reduced the stearic hindrance and resulted in immediate precipitation ZrO_2 particles. The faster rate of alcoholysis of the ZEP2 sol,

possibly gave smaller ZrO_2 nano-particles since Kumazawa *et al* (1993) reported that a faster reaction resulted in finer nano-particles. Hence the ZEP2 powders displayed a weaker FTIR spectra in comparison with the ZE2 powders.

FTIR studies showed that the non-aqueoues sol-gel reaction resulted in the synthesis of a ZrO_2-complex. The presence of OH groups has also been reported for the aqueous-derived ZrO_2 powders and was attributed to surface adsorption of water molecules from the atmosphere (Bokhimi *et al*, 1998 and Razaei *et al*, 2007). The bending and stretching vibrations of the OH groups were also attributed to the structural water corresponding to the Zr-OH bond (Sarkar*, et al*, 2006). The presence of organic residues was in agreement with the findings of Su and Wang (2011) and Geethalaskmi (2012) and was a direct consequence of the adsorption of etOH onto the particle surfaces as well as the terminal bonds of the Zr-O-Zr structure.

The change in liquid physical properties due to the presence of the insulating nano-particles correlated well with that observed for the TiO_2 sols and in the literature (Jayasinghe and Edirisinghe, 2002 and Li *et al*, 2007). Theoretically, zirconium (IV) propoxide gives finer nano-particles in comparison with zirconium isopropoxide isopropanol complex. Therefore the ZEP2 sol was slightly less dense than the ZE2 sol which in turn resulted in lower viscosity and surface tension of the ZEP2 sol with respect to the ZE2 sol, although the electrical conductivity was higher. Furthermore the theoretical density of ZrO_2 is higher than that of TiO_2. This affected the liquid physical properties.

5.10.2 Electrostatic atomisation of ZrO_2 sols

Similarly to the TiO_2 sols, the ZrO_2 sols underwent electrospraying in the stable cone-jet mode for a given range of applied voltage and fow rate. The higher maximum flow rate regime of the ZE2 sol in comparison with the ZEP2 sol was a direct consequence of the lower electrical conductivity and higher surface tension of the ZE2 sol which increased the maximum sol flow rate in accordance with Equation 4.3. The density of the sols was considered to have a marginal effect on the variation in the flow rate regime since there was no significant difference in the sol densities. A higher surface tension was able to support the weight of the liquid cone at higher flow rates whreas for a lower electrical conductivity the relaxation time was still within acceptable limits as the current through the liquid cone was increased which reduced the relaxation time in comparison with the hydrodynamic time. Hence the maximum sol flow rate of the ZrO_2 sols was higher than that of the TiO_2 sols. The similarity in the applied voltage obtained

for both the ZrO_2 sols was related to the corresponding similarity in the surface tension. However, the lower surface tension of the TE2 sol with respect to the ZrO_2 sols resulted in lower onset and maximal voltages for the former with respect to the latter as the operating voltage scales with the surface tension (Smith, 1986).

The lower electrical conductivity of the ZrO2 sols also increased the jet diameter which in turn increased the primary droplet diameter and relic diameter with respect to the TE2 sols. The viscosity of the ZrO_2 sols was too low to have a significant effect on the average droplet diameter.

5.10.3 ZrO_2 film deposition

Similarly to the TiO_2 films, the ZrO_2 film morphology was affected by the deposition parameters such as deposition time, needle to substrate distance and sol flow rate. The results showed that the film roughness was influenced by deposition time. At shorter deposition times, the droplets arriving at the substrate spread easily on the metal surface which presented a high surface tension and hence, promoted droplet spreading similarly to the findings of Nguyen and Djurado (2001) and Neagu *et al* (2006). At longer deposition times, the droplets arriving at the substrate were unable to spread on the previously deposited oxide layer which resulted in the formation of rough spots. The relatively homogeneous morphology of the ZE2 films with respect to the ZEP2 films suggested that the ZE2 films had a higher surface tension in comparison with films deposited using the ZEP2 sol which promoted droplet spreading. The variation in ZrO_2 morphology was also indirectly related to the effect of droplet size.

The smaller ZEP2 droplets underwent a higher degree of evaporation due to a higher surface area. Thus the droplets arriving at the surface contained a lower amount of liquid phase which reduced the viscosity. There could also be a difference in surface tension of the deposited oxide layers. The results obtained suggest that the films produced using the ZEP2 sol had a higher surface tension in comparison with the films deposited using the ZE2 sol. Therefore, the arriving droplets were unable to spread easily on the film surface and formed rough spots. Subsequent droplets were therefore attracted to the rough spots due to preferential landing, which increased the roughness of the films at higher deposition times as reported by Nguyen and Djurado (2001) and Neagu *et al* (2006).

An increase in flow rate also had opposing effects on the ZrO_2 films deposited from the different sols. For the ZEP2 sol, low to moderate flow rates gave finer droplets which

underwent severe solvent evaporation during transportation to the substrate, thereby increasing the viscosity. This resulted in insufficient droplet spreaing and coalescence, giving rise to rough spots. Thus film growth was strongly driven by preferential landing. At higher flow rates (>10 μl/min) larger droplets were produced. These contained a larger quantity of liquid phase due to reduced solvent evaporation during droplet transport. Thus droplets spread easily despite the low surface energy of the underlyng film. Also, the primary droplets were not affected by preferential landing. On the other hand, an increase in sol flow rate also increased the polydispersivity of the droplets. Therefore, the droplets produced were a mixture of primary droplets and secondary droplets and satellites with a smaller average diameter. These underwent severe solvent evaporation due to their much smaller diameters and were unable to spread easily at the substrate due to their higher viscosity. Thus the films obtained at higher films tended to be relatively smooth with occasional rough spots contrary to literature findings by Neagu *et al* (2006).

For the ZE2 sol, the electrospray droplets were able to spread easily due to the higher surface tension of the underlying films even at low flow rates. Furthermore, the droplets produced contained a larger amount of liquid phase which promoted droplet coalescence. Hence the ZE2 films were generally smooth for low-high flow rates similarly to films obtained by Neagu *et al* (2006). However, the presence of secondary droplets and satellites at even higher flow rates caused a slight increase in surface roughness.

For both sols, the presence of microcracking at a shorter needle to substrate distance was indicative of the arrival of “wet” droplets at the surface. The large quantity of liquid enables droplet spreading to give the dense and continuous morphology. However, solvent evaporation caused volume shrinkage which caused high stresses within the film. Hence microcracking occurred. An increase in needle to substrate distance however, reduced the average primary droplet diameter due to solvent evaporation which in turn reduced the droplet viscosity. Therefore the films deposited at larger needle to substrate distances consisted of a dense and uniform sub-layer with occasional discrete particle agglomerates similarly to literature findings (Neagu *et al,* 2006).

Generally, the results demonstrated that the ZrO_2 film morphology obtained was due to the interplay between the nozzle-substrate distance, sol flow rate, and deposition time. However, the first two of the parameters were directly correlated as they both

influenced the equilibrium between the flux of the incoming liquid phase and the solvent evaporation at the substrate surface.

Annealing at 600°C caused the evolution of the ZrO_2 phase as follows;

$$2[Zr(OR')_3O] \xrightarrow{\text{air, } 600°C} ZrO_2 + 3CO_2 + H_2O \qquad (5.3)$$

The reduction in surface roughness due annealing at 600°C was attributed to solute diffusion.

The morphology of the ZrO_2 films obtained in these studies was significantly different from that reported in the literature. Both Nguyen and Djurado (2001) and Neagu *et al* (2006) reported on dense as well as coral-like morphologies whereas the films in this study were flake-like or dense and featureless. The variation in morphology could be attributed to a number of factors such as a difference in deposition parameters such as time, flow rate and needle to substrate distance. Moreover, these authors reported on the use of heated substrates and yet such substrates affect the monodispersity of the electrosprayed droplets in the vicinity of the substrate. It is also thought that the ZrO_2 nano-particle synthesis method could have affected the film formation mechanism. For example Neagu *et al* (2006) reported on the use of precursor salts during the sol-gel process whereas the organometallic route was used in this research. The higher thickness of the ZrO_2 films with respect to the TiO_2 films was attributed to the higher density of the former which resulted in a higher film growth rate.

5.10.4 ZrO_2 film characterisation

The Raman spectra obtained from the ZE2 and ZEP2 films showed that there was no significant difference in the chemical composition of the films. Both film types were composed of M-ZrO_2 and T-ZrO_2. This was in contrast to the phase diagram of ZrO_2 whereby M-ZrO_2 $\overset{1700^{\circ}C}{\Leftrightarrow}$ T-ZrO_2 $\overset{2300^{\circ}C}{\Leftrightarrow}$ C-ZrO_2. A possible explanation for the presence of T-ZrO_2 after low tempearature annealing is the similarity in the crystallographic structure of the amorphous phase and T-ZrO_2. Certain interatomic distances within amorphous ZrO_2 are similar to those found in T-ZrO_2. Thus the two phases have a similar short range order. The energy barrier between the amorphous phase and T-ZrO_2 is less than that between amorphous phase and M-ZrO_2, causing small crystallites of T-ZrO_2 phase with defectively coordinated O_2 and vacancies to selectively form at low temperatures. The T-ZrO_2 phase was stabilized by a crystallite size effect whereas M-ZrO_2 has a lower bulk free energy. T-ZrO_2 has a lower surface

free energy. For crystallites below a certain critical size, the surface energy term dominates the bulk energy term, stabilizing the T-ZrO_2 phase (Shukla and Seal, 2003). The T-ZrO_2 phase was therefore stabilized by small crystal size as well as the presence of vacancies and OH groups which were formed during the sol-gel reaction (Bokhimi *et al*, 1998 and Razaei *et al*, 2007).

Annealing at 600°C caused the crystallization of the pre-existing T-ZrO_2 and resulted in the removal of the organic contaminants and adsorbed water. The lattice defects created by the evolution of the impurities caused the nucleation of further T-ZrO_2 phase. The removal of the OH groups due to the high temperature annealing however, destabilized the T-ZrO_2 structure and caused the irreversible transformation to M-ZrO_2 phase on cooling (Santos *et al*, 2008). The presence of M-ZrO_2 could also be explained by the presence of heterogeneous nucleation sites or embryos within the structure of the T-ZrO_2 particles which lowered the activation energy for the T-M transformation.

Basically, an embryo is an intermediate structure between the M-ZrO_2 and the T-ZrO_2 phases, and is formed in a stress field in the crystallite. Structural defects such as a dislocation loop create a stress field in the crystal for an embryo to grow or stresses at the crystallite interface create a stress field in the particle for the embryo to grow. The embryo does not have distinct boundaries but consists of a gradual transition from the parent crystal structure to the final martensitic embryo structure. For the embryo to form, the stress field must achieve a certain volume within the crystallite. The probability of achieving this critical volume is proportional to crystallite size. Embryos are formed in a range of embryo sizes. Each embryo has a temperature below which it will convert its parent crystallite from tetragonal to monoclinic phase (Ward and Ko, 1993).

Defects formed during the powder synthesis provided nucleation sites for embryo formation. On heating the films at 600 °C, the embryos grew as their size determined at what temperature the embryo caused its parent crystallite to transform. When the sample temperature fell below this temperature the embryo caused its parent crystallite to transform. The probability of a crystallite containing an embryo at the critical size is directly proportional to the crystallite size. A material with larger crystallites shows more T→M transformation upon cooling. Therefore the ZE2 films contained more M-ZrO_2 on cooling which explains the lower T/M ratio compared with the ZE2P films. The ZE2 powders also had larger particle diameter which further promoted the formation of M-ZrO_2.

The higher surface roughness of the ZEP2 films with respect to the ZE2 films was attributed to the difference in the film formation mechanism which in turn affected the film morphology. The ZE2 sol droplets arriving at the substrate contained a larger quantity of liquid phase which promoted droplet spreading and led to the deposition on of more dense films. In contrast, the ZEP2 sol droplets underwent severe evaporation during flight which resulted in insufficient coalescence of neighbouring droplets. This in turn gave less uniform film morphology. The results also suggested that the ZEP2 films had a higher surface tension than the ZE2 films which further impeded droplet spreading and affected the film morphology.

The water contact angle measurements demonstrated that the ZrO_2 films were highly hydrophilic (Θ<70°). However, the slight variation in average water contact angles of the ZEP2 films in comparison with the ZE2 films was attributed to the larger surface roughness of the ZEP2 films. The surface topography of the ZEP2 films provided a larger interfacial area films for the spreading of liquid. The rougher film topography also lowered the surface tension which increased the surface energy. As a metal oxide, ZrO_2 has a high surface energy due to the formation of highly reactive OH radicals from the reaction between ZrO_2 and the surface adsorbed water. However, it has also been reported that the wettability of ZrO_2 is dependent on the polymorphs present (Bachiller-Baez *et al,* 1998 and Jung and Bell, 2000). M-ZrO_2 has been found to have a higher density of surface OH groups in comparison with T-ZrO_2. Thus the ZE2 films with a lower T/M ratio had a higher surface OH group density in comparison with the ZEP2 films, which resulted in increased hydrocarbon adsorption. Hence the ZE2 films were less hydrophilic than the ZEP2 films.

5.10.5 Biocompatibility of ZrO_2 films

The results showed that the electrosprayed ZrO_2 films promoted the attachment, adhesion and proliferation of osteoblast-like MG63 cells, similarly to ZrO_2 films deposited using alternative methods. Wang *et al* (2010) reported that plasma sprayed M-ZrO_2 supported the continuous proliferation of MG63 cells over an incubation period of 1-48 hrs. In previous studies Liu *et a*l (2006) noted that bone marrow mesenchymal cells proliferated on cathode arc deposited ZrO_2 films over an incubation period of 4 days.

The greater stimulatory effect of the ZEP2 films on the attachment and proliferation of the MG63 cells in comparison with the ZE2 films was firstly attributed to a difference in the surface roughness. The higher surface roughness of the ZEP2 films promoted

protein adsorption and also provided more focal adhesion points for initial cell attachment. This in turn promoted cell growth and proliferation as observed. The cellular response was also affected by the phase composition of the ZrO_2 films which affected the wettability of the films. The lower wettability of the ZE2 films with respect to the ZEP2 films could have resulted in lower protein adsorption. Thus the ZEP2 films were more conducive for the initial attachment of the MG63 cells which in turn enhanced cell proliferation.

The *in vitro* cellular response of the electrosprayed ZrO_2 films was further affected by the crystal size. The FTIR spectra and liquid physical properties indicated a smaller crystallite size for the ZEP2 powders in comparison with the ZE2 powders. ZrO_2 particles are negatively charged in physiological fluids (Liu *et al,* 2006). However, it has been reported that finer nanocrystalline particles have a higher surface charge density than larger ones (Liu *et al,* 2006 and Wang *et al,* 2010). Generally, surface or interfacial tension diminishes with decreasing particle size as a result of the increase in the potential energy of the bulk atoms of the particles. Smaller particles with increased molar free energy adsorb molecules or ions on to their surfaces in order to decrease total free energy and to become more stable. Thus it can be proposed that the ZEP2 particles adsorbed a higher proportion of protein from the cell culture medium in comparison with the ZE2, which enhanced initial cell attachment and subsequent proliferation.

The results obtained from the cell proliferation tests also demonstrated that the ZrO_2 films displayed a poor initial cellular response, in comparison with the Ti alloy control surface despite being more hydrophilic. The low proliferation observed after 1 day of cell culture was indicative of low initial cell attachment. This affected the subsequent proliferation. A possible explanation for this could be the higher surface roughness of the Ti alloy which promoted protein adsorption and also provided more focal for initial cell attachment.

5.10.6 Scratch resistance of ZrO_2 films

The lack of film damage or debris for a load of 0.5 kg was indicative of a high degree of film cohesion and film-substrate adhesion for the electrosprayed ZrO_2 films. However, the lower scratch width and hence higher scratch hardness of the ZEP2 suggested that the ZEP2 films were slightly more resistant to indentation.. The slight difference in mechanical properties of the electrosprayed ZrO_2 could be explained by the difference in phase composition. It is well established that T-ZrO_2 has superior mechanical

properties compared to M-ZrO_2 (Wang *etal*, 2010). Thus the ZEP2 films with a higher T/M ratio exhibited a higher scratch resistance compared to the ZE2 films. It is also possible that the ZEP2 sol gave finer particles which had more grain boundaries and therefore impeded crack propagation, which in turn enhanced the scratch resistance of the ZEP2 films with respect to the ZE2 films.

5.11 Conclusions

The precusor type affected the final product obtained from the sol-gel process. The as-prepared ZEP2 and ZE2 powders were mainly composed of ZrO_2-complex. The ZE2 powders appeared to be more crystalline than the ZEP2 powders which was indicative of a larger crystallite size. The phase composition of the resultant electrosprayed films was also affected by the precursor type. The ZEP2 film had a higher T/M ratio in comparison with the ZE2 films. The precursor type also affected the liquid physical properties of the sols as well as the electrospray process. ZE2 sol synthesized using a Zirconium propoxide isopropanol complex precursor extended the maximum flow rate regime to higher values compared to the ZEP2 sol synthesized using a zirconia (IV) propoxide precursor. The maximum operating voltage range was observed at a flow rate of approximately 7 µl/min for the ZEP2 sol whereas the ZE2 gave a maximum operating volatage range at 11 µlmin. Thus the ZE2 sol was more beneficial from a processing point of view.

The morphology of the electrosprayed ZrO_2 films was affected by the deposition parameters and the variation in film morphology displayed a similar trend to that observed in the case of the TiO_2 films. For both film types, uniform and crack-free films were deposited at a needle to substrate distance of 20 mm and a spray duration of 180 s at a flow rate of 5 µl/min. The needle internal diameter and sol concentration were fixed at 330 µm and 2 wt% respectively. However, the ZEP2 films were rougher than the ZE2 films which enhanced the wettability of these films.

The electrosprayed ZrO_2 films were biocompatible and promoted the initial attachment of MG63 cells and their subsequent proliferation over a 7 day test period. However, the ZEP2 films displayed a better *in vitro* cellular response compared to the ZE2 films.

The electrosprayed ZrO_2 films further displayed superior mechanical integrity in terms of scratch resistance compared to the electrosprayed TiO_2 films. The ZEP2 films exhibited superior resistance than the ZE2 films. Thus the ZEP2 precursor was considered to be more beneficial for the deposition of biocompatible electrosprayed

ZrO_2 films with superior mechanical integrity. However, the poor bioactivity of the ZrO_2 films with respect to the TiO_2 films suggested there was a need to further enhance the biocompatibility of the ZrO_2 films.

Chapter 6 Electrospray preparation and characterisation of electrosprayed bioceramic composite films

HA is well known for its biocompatibility and osteoconductivity, which induce the formation of a strong interface between the implant surface and hard tissues. As a bulk material, however, HA is highly brittle and relatively weak compared to cortical bone as well as metallic implants and alternative ceramics such as TiO_2 and ZrO_2. This limits the use of HA to non-load bearing parts of the skeleton, such as middle ear implants. Consequently, HA is used as a coating on metal implants which combines the superior mechanical properties of the metallic implants with the excellent bioactivity of HA. However, the limitations of HA coated implants are well-documented. Issues such as HA degradation during film deposition and HA delamination *in vivo* and *in vitro* have been reported and are ultimately attributed to the inherent weakness of HA as well as the film properties as determined by plasma spraying which is the most commonly used deposition method.

Two phase TiO_2/HA and ZrO_2/HA films have shown great promise owing to their enhanced biocompatibility, mechanical integrity and film-metal interfacial adhesion. HA and toughening secondary phases such as TiO_2 or ZrO_2 are typically deposited onto the Ti metal substrate as composite or functionally graded films. Toughening secondary phases can also be inserted as a buffer layer between HA and the Ti metal substrate. Two phase TiO_2/HA and ZrO_2/HA films have been deposited using several techniques including thermal spraying, physical vapor deposition methods such as sputtering and wet techniques such as micro-arc deposition. However, these deposition methods are associated with a range of short comings. Thermal spray techniques typically result in thicker films and involve the use of high processing temperatures which are detrimental to the film material and the underlying metal substrate whereas the physical vapour deposition techniques are generally cumbersome with a low deposition rate. The wet methods on the other hand, require precise processing conditions.

This chapter investigates the deposition and comparison of novel electrosprayed two-phase TiO_2/HA and ZrO_2/HA films. Two-phase suspensions were prepared by mixing the toughening phases and HA in the ratios; 75wt%:25wt%, 50wt%:50wt% and 25 wt%:75wt%. The suspensions were then labeled T75H25, T50H50, T25H75, Z75H25,

Z50H50 and Z25H75, respectively. Single phase HA, TiO_2 and ZrO_2 suspensions were used as controls and these were referred to as H100, T100 and Z100 respectively.

The deposition parameters utilised in the electrospray deposition of the HA films are summarised in **Table 6.1.**

Table 6.1 Deposition parameters utilized in the electrospraying of HA suspensions

Study	Fixed parameters	Variable parameters
Mode map selection	D_{needle}=510 µm, d=20mm, sol=HA (0-10 EG) TiO_2/HA, ZrO_2/HA	F=1-60 µl/min and V=3.7-5.0 kV
Deposition time	D_{needle}=510 µm d=20mm sol=HA F=10 µl/min	T=30-600 s
Flow rate	D_{needle}=510 µm, d=20mm, sol=HA, T=60 s	F=5-30 µl/min
Needle to substrate distance	D_{needle}=510 µm, sol=HA, T=60 s, F=10 µl/min	d=10-50mm
Solvent type	D_{needle}=510 µm, T=60 s, F=10 µl/min, d=20 mm	Solvent=etOH, ethylene glycol (EG)

6.1 Synthesis and characterisation of HA powders

HA was synthesized from the reaction between orthophosphoric acid and calcium hydroxide according to equation 6.1 (Saeri *et al,* 2003);

$$10\ Ca(OH)_2 + 6\ H_3PO_4 \longrightarrow Ca_{10}(PO_4)_6(OH)_2 + 18H_2O \qquad (6.1)$$

The HA suspension was air dried in order to determine the phase purity and composition of the resultant powders. The FTIR spectrum of the HA powder is shown in **Figure 6.1**. The phase purity of the HA was demonstrated from the vibration modes of PO_4^{3-} in the apatite structure at 470 cm^{-1} (v_2), 564 cm^{-1} (v_4), 604 cm^{-1} (v_4), 960 cm^{-1} (v_1) and 1037 cm^{-1} (v_3). The powders further exhibited weak peaks around 877 cm^{-1} and 1426 cm^{-1} due to the stretching vibrations of the CO_3^{2-} and NO_3^{2-} ions respectively, and the stretching vibrations of the OH^- groups were signified by the weak

peaks around 1629 cm^{-1}, 2924 cm^{-1} and 3463 cm^{-1}. The wave numbers and their corresponding assignments are summarized in **Table 6.2**.

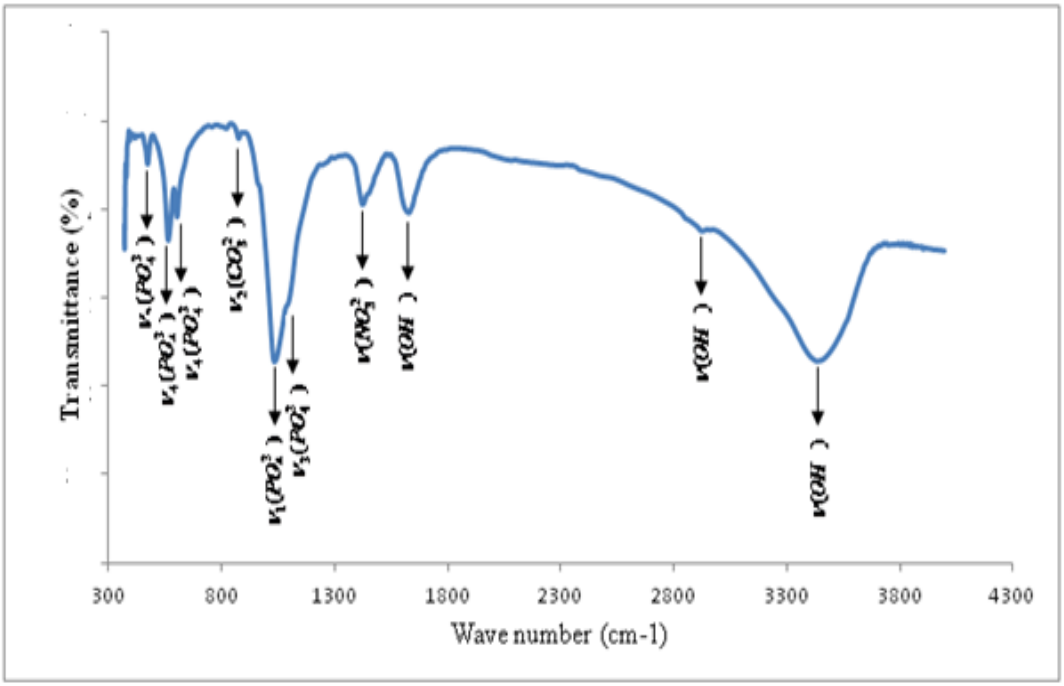

Figure 6.1 FTIR spectrum of air dried HA powders. The powders were dried under ambient conditions for 24 hrs.

Table 6.2 Characteristic wave numbers of HA powders

Wave number (cm^{-1})	Assignment
470	$\nu_2(PO_4^{3-})$
564	$\nu_4(PO_4^{3-})$
604	$\nu_4(PO_4^{3-})$
877	$\nu_2(CO_3^{2-})$
961	$\nu_1(PO_4^{3-})$
1037	$\nu_3(PO_4^{3-})$
1426	$\nu(NO_3^{2-})$
1629	$\nu(OH^-)$ adsorbed water
2924	$\nu(OH^-)$
3463	$\nu(OH^-)$ adsorbed water

6.2 Liquid physical properties of HA suspensions

For comparison with the TiO_2 and ZrO_2 sols, and subsequenty the preparation of the composite suspensions, 2 wt% HA suspension was initially prepared by diluting the original water based 20wt% suspension with etOH. The key liquid physical properties of the HA suspension are summarised in **Table 6.3**. The presence of the HA powders caused a slight increase in the density and also caused a five-fold increase in the viscosity. The surface tension was also increased by approximately 40% whereas the electrical conductivity was dramatically reduced by 75%.

Table 6.3 Liquid physical properties of bioceramic sols/suspensions

Property	HA	etOH
Density (kgm^{-3})	813	790
Surface tension (mNm^{-1})	34.50	23.30
Viscosity (mPaS)	5.57	1.30
Electrical conductivity $x10^{-4}$ (Sm^{-1})	0.80	3.4

6.3 Mode map selection

The ability of the suspension to atomise was assessed by observing the jet formation at the needle exit over a 10 minute period. A stable cone-jet was successfully achieved at flow rates of 1-30 µl/min and a needle to substrate distance of 20 mm. However, needle blockage was found to consistently occur resulting in intermittent dripping at the needle exit. Therefore the needle internal diameter was increased from 300 to 500 µm. Mode map selection was conducted by varying the applied voltage and suspension flow rate. The relationship between these two parameters is shown in **Figure 6.2**. At a low flow rate of 1µl/min, the onset voltage for stable cone jet formation occurred at approximately 4.1 kV. The spray mode abruptly changed to the multijet mode at 4.5 kV. Upon increasing the flow rate regime, the stable cone jet domain remained relatively broad in the applied voltage range of 4.0-4.6 kV. At flow rates >9 µl/min the domain was broader and the stable cone jet was obtained in the applied voltage window of 4.0-4.6 kV. At higher flow rates (> 13 µl/min) the domain became narrow and converged at approximately 39 µl/min. Beyond this flow rate, the jet became unstable and so coatings would not be obtained. A flow rate of 10 µl/min was selected as it gave a wide operating voltage range (4.0-4.6 kV).

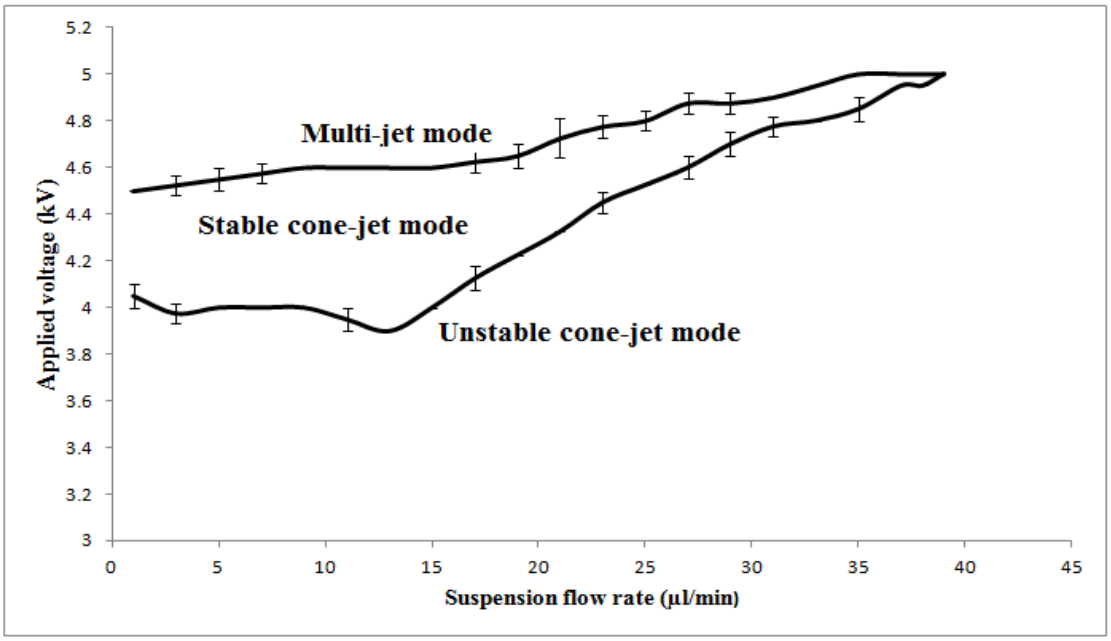

Figure 6.2 Stable cone-jet mode map of a 2wt% HA suspension electrosprayed at a needle to ground electrode distance of 30 mm with a needle of intrnal diameter 500 um.

6.4 HA film optimisation

In order to obtain, uniform and crack-free films, the effect of the deposition parameters on the HA film morphology was assessed. The morphological optimisation studies were conducted by utilising the deposition parameters as summarised in **Table 6.1**.

6.4.1 Influence of time

The effect of deposition time on the morphology of the HA films is shown in **Figure 6.3**. For a spray time of 30s, the films produced displayed a non-homogeneous morphology and consisted of a dense and continuous layer with occasional spherical particle agglomerates (Type 2 morphology). On increasing the spray time to 60 s, the films were more homogeneous and the morphology comprised of a uniform and dense layer of HA particle agglomerates. The films displayed a cauliflower-like morphology. Thus the film displayed a relatively rough topography (Type 3 morphology).

A further increase in spray time to 600s enhanced film homogeneity and resulted in the formation of HA particle agglomerates with a high degree of packing and roughness (Type 4 morphology). The results obtained showed that film morphology changed from Type 2 to Type 4 morphology on increasing the deposition time. The film uniformity was increased by deposition time. Consequently a spray time of 60s was considered to

be adequate for the deposition of uniform and dense HA films as a longer deposition time could also lead to the deposition of thicker films with large residual stresses.

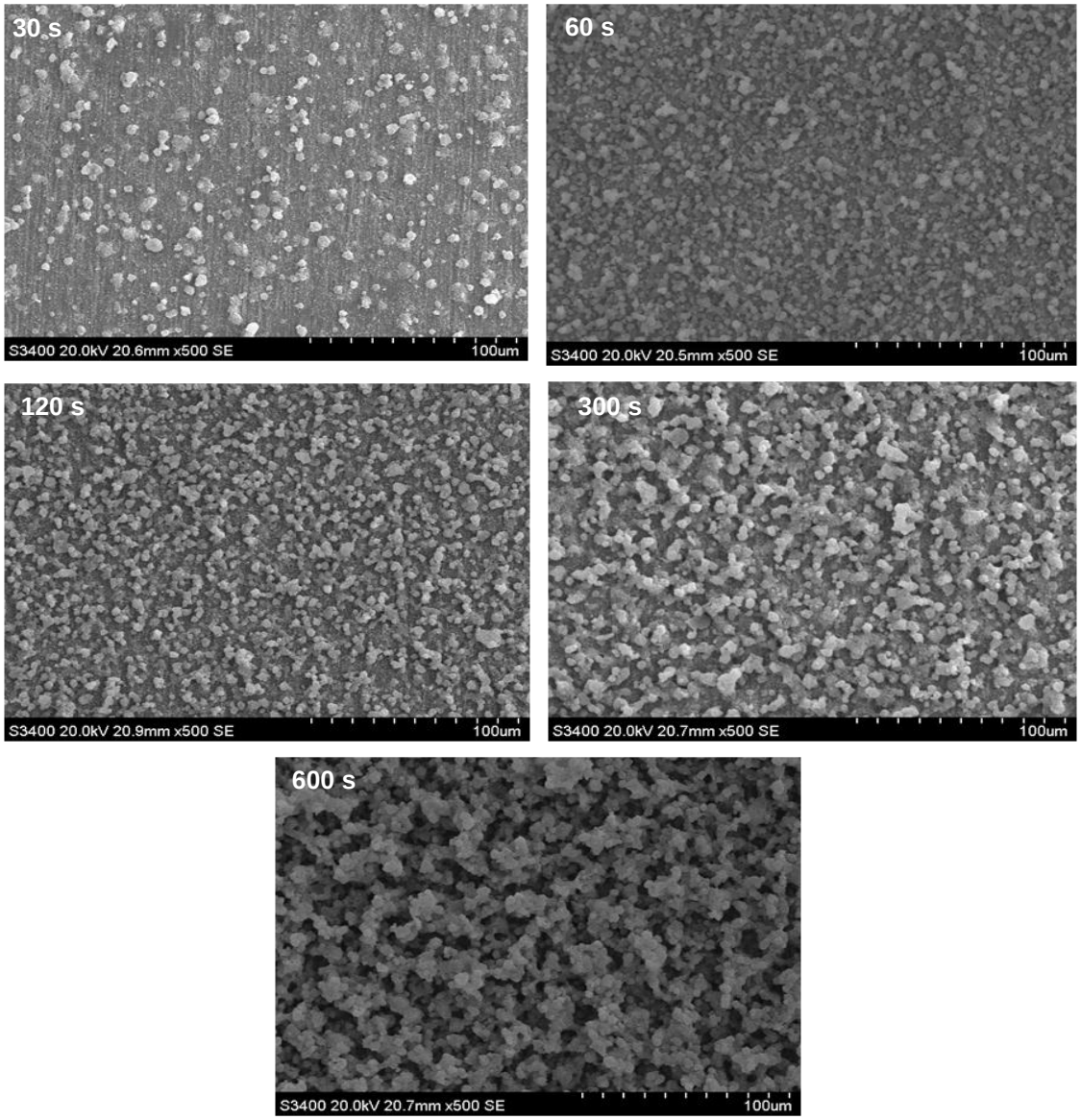

Figure 6.3 Scanning electron micrographs of HA films electrosprayed at 30-600 s. The suspension was electrosprayed at a flow rate of 10 μl/min using a needle of internal diameter 510 μm set at 20 mm from the ground substrate

6.4.2 Influence of needle to substrate distance

The morphology of HA films deposited at needle to substrate distances of 10-50 mm is shown in **Figure 6.4**. At a needle to substrate distance of 10 mm the films displayed a highly uniform and rough topography (Type 4 morphology). The film morphology was composed densely packed HA agglomerates. At a distance of 20mm, there was a reduction in the size of the particle agglomerates. The film was relatively rougher than that obtained at a needle to substrate distance of 10 mm and was also composed of a

layer of highly packed particle agglomerates. Upon increasing the needle to substrate distance from 20 to 50 mm, the films exhibited a relatively smoother topography and were comprised of a dense layer with occasional agglomerations (Type 2 morphology). This indicated that the density and packing of the agglomerates was reduced by an increase in the needle to substrate distance which in turn reduced the surface roughness.

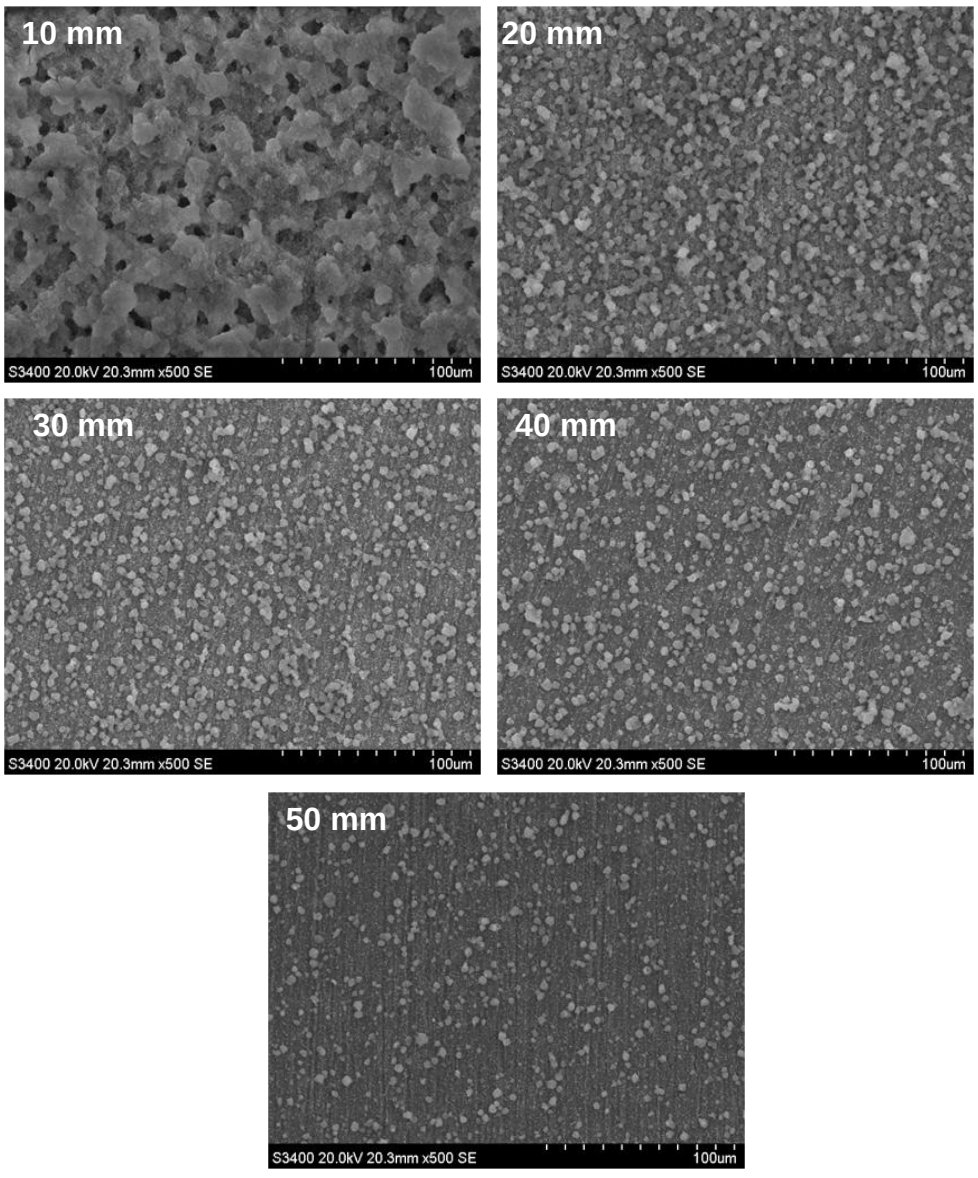

Figure 6.4 Scanning electron micrograph of HA films deposited at 10-50 mm. The suspension was electrosprayed for 60 s at a flow rate of 10 µl/min using a needle of internal diameter 510 µm .

The variation of the needle to substrate distance also increased the diameter of the spray area similarly to the TiO_2 and ZrO_2 sols. As summarized in **Table 6.4**, the

diameter of the spray area increased from approximately 19 mm to 80 mm due to a corresponding increase in needle to substrate distance from 10 mm to 50 mm. However, an intermediate distance of 20 mm was selected for use in further experiments on the basis film homogeneity and reasonable spray area. Moreover, an intermediate needle to substrate distance was also considered to be suitable in order to minimise the deposition time required for obtaining satisfactory substrate coverage.

Table 6.4 Variation of spray diameter with the needle to substrate distance for a 2 wt% HA suspension

Needle to substrate distance (mm)	Spray diameter (mm)
10	18.74±0.08
20	36.62±0.19
30	47.75±0.17
40	70.94±0.63
50	81.62±0.33

6.4.3 Influence of suspension flow rate

Figure 6.5. At the lowest flow rate of 5 µl/min, the films were uniform with a dense layer of particle agglomerates (Type 4 morphology). Upon increasing the flow rate to 10 µl/min, the films became more homogeneous and also comprised of densely packed spherical agglomerates (Type 4 morphology). A marginal reduction in film roughness was also evident. A further increase in suspension flow rate to 30 µl/min caused a more dense and homogeneous film morphology. The particle agglomerates were no longer distinguishable and the films appeared to be marginally smoother than those obtained at lower flow rates. However, a flow rate of 10 µl/min was selected for use in the subsequent experimental work as the maximum operating voltage range was attained at this flow rate. Moreover, a lower suspension flow rate was also considered to be more beneficial in terms of the achievement of finer and monodisperse droplets as reported in the literature.

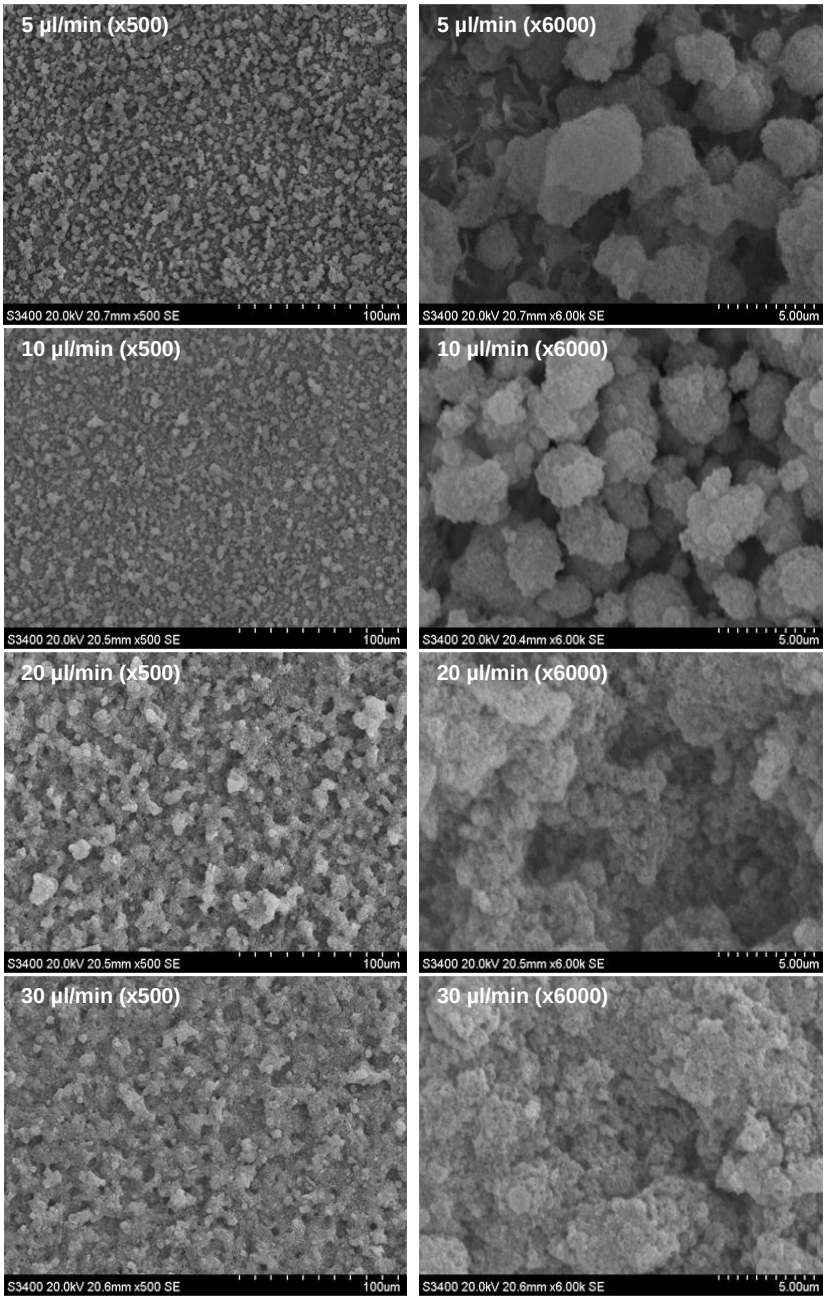

Figure 6.5 Scanning electron micrographs of HA films deposited at flow rates of 5-30 ul/min. The suspension was electrosprayed for 60 s using a needle of internal diameter 510 µm set at a distance of 20 mm from the ground substrate.

6.4.4 Influence of solvent type

The porous and cauliflower-like morphology of the HA films as presented in the previous sections was an indication of a high agglomeration tendency of the HA nano particles. However, Chen *et al* (1996) and later Ghimbeu *et al* (2007) reported that highly porous films generally display poor film cohesion and film-substrate interfacial bonding. Based on these findings, it was hypothesized that such a highly agglomerated morphology could have an adverse effect on the efficacy of the implant owing to poor film cohesion.

Solvent type plays a major role in the determination of the film morphology. This is a direct consequence of the solvent volatility. The benefits of a lower solvent volatility have been documented by several researchers. For example, Taniguchi (2008) reported that the morphology of samaria doped ceria (SDC) films could be changed from highly particulate to relatively dense by using a less volatile solvent such as butyl carbitol as opposed to highly volatile etOH. Hence it was hypothesized that an improvement in the homogeneity and density of the HA films could be achieved due to the utilisation of a highly volatile solvent carrier such as ethylene glycol (EG). 2-10 wt% was added to etOH prior to HA addition and the suspensions were labelled HA(2EG), HA(6EG) and HA(10EG).

6.4.4.1 Liquid physical properties

Table 6.5 compares the liquid physical properties of the HA suspensions. The density was increased from 814 to 884 kgm^{-3} as the proportion of EG was increased from 0 to 10 wt%. The suspension viscosity also displayed a positive correlation to the EG concentration and as such was varied from 5.57 to 8.87 mPaS as the EG concentration was increased from 0 to 10 wt%. The surface tension was also slightly increased from 35.9 to 39.2 mN/m due to an increase in the EG concentration. However, the electrical conductivity was also reduced from 0.8 to 0.5 Sm^{-1}.

Table 6.5 Variation of liquid physical properties with EG concentration

Suspension	Viscosity (mPaS)	Surface tension (mN/m)	Electrical conductivity (Sm^{-1})	Density (kgm^{-3})
HA	5.57	35.90	0.80	814
HA(2EG)	6.80	36.60	0.70	822
HA(6EG)	7.06	37.50	0.63	839
HA(10EG)	8.87	39.20	0.50	884

6.4.4.2 Mode map selection

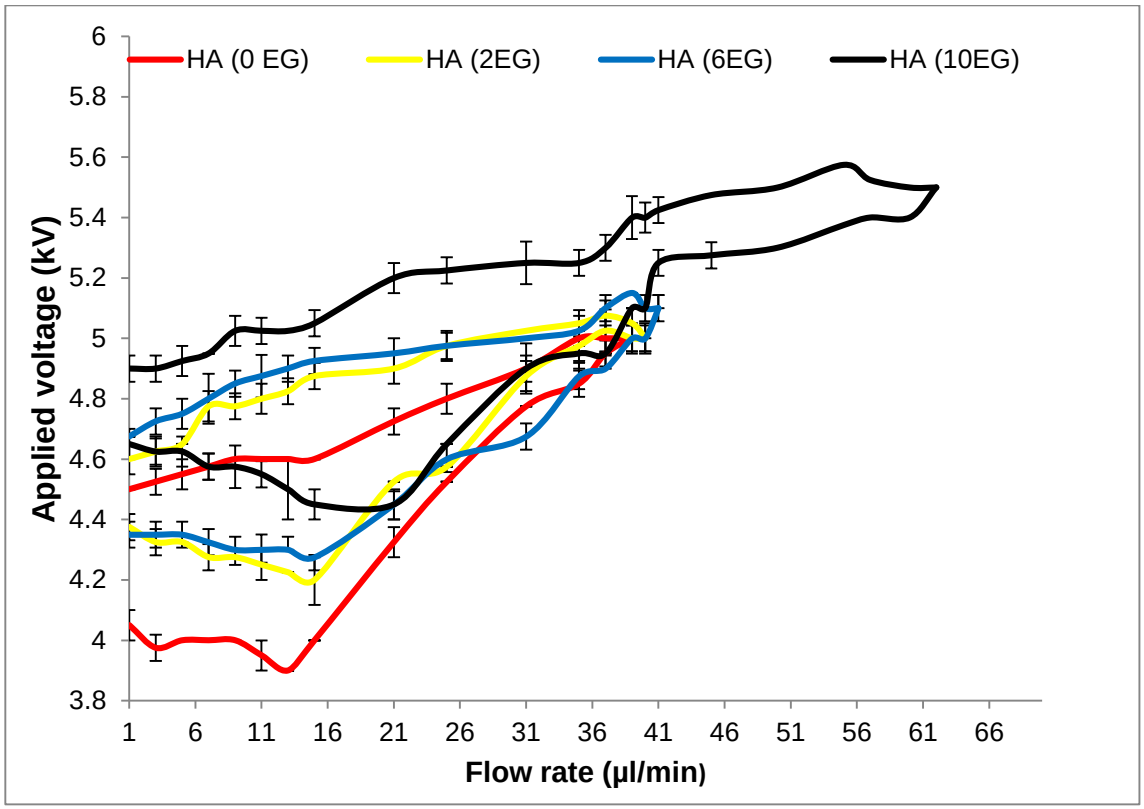

Figure 6.6 Effect of EG concentration on stable cone-jet mode maps of HA suspensions. The suspensions were electrosprayed using a needle with an internal diameter of 510 µm and a needle to substrate distance of 20 mm.

Figure 6.6 shows the stable cone-jet mode maps obtained using the HA suspensions. There was an increase in the maximum suspension flow rate from 39 to 62 µl/min as the EG concentration was increased from 0 to 10 wt%. The overall applied voltage range for stable cone-jet formation were also increased from 3.9-4.6 to 4.5-5.5 kV due to an increase in the EG concentration. Furthermore the flow rate at which the maximum operating voltage range could be attained for each suspension was shifted from 13 µl/min to 20 µl/min. These results showed that the electrospray process was affected by the HA suspension composition in terms of EG concentration. A higher EG concentration was considered to enhance the efficacy of the electrospray process which could be of great benefit in potential industrial applications. The electrospray characteristics of the HA suspensions are shown in **Table 6.6**.

Table 6.6 Comparison of electrospray characteristics of HA (0-10 EG) suspensions

Sol	F_{max}(µl/min)	Overall voltage (kV)	Δv_{max}(kV)	$F_{\Delta vmax}$ (µl/min)
HA	39	3.9-5.0	3.9-4.6	13
HA (2EG)	40	4.2-5.1	4.2-4.9	15
HA (6EG)	41	4.2-5.1	4.2-4.9	16
HA(10EG)	62	4.5-5.5	4.4-5.2	20

6.4.4.3 Droplet relic measurements

Table 6.7 compares the mean droplet relic diameter obtained by electrospraying the HA suspensions with increased EG concentrations

Table 6.7 Comparison of average droplet relic diameter obtained using HA suspensions with different concentrations of EG electrosprayed at a suspension flow rate of 10 µl/min and a needle to substrate distance of 20 mm (n=35).

EG concentration (wt%)	Average droplet relic diameter (µm)	Spray area (mm)	Estimated thickness (nm)
0	2.3±0.2	36.7±0.3	95.0±0.9
2	2.3±0.4	34.4±0.4	139.9±0.4
6	2.4±0.3	33.9±0.7	322.0±1.2
10	2.5±0.6	32.0±0.8	871.3±4.6

There was no significant difference in the average droplet relic diameter obtained for the HA suspensions with EG concentration of 0-6 wt%. The average droplet relic diameter was approximately 2.3 µm. However, the mean droplet relic diameter obtained using the HA suspension with an EG concentration of 10wt% was statistically higher than that obtained using the HA suspensions with a lower EG concentration ($p<0.05$). In general, the average droplet relic diameter displayed a positive correlation to the EG concentration. It was hypothesized that the variation in average relic diameter could affect the film morphology.

6.4.4.4 Film morphology

Figure 6.7 compares the morphology of the HA films prepared by the electrospraying of the HA suspensions.

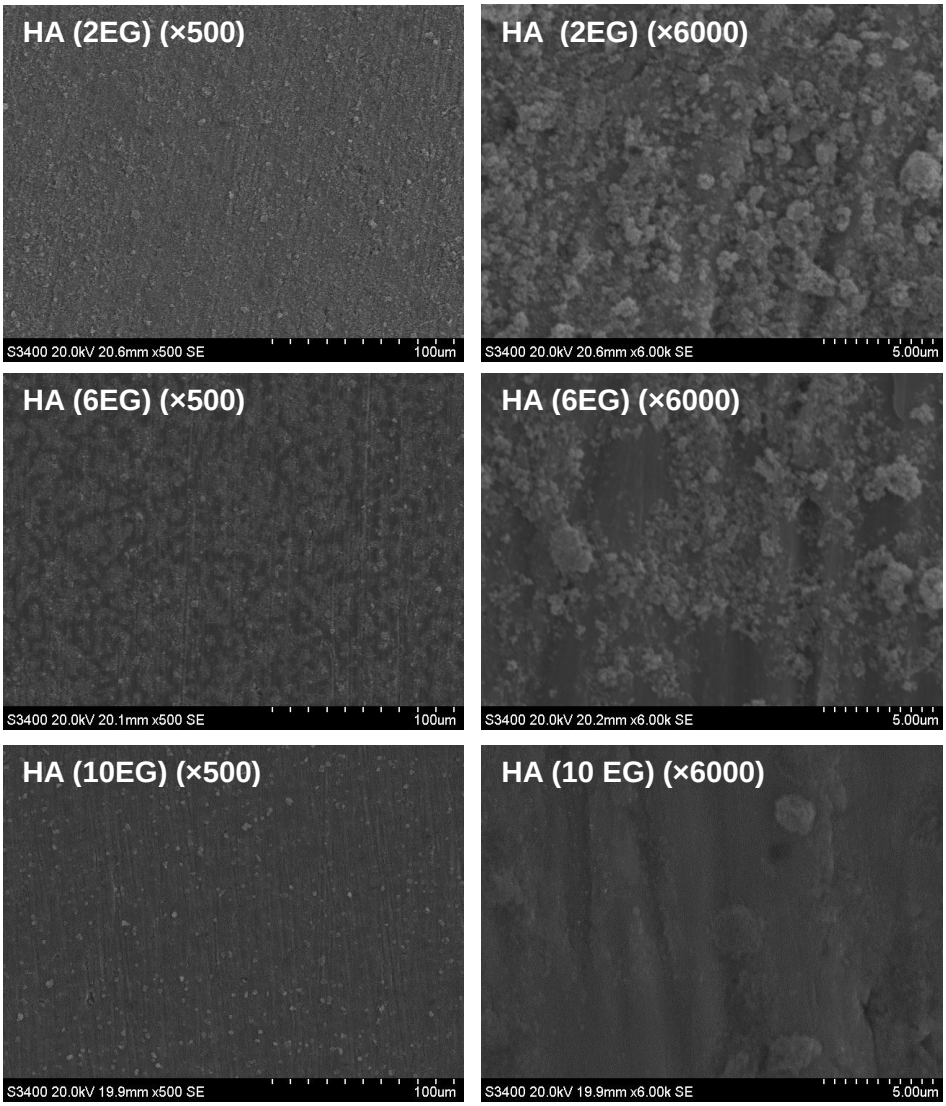

Figure 6.7 Scanning electron micrographs showing the morphology of HA films obtained using HA suspensions with different concentrations of EG. The suspensions were electrosprayed for 60s at a flow rate of 10 μl/min using a needle with an internal diameter of 510 μm and a needle to substrate distance of 20 mm.

For a low EG concentration, the HA films appeared to be rougher. The HA particles were clearly visible on the films surface. The films produced comprised of a dense bottom layer with a high number of small HA agglomerates. The films deposited from the HA (6EG) were marginally smoother and consisted of a dense and continuous bottom layer with occasional particle agglomerates and rough spots. For the HA (10EG) suspension, the films produced appeared to be highly dense and smooth with a small number of particle agglomerates. Generally, the number of HA particle agglomerates was reduced by an increase in EG concentration. The results showed that the HA film morphology could be controlled by reducing the volatility of the solvent

carrier. Hence the film morphology was varied from rough to smooth by increasing the concentration of EG. An increase in concentration of EG also caused a marginal reduction in the diameter of the spray area as summarized in **Table 6.7**. The spray diameter obtained using the HA suspension was statistically higher than that obtained in the presence of EG ($P<0.05$). However, there was no significant difference in the spray diameter obtained using the HA (2EG)-HA (6EG) suspensions. The estimated thickness of the HA films obtained using the different suspensions is compared in **Table 6.7**. The estimated thickness was directly proportional to the concentration of EG ($P<0.05$).

The addition of EG was also considered to be advantageous from an electrospray point of view as seen from the higher operating voltages and maximum suspension flow rates achieved. However, an intermediate EG concentration of 6 wt% was selected for use in further investigations owing to the reasonable homogeneity of the films obtained as indicated by the non-porous morphology of the films. Additionally, the films obtained using the HA (6EG) suspension appeared to be relatively rough. Thus it was hypothesized that the rougher film surface would enhance the initial cellular response as reported in the literature. The HA (6EG) suspensions were henceforth labelled H100 unless stated otherwise.

6.5 Liquid physical properties of two-phase bioceramic suspensions

The liquid physical properties of the TiO_2/HA and ZrO_2/HA suspensions are compared in **Table 6.8**. For the TiO_2/HA suspensions, an increase in the HA content from 0 to 100 wt% caused a slight increase in density. Similarly, an increase in HA concentration from 0-100 wt% in the ZrO_2/HA suspensions resulted in an increase in suspension density. Moreover, the densities of the TiO_2/HA suspensions was slightly lower than that of the ZrO_2/HA suspensions. The viscosity of the two-phase suspensions was significantly increased by an increase in the HA content. The viscosity of the TiO_2/HA suspensions was increased by approximately 80% whereas that of the ZrO_2/HA suspensions was increased by approximately 60%. An increase in the HA also caused a two-fold increment in the surface tension of the TiO_2/HA and ZrO_2/HA suspensions. However, the electrical conductivity of the suspensions displayed a negative correlation with the HA content and was reduced by approximately two thirds for both the TiO_2/HA and ZrO_2/HA suspensions. In general, the density, viscosity and surface tension of the ZrO_2/HA suspensions were higher than that of the HA/TiO_2 suspensions, although the electrical conductivity was lower.

Table 6.8 Liquid physical properties of two-phase bioceramic suspensions

Suspension	Viscosity (mPa S)	Surface tension (mN/M)	Electrical conductivity $\times 10^{-4}$ (Sm^{-1})	Density (kgm^{-3})
T100	3.11±0.02	29.80±0.17	2.53±0.05	801±0.03
75T25H	4.14±0.02	30.30±0.08	1.73±0.09	812±0.01
50T50H	4.70±0.03	34.60±0.08	1.27±0.05	819±0.03
25T75H	5.74±0.06	35.90±0.01	1.10±0.01	827±0.05
Z100	4.30±0.06	30.77±0.08	2.30±0.01	809±0.03
75Z25H	4.85±0.04	33.60±0.09	1.10±0.01	821±0.08
50Z50H	5.20±0.06	35.80±0.02	0.90±0.01	829±0.02
25Z75H	6.63±0.04	36.70±0.09	0.83±0.05	835±0.01
H100	7.06±0.06	37.50±0.03	0.63±0.01	839±0.03

6.6 Electrospray processing of two-phase bioceramic suspensions

6.6.1 Mode map selection

Figure 6.8 shows the stable cone-jet mode maps obtained using the TiO_2/ HA suspensions. The maximum suspension flow rate was increased from 27 µl/min to 40 µl/min as the HA concentration was increased from 0-100 wt%. An increase in the HA concentration also caused a slight increase in the onset and maximal operating voltage from 4.1-4.9 kV to 4.2-5.1 kV and further extended the flow rate at which the maximum operating voltage could be attained from 7 to 15 µl/min. The electrospray characteristics of the HA/TiO_2 suspensions are summarized in **Table 6.9.**

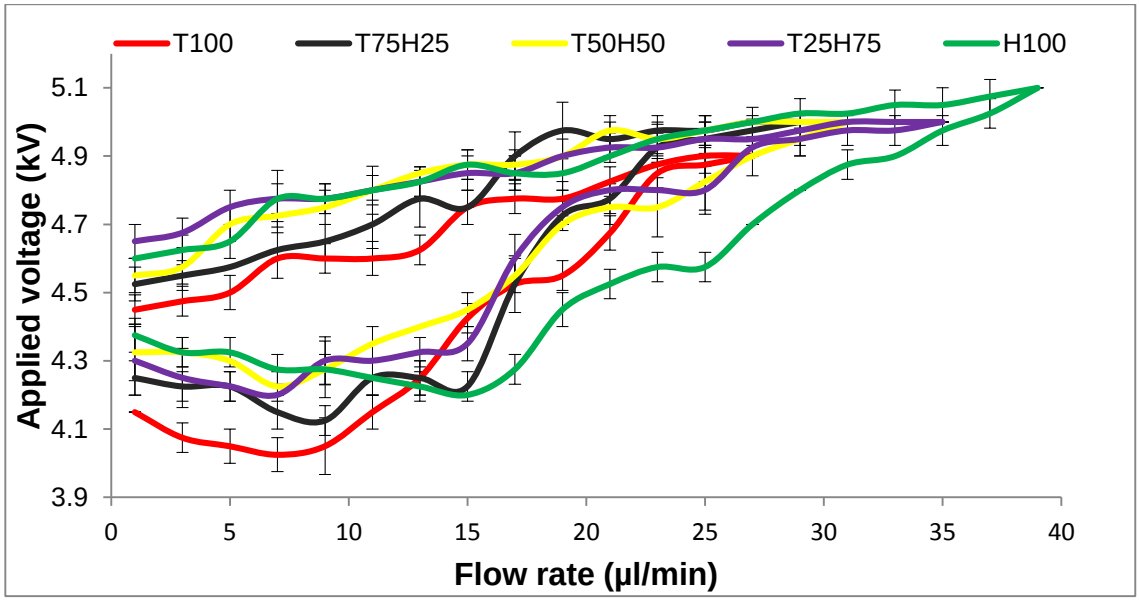

Figure 6.8 Stable cone-jet mode map selection for TiO_2/HA suspensions electrosprayed using a needle of internal diameter 510 µm fixed at a distance of 20 mm above the ground electrode.

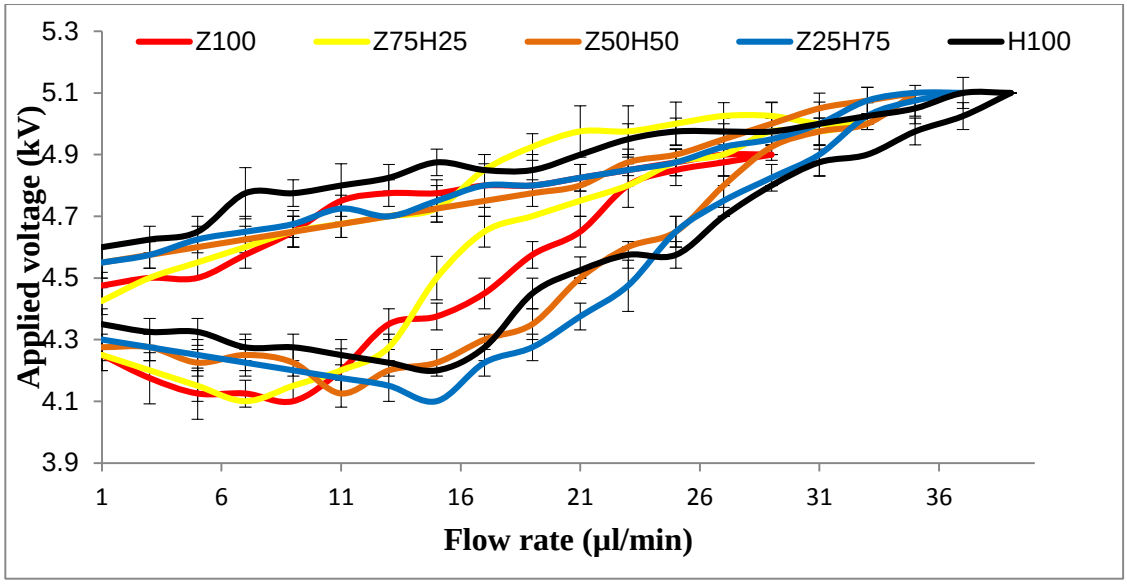

Figure 6.9 Stable cone-jet mode map selection for ZrO_2/HA electrosprayed using a needle of internal diameter 510 µm fixed at a distance of 20 mm above the ground electrode

Figure 6.9 shows the stable cone jet mode maps obtained using the ZrO_2/HA suspensions. Similarly to the TiO_2/HA suspensions, an increase in the HA concentration extended the flow rate regime from 29 µl/min to 40 µl/min and also increased the operating voltage range from 4.1-4.9 kV to 4.2-5.1 kV. There was also an increase in the flow rate at which the maximum operating voltage range could be obtained from 9 to 15 µl/min. The electrospray characteristics of the ZrO_2/HA are presented in **Table 6.9** and compared with those of the TiO_2/HA suspensions.

Table 6.9 Electrospray characteristics of single and two phase bioceramic suspensions electrosprayed using a needle of internal diameter 510 µm fixed at a distance of 20 mm above the ground electrode

Suspension	Maximum suspension flow rate (µl/min)	Overall operating voltage range (kV)	Δv_{max}	$F\Delta v_{max}$
T100	27	4.1-4.9	4.0-4.7	7
T75H25	29	4.1-5.0	4.1-4.7	9
T50H50	31	4.2-5.0	4.3-4.8	11
T2575H	35	4.2-5.0	4.3-4.8	13
Z100	29	4.1-4.9	4.1-4.6	9
Z75H25	33	4.1-5.0	4.1-4.7	9
Z50H50	35	4.1-5.0	4.1-4.8	11
Z25H75	37	4.2-5.1	4.1-4.8	15
H100	40	4.2-5.1	4.2-4.8	15

Generally, there was no significant difference in the operating voltage and flow rate of the TiO_2/HA and ZrO_2/HA suspensions. However, a suspension flow rate of 10 µl/min was selected for use in further investigations based on earlier studies conducted using the single phase HA suspensions.

6.6.2 Droplet relic measurements

Table 6.10 Spray diameter (n=3) and average relic diameter (n=50) obtained using different bioceramics electrosprayed at a flow rate of 10 µl/min using a needle of internal diameter 510 µm fixed at a distance of 20 mm above the ground electrode. A p value <0.05 was considered to be significant

Suspension	Spray diameter (mm)	Average relic diameter (µm)
T100	41.5±0.4	1.2±0.2
T75H25	40.4±0.6	1.5±0.4
T50H50	38.3±0.1	1.9±0.4
T2575H	36.3±0.7	1.9±0.2
Z100	40.0±0.3	1.3±0.2
Z75H25	37.3±0.2	1.7±0.4
Z50H50	35.5±0.3	1.9±0.4
Z25H75	35.0±0.7	2.1±0.2
H100	33.9±0.7	2.3±0.4

Table 6.10 compares the average droplet relic diameter obtained using the two-phase sols. For both suspension systems there was a positive relationship between the HA content and the mean droplet relic diameter. For the TiO_2/HA suspensions, the mean droplet relic diameter was increased from 1.2 to 1.9 µm upon increasing the HA content from 0 to 75 wt%. Similarly, the mean droplet relic diameter obtained using the ZrO_2/HA suspensions was increased from 1.3 to 2.0 µm due to increasing the HA content from 0 to 75 wt%. The HA suspension gave a mean droplet relic diameter of approximately 2.3 µm. Hence, the mean droplet relic diameter affected the film morphology.

6.6.3 Spray diameter measurements

The spray diameters obtained using the TiO_2/HA and ZrO_2/HA suspensions are presented in **Table 6.10**. For both the TiO_2/HA and ZrO_2/HA suspensions, the spray diameter was significantly reduced due to an increase in the HA content ($p<0.05$).

However, the spray diameter obtained using the TiO_2/HA suspension was larger than that obtained using the ZrO_2/HA suspensions.

6.6.4 Film deposition

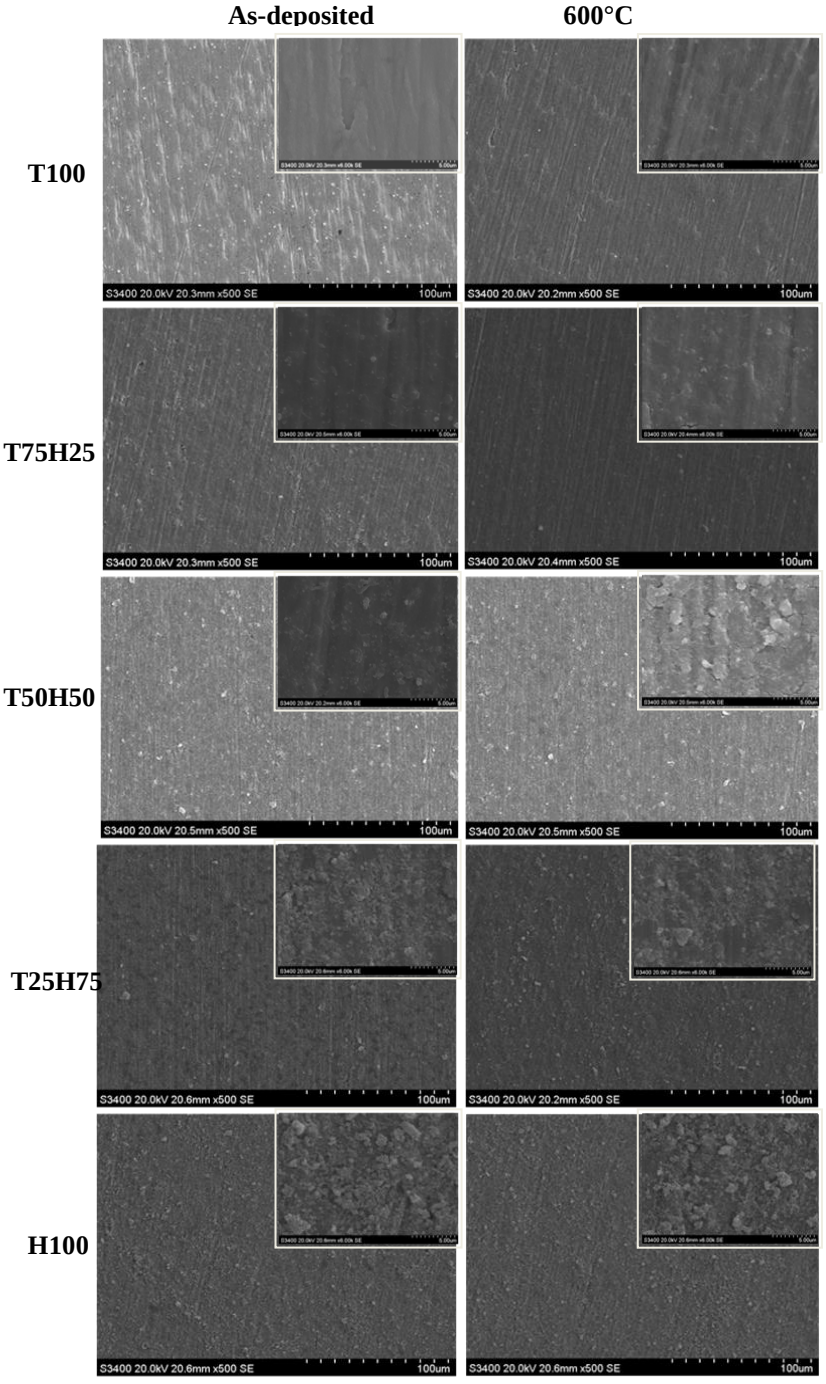

Figure 6.10 Scanning electron micrographs of as deposited and annealed TiO_2 /HA films. The films were deposited at a flow rate of 10 µl/min using a needle of internal diameter of 510 µm fixed at a distance of 20 mm. The films were annealed at a temperature of 600°C

Figure 6.10 shows the morphology of the as-deposited and annealed TiO_2/HA films. The TiO_2 suspension gave highly homogeneous films. The films consisted of a dense layer with with occasional spherulites. The T75H25 suspension also gave dense and featureless films. Increasing the HA concentration to 50 wt% caused the deposition of dense and continuous films with some rough spots. And a further increase in HA content gave rougher films. The films were composed of a continuous sub layer with regions of rough patches and occasional particle agglomerates.

The morphology of the annealed TiO_2/HA films was very similar to that of the as-deposited films. However, the post deposition heat treatment led to the disappearance of the spherulites on the TiO_2 surface and caused the appearance of a small number of microcracks were observed on the surfaces of the TiO_2 and 75TH25 films.

.**Figure 6.11** shows the morphology of the ZrO_2/HA films. The ZrO_2 film was quite dense and continuous with a small number of agglomerates. The Z75H25 film comprised of a dense and continuous layer with some rough patches. Upon increasing the HA concentration from 25-75 wt%, the films obtained displayed a high degree of roughness.

The morphology of the ZrO_2/HA composite films also did not differ significantly from that of the as-deposited films. The roughness of the films was increased by the HA content. Similarly to the TiO_2/HA films, the post deposition heat treatment caused the shrinkage of the spherulites on the ZrO_2 films. For both film systems the absence of additional morphological features due to heat treatment at 600ºC indicated that the film morphology was not adversely affected by the annealing process. It seems that annealing did not alter the surface morphology of the electrosprayed TiO_2/HA and ZrO_2/HA films. However, the films deposited from the ZrO_2/HA suspensions appeared to be rougher than those obtained using the TiO_2/HA suspensions.

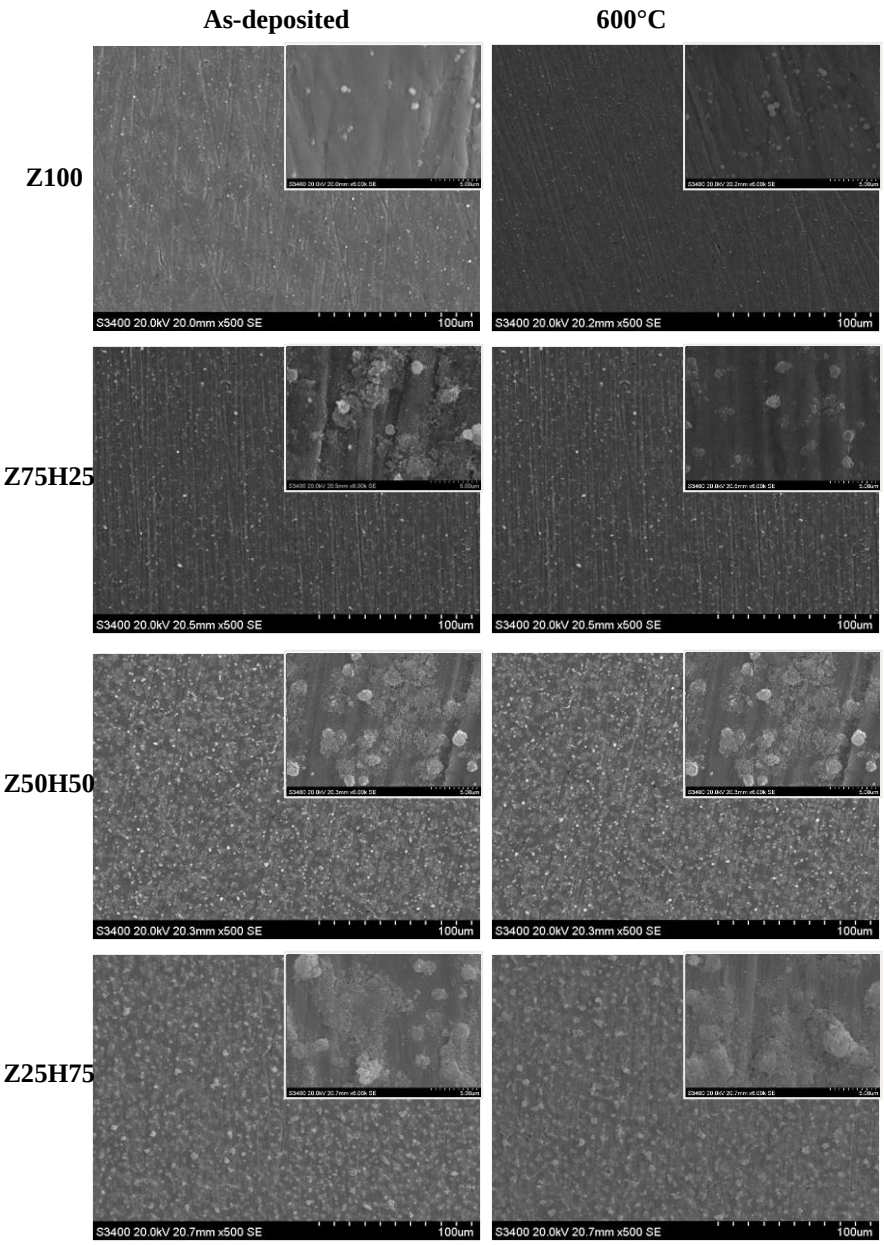

Figure 6.11 Scanning electron micrographs of as deposited and annealed HA/ZrO_2 films. The films were deposited at a flow rate of 10 μl/min using a needle of internal diameter of 510 μm fixed at a distance of 20 mm. The films were annealed at a temperature of 600°C

The estimated film thickness of the two-phase bioceramic films is summarized in **Table 6.11**. As shown, the estimated thickness was dramatically increased due to a corresponding increase in HA content for both the TiO_2/HA and ZrO_2/HA films. Furthermore, the ZrO_2/HA films were thicker than the TiO_2/HA films.

Table 6.11 Comparison of estimated thickness of TiO_2/HA and ZrO_2/HA films

Suspension	Estimated thickness(nm)
T100	91.8±1.1
T75H25	101.4±3.1
T50H50	184.6±3.2
T2575H	247.1±1.9
Z100	96.9±1.0
Z75H25	118.3±2.5
Z50H50	208.1±1.9
Z25H75	260.7±1.7
H100	332.0±2.9

6.7 Characterization of film characteristics

6.7.1 Phase composition

The phase composition of the composite films was analyzed using Raman spectroscopy and the results are shown in **Figures 6.12** and **6.13**.

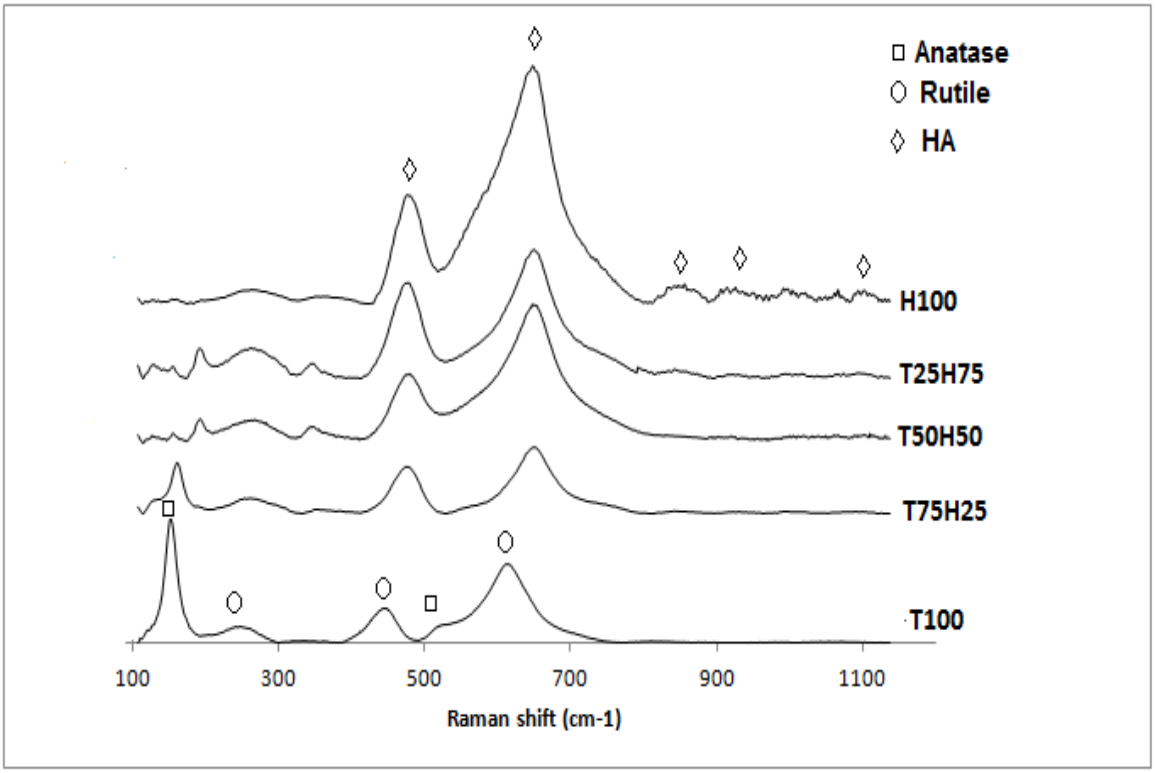

Figure 6.12 Raman spectra of TiO_2/HA composite coatings annealed at a temperature of 600°C for 1 hr.

The phase composition of the TiO_2/HA films is shown in **Figure 6.12**. The TiO_2 films displayed characteristic peaks due to the anatase and rutile phases as expected. However, the addition of HA resulted in the reduction in the peak intensity owing to the anatase phase. There was also a slight shift in the peak position from 447 to 460 cm^{-1} and 608 to 620 cm^{-1} due to the presence of HA. The dominant peaks due to HA displayed an increase in intensity upon increasing the HA composition from 0 to 100 wt%.

Similarly, in the case of the the ZrO_2/HA system (**Figure 6.13**), the ZrO_2 films exhibited characteristic peaks due to monoclinic and tetragonal ZrO_2. On adding HA, the characteristic peaks due to ZrO_2 gradually disappeared whereas the peaks due to HA became stronger as the HA content increased.

The absence of secondary phases for both the TiO_2/HA and ZrO_2/HA composite films was an indication of the phase purity of the composite films and also demonstrated that no chemical reaction occurred between HA and the toughening phases.

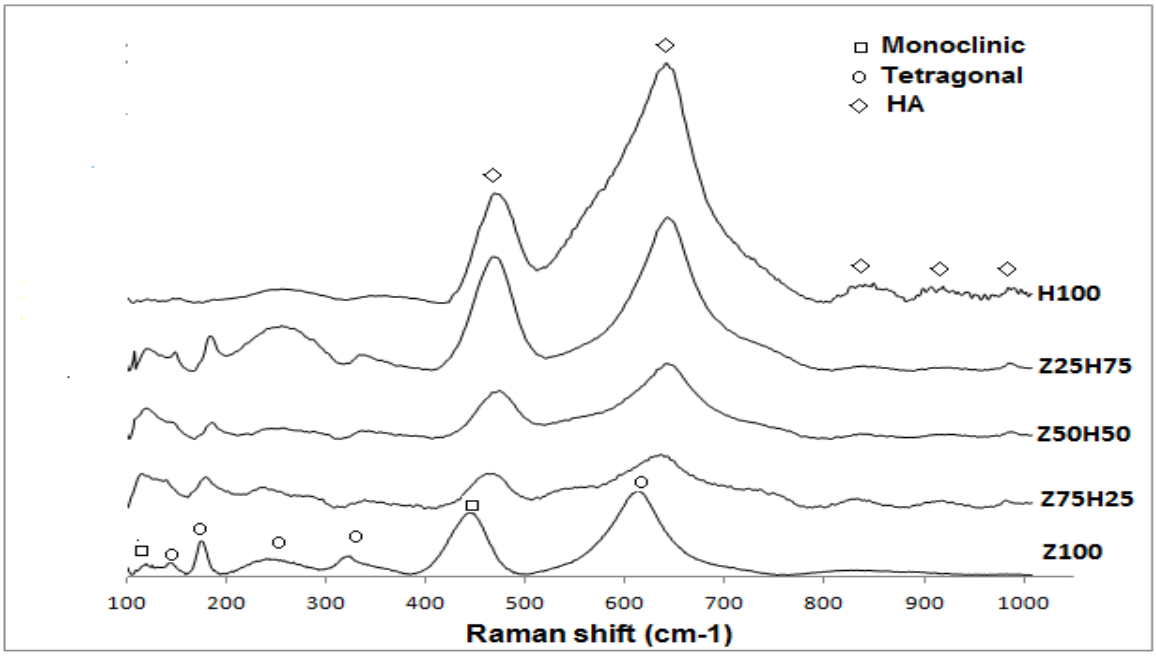

Figure 6.13 Raman spectra of ZrO_2/HA composite coatings coatings annealed at a temperature of 600°C for 1 hr.

6.7.2 Surface roughness

The average surface roughness of the TiO_2/HA films is compared in **Table 6.12**. The T100 films had an average surface roughness parameter (R_a) of approximately 0.7 µm

which was increased to approximately 1.0 μm on increasing the HA content to 100 wt%.

The ZrO_2/HA films displayed a similar trend. The Z100 films had an R_a value of approximately 0.8 μm which was slightly increased to approximately 0.9 μm upon increasing the HA content from 25 to 75 wt%. The results obtained showed that there was a positive correlation between the average surface roughness and the HA content. This was in agreement with the observations of the film surface morphology from SEM examination.

Table 6.12 Surface characteristics of bioceramic composite films

Film	Surface roughness (μm)	Water contact angle °
T100	0.7±0.03	9.63±0.40
7T5H25	0.8±0.02	6.95±0.47
T50H50	0.8±0.03	5.17±0.53
25T75H	0.9±0.06	2.70±0.10
Z100	0.8±0.03	12.40±0.49
75Z25H	0.8±0.04	9.45±0.61
50Z50H	0.9±0.05	6.99±0.57
25Z75H	0.9±0.03	3.19±0.45
H100	1.0±0.07	1.57±0.22

6.7.3 Wettability

The wettability of the two-phase bioceramic films was determined by measuring the water contact angles. The TiO_2 films had a mean water contact angle of approximately 9.6°. However, the presence of 25 wt% HA in the film reduced the water contact angle to 7.0°. A further increase in the HA content reduced the water contact angle to approximately 1.6°.

For the ZrO_2/HA films, a water contact angle of 12.40° was given by the ZrO_2 films. This was further reduced to 3.2° due to the presence of HA. The water contact angles of the composite films are compared in **Table 6.12**. The results showed that there was a negative correlation between the HA content and the water contact angle, which indicated that the film wettability can be enhanced by the presence of HA. The results also showed that the ZrO_2/HA composite films exhibited larger water contact angles in comparison to the TiO_2/HA composite films. This suggested that the TiO_2/HA composite films were more hydrophilic than the ZrO_2/HA films.

6.8 *In vitro* characterization

The bioactivity of the bioceramic films was assessed via *in vitro* acellular study in SBF followed by *in vitro* cell culture.

6.8.1 Assessment of bioactivity in SBF

The change in morphology of the TiO_2/HA films after immersion in SBF for 7-21 days is shown in **Figure 6.14**. All the films exhibited a thin layer of deposit after 7 days of immersion in SBF. The layer on the T100 films was relatively smooth and discontinuous. However, the deposited layer on the T75H25 films was more continuous and also exhibited regions of smooth regions as well as the signature cauliflower structure associated with apatite nucleation. Similar structures were observed on the T50H50 films although there was an increase in the number of the spherulites. The deposited layer on the T25H75 film surface appeared to be rougher and consisted of porous, smooth regions as well as several large spherulites. The spherulites generally displayed a smooth texture although the signature plate-like structure associated with apatite crystals was evident under the smooth layer on the apatite globules. The HA particles arising from the film were no longer visible. The HA film exhibited a similar morphology. The thickness of the deposited layer appeared to increase with a corresponding increment in HA content.

After 14 days, the TiO_2 films appeared to be fully covered by a smooth and featureless layer. The T75H25 films also exhibited a smooth and featureless layer with occasional featureless globules. On the other hand, the morphology of the T50H50, T25H75 and HA films was significantly different. The film surfaces were relatively inhomogeneous and rough with large globular structures. On closer examination, the film surfaces were highly porous with occasional cracks. Plate-like structures were evident in some regions beneath the smooth top layer.

At 21 days, The TiO_2 films displayed a porous and rough layer with occasional smooth regions. In contrast, the T75H25 film displayed a relatively smooth but porous layer. For the 50-100 wt% HA films, the film surfaces were highly inhomogeneous with a highly porous and globular microstructure. Moreover, the surface layers on the HA films were severely cracked. The deposited layers appeared to thicken with immersion time.

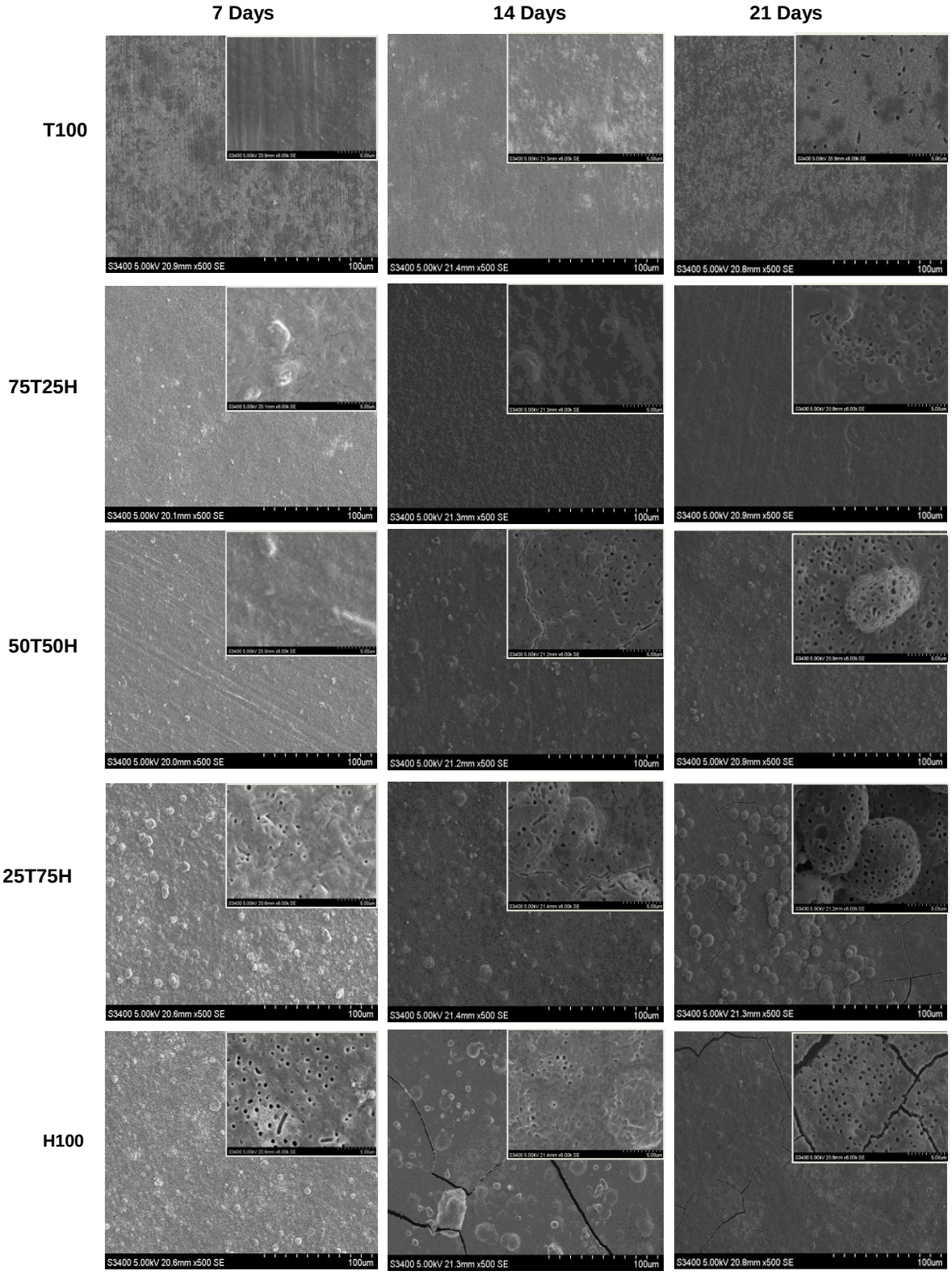

Figure 6.14 Scanning electron micrographs showing the morphology of the TiO_2/HA films after immersion in SBF at a pH for 7-21 days.

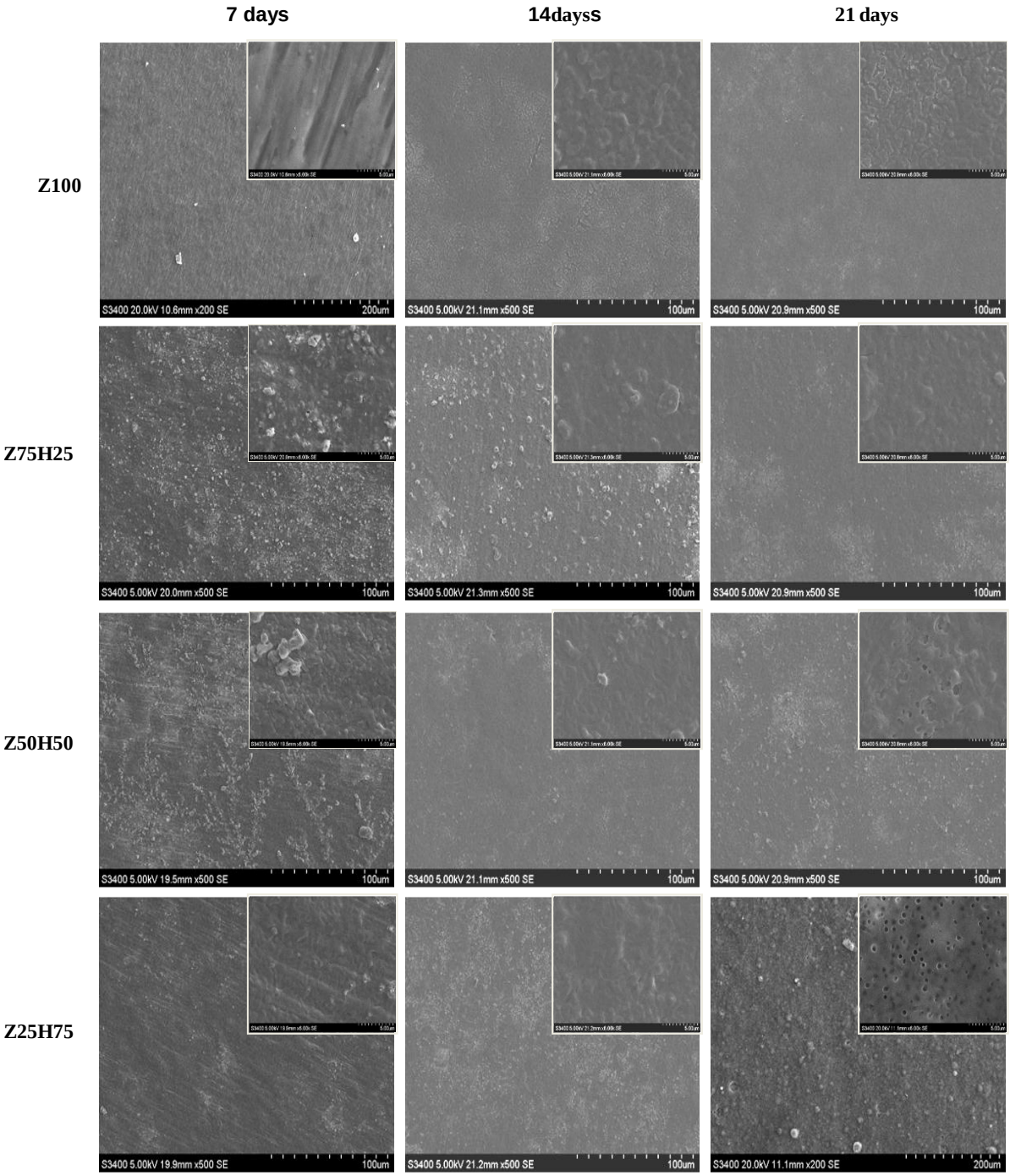

Figure 6.15 Scanning electron micrographs showing the morphology of the ZrO_2/HA films after immersion in SBF at a pH of 7.4 for 7-21 days.

The change in film morphology of the ZrO_2/HA films after immersion in SBF for 7-21 days is shown in **Figure 6.15**. For the ZrO_2 films, the film morphology after immersion in SBF for 7 days appeared to be relatively unchanged with the exception of a small number of particulate deposits. However, there was a thin and discontinuous deposited layer on the Z75H25 films. The area coverage of the deposited appeared to increase

with the HA concentration. However, the deposited layers on the ZrO_2/HA appeared to be relatively smoother than those on the TiO_2/HA films.

After 14 days, the Z100 films were fully covered by a smooth and continuous layer. A similar morphology was evident for the deposited layers on the Z75H25 films. On the other hand, the layers on the Z50H50 films and Z25H75 displayed a relatively smooth morphology with small and smooth spherulites. For an immersion period of 21 days, the ZrO_2 film exhibited a smooth and homogeneous surface layer similarly to the Z75H25 films. The Z50H50 films displayed a slightly porous but smooth surface layer. Occasional spherulites were also evident on the film surface. The surface layer on the Z25H75 films was smooth and highly porous with several large spherulites. The morphology deposited layer on the TiO_2/HA films appeared to be thicker and rougher than on the ZrO_2/HA films for the same time point. However for the TiO_2/HA system films with an HA composition >50 wt% exhibited enhanced bioactivity whereas the ZrO_2/HA system exhibited enhanced bioactivity for an HA content >75wt%.

6.8.2 *In vitro* cellular response of bioceramic composite films

6.8.2.1 Influence of film composition on cell proliferation

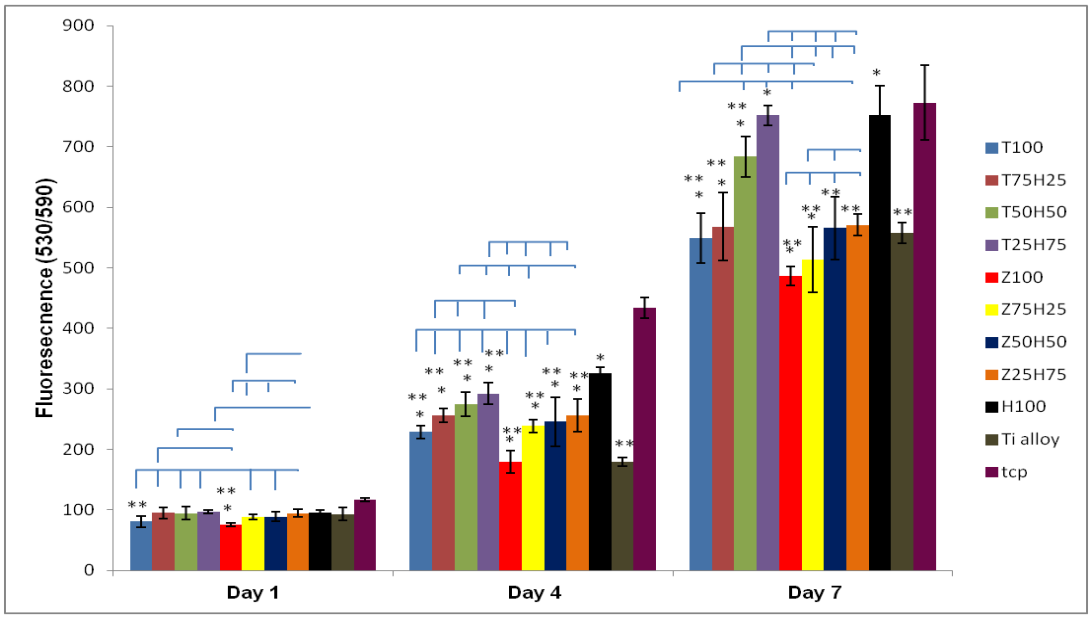

Figure 6.16 Proliferation of MG63 cells on bioceramic composite films over an incubation period of 7 days. Results represent mean±s.d of triplicates obtained from 3 different experiments (n=12). Horizontal brackets indicate a statistical difference between groups ($p<0.05$). Asteriks (*) indicate a statistical difference compared with the uncoated Ti alloy control ($p<0.05$). (**) indicate a statistical difference compared with HA

The proliferation of MG63 cells on ZrO_2/HA and TiO_2/HA composite films is shown in **Figure 6.16**. For the TiO_2/HA films, the T100 films displayed the lowest cell proliferation compared to the 25-100HA films as well as the uncoated Ti alloy after 1 day of cell culture. There was no significant difference in cell proliferation on the 25-75 HA films. Moreover cell proliferation on the samples was comparable to that on the uncoated Ti alloy. However, the H100 film exhibited the highest cell proliferation at this time point.

After a cell culture period of 4 days, the T100 film bore the lowest cell proliferation compared to the 25-100 HA films although the cellular response was similar to that on the uncoated Ti alloy. Cell proliferation on the 7T5H25 film was higher than on the uncoated Ti alloy although less than on the 50-100 HA films. There was no statistical difference in cell proliferation on the 50-75 HA films although these films displayed enhanced cellular response compared to the uncoated Ti alloy. The H100 film exhibited the highest cellular response. On day 7, all the films showed an increased cellular response compared to the uncoated Ti alloy and the cell proliferation increased with the proportion of HA.

On day 1, there was no significant difference in cell proliferation on the Z100 and Z75H25 films. Furthermore, these films showed lower cell proliferation compared to the 50-100HA films and the uncoated Ti alloy. Equally, there was no significant difference in cell proliferation on the 50-75 HA films and the uncoated Ti alloy. There was also no significant difference in cell proliferation on the HA and the uncoated Ti alloy. However, the HA film exhibited the highest proliferation at this time point.

On day 4, the cell proliferation on the Z100 film was comparable to that on the uncoated Ti alloy but significantly lower than on the 25-100HA films. Also, there was no significant difference in cell proliferation on the Z75H25H and Z50H50H films, which further exhibited a higher cell proliferation compared to the uncoated Ti alloy. The cell proliferation on the Z2575H film was statistically higher than on the Z75H25 and Z50H50H films as well as the uncoated Ti alloy. The HA films encouraged the highest cell proliferation at this time point.

On day 7, the Z100 film was found to exhibit the lowest cell proliferation compared to the other test surfaces. There was no significant difference in cell proliferation on the Z75H25 film and the Z50H50 film which, was in turn higher than on the uncoated Ti alloy. The Z25H75 film encouraged a higher rate of cell growth compared to the 0-50HA films and the uncoated Ti alloy whereas the HA film bore the highest cell proliferation. These results demonstrated that the *in vitro* cellular response to ZrO_2 films can be improved by the addition of HA. Moreover, cell proliferation displayed a positive

correlation with the proportion of HA present in the film.Therefore, the *in vitro* cellular response was improved by the presence of HA.

The ZrO_2/HA and TiO_2/HA films were also compared and the cell proliferation on the T100 was statistically higher than on the Z100 films. However, cell proliferation on the T100 film was also similar to that on the Z75H25 film but lower than on the Z50H50 and Z25H75 films. Cell proliferation on the T75H25H film was comparable to that on the ZrO_2/HA films. Equally, there was no significant difference in cell proliferation on the T50H50 film and the ZrO_2/HA films. However, cell proliferation on the T25H75 film was statistically higher than on the ZrO_2/HA films.

On day 4, the cell proliferation on the T100 films was statistically higher than on the Z100 films and was comparable to that on the Z75H25 and Z50H50 films. This film surface also displayed a decreased cellular response compared to the Z25H75 film. Cell proliferation on the T50H50 film was significantly higher than on the ZrO_2/HA films. Similarly, the T25H75 film was higher than on the ZrO_2/HA films.

On day 7, the T100 film was statistically higher than on the Z100 film and comparable to the 75ZH25 and Z50H50 films. This film however, displayed lower cell proliferation compared to the Z25H75 film. Furthermore, it was observed that the 25-75 HA (TiO_2) films exhibited higher cell proliferation compared to the ZrO_2/HA at this time period. Consequently, it was deduced that the HA/TiO_2 films had a better stimulatory effect on cell growth compared to the ZrO_2/HA films. Equally, the results also showed the presence of HA accelerated the growth of MG63 cells. Thus further studies were conducted on the stimulatory effect of the TiO_2/HA composite films.

6.8.2.2 Influence of film composition on protein secretion

The effect of surface composition on the secretion of protein by MG63 cells is shown in **Figure 6.17**. On day 1, there was no statistical difference in protein secretion on the T100 and T75H25 films and the uncoated Ti alloy. However, the H100 film displayed the highest protein secretion at this time. A similar pattern was evident on the film samples after 7 days of cell culture. However after 14 days of cell culture some variations in protein secretion were observed. There was no significant difference in protein secretion on the T100 and T75H25 films and the uncoated Ti alloy. The 50-100 HA films demonstrated statistically higher protein secretion than the latter test surfaces. Similarly, after 21 days of cell culture, the protein secretion on the T100 and T75H25 films was similar and also on comparable to that on the uncoated Ti alloy. A significant

increase in protein secretion was observed as the HA proportion increased from 50-100 wt%. Furthermore, these samples encouraged higher protein secretion compared to the uncoated Ti alloy. Thus it was deduced that protein secretion was sensitive to the presence of HA. In particular, initial protein secretion was not affected by an increase in HA proportion. However, at longer incubation periods, the protein secretion was directly proportional to the amount of HA present

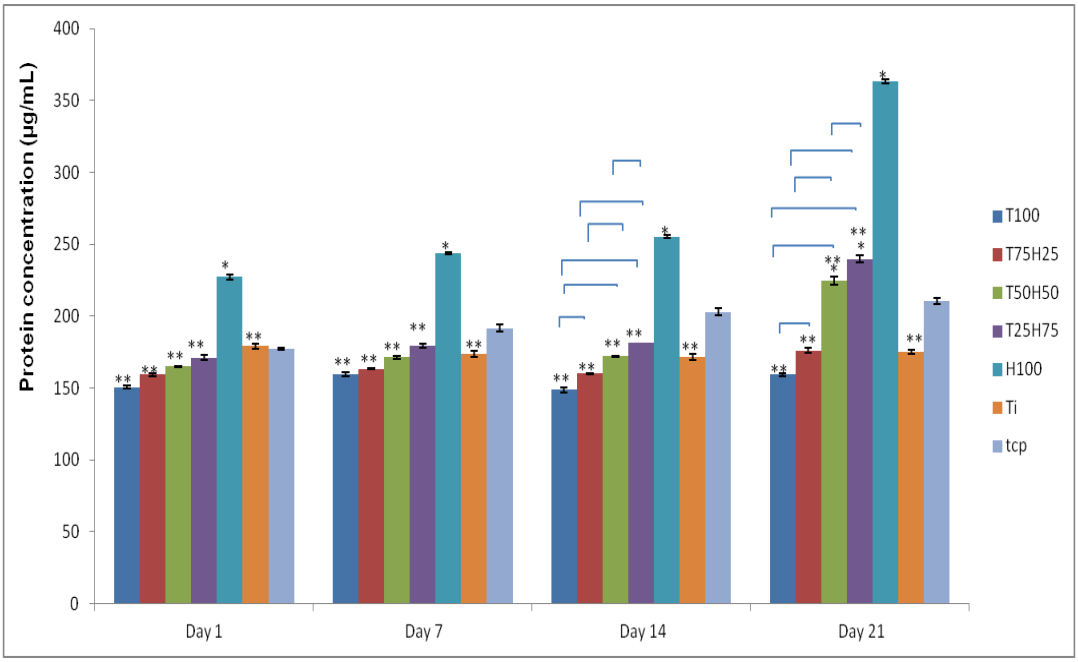

Figure 6.17 Protein secretion of MG63 cells on TiO_2/HA composite films over 21 days. Results represent mean±s.d of triplicates obtained from 3 different experiments (n=12). Horizontal brackets indicate a statistical difference between groups ($p<0.05$). Asteriks (*) indicate a statistical difference compared with the uncoated Ti alloy control ($p<0.05$). (**) indicate a statistical difference compared with HA

6.8.2.3 Influence of film composition on cellular morphology

The morphology of MG63 cells on the TiO_2/HA films is shown in **Figure 6.18**. On all the films, the cells exhibited a polygonal and flattened morphology. Some rounded up cells were also evident on the film surfaces. Furthermore, an increase in cell density on the film surfaces was observed as the HA content was increased from 0-100 wt%.

At day 7, it was observed that the film surfaces were completely covered by cell layers which indicated that cell proliferation had occurred as shown from the AlamarBlue™ studies. In the case of the 0-50 HA films, the cell layer appeared to be thin with a small number of cracks. However, for the 75-100 HA films, the cell layers appeared to be

relatively thick and uniform further confirming that the presence of HA was able to improve the in vitro cellular response of composite films

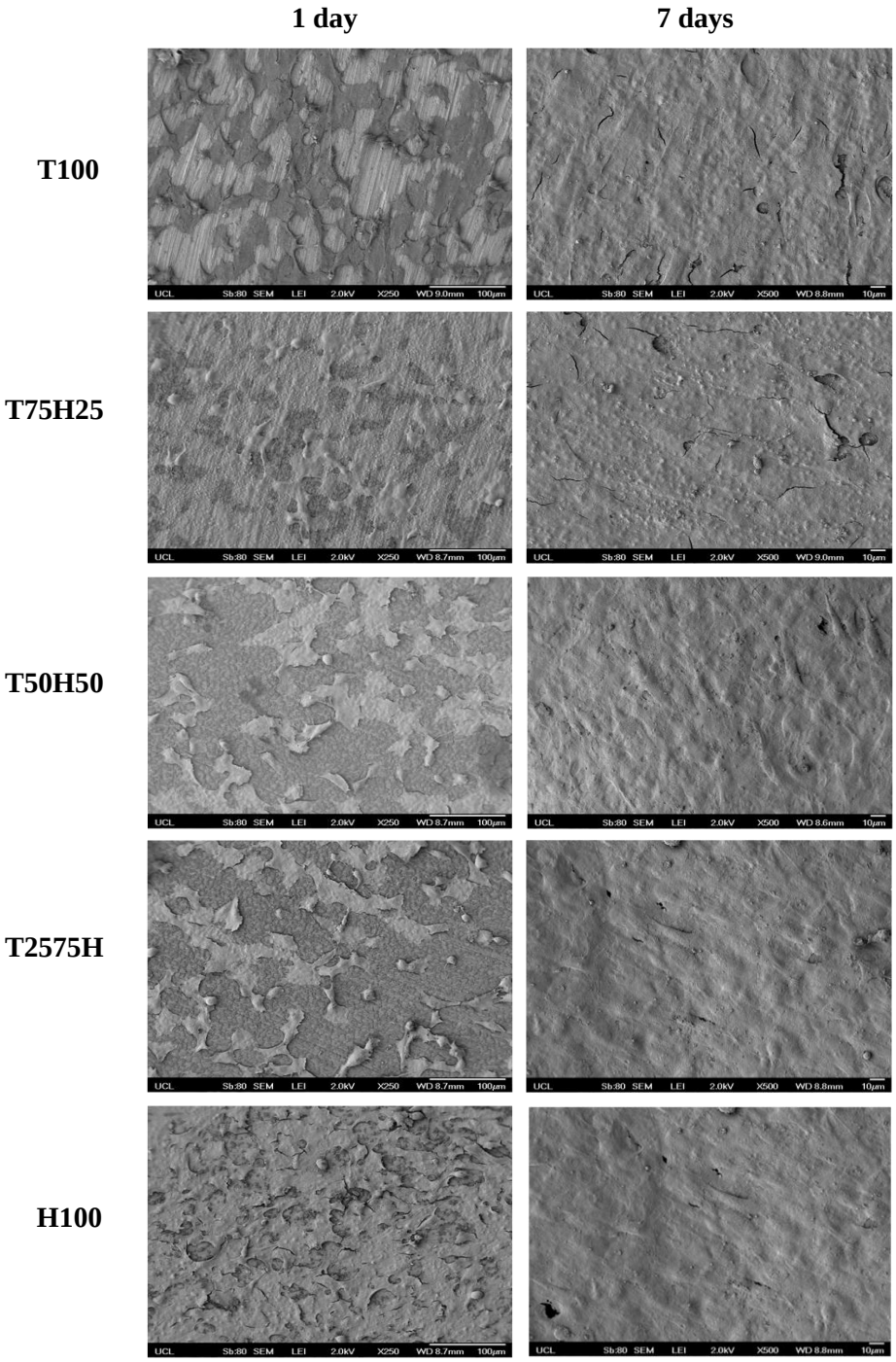

Figure 6.18 Scanning electron micrographs of MG63 cells attached to TiO_2 / HA composite films after day 1 and day 7

.The morphology of MG63 cells on pure phase ZrO_2/HA composite films after 1 day of cell culture is shown in **Figure 6.19.** A flattened and polygonal cell morphology was observed on all the film samples. Adjacent cells were also observed to be joined

together resulting in the formation of a cell monolayer on the film surfaces. However, the density of the cell layer was increased by the proportion of HA in the films, which further confirmed that initial attachment was enhanced by the presence of HA.

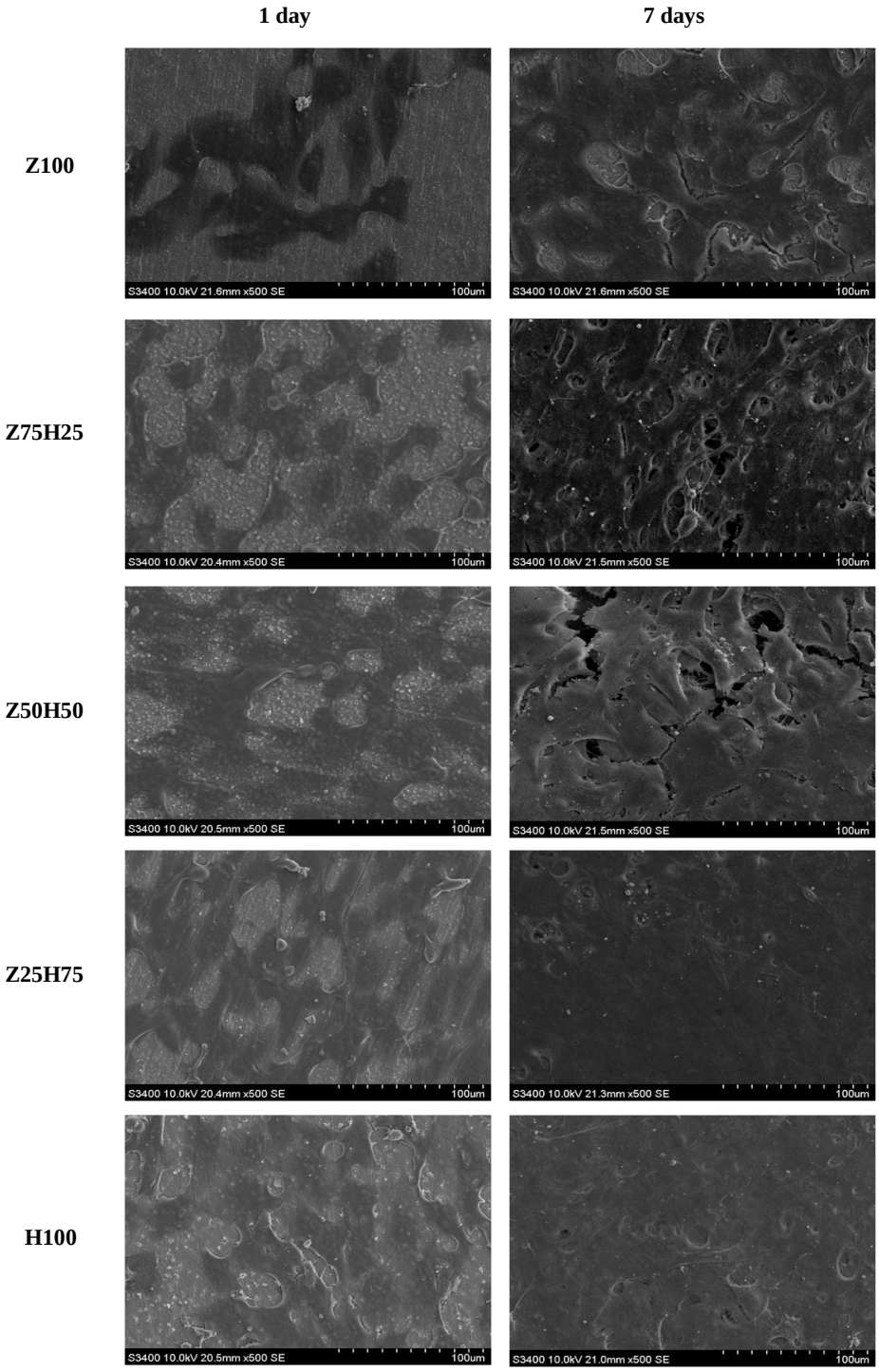

Figure 6.19 Scanning electron micrographs of MG63 cells attached to ZrO_2/HA composite films at day 1 and day 7

At day 7, all the films exhibited an increase in cell coverage. In particular the coverage of the films by the cell layer was higher for the films with higher HA content; On the ZrO_2 film, numerous cells were observed which were attached to each other, although the film surface was still visible. For the Z75H25 film with increased HA proportion, cell multilayers were observed. However, the film surface was no longer evident. Upon increasing the HA proportion from 25-100 wt%, the cell layer became more uniform and dense. This was a further confirmation the cellular response of the ZrO_2 films over the 7 day test period was enhanced by the presence of HA.

6.9 Scratch resistance of bioceramic composite films

6.9.1 Scratch morphology

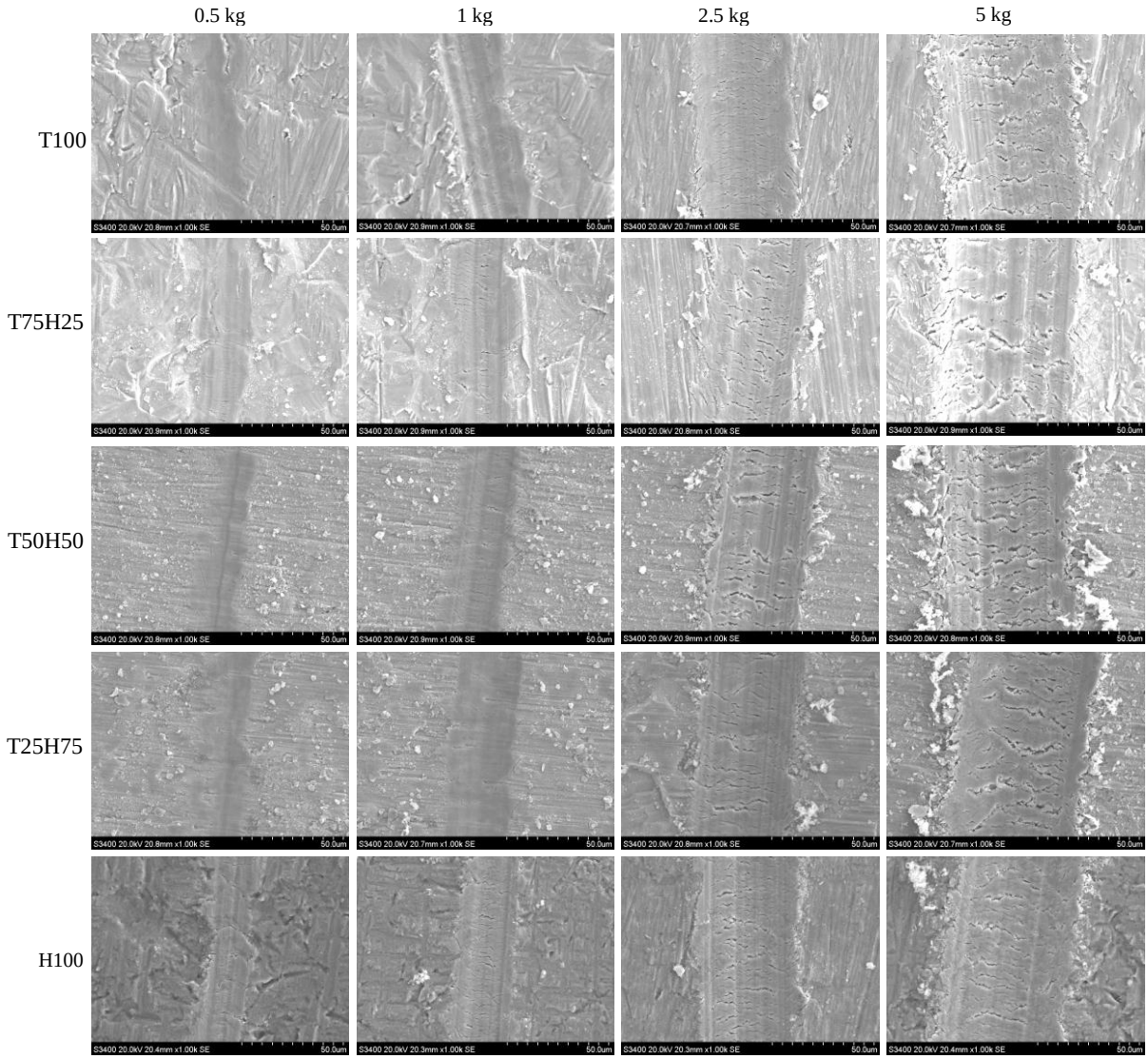

Figure 6.20 Scanning electron micrographs of scratch morphology on TiO_2/HA films. The films were subjected to loads of 0.5 to 5 kg

Figure 6.20 shows the scratch morphology on the TiO_2/HA films. For a scratch load of 0.5 kg, all the film surfaces displayed poorly defined scratch tracks with little or no transverse cracking. In particular, the edges of the scratch tracks on the TiO_2 and T75H25 films were indistinguishable. For a scratch load of 1 kg, the scratch width was increased on all the test samples. Well-defined scratches were evident on all the film surfaces with little or no debris along the scratch edges. However, tranverse cracking was evident in all the scratches with the exception of the TiO_2 films. Also, the HA film displayed a high number of transverse cracks. A further increase in the scratch load to 5kg resulted in larger scratch widths, as expected on all the films. This also led to an increase in the severity of the transverse cracks as well as debris formation. However, the scratch width appeared to increase with the HA content.

HA/TiO_2 films, a scratch load of 0.5 kg caused poorly defined scratch tracks. No transverse cracking or debris were evident. An increase in the scratch load to 1 kg produced well defined scratches on all the film surfaces with little or no transverse cracking or debris with the exception of the 25ZH75 films. Raising the scratch load to 5 kg caused larger scratch widths with transverse cracking and debris. The scratch width also appeared to increase with the HA content, and the ZrO_2/HA appeared to display less damage than the TiO_2/HA films which was an indication of superior film cohesion and adhesion.

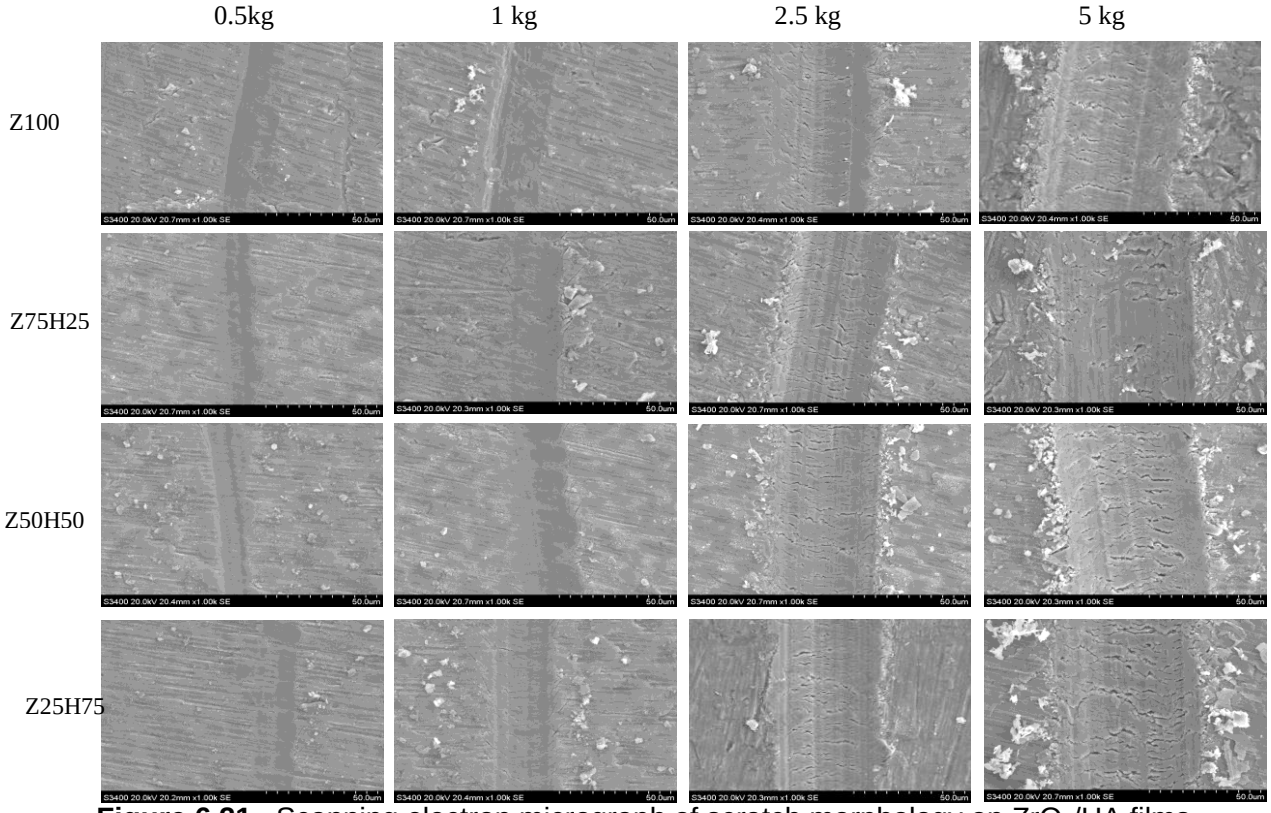

Figure 6.21 Scanning electron micrograph of scratch morphology on ZrO_2/HA films. The films were subjected to loads of 0.5 to 5 kg

Figure 6.21 shows the scratch morphology on the ZrO_2/HA films. Similarly to the HA/TiO_2 films, a scratch load of 0.5 kg caused poorly defined scratch tracks. No transverse cracking or debris were evident. An increase in the scratch load to 1 kg produced well defined scratches on all the film surfaces with little or no transverse cracking or debris with the exception of the 25ZH75 films. Raising the scratch load to 5 kg caused larger scratch widths with transverse cracking and debris. The scratch width also appeared to increase with the HA content, and the ZrO_2/HA appeared to display less damage than the TiO_2/HA films which was an indication of superior film cohesion and adhesion

6.9.2 Scratch width

Table 6.13 shows the variation of scratch width with HA composition of the TiO_2/HA and ZrO_2/HA films. For the TiO_2/HA films a scratch load of 0.5 kg, the scratch width was increased from 101 to 115 µm as the HA content was increased from 0 to 100 wt%. A scratch load of 1 kg gave a scratch widths in the range 146 to 165 µm as the HA content was increased from 0 to 100 wt%. Similarly for scratch loads of 2.5 and 5 kg, scratch widths of 233-257 µm and 335-377 µm respectively were obtained.

For the ZrO_2/HA films, a scratch load of 0.5 kg gave scratch width of approximately 72 to 115 µm as the HA content was increased whereas the scratch width obtained using a scratch load of 1 kg ranged from 117 µm to 146 µm. A further increase in scratch load increased the scratch width to 238 to 257 µm for a scratch load of 2.5 kg and 322 to 357 µm for a scratch load of 5 kg. In general, the scratch widths obtained on the ZrO_2/HA were lower than on the TiO_2/HA films.

Table 6.13 Comparison of scratch width on TiO_2/HA and ZrO_2/HA films subjected to scratch loads of 0.5 to 5 kg (n=15).

Surface	Scratch width (µm)			
	0.5 kg	1 kg	2.5 kg	5 kg
T100	101.3±5.6	146.8±9.6	233.4±13.5	335.6±9.4
T75H25	108.4±10.4	151.1±7.7	242.6±7.7	349.4±8.1
T50H50	110.7±11.6	152.7±12.9	247.4±12.9	349.9±20.4
T25H75	111.8±7.7	160.0±6.9	257.5±6.9	358.6±9.8
Z100	72.5±6.0	117.7±4.8	230.1±7.9	322.9±10.3
Z75H25	73.5±7.5	120.9±11.1	238.7±6.7	337.8±13.4
Z50H50	92.6±7.4	131.8±5.3	240.2±11.	340.4±9.0
Z25H75	108.7±9.8	136.9±7.7	250.2±15.4	354.6±11.7
H100	115.7±7.2	165.8±9.3	257.8±6.8	377.7±11.5

6.9.3 Scratch hardness

Table 6.14 Comparison of scratch hardness of HA/TiO_2 and HA/ZrO_2 films (n=15)

Film	Scratch hardness (μm)
T100	1.2±0.2
T75H25	1.1±0.1
T50H50	1.0±0.1
T25H75	1.0±0.2
Z100	1.9±0.1
Z75H25	1.8±0.3
Z50H50	1.5±0.2
Z25H75	1.4±0.2
H100	0.9±0.1

The scratch hardness was calculated for a scratch load of 1 kg which resulted in transverse cracking for most of the film surfaces. The scratch hardness of the films has been compared in **Table 6.14**. The results showed that the scratch hardness of the TiO_2/HA films was reduced by approximately 25% on increasing the HA content from 0 to 100 wt%. The scratch hardness of the ZrO_2/HA films was reduced by approximately 50% on increasing the HA content from 0 to 100 wt%. Furthermore, the scratch hardness of the ZrO_2/HA films was statistically higher than that of the TiO_2/HA films. These findings were in agreement with the results obtained from the scratch width measurements and were a strong indication that the presence of Z100 was more beneficial in the enhancement of the mechanical integrity of HA films.

6.10 Electrospray deposition of bioceramic bi layer and functionally graded films

Using the optimized spray parameters obtained from the HA suspension, buffer layer films were deposited by firstly electrospraying the T100 or Z100 suspensions for 10s. These were denoted as HA-TiO_2 and HA-ZrO_2 respectively. HA nano-particles were then deposited on the previously deposited bioceramic film for 50 s. Functionally graded films were deposited by sequentially electrospraying the 0-100 wt% HA suspensions for a duration of 12 s. These were then denoted as HA (TiO_2) and HA(ZrO_2) respectively. The estimated thickness of the bi-layer films and functionally graded films is summarized in **Table 6.15.** As shown the TiO_2-based films were slightly thinner than the ZrO_2-based films. The bi-layer films were also estimated to be thicker than the functionally graded films. However, the HA films were thicker then the two-phase films. The films obtained were subsequently annealed at 600 °C for 1 hr.

Table 6.15 Comparison of estimated thickness of bi-layer and functionally graded films (n=15)

Sample	Estimated thickness (μm)
HA	332.64±1.27
HA-TiO_2	280.68±10.74
HA (TiO_2)	289.53±10.90
HA-ZrO_2	182.90±0.90
HA (ZrO_2)	205.13±5.40

6.10.1 Film morphology

Figure 6.22 compares the morphology of the HA-TiO_2, HA (TiO_2), HA-ZrO_2, HA (ZrO_2) and HA films after annealing at 600 °C. The films displayed a similar morphology. The films were composed of a dense and continuous bottom layer with rough patches and occasional particle agglomeration. However the TiO_2 based films appeared to be marginally smoother than the ZrO_2 based films.

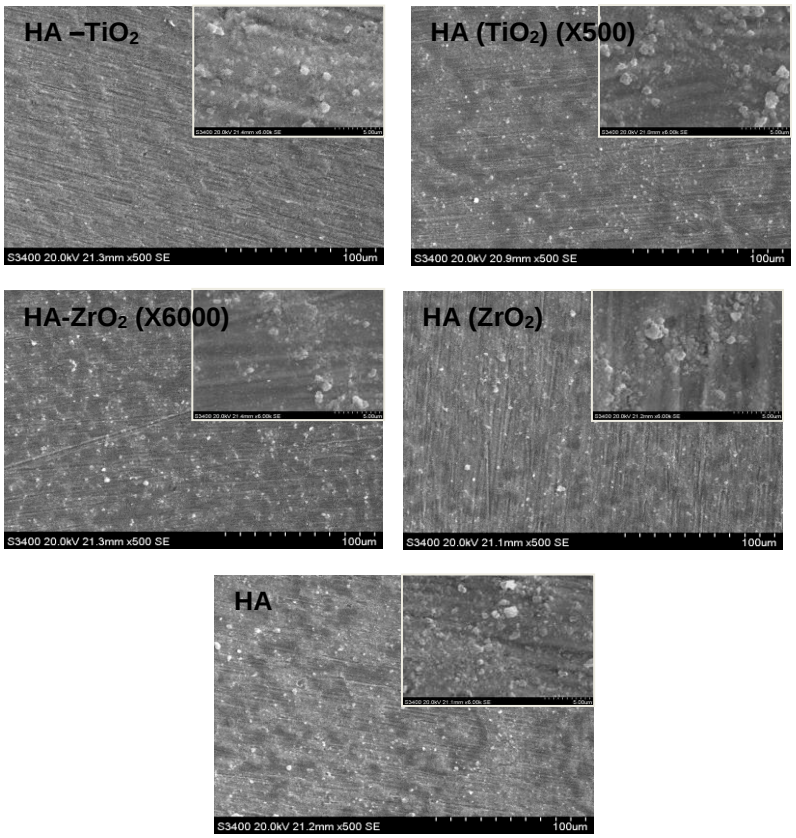

Figure 6.22 Scanning electron micrographs of two-layer and functionally graded bioceramic films

6.10.2 *In vitro* characterisation

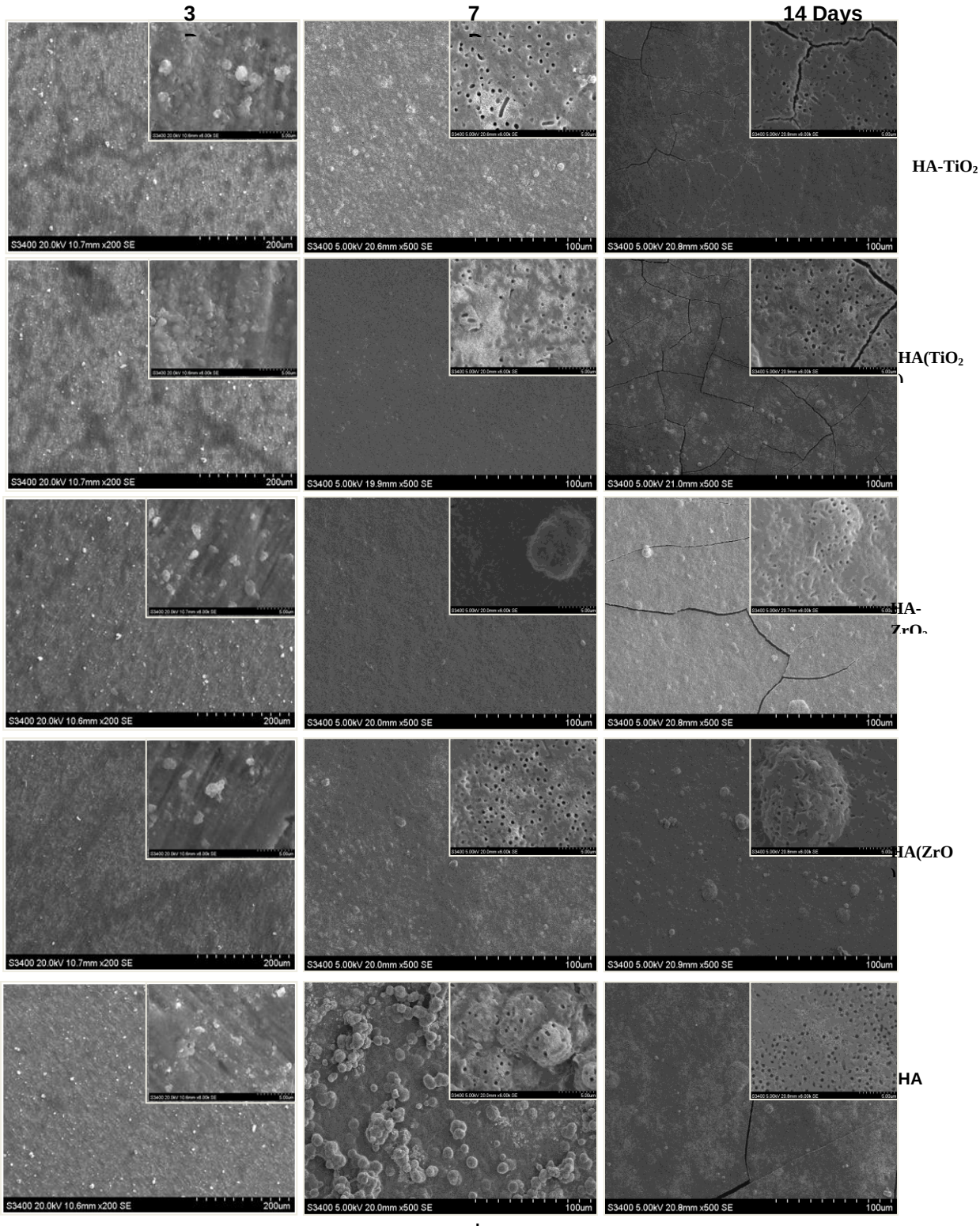

Figure 6.23 Scanning electron micrographs of HA-based two-layer and functionally graded films in comparison with HA after immersion in SBF for 3 to14 days

Figure 6.23 shows the morphology of the films after immersion in SBF. After an immersion period of 3 days, all the films displayed a similar morphology. All the films displayed a patchy but smooth and homogeneous surface layer on top of the granular HA layer. After an incubation period of 7 days, the HA-TiO_2 films displayed a relatively rough and globular surface layer. On close examination, the surface layer was slightly porous and smooth although the signature plate-like structures associated with apatite formation were visible in some regions beneath the smooth layer. A similar morphology was evident for the HA(TiO_2) and HA(ZrO_2) films. On the other hand, the HA-ZrO_2 film displayed a relatively uniform and featureless surface layer. In contrast, the HA film displayed a highly globular and porous surface layer. For an immersion period of 14 days, all the film surfaces displayed a globular and porous surface layer was observed. The surface layer also displayed occasional cracking. These results indicated that the TiO_2 and ZrO_2 based buffer layer and functionally graded films were highly bioactive. Moreover, there was no significant difference in the apatite initiation time of the films.

6.10.3 Scratch resistance

6.10.3.1 Scratch morphology

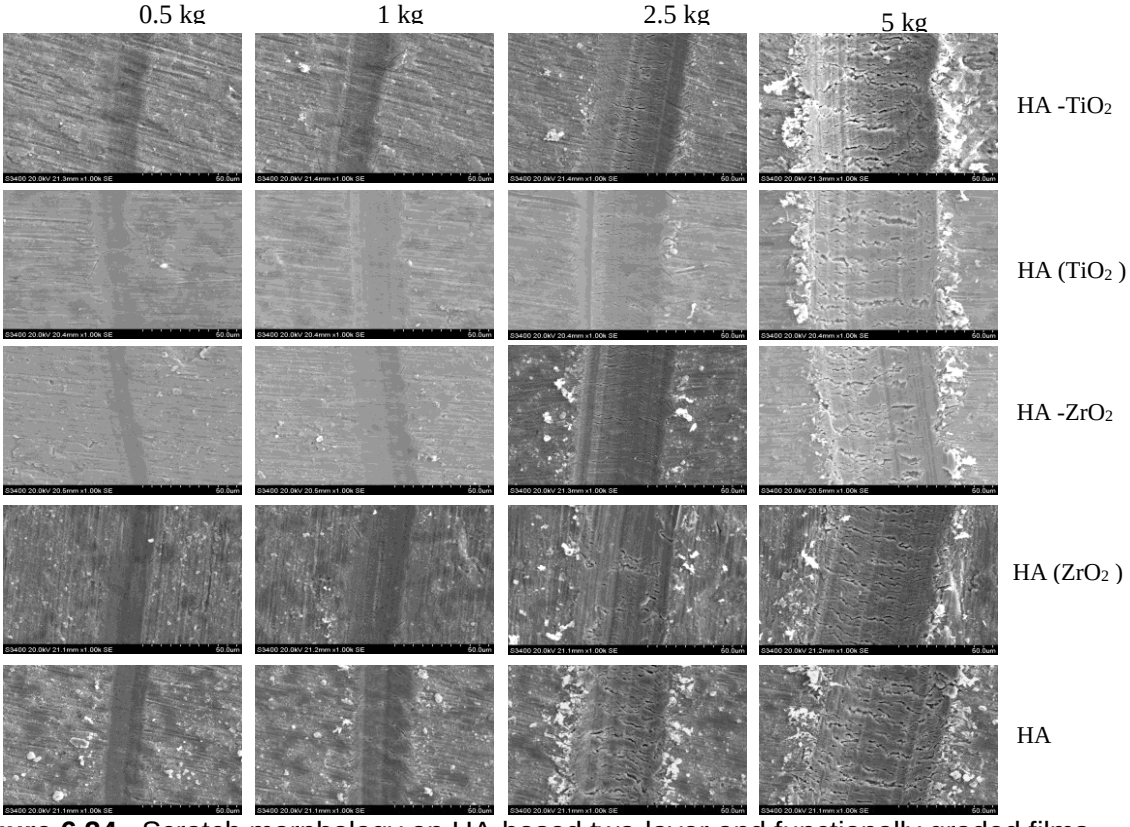

Figure 6.24 Scratch morphology on HA-based two-layer and functionally graded films subjected to scratch loads of 0.5-5 kg. HA films were used as controls.

The films were subjected to scratch loads of 0.5-5 kg as previously discussed. And the scratch morphology is shown in **Figure 6.24.** For a scratch load of 0.5 kg all the films displayed poorly defined scratch tracks with little or no debris. There was no transverse cracking along any of the scratch tracks. A similar scratch morphology was observed for a scratch load of 1 kg. On increasing the scratch load to 2.5 kg, the films displayed well-defined scratch tracks with transverse cracking. In particular, the HA films displayed a high number of transverse cracks. Particle debris was evident along the scratch tracks. A further increase in scratch load to 5 kg increased the scratch width. Additionally, the severity of the transverse cracks was increased.

6.10.3.2 Scratch width

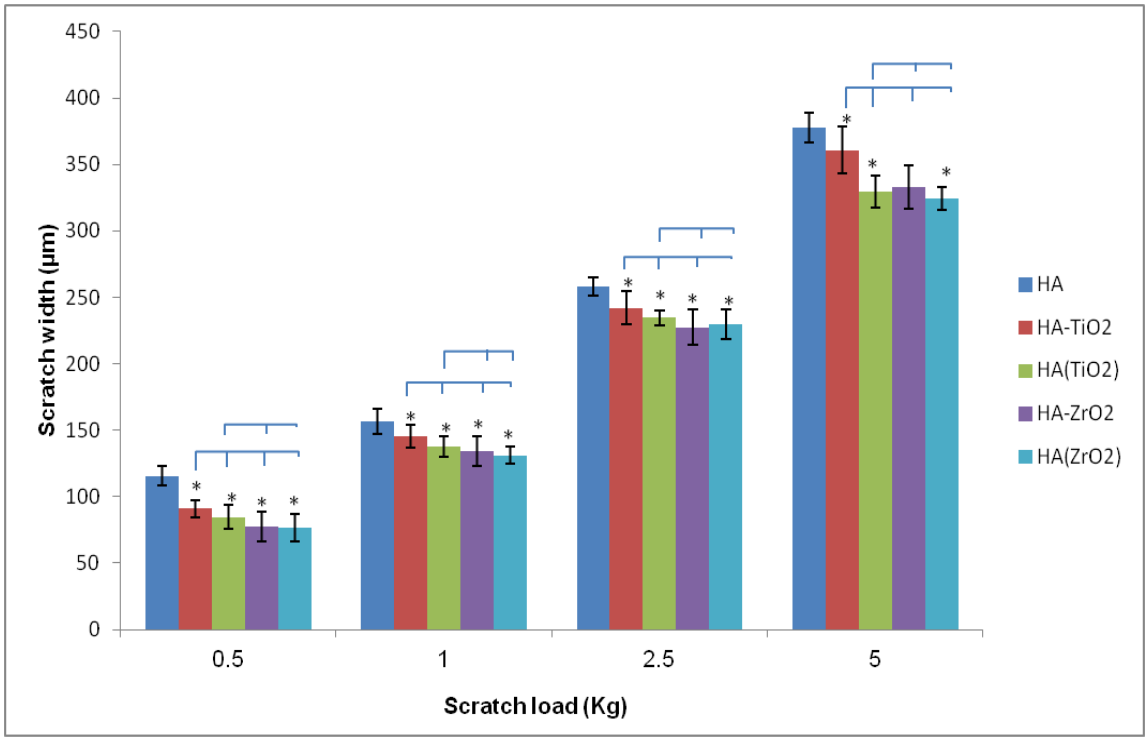

Figure 6.25 Scratch widths ontained on HA based two layer and functionally graded films subjected to loads of 0.5-5 kg. Results represent mean±s.d of triplicates obtained from 3 different experiments. 5 measurements were made for each sample (n=15) Asteriks (*) indicate a statistical difference compared with the HA films ($p<0.05$)

The scratch width obtained on the HA-based films is compared **in Figure 6.25**. For a scratch load of 0.5 kg, the HA film displayed a scratch width of approximately 115 µm. However, the scratch width was reduced to approximately 90µm for the HA-TiO_2 films and approximately 85 µm for the HA/TiO_2 film. The HA-ZrO_2 and HA /ZrO_2 films gave

mean scratch widths of 78 µm and 76 µm respectively. For a scratch load of 1 kg, the scratch width was in the range 131-146 µm and was in the order HA<HA-TiO_2<HA(TiO_2)<HA-ZrO_2<HA(ZrO_2). A similar trend was observed for the 2.5 and 5 kg scratch loads. These gave scratch loads in the range 229-257 µm and 333-377 µm for the 2.5 kg and 5 kg respectively.

6.10.3.3 Scratch hardness

The scratch hardness of the films is compared in **Table 6.16**. The scratch hardness of the films generally increased in the order HA<HA-TiO_2<HA(TiO_2)<HA-ZrO_2<HA(ZrO_2). This was in agreement with the scratch width measurements. This findings showed that a graded film with HA and ZrO_2 phase had superior scratch resistance.

Table 6.16 Scratch hardness of two-phase bioceramic films subjected to a critical load of 1 kg (n=15)

Film	Scratch hardness (GPa)
HA	0.9±0.2
HA-TiO_2	1.4±0.2
HA (TiO_2)	1.2±0.2
HA-ZrO_2	1.8±0.3
HA(ZrO_2)	1.4±0.1

6.11 Discussion

6.11.1 HA composition

The FTIR spectra obtained from the air dried HA powders was comparable to literature findings as reported by Rehman and Bonfield (1997) as well as Granados-Correas *et al*, (2010). From the FTIR spectrum it was evident that the precipitation reaction resulted in the synthesis of relatively phase pure HA powders. However, the presence of the carbonate ions was attributed to adsorption of CO_2 from the atmosphere as well as the water involved in the reaction. The nitrate ions were mainly due to the residual presence of NH_3 used to adjust the pH during the precipitation reaction. The presence of the OH vibrations was related to the crystal lattice OH groups and also indicated that water molecules also adsorbed on to the HA powders after the chemical reaction.

6.11.2 Liquid physical properties

As expected, the presence of the insulating nano-particles affected the liquid physical properties of the organic solvents. However, the variation in liquid physical properties of the HA (2-10 EG) suspension in comparison with the HA suspension were related to those of EG. Furthermore, the change in the liquid physical properties of the two-component suspensions with the increase in HA content suggested that the HA particles were heavier than the TiO_2 and ZrO_2 particles. The difference in particle weight could also explain the variation in the liquid physical properties of the TiO_2/HA and ZrO_2/HA suspensions.

6.11.3 Electrospraying of bioceramic suspensions

The results showed that the stable cone-jet regime was affected by the solvent composition. The higher maximum suspension flow rates of the HA (EG) suspensions in comparison with the HA suspension were primarily attributed to the higher surface tension and lower electrical conductivity of these suspensions which counteracted the effect of the increase in density as the maximum suspension flow rate is directly proportional to the surface tension and inversely related to the the electrical conductivity and density (Smith, 1986). A higher surface tension also increased the onset and maximal voltage since the applied voltage scales with the surface tension (Smith, 1986). The results also demonstrated that the stable cone-jet regime the two-component suspension were dependent on the phase composition. This was expected as an increment in HA content lowered the electrical conductivity but increased the surface tension which were the predominant factors affecting the flow rate and applied voltage regime. Thus the ZrO_2/HA suspensions gave higher maximum suspension flow rates compared to the TiO_2/HA suspensions.

The increase in average droplet relic diameter with EG and HA content was predominantly caused by the increase in density and reduction of electrical conductivity which overcame the effect of the increase in surface tension since the droplet diameter is directly proportional to the density and inversely proportional to the surface tension and electrical conductivity (Ganan-Calvo *et al,* 1997). Thus an increase in HA or etOH content possibly increased the jet diameter which gave larger droplets.

6.11.4 Morphology optimisation of two-phase bioceramic films

The scanning electron microscopy revealed that the morphology of the HA films was significantly different from that of the TiO_2 and ZrO_2 films. This was mainly attributed to

the effects of particle agglomeration. The high tendency of the HA particle agglomeration suggested that the HA powders had a comparatively high surface energy per unit weight. Agglomeration lowers the total surface energy to stabilize the system (Balachandran *et al*, 2001 and Miao *et al*, 2002). The cauliflower morphology of the HA films can be explained by the following mechanism: Initially, the droplets arriving at the substrate readily wetted the metal substrate which presented a lower surface tension resulting in a continuous and flat film. However, subsequent droplets were unable to adequately spread on the previously deposited HA layer due to an increase in surface tension. Consequently, the HA particles agglomerated resulting in the presence of discrete spherical particles on the film surface. The agglomerates acted as asperities of high curvature on the film surface and hence served as areas of preferential landing for subsequent droplets. The growing agglomerates finally met the neighbouring agglomerates, thereby rendering the cauliflower morphology as the deposition time was increased.

For a short spray distance larger droplets arrived at the substrate. However, due to slow spreading at the ceramic surface particle agglomeration occurred ultimately resulting in a highly rough and cauliflower like morphology. An increase in needle to substrate distance reduced the droplet size due to solvent evaporation. Hence particle growth did not occur which resulted in the deposition of flat and continuous layers with discrete particle agglomerates. For a low suspension flow rate such as 5 µl/min, smaller droplets were produced since the droplet diameter generally scales with the cube root of the flow rate. Therefore the smaller droplets produced underwent severe drying in flight due to their larger specific area, resulting in the deposition particle agglomerates at the substrate surface. Increasing the flow rate, increased the droplet diameter both in terms of liquid phase and HA content. The former improved the droplet spreading characteristics whereas the latter caused the growth of the particle agglomerates towards each other, which increased the film homogeneity.

The reduction in spray diameter due to the increase in EG concentration was attributed to the lower charge per unit mass as a result of the lower electrical conductivity of the suspensions which gave larger droplet diameters. Consequently there was a lower repulsive force between the droplets during flight. This reduced the droplet divergence and gave smaller spray diameters although the thickness was increased.

The lower surface roughness of the HA (EG) films was attributed to the reduction in volatility due to the interactions between EG with a boiling point of 197°C and etOH with a boiling point of 78°C. Thus droplets arriving at the substrate were relatively “wet”.

The amount of liquid phase decreased in the order HA (10EG)>HA (6EG)>HA (2EG). A higher amount of liquid phase enhanced the droplet spreading characteristics. Furthermore, larger droplets did not undergo preferential landing. This resulted in the deposition of more dense and continuous films with less agglomeration.

The higher roughness of the TiO_2/HA and ZrO_2/HA films with respect to the single component TiO_2 and ZrO_2 films was ascribed to the effects of surface tension at the substrate as well as suspension viscosity and particle agglomeration. For the T100 and Z100 suspensions, the droplets arriving at the substrate had a low viscosity and were therefore able to spread easily on the substrate as well as on the subsequently deposited oxide layer. On adding HA, the droplets arriving at the substrate became more viscous both due to the viscous nature of the initial suspensions as well as solvent evaporation. Thus although the initial droplets were able to spread easily on the metal substrate which presented a high surface tension, subsequent droplets were unable to spread easily on the previously deposited bioceramic layer. This was due to the high droplet viscosity and the low surface tension of the film. At the same time, the HA nano-particles had a high tendency to agglomerate. The higher thickness of the two-phase films with respect to the single phase films could be attributed to their higher viscosity and smaller spray area which was a result of the lower charge to mass ratio. The higher roughness of the ZrO_2/HA films with respect to the TiO_2/HA films was a direct consequence of the higher viscosity of the ZrO_2/HA suspensions which reduced the droplet spreading rate.

6.11.5 Phase composition of the two-phase bioceramic films

The Raman spectra of the TiO_2/HA and ZrO_2/HA films revealed that only HA, TiO_2 and ZrO_2 phases were present without the formation of other phases at the annealing temperature of 600°C, which suggested a high thermal stability of the HA, TiO_2 and ZrO_2 structures. This was in agreement with the results obtained using the powder samples but in contrast with the results of TiO_2/HA and ZrO_2/HA composite films obtained by other methods where additional compounds were observed. For example, Li *et al* (2003) reported the presence of CaO, α-TCP and $CaTiO_3$, following deposition of HA/TiO_2 films via HVOF spraying while Khor *et al* (2000) had earlier observed that plasma-sprayed HA/ZrO_2 films contained CaO, TCP, TTCP and $CaZrO_3$ in addition to HA and ZrO_2. The difference in the phase composition of the electrosprayed TiO_2/HA and ZrO_2/HA films and the literature findings could be explained by the difference in processing conditions. The thermal spray methods typically involve processing

temperatures involve temperatures of up to 10000°C which are much higher than the decomposition temperature of HA (~1100°C). The decomposition of HA results in the formation of CaO, TCP and TTCP. Mutual reaction between TiO_2 and CaO from HA at 1410 °C results in the formation of $CaTiO_3$ whereas the reaction between CaO and ZrO_2 resulted in the formation of $CaZrO_3$. The presence of CaO, TCP and TTCP reduces the stability of the composite films in physiological fluids, although $CaTiO_3$ and $CaZrO_3$ have been associated with the enhancement of the cohesive and adhesive strength of HA based films. Thus the annealing temperature of 600 °C was too low to cause the thermal decomposition of HA and also prevented the degradation of the mechanical properties of the metal substrate. However, the heat treatment also caused the pyrolysis of the organic residues from the films which explains the disappearance of the spherulites from the T100 and Z100 films after annealing at 600°C.

6.11.6 Surface properties of the two-phase bioceramic films

The surface roughness exhibited a positive correlation to the HA content. The higher surface roughness (R_a) of the two-component films with respect to the singe component films was related to the high agglomeration tendency of the HA phase and the difference in the film deposition mechanism due to the effects of viscosity. However, the films obtained in this research were rougher than the sol-gel composite films reported in the literature. For example, Harle *et al* (2006) obtained TiO_2/HA composite films with a surface roughness of approximately 0.22 µm whereas Kim *et al* (2005) reported on TiO_2/HA films with R_a parameters of 0.59-0.69 µm. The difference in film roughness could firstly be attributed to the difference in the deposition techniques. These authors reported on a combination of sol-gel synthesis and dipping, whereas sol-gel synthesis was combined with electrospraying in this study. The different film deposition techniques had different film formation mechanisms which could have resulted in different film morphologies. These authors also utilised higher quantities of TiO_2 (10-30 mol%), which could have affected the surface roughness.

The results showed that the ZrO_2 films were relatively hydrophobic in comparison to the TiO_2 films, which was in agreement with the findings of Takeda and Fukawa (2005). These authors noted that water contact angles of magnetron sputtered metal oxide films decreased in the order ZrO_2> CrO_x> TiO_2> SnO_2> SiO_2. As discussed in preceding sections, the water contact angle is affected by surface roughness as well as surface energy. However, there was no significant difference in surface roughness of

the electrospray ZrO_2 and TiO_2 films which indicated that the difference in hydrophilicity was not due to surface roughness but due to the surface chemical properties.

Metal oxides are well known for their tendency to adsorb organic compounds from the atmosphere. However, the adsorption of organic substances depends on the surface OH group density as the OH groups work as effective adsorption or reactive sites. The formation ability of the surface OH groups is dependent on the negative charge density on the oxygen atoms of the metal oxides. This parameter is highly influenced by the electronegativity of the metal atom. Hence, the binding energy of the electrons in a certain atom is highly influenced by the electronegativity of the atoms directly bound to the particular atom. Generally, the OH group density increases with the electronegativity difference between oxygen and the metal atom. It has been reported that Zr atoms are more electronegative than Ti atoms (Takeda and Fukawa, 2005). O_2 atoms have a lower binding energy in ZrO_2 than in TiO_2 which results in a higher oxygen negative charge density for ZrO_2 in comparison with TiO_2. Therefore it can be suggested that the electrosprayed ZrO_2 films had a higher surface OH group density than the electrosprayed TiO_2 films. This resulted in a higher degree of organic compound adsorption by the ZrO_2 films with respect to the TiO_2 films. The presence of the organic compounds reduced the wettability of the ZrO_2 films by obstructing the surface OH groups which promote wetting via the formation of hydrogen bonds with the water molecules.

The results also showed that the wettability of the composite films was enhanced by the presence of HA. For the TiO_2 and ZrO_2 films, the film wettability was mainly attributed to the presence of the surface hydroxyl groups, which encourage surface wetting by water due to hydrogen bonding and weak Van Der Waal's forces. However, the slightly higher water contact angle of the ZrO_2 films was an indication of a lower number of surface hydroxyl groups. In the presence of HA, the wettability was augmented by the presence of the Ca^{2+} and PO_4^{3-} ions which are highly hydrophilic components. An in increase in HA content also increased the surface roughness which further increased the interfacial area of contact with the wetting fluid.

6.11.7 *In vitro* characterisation of the two phase bioceramic films

6.11.7.1 SBF study

The apatite formation rate appeared to be affected by the HA content. The results showed that the apatite nucleation time was reduced by the presence of HA. This was

attributed to the difference in the apatite formation mechanism for the different bioceramics. For the TiO_2 and ZrO_2 films, bone-like apatite formation was attributed to the presence of the surface hydroxyl groups (Uchida *et al*, 2002 and Huang *et al*, 2005). The OH functional groups have isoelectric zero points at pH values much lower than 7 and thus are negatively charged upon immersion physiological fluids (Hanawa *et al*, 1998 and Kokubo *et al*, 2003). The surface potential of the oxide layers however, increases with soaking time up to a maximum positive value then decreases with soaking time and reaches a negative value again before converging to a constant negative value. The negatively charged Ti-OH and Zr-OH combine selectively with the Ca^{2+} ions in the fluid to form $CaTiO_3$ or $CaZrO_3$. As the Ca^{2+} ions accumulate at the surface, it gradually gains a positive charge. The positively charged surface subsequently combined with the negatively charged PO_4^{3-} ions to form CaP nuclei with lower surface energies. Once the CaP nuclei are formed, they grow spontaneously by consuming the Ca^{2+} and PO_4^{3-} in the surrounding fluid which is highly supersaturated with respect to apatite. The CaP phase spontaneously transforms into apatite which is the stable phase in the body environment (Kokubo *et al*, 2003). The Ti-OH and Zr-OH functional groups could also have provided effective epitaxial nucleation sites for the apatite crystals. For the HA films, the apatite nucleation and growth process was mainly due to two mechanisms which include dissolution and subsequent precipitation of ions between HA and SBF as well as a negatively charged surface. Immersing HA in SBF results in the dissolution of Ca^{2+} and PO_4^{3-} ions which increases the pH and the ionic activity product (IP).

The IP is obtained as follows;

$$IP=(\alpha Ca^{2+})10(\alpha PO_4^{3-})_6(\alpha OH^-)_2=(\gamma Ca^{2+})10(\gamma PO_4^{3-})_6(\gamma OH^-)_2\times[Ca^{2+}]10[PO_4^{3-}]_6[0H^-]_2 \quad (7.1)$$

Where α and γ are the activity and the activity coefficient and the square bracket is the ionic concentrations.

An increase in the IP value causes an increase in the degree of ionic supersaturation whereas the dissolution of the Ca^{2+} ions from the HA surface provides a surface with a low interface energy which facilitates the formation of apatite. According to classical nucleation theory, the rate of apatite nucleation can be enhanced by raising the degree of supersaturation or reducing the interfacial area. Therefore, on soaking the HA samples in SBF for 1 day, apatite formation is accelerated by both the high degree of superstauration and the low interface energy. Conseqently, the HA samples undergo

two processes, namely, the dissolution during the initial 24 h and the subsequent precipitation.

Immersion in SBF also causes an increase in the Ca/P ratio from 1.67 to 1.8 within 3 hrs and then decreases to 1.41 within 6 hrs. This results in the variation of the isoelectric zero point of the surface with soaking time. Initially, the HA surface is negatively charged. However, the surface potential increases to a maximum positive value within 3 hrs and then decreases rapidly to a negative value within 6 hrs before gradually converging to a constant negative value. The surface OH- and PO_4^{3-}ions selectively combine with the Ca^{2+} ions to form Ca-rich calcium phosphate. The accumulation of the Ca^{2+} ions at the surface induces an overall positive charge at the surface which combines with the PO_4^{3-} ions to form amorphous calcium phosphate with a low Ca/P ratio according to the equation

$$10\ Ca^{2+} + 6PO_4^{3-} + 2OH^- \rightarrow Ca_{10}(PO_4)_6(OH)_2 \qquad (6.2)$$

The amorphous CaP phase typically appears within 3 hrs of immersion and eventually converts in to bone-like apatite. These mechanisms explain the surface changes on the HA and HA-based two-layer and functionally graded films within 3-7 days of immersion in SBF. The formation of the apatite layer on the HA containing films was further enhanced by the roughness of the films since bone-like apatite is favourable in pores and chasms which offer a low interface energy (Huang, *et al*, 2007). The topographical undulations due to the particle agglomerates on the HA films provided pores in which the nucleation work was low.

For the TiO_2/HA and ZrO_2/HA films, the nucleation and growth of the bone-like apatite was affected by a combination of the surface hydroxyl groups, film roughness as well as the dissolution and precipitation of the HA phase. However, the greater coverage and thickness of the apatite layers on the TiO_2/HA films with respect to those on the ZrO_2/HA films suggested that the TiO_2/HA films had a shorter apatite nucleation time in comparison with the ZrO_2/HA films and was also implied that the TiO_2/HA films were more bioactive than the ZrO_2/HA films. This could firstly be ascribed to a difference in the number of surface hydroxyl groups as a high number of surface hydroxyl groups provides more adsorption sites for the Ca^{2+} ions (Li *et al*, 1994 and Hanawa *et al*, 1998). The longer apatite formation time of the ZrO_2/HA films was a further indication that the former had a lower number of surface hydroxyl groups. Also, it is possible that the TiO_2/HA films were more negatively charged than the ZrO_2/HA films on immersion in SBF since the isoelectric point of TiO_2 (pH=6) is lower than that of ZrO_2 (pH=6.7). On

the other hand, the complete apatite coverage on all the films after 21 days implied that there was no significant difference in the bioactivity of the TiO_2/HA and ZrO_2/HA in the longer term.

6.11.7.2 Cell culture studies

From the cell proliferation data, it was clear that the ZrO_2 films had a less stimulatory effect on the proliferation of the MG63 cells. This was in contrast to the results obtained by Zhang *et al* (2012). These authors reported that MG63 cells exhibited a better *in vitro* response to cathodic arc deposited ZrO_2 films in comparison to TiO_2 films in terms of proliferation and ALP secretion. A possible explanation for this discrepancy could be the difference in surface roughness. Zhang *et al* (2012) reportedly obtained a surface roughness of 0.256 nm for the ZrO_2 films whereas the TiO_2 films had a surface roughness of 0.054 nm. However, in this study, the difference in *in vitro* cellular response was mainly due to a difference in wettability as there was no significant difference in surface roughness of the ZrO_2 and TiO_2 films. The higher wettability of the TiO_2 films could have enhanced protein adsorption and subsequently initial cell attachment and proliferation. The TiO_2 films could also have been more negatively charged than the ZrO_2 films on immersion in cell medium which could have promoted interactions between the cells and the film surface.

The results further showed that the presence of HA caused an enhancement in the cell proliferation and a flattened cell morphology with several cytoplasmic processes. This was in agreement with literature findings by Kim *et al* (2005) and Harle *et al* (2006). These authors reported that the MG63 cell population was higher on the HA films as well as on the composite films with a higher HA content over a 4 day period. At the same time, the total protein secretion on the electrosprayed composite films was enhanced by the presence of HA. This was in agreements with the findings of Ramires *et al* (2001) who observed that the ALP activity as well as the collagen and osteocalcin secretion were higher in the composite films with a higher HA concentration. Elsewhere, Harle *et al* (2006) found that osteopontin secretion was up-regulated by an increase in HA content whereas Kim *et al* (2005) found that the ALP activity was enhanced by an increase in the HA content in the composite films. ALP is a known marker for osteogenic and osteoblastic cells which undergo sequential differentiation processes resulting in the eventual formation of bone. The catalytic activity of ALP enhances the secretion of other extracellular matrix proteins. Hence ALP is a marker for early osteoblast differentiation. Osteocalcin is a bone specific differentiation marker

which stimulates mineralization at a much later stage. Therefore the presence of HA in the electrosprayed films enhanced all aspects of the MG63 cell response from proliferation to expression of many phenotypes and mineralization all of which constitute the whole bone-formation process.

On the other hand, Kim *et al* (2004) reported that there was no significant difference in the cell proliferation on the HA films and the HA-TiO_2 two layer films. This was an indication that the initial cellular response was mainly affected by the film outer surface. Thus it was expected that there would be no significant difference in the cellular response on the electrosprayed HA based two layer and functionally graded films.

The enhancement in bioactivity of the TiO_2/HA and ZrO_2/HA in comparison to the single component TiO_2 and ZrO_2 films was attributed firstly to the wettability of the films surfaces which improved the interactions between the water based cell medium and the film surfaces resulting in enhanced protein adsorption. An increase in HA content also increased the surface roughness and provided more focal contacts for cell adhesion. The films were also probably negatively charged on immersion in the cell medium (pH=7.4) which resulted in electrostatic interactions between the film surface and the adhesion proteins and cells. Ca^{2+} could also have been released from the HA structure and penetrated the cell membrane thereby activating the cells as Ca^{2+} play a critical role in cell signaling by stimulating the expression of genes such as osteopontin which promote cell proliferation and differentiation (Jung *et al*, 2010) .

6.11.8 Scratch resistance of two-phase bioceramic films

The scratch resistance as quantified by scratch width measurements and scratch hardness declined with an increase in the HA content. Similar findings have also been reported elsewhere although different assessment techniques were used. Kim *et al* (2005) reported that the bond strength was increased from 37 MPa to 56 MPa due to the addition of 30 mol% TiO_2. More recently, Qiu *et al* (2010) noted that the tensile bond strength could be increased from 13.4 Pa to 24.2 MPa due to the presence of ZrO_2 whereas De-Jun *et al* (2012) reported that an increase in HA content reduced the bond strength of HA/ZrO_2 composite films from 20 N to 17.5 N. Therefore, the mechanical properties of HA films are generally improved by the presence of TiO_2 or ZrO_2 irrespective of the fabrication method. The strengthening mechanisms of TiO_2 and ZrO_2 are often mainly attributed to chemical bonding between HA and the toughening phase resulting in the formation of $CaTiO_3$ or $CaZrO_3$. However, the use of a low annealing temperature in the current research meant that these additional phases were

not formed. Therefore the strengthening mechanism of the TiO_2 and ZrO_2 phases was more likely due to dispersion strengthening of the tougher TiO_2 and ZrO_2 particles mixed with the HA phase. The strengthening effect of the toughening phases could also be attributed to the reduction in the mismatch in the coefficient of thermal expansivity (CTE). The CTE of HA is 15×10-6/°C whereas that of Ti alloy is 8.6×10-6/°C. The CTEs of TiO_2 and ZrO_2 are 9×10-6/°C and 7.3×10-6/°C, respectively. Therefore, the overall CTE of the films were reduced. The presence of TiO_2 and ZrO_2 reduced the occurrence of residual stresses which are known to bring about micro-cracking followed by a reduction in film cohesion and adhesion (Kim *et al*, 2005 and De-Jum *et al*, 2012).

A further aim of this research was to compare the scratch resistance of the composite films with the HA-based two layer and functionally graded films. The results showed that the latter were less susceptible to scratch penetration with respect to the former. However, Chou and Chang (2002) found that the HA-ZrO_2 two-layer films gave a higher tensile bond strength that the HA/ZrO_2 composite films. The superior enhancing effect of the two layer films was attributed to a combination of chemical bonding, a reduction in the CTE mismatch and a rougher buffer layer surface. On the other hand, the TiO_2 and ZrO_2 films obtained in the current research were significantly smoother than the underlying metal substrate which ruled out a higher degree of interlocking with the buffer layer as a strengthening mechanism. Therefore, the strengthening mechanism of the two-layer films in this research was mainly due to a reduction in the CTE mismatch whereas the functionally graded films were strengthened by a combination of dispersion strengthening and a reduction in the CTE mismatch. Moreover, for the functionally graded films, the change in film composition was gradual which in turn resulted in a more gradual change the film properties through the film depth. Therefore these films displayed a lower susceptibility to scratch in comparison with the other films,

Generally, the ZrO_2/HA films were slightly superior to the TiO_2/HA films in terms of scratch resistance. This was a direct consequence of the lower CTE and superior hardness and fracture toughness of ZrO_2.

6.12 Conclusions

Novel TiO_2/HA and ZrO_2/HA films were successfully prepared by electrospraying. The liquid physical properties of the suspensions were affected by the HA content which in turn influenced the electrospray process. The maximum suspension flow rate, applied

flow rate and average droplet relic diameter were increased by an increment in HA content. The surface roughness and wettability of the films were increased by the HA content. This improved the *in vitro* response of the films in terms of bone-like apatite nucleation and the initial cellular response. However, an increase in HA content also caused a decline in the integrity of the films as evidenced by the scratch hardness. However, the HA/TiO_2 composite films were considered to be more suitable for use in biomedical applications due to their reasonable bioactivity and scratch resistance. In particular, a film composition of 50 wt% TiO_2:50 wt% HA was considered to offer a good combination of bioactivity and scratch hardness.

Novel electrosprayed HA-based two-layer and functionally graded films were also synthesized. The bioactivity of these films was comparable to that of the single layer HA films. Furthermore, these films displayed enhanced film cohesion in comparison to the latter. A graded film with the HA and ZrO_2 phases gave an optimum combination of bioactivity and mechanical integrity.

Chapter 7 Conclusions and future work

7.1 Conclusions

The investigations and results of this thesis revealed the following;

On the electrospray processing of TiO_2 films

The electrospray depsotion of 2-8 wt% TiO_2 sols was studied. The electrospray process was greatly influenced by the sol concentration and the needle internal diameter. An increase in the needle internal diameter or sol concentration increased the range of sol flow rate for electrospraying in the stable cone-jet mode and also increased the applied voltage. This could be useful when upscaling the electrospray process for the preparation of TiO_2 films as the film deposition time could be reduced, thereby improving the process efficiency.

The morphology of the TiO_2 films was affected by apparatus-related depositon parameters, such as needle to substrate distance, sol flow rate, and deposition time as well as sol-related parameters, such as the solvent carrier and sol concentration. Uniform and crack-free TiO_2 films were obtained on electrospraying 2 wt% TiO_2 sols with a needle internal diameter of 300 µm set at a needle to substrate distance of 20 mm and a sol flow rate of 5 µl/min. However, under the optimized electrospray parameters, the prOH solvent gave dense and continuous films whereas etOH gave fractal-like but homogeneous films. Therefore, the morphology of the electrospray TiO_2 films can be effectively controlled by varying the organic solvent carrier and deposition parameters in order to obtain different.morphologies for various applications.

The film properties such as phase composition, surface roughness and wettability were affected by annealing temperature; an increase in annealing temperature from 300 to 600 °C increased the film crystallinity and surface roughness and also enhanced the wettability. The use of different organic solvents had no significant effect on the phase composition but affected the surface roughness and water contact angles were affected. Thus the physical properties of electrospray TiO_2 films can be controlled by varying the organic solvent carrier during TiO_2 synthess or carrying out post deposition heat treatment.

The initial cellular response in terms of cell attachment and proliferation was enhanced by increasing the annealing temperature and also indirectly affected by solvent type. An annealing temperature of 600 °C had the highest stimulatory effect on the

proliferation of MG63 cells and facilitated better initial attachment of the osteoblast-like cells. The TiO_2 films deposited using etOH as a solvent carrier also displayed a better initial cellular response. Thus, the biocompatibility of electrospray TiO_2 films can be improved by varying the organic solvent carrier during TiO_2 synthess or carrying out post deposition heat treatment.

The scratch resistance of the TiO_2 films was enhanced by an increase in annealing temperature. The films annealed at 600 °C displayed the lowest scratch width and hence the highest scratch hardness. The films deposited using the etOH solvent also displayed a higher resistance to scratch penetration than those deposited using the prOH solvent carrier. Hence, the mechanical integrity of electrospray film can be controlled by subjecting the electrospray TiO_2 films to post deposition heat treatment or by using etOH as a solvent carrier.

Electrospray TiO_2 films deposited using etOH as a solvent carrier followed by annealing at 600°C are more favourable for MG63 attachment and proliferation and also give improved mechanical integrity.

On deposition of ZrO_2 films

2 wt% ZrO_2 sols were prepared by varying the precursor type. There was no significant difference in the liquid physical properties obtained using the ZrO_2 precursors. The ZrO_2 sols were successfully atomised using the stable cone-jet modefor a range of flow rates and applied voltage. Although, there was no significant difference in the average droplet relic diameter and applied voltage obtained using the different sols, the ZE2 sol obtained using the zirconium isopropoxide isopropanol complex as a precursor gave a higher maximum sol flow rate compared to the ZEP2 sol obtained using zirconium (IV) propoxide as a precursor. Thus, the electrospray process could be varied by using different precursors. The zirconium isopropoxide isopropanol complex precursor was considered to be more beneficial from a processing point of view.

The ZrO_2 morphology was affected by the deposition parameters. Uniform substrate coverage and defect free morphology were obtained at a sol flow rate of 5 µl/min and a needle to substrate distance of 20-30 mm over a duration of 120-180 s. However, the ZE2 sol generally gave dense and continuous films whereas the ZEP2 sol gave uniform and fractal-like films. Therefore, the morphology of the electrospray ZrO_2 films

can be controlled by the utilization of different starting precursors in addition to varying the deposition parameters.

The films were mainly composed of monoclinic and tetragonal phase. There was a slight variation in the surface roughness and water contact angles. Thus there was no significant difference in the chemical and physical properties of ZrO_2 films as a result of the utilization of different precursors.

The ZrO2 films were biocompatible inasmuch as they promoted the initial attachment and proliferation of osteoblast-like cells. However, the films obtained using zirconium (IV) propoxide (ZEP2 sol) had a greater stimulatory effect on the MG63 cells in terms of cell proliferation compared to the films obtained using the zirconium propoxide isopropanol complex precursor (ZE2 sol). Furthermore, ZEP2 films gave smaller scratch widths and hence, higher scratch hardness compared to the ZE2 films. Thus films deposited using the zirconium (IV) propoxide precursor were more favourable in terms of mechanical integrity and *in vitro* biocompatibility.

On deposition of two-phase composite films

HA nano-particles were successfully synthesized and a range of HA suspensions prepared. The liquid physical properties were affected by the composition of the organic solvent-carrier. This in turn affected the electrospray process. The applied voltage and maximum suspension flow rate were increased by the use of a less volatile organic solvent such as ethylene glycol (EG). Hence, the efficacy of the electrospray processing of HA suspensions can be improved by varying the composition of the organic solvent carrier as higher flow rates can reduce the deposition time. This could be advantageous when upscaling the electrospray process for industrial applications.

The morphology of the HA films was also affected by the deposition parameters. Uniform surface coverage was achieved by electrospraying the HA suspensions with a needle of internal diameter 500 µm at a flow rate of 10 µl/min and a needle to substrate distance of 30 mm for 60s. However, the morphology of the electrospray HA films varied from highly porous to highly dense depending on the composition of the organic solvent. Thus, the morphology of electrospray HA films can be effectively controlled by changing the deposition parameters and varying the solvent composition in order to obtain the desired porosity.

The two-phase TiO_2/HA and ZrO_2/HA suspensions were successfully prepared. The liquid physical properties were affected by the HA content, which in turn influenced the

electrospray process. The maximum suspension flow rate and applied voltage were elevated to higher values, whereas the average droplet relic diameter was increased. Dense and uniform films were obtained at a flow rate of 10 µl/min and a needle to substrate distance of 20 mm and a spray duration of 60s. The surface roughness was increased by the HA content whereas the water contact angles were reduced.

All the films were able to initiate the formation of bone-like apatite upon immersion in SBF. However, the nucleation time was reduced by the presence of HA.The initial cellular response was also enhanced by the presence of HA. Consequently, an increase in HA content resulted in higher cell proliferation and protein secretion. Hence the biocompatibility of the electrospray TiO_2 and ZrO_2 films can be improved by the addition of HA.On the other hand, the TiO_2/HA films had a greater stimulatory effect on the initial cellular response compared to the ZrO_2/HA films. Hence the TiO_2/HA system is more favourable for biomedical applications in terms of bioactivity.

The scratch resistance was adversely affected by the presence of HA. The scratch width was increased by an increase in HA content which in turn reduced the scratch hardness. The ZrO_2/HA films generally exhibited lower scratch widths and highr scratch hardness. Hence the ZrO_2/HA system was considered to be more favourable in terms of mechanical integrity. However, the T50H50 films were gave a good compromise in terms of bioactivity and scratch resistance.

HA-based bi-layer and functionally graded films were successfully electrosprayed and displayed a rough surface morphology and were able to initiate the formation of bone-like apatite and there was no significant difference in the apatite nucleation time. Hence, the bioactivity of the electrospray bi-layer and functionally graded films was comparable to that of the electrospray HA films.

The HA-based bi-layer and functionally graded films also exhibited enhanced resistance to scratch when compared to the composite films. However, the functionally graded films displayed higher scratch hardness compared to the bi-layer films. Moreover, the HA-based ZrO_2 films exhibited a lower susceptibility to scratch indentation. Thus the mechanical integrity of the HA films could further be enhanced by grading the film composition with ZrO_2 as a secondary phase. A functionally graded ZrO_2 and HA film gave superior mechanical integrity.

7.2 Future work

Based on the research carried out and the outcome of this thesis, the following recommendations can be made for future work.

As the sol-gel synthesis of TiO_2 and ZrO_2 using different organic solvents and precursors resulted in sols with different liquid physical properties, the effect of the former on the particle shape and diameter of the final product should be investigated. The influence of the presence of additives, such as stabilizing agents on the particle characteristics should also be determined. The particle characteristics could also be changed by utilizing a wider range of organic solvents, oxide precursors and stabilizing agents. The influence of the sol concentration on the particle characteristics should aso be established.

Since the liquid physical properties affect the electrospray process, the effect of the powder particle characteristics on the latter should be determined. Electrospray mode maps should be plotted in order to establish the particle characteristics that would give the largest operating flow rate and (or) voltage regime, and provide more versatility for the upscaling of the electrospray process for the industrial application. Similarly, the influence of particle characteristics on the film morphology should be examined. Furthermore, the effect of particle characteristics, solvent type and additive type on the film thickness should be assessed since the latter plays a critical role in determining the longevity of the films in terms of bioactivity and mechanical integrity.

Based on the advantages of HA sols in comparison with suspensions, for example aging stability, the sol-gel process can be extended to the synthesis of HA nano-particles. A range of sol concentrations should be prepared and compared in terms of liquid physical properties and particle characteristics. Electrospray mode maps should also be plotted and the HA film morphology optimized through varying the deposition parameters such as needle to substrate distance, spray time, flow rate and concentration. The optimal HA sol should also be compared with an HA suspension of a similar concentration. Additionally, the HA sols could be utilized in the synthesis of the two-phase sols.

In this research, the annealing temperature was set at 600°C based on the studies conducted on the TiO_2 films. However, the ZrO_2 and HA films should be annealed at a range of temperatures in order to establish the effect of temperature on the film morphology and phase composition as well as the bioactivity and mechanical properties.

The film morphology of electrospray films can also be affected by the substrate temperature during film deposition. Therefore, the influence of substrate temperature on the film morphology should be investigated for each different bioceramic. The main aim would be to establish the substrate temperature at which uniform and defective films could be obtained.

The SBF studies should be expanded to account for the influence of factors such as sol concentration, annealing temperature and particle characteristics on the ability to initiate the nucleation of bone-like apatite. The stability of the bioceramic films should be investigated by conducting ion leakage studies on immersion in SBF.

In this research it has been demonstrated that the proliferation of the MG63 osteoblast-like cells was enhanced by the annealing temperature of the TiO_2 films and the HA content in the HA/TiO_2 or HA/ZrO_2 films. Additionally, the total protein secreted by the cells was affected by the HA content. However, the influence of the aforementioned parameters on the other cellular functions such as differentiation and mineralization by measuring the ALP and osteocalcin secretion. Cell viability should also be investigated by carrying out live-dead staining and cell counting. The influence of factors such as particle characteristics and sol concentration should be assessed. Such studies would provide a more comprehensive understanding of the *in vitro* cellular response to the electrospray bioceramic films.

The SBF studies conducted on the HA/TiO_2 and HA/ZrO_2 functionally graded films and the HA-TiO_2 and HA-ZrO_2 two layer films showed increased apatite formation which suggested that these films have the ability to promote tissue growth and bond to living bone *in vivo.* However, these films should be compared with the composite films and the single phase HA, TiO_2 and ZrO_2 films by carrying out a systematic set of experiments involving cell culture work. Osteoblast-like cells could be seeded on to the films and experiments carried out over a 21 day period to observe the cell attachment, viability, proliferation and mineralization in order to confirm their suitability to promote bone tissue growth.

Good antimicrobial properties of the bioactive films are critical for the prevention of infection at the implantation site. Therefore, it is suggested that a systematic characterization of the antimicrobial properties of the electrosprayed bioceramic films needs to be carried out. The films should be inoculated with suspensions containing bacteria such as staphylococcus aureus and Escherichia coli which are frequently implicated in infections at implantation sites. The influence of factors such as annealing temperature, particle size and HA content on the rate of bactericide over a period of 24

hrs could be assessed. Additionally, the antimicrobial properties of the electrospray bioceramic films could be compared with those of the bioceramic nano-particles.

Since the wettability and ultimately the bioactivity of the TiO_2 and ZrO_2 films were attributed to the presence of surface hydroxyl groups, XPS studies could be conducted to characterize the surface density of the OH groups. The film wettability could also be enhanced by irradiating the samples with UV light and varying the wavelength and irradiation time and determining the effect on the *in vitro* biocompatibility and antimicrobial properties.

Animal studies are a powerful tool in the determination of implant behavior *in vivo*. Therefore *in vivo* can be carried out in order to further verify the biocompatibility of the electrosprayed bioceramic films. The electrospray process could firstly be adapted for film deposition on cylindrical substrates. The *in vivo* characteristics of the coated rods should be studied by implantation in the femurs of an animal model for example mini pigs. The bone tissue reaction of the implants should then be investigated on extracting the implants after a given implantation period. Histological examination could then be carried out and the bone to implant contact area measured. Pull out tests could also be carried out in order to determine the bond strength at the bone-implant interface.

The interfacial bonding strength of the bioactive coating to the substrate is also critical in determining the longevity of the implant *in vivo*. It is therefore suggested that the adhesive and cohesive strength of the bioceramic films is comprehensively and quantitatively characterized by measuring the critical load during scratch testing that is required to remove the films from the substrate. The influence of annealing temperature, thickness and HA content should be assessed.

Based on the previous studies, the Young's modulus and fracture toughness of the electrospray bioceramic films should be assessed and compared, in order to fully establish the mechanical properties of the electrospray films.

References

Abbas, M.A., and Latham, J. (1967) The instability of evaporating charged drops. *Journal of Fluid Mechanic*s, **30**, 663-670.

Aebli, N., Krebs, J., Stich, H., Schwalder, P., Walton, M., Shwenke, D., Gruner, H., Gasser, B., and Theis, J.C., (2003) Iin vivo comparison of the osseointegration of vacuum plasma sprayed titanium and hydroxyapatite-coated implants, *Journal of Biomedical Materials Research*, **66A**, 356-363.

Adachi, S., Arai, T. and Kobayashi, K. (1996) Chemical treatment of Si (1 1 1) surfaces in F-based aqueous solutions. *Journal of Applied Physics*, **80**, 5422-5426.

Aisa, M.C., Rahman, S., Senin, U., Maggio, D. & Russell, R.G. (1996) Cathepsin B activity in normal human osteoblas-like cells and human osteoblastic osteosarcoma cells (MG-63): regulation by interleukin-I beta and parathyroid hormone. *Acta Biochemistry and Biophysics* **1290**: 29-36.

Anseleme, K., Bigerelle, M., Noel, B., Dufresne, E .M ., Judas, D., Lost, A., and Hardouin, P. (2000) Qualitative and quantitative study of human osteoblast adhesion on materials with various surface roughnesses, *Journal of Biomedical Materials Research*, **49A**, 155-166.

Anseleme, K. and Bigerelle, M. (2005) Topography effects of pure titanium substrates on human osteoblast long term adhesion, *Acta Biomaterialia*, **1**, 211-222.

Anseleme, K., Ponche, A. and Bigerelle, M. (2010) Relative influence of surface topography and surface chemistry on cell response to bone implant materials. Part 2: Biological aspects. *Proceedings of the Institute of Mechanical Engineering, Part H, Engineering in Medicine*, **224**, 1487-1507.

Bachiller-Baeza, B., Rodriguez-Ramos, I. and Guerrero-Ruiz, A. (1998) Interaction of carbon with the surface of zirconia polymorphs. *Langmuir*, **14**, 3556-3564.

Bachle, M. & Kohal, R.J. (2004) A systematic review of the influence of different titanium surfaces on proliferation, differentiation and protein synthesis of osteoblast-like MG63 cells. *Clinical Oral Implant Research* **15**: 683-692.

Balachandran, W., Ahmad, C..N., and Machowski, W. (1992) Electrostatic atomization of conducting liquids using AC superimposed on DC field. *Conference record of the 1992 IEEE industry applications society annual meeting*, **2**, 1369-1373.

Balachandran W, Miao P and Xiao P. (2001) Electrospray of fine droplets of ceramic suspensions for thin film preparation. *Journal of electrostatics*, **50**, 249-263.

Baur, W.H. (1961) Atomabstande und Bindungswinkel im Brookit, TiO_2. *Acta Crystallographica,* **14**, 214-216.

Bauer G. (1990) Biomechanical aspects of osseointegration. *Handbook of bioactive ceramics, Florida*, CRC press, 81-97.

Behnajady, M.A., Eskanderloo, H., Modirshala, N., and Shokir, M. (2011) Investigation of the effect of sol-gel synthesis variables on structural and photocatalytic properties of TiO_2 nanoparticles. *Desalination*, **278**, 10-17.

Berndt, C.C and Lin, C.K. (1993) Measurement adhesion for thermally sprayed materials. *Journal of adhesion science and technology*, **7**, 1235-1264.

Bezrodna, T., Puchovska, G., Shimanovska, V. and Baran, J. (2004) 5CB liquid crystal as a specific probe for surface studies of metal-doped TiO_2 (anatase) nanoparticles. *Molecular Crystals and Liquid Crystals,* **413**, 71-80.

Blalock, T.L., Bui, X., Naragon, R. and Robiei, A. (2008) Effect of substrate temperature on mechanical properties of calcium phosphate coatings. *Journal of biomedical materials research B; Applied biomaterials***, 85**, 60-67.

Bokhimi, X., Morales, A., Novaro, O., Portilla, M., Lopez, T., Tzompanizi, F. and Gomez, R. (1998) Tetragonal nanophase stabilization in non-doped sol-gel zirconia prepared with different hydrolysis catalysts, *Journal of Solid State Chemistry*, **135**, 28-35.

Bonfield, W. (1988) Composites for bone replacement. *Journal of Biomedical Engineering*, **10,** 522-526.

Boyan, B.D., Schwartz, Z., Bonewald, L.F. & Swain, L.D. (1989) Localization of1,25-(OH)2D3-responsive alkaline phosphatise in osteoblast-like cells (ROS17/2.8, MG63 and MC3T3) and growth cartilage cells in culture. *Journal ofBiological Chemistry* **264**: 11879-11886

Branzoi, V., Loroc, M., Branzoi, F., Sbarcea, G. and Marinesco, V. (2010) Surface characterization and electrochemical behaviour of non biomedical Zr-based metal/ceramic composite in fetal bovine serum, *Roumaine de Chimie*, **55**, 585-597.

Breme J, Zhou Y and Groh L. (1995) Development of a titanium alloy suitable for an Optimised coating with Hydroxyapatite, *Biomaterials*, **16**, 239-244.

Brossa F, Cigada A, Chiesa R ,Parachini L, and Consonni C. (1994) Post deposition treatment effects on hydroxyapatite vacuum plasma spray coatings. Journal *of Materials Science; Materials in Medicine*, **5**, 855-857.

Browne, M. and Gregson, P.J. (2000). Effect of mechanical surface pre-treatment on metal ion release, *Biomaterials*, **21**, 385-392.

Calleja, G., Serrano, P.D., Sanz, R., Pizzaro, P. and Garcia, A. (2004) Study on the synthesis of high surface area mesoporous TiO2 in the presence of non ionic surfactants. *Industrial Engineering Chemistry Research*, **43**, 2485-2492.

Caracoche, M.C., Rivas, P.C., Cervera, M.M., Caruso, R., Benavides, E., de Sanctis, O. and Escobar, M.E. (2000) Zirconium oxide structure prepared by the sol-gel route;1, Role pf the alcoholic solvent, *Journal of the American Ceramic Society*, **83**, 377-384.

Chang E., Chang W.J., Wang B.C. and Yang C.Y. (2001) Plasma spraying of zirconia-reinforced hydroxyapatite composite coatings on titanium Part I: Phase, microstructure and bonding strength. *Journal of materials science; Materials in science*, **8**, 193-200.

Charnley, J. (1972) The long term results of low friction arthroplasty of the hip performes as a primary intervention. *Journal of Bone and Joint Surgery*, **54 B**, 61-76.

Chen, D. R., Pui, D. Y. H., and Kaufman, S. L. (1995) Electrospraying of conducting liquids for monodisperse aerosol generation in the 4 nm to 1.8μm diameter range. *Journal of Aerosol Science*, **26**, 963-977.

Chen, C.H., Kelder, E.M., van der Put, P.J.J.M., and Schoonman, J (1996) Morphology control of thin LiCoO2 films fabricated using the electrostatic spray deposition (ESD) technique. *Journal of Materials Chemistry*, **6**, 765-771.

Chen, C.H., Emond, M.H.J., Kelder, E.M., Meester, B., and Schoonman, J. (1999) Electrostatic sol-spray deposition of nanostructured ceramic thin films. *Journal of Aerosol Science*, **30**, 959-967.

Chen C.C., Huang T.H., Kao C.T. and Ding S.J. (2006) Characterization of Functionally Graded Hydroxyapatite/Titanium Composite Coatings Plasma-Sprayed on Ti Alloys. *Journal of Biomedical Materials Research Applied Biomaterials,* **78B**: 146–152, 2006.

Chen, C.H., Kelder, E.M., Jak, M.J.G. and Schoonman, J. (1996) Electrostatic spray deposition of thin layers of cathode aterials for lithium battery, *Solid State Ionics*, **86-88**, 1301-1306.

Chen, C. Kelder, E.M., Van der Put, P.J.J.M, and Schoonman, J. (1996) Morphology control of thin LiCoO2 films fabricated using the electrostatic spray deposition (ESD) technique, *Journal of Materials Chemistry*, **6**, 765-771.

Choi J.M., Kim H.E. and Lee I.S. (2000) Ion beam assisted deposition of Hydroxyapatite coating layer on Ti based metal substrate. *Biomaterials*, **21**, 469-473.

Chou, B.Y. and Chang, E. (1999) Microstructural haracterization of plasma sprayed hydroxyapatite 10 wt% ZrO_2 composite coating on titanium, *Biomaterials,* **20**, 1823-1832.

Chou B.Y. and Chang E. (2001) Interface investigation of plasma sprayed hydroxyapatite coating on titanium alloy with ZrO_2 intermediate layer as bond coat. *Scripta materialia*, **45**, 487-495.

Chou B.Y. and Chang E. (2002A) Plasma sprayed Zirconia bond coat as an intermediate layer for Hydroxyapatite coating on titanium alloy substrate. *Journal of materials science; materials in medicine*, **13**, 589-595.

Chou, B.Y. and Chang, E. (2002) Plasma sprayed hydroxyapatite coating on titanium alloy with ZrO_2-second phase and ZrO_2 intermediate layer. *Surface and Coatings Technology*, **153,** 84-92.

Chung, C.J, Su, R.T, Chu, H.J., Chen, H.T., Tsou, H.K. and He, J.L (2013) Plasma electrolytic oxidation of titanium and improvement in osseointegration, *Journal of Biomedical Materials Research*, **101 B**, 1023-1030.

Cigada A., Chiesa R., Parrachini L. and Consonni C. (1993) Adhesion properties of plasma sprayed hydroxyapatite coatings for orthopaedic prostheses. *Biomedical materials and engineering,* **3**, 127-136.

Cimpean, A., Popescu, S., Ciofragecho, C.M.and Gleizes, A.N.(2011) Effects of LP-MOVCD prepared TiO_2 thin films on the *in vitro* behavior of gingival fibroblasts. *Materials Chemistry and Physics*, **125**, 485-492.

Clarke, I. and Allen, G. (2000) Clinical and hip simulator comparisons of ceramics on polyethylene and metal on polyethylene wear, *Clinical Orthopaedics and Related Research*, **379**, 34-40.

Cleries L.,Fernandez-Pradas J.M., Sardin G. and Morenza J.L. (1998) Dissolution behaviour of calcium phosphate coatings obtained by laser ablation*. Biomaterials*, **19**, 1483-1487.

Cloupeau M. and Prunet-Foch B. (1989) Electrostatic spraying of liquids in cone-jet mode. *Journal of Electrostatics*, **22**, 135-159.

Cloupeau M. and Prunet-Foch B. (1990) Electrostatic spraying of liquids: main functioning modes. *Journal of Aerosol science*, **25**, 165-184.

Cloupeau, M. and Prunet-Foch, B. (1994) Electrohydrodynamic spraying functioning modes: a critical review. *Journal of aerosol science*, **25**, 1021-1036.

Clover, J. & Gowen, M. (1994) Are MG63 and HOS TE85 human osteosarcoma celllines representative models of the osteoblastic phenotype?*Bone* **15**: 585-591.

Cook, S.D., Thomas, K.A., Delton, J.E., Volkman, T.K., Whitecloud, T.S. and Key, J.F. (1992) Hydroxyalpatite coating of porous implants improves bone in-growth and interface attcahcment strength, *Journal of Biomedical Materials Research*, **26**, 989-1001.

Cromer, D.T., and Herrington, K. (1955) The structures of anatase and rutile. *Journal of the American Chemical Society*, **77**, 4708-4709.

Cui, X., Kim, H.M., Kawashita, M., Wang, L., Xiong, T., Kokubo, T. and Nakamura, T. (2010) Apatite formation on anodized Ti6Al4V alloy in simulated body fluids, *Metallic Materials International*, **16**, 407-412.

Cullinane, D.M. & Salisbury, K. T. (2004) Biomechanics. IN HOLLINGER, J. O.,EINHORN, T. A., DOLL, B. A. & SFEIR, C. (Eds.) *Bone Tissue Engineering.* BocaRaton (US), CRC Press, p. 261-263.

Czarderna, A.W., Rao, C.N.R., and Honig, J.M. (1958) The anatase-rutile transition kinetics of the transformation of the anatase phase, *Transactions of the Faraday society*, **54**, 1069-1073.

D'Lima, D., Lemperle, S., Chen, D., Holmes, R., and Colwell, C.J. (1998) Bone response to implant surface morphology. *Journal of Arthroplasty*, **13**, 928-934.

Daculsi, G., LeGeros, R.Z., Nry, E., Lynch, K. and Kerebel, B. (1989) Transformation of biphasic calcium phosphate ceramics *in vivo*; ultrastructural and physicochemical characterization. *Journal of Biomedical Materials Research*, **23**, 883-894.

Dadash, M.S., Esfahanz, M.N., Ebrahimi, R., Karbasi, S. and Vali, H. (2010) A comparative study on mechanical and adhesion properties of calcinated and non-calcinated nano bioglass-titania nona composite coatings on stainless steel substrates, *Transations F: Nanotechnology,* **12,** 66-72.

Dattani, R. (2007) Femoral osteolysis following total hip replacement. *Postgraduate Medical Journal*, **83**, 312-316.

Davies, J.T and Rideal, E.K. (1961) *Interfacial Phenomena*, Academic, New York.

Davies, L., Daza, L. and Grange, P. (1995) Synthesis of zirconium oxide by hydrolysis of zirconium alkoxide, *Journal of Materials Science*, **30**, 5087-5092.

de Groot. K., Geesink,R., Klein.C.P.A.T., and Serekian.P (1987) Plasma sprayed coatings of hydroxlapatite. *Journal of biomedical materials research*, **21**, 1375-1381.

de Groot, K., Wolke, J.G.C and Jansen ,J.A. (1998) Calcium phosphate coatings for medical implants. *Proceedings of the institute of mechanical engineers*, **212**, 137-147.

De la Mora, J.F. (1992) The effect of charge emission from electrified liquid cone. *Journal of Fluid Mechanics*, **243**, 561-574.

De la Mora, J.F., and Loscertales, I.G. (1994) The current emitted by highly conducting Taylor cones. *Journal of Fluid Mechanics*, **260**, 155-184.

De With, G., Van Dijk, H.J.A., Hattu, N. and Prijs, K. (1981) Preparation, microstructure and mechanical properties of dense polycrystalline hydroxyapatite. *Journal of Materials Science*, **16**, 1592-1598.

DeJun, K., Dan, L., Zhang, W.Y. and Zheng, Z.C. (2012) Mecanical properties of hydroxyapatite-zirconia coatings prepared by magnetron-sputtering. *Transactions of the Non-ferrous Metal Society of China*, **22**, 104-110.

Depprich, R., Zipprich, H., Ommerborn, M., Noujok, C., Wiesmann, H.P., Krattanvorncharoen, S., Lauer, H.C., Meyer, U., Kubler, N.R. and Handschel, J. (2008) Osseointegration of zirconia implants compared with titanium; an *in vivo* study, *Head and Face Medicine*, **4**, 30-37.

Derbyshire, B., Fisher, J., Dowson, D., Hardaker, C. and Brummitt, K. (1994) Comparative study of the wear of UHWPWE with zirconia ceramic and stainless steel femoral heads in artificial hip joint, *Medical Engineering and Physics*, **18**, 229-236.

Desagne, I., Basle, M.F, Demais, V., Huri, G., Lesourd, M., Grolleau, B., Mercier, L. and Chappard, D. (1999) Effect of roughness, fibronectin and vitronectin on attachment, spreading and proliferation of human osteoblast-like cells (SaOS-2) on titanium surfaces. *Calcified Tissue International*, **6**, 499-507.

Ding, S.J., Lee, T.L. and Chu, Y.H (2003) Environmental effect on bond strength of magnetron-sputtered hydroxyapatite/titanium coatings. *Journal of Materials Science Letters,* **22**, 479-482.

Ding, S.J., Ju, C.P. and Lin, J.H.C. (1999a) Characterization of hydroxyapatite and titanium coatings sputtered on Ti6Al4V substrate. *Journal of Biomedical materials research*, **44A**, 266-279.

Ding S.J., Ju C.P and Lin J.H.C (1999b) Immersion behaviour of RF-magnetron assisted sputtered hydroxyapatite/titanium coatings in simulated body fluid. *Journal of biomedical materials research*, **47B**, 551-563.

Duan, G., Zhang, C., Li, A., Yang, X., Lu, L. and Wang, X. (2008) Preparation and characterization of mesoporous zirconia made by using poly (methyl methacrylate) template, *Nanoscale Research Letters*, **3**, 118-122.

Ducheyne, P. and Healy, K. (1988) The effect of plasma sprayed calcium phosphate ceramic coatings on the metal ion release from porous titanium and cobalt chromium alloys. Journal of Biomedical Materials Research, **2**, 1137-1163.

Ergun, C., Doremus, R. and Lanford, W. (2003) Hydroxylapatite and titanium: interfacial reactions. Journal of Biomedical Materials Research, **65A**, 336-343.

Feng, B., Weng, J., Yang, B.C., Qu, S.X., and Zhang, X.D. (2003) Characterization of surface oxide films on titanium and adhesion of osteoblasts. *Biomaterials*, **24**, 4663-4670.

Fernandez-Pradas, J.M., Cleries, L., Martinez, E., Sardin, G., Esteve, J. and Morenza, J.L (2001) Influence of thickness on the properties of hydroxyapatite coatings deposited by KrF laser ablation,.*Biomaterials*, **22**, 2171-2175.

Fernandez-Pradas, J.M., Cleries, L, Sardin, G. and Morenza, J.L. (2002) Characterisation of Calcium Phosphate coatings deposited by Nd:YAG laser ablation at 355nm:Influence of thickness,. *Biomaterials*, **23**, 1989-1994.

Filliagi, M.J., Coombs, N.A. and Pilliar, R.M. (1991) Characterisation of the interface in the plasma sprayed HA coating/Ti-6Al-4V implant system. *Journal of Biomedical Materials Research*, **25**, 1211-1229.

Filiaggi, M. J., Pilliar, R.M, and Coombs, N.A. (1993) Post-plasma-spraying heat treatment of the HAcoating/Ti-6Al-4V implant system. *Journal of Biomedical Materials Research*, **27**, 191-198.

FDA Calcium Phosphate (CaP) coating draft guidance for preparation of FDA submissions for orthopaedic and dental endosseous implants, Washington DC, *Food and drug administration*, 1992, 1-14.

Francheschi, R.T., James, W.M. & Zerlough. Dihydroxyvitamin D3 specific regulation of growth, morphology and fibronectin in a human osteosarcoma cell line. *Journal of Cellular Physiology* **123**: 401-409.

Frauchiger, V.M., Schlottig, F., Gasser, B. and Textor, M. (2004) Anodic plasma chemical treatment of CP titanium surfaces for biomedical applications. *Biomaterials*, **25**, 593-606.

Frayssinet, P., Torrene, F., Rouquet, N., Conte, P., Delga, C. and Bonel, G. (1994) Comparative biological properties of HA plasma sprayed coatings having different crystallinites, *Journal of Materials Science; Materials in Medicine*, **5**,11-17.

Fu, L., Khor, K.A. and Lim, J.P. (2001) Processing, microstructure and mechanical properties of yttria stabilized zirconia reinforced hydroxyapatite coatings. *Materials Science and Engineering A*, **316** , 46–51.

Fu, L., Khor, K.A. and Lim, J.P. (2001) The evaluation of powder processing on microstructure and mechanical properties of hydroxyapatite(HA)/yttria stabilized zirconia(YSZ)composite coatings, *Surface and Coatings Technology*, **140**, 263-268.

Furlong, R.J. and Osborn, J.F. (1991) Fixation of hip prostheses by Hydroxyapatite ceramic coatings. *Journal of Bone and Joint surgery*, **73B**, 741-745.

Gahlert, M., Gudehus, T., Eichorn, S., Stainhauser, E., Kniha, H. an Erhardt, W. (2007) Biomehcanical and histomorphometric comparison between zirconia implants with varying surface textures and a titanium implant in the maxilla of miniature pigs. *Clinical Oral Implants Research*, **18**, 662-668.

Gahlert, M., Rohling, S., Weiland, M., Sprecher, C.M., Kniha, H. and Milz, S. (2009) Osseointegration of zirconia and titanium dental implants; a histological and histomorphometrical study in the maxilla of pigs, *Clinical Oral Implants Research*, **20**, 1247-1253.

Ganan-Calvo, A.M., Lasheras, J.C., Davila, J., and Barrero, A (994) The electrostatic spray emitted from an electrified meniscus. *Journal of Aerosol Science*, **25**, 1121-1142.

Ganan-Calvo, A.M., Davila, J. and Berrero A. (1997) Current and droplet size in the electrospraying of liquids; scaling laws, *Journal of Aerosol science*, **28**, 249-275.

Geesink, R., de Groot, K.,and Klein, C.P.A.T. (1987) Chemical implant fixation using Hydroxylapatite coatings, *Clinical Orthopaedics*, **225**, 147-170.

Geethalakshi, K., Prabharan, T. and Hemalatha J. (2012) Dielectric studies on nano zirconium dioxide synthesized through co-precicpitation process, *World Academy of Science, Engineering and Technology*, **64**, 179-182.

Ghimbeu, C.M., Van Landschoot, R.C., Schoonman, J. and Lembreras, M. (2007) Preparation and characterization of SnO_2 and Cu-doped SnO_2 thin films using electrostatic spray deposition (ESD). *Journal of the European Ceramic Society*, **27**, 207-213.

Goff, J.P., Hayes, W. Hull, S., Hutchings, M.T. and Clausen, K.N. (1999) Defect structure of yttria-stabilized zirconia and its influence on the ionic conductivity at elevated temperatures. *Physics Reviews B*, 59, 14202–14219.

Gonzalez, J.E.G and Mirza-Rosca, J.C. (1999) Study of the corrosion behaviour of titanium and some of its alloys for biomedical and dental implant application,*Journal of Electroanalytical Chemistry*, **471**, 109-115.

Goodman, S.B., Ma, T., Chiu, R., Ramachandran, R. and Smith, R.L. (2008) Effects of orthopaedic wear particles on osteiprogenitor cells, *Biomaterials*, **27**, 6096-6101.

Goske, J., Muller, T.,Kachler, W., Holzwarth, U., Zeiler, G. and Schuh, A. in Pechion L(ED), 2004, Surface characterisation of shot peened implants with glass beads in total hip arthroplasty Applied mineralogy, Sao Paolo, 199-206.

Grace, J.M., and Marijnissen, J.C.M. (1994) A review of liquid atomization by electrical means. *Journal of Aerosol Science*, **25**, 1005-1019.

Granados-Correa, F., Bonifacio-Martinez, J., and Serrano-Gomez, J. (2010) Synthesis and characterization of calcium phosphate and its relation to CR(VI) adsorption properties, *Revista Internacial de Contaminacion Ambiental*, **26**, 129-134.

Gross, K.A, Berndt, C.C and Herman, H. (1998) Amorphous formation in plasma sprayed Hydroxyapatite coatings. *Journal of Biomedical Materials Research*, 39, 407-414.

Gu, Y.W., Khor, K.A, and Cheang, P. (2003) In vitro studies of plasma-sprayed hydroxyapatite/Ti-6Al-4V composite coatings in simulated body fluid (SBF). *Biomaterials*, **24**, 1603–1611.

Gu, Y.W., Khor, K.A., Pan, D. and Cheang, P. (2004), Activity of plasma sprayed yttria stabilized zirconia reinforced hydroxyapatite/Ti–6Al–4V composite coatings in simulated body fluid, *Biomaterials*, **25**, 3177–3185.

Guleryuz, H. and Cimenoglu, H. (2003) Effect of thermal oxidation on corrosion and corrosion wear of Ti6Al4V alloy, *Biomaterials*, **25**, 3325-3333.

Güleryüz, H. and Lu, H.C. (2004) Effect of thermal oxidation on corrosion and corrosion–wear behaviour of a Ti–6Al–4V alloy, *Biomaterials,* **25**, 3325-3333.

Haman, J.D., Lucas, L.C. and Crawmer, D. (1995) Characterization of high velocity oxy-fuel combustion sprayed hydroxyapatite, *Biomaterials*, **16**, 229-237.

Hanawa, T., Koh, M., Doi, H., Uai, H., Murakami, K. and Hamanaa, H. (1998) Amount of hydroxyl radical on calcium ion implanted titanium and point of zero charge of consistent oxide of the surface modified layer. *Journal of Materials Science: Materials in Medicine*, **9**, 89-92.

Harman, J.P, Chittur, K.K., Crawmer, D.E. and Lucas, L.C., (1999) Analytical and mechanical testing of high velocity oxy-fuel thermal sprayed and plasma sprayed calcium phosphate coatings, *Journal of Biomedical Materials Research B; Applied biomaterials*, **48**, 856-860.

Hamdi, M. and Ektessabi. A.M. (2001) Electron beam deposition of thin bioceramic film for biomedical implants*. Thin Solid films*, **398-399**, 385-390.

Han, Y., Nan, J., Xu, K. and Lu, J. (1999) Residual stresses in plasma sprayed hydroxyapatite coatings. *Journal of Materials Science Letters*, **18**, 1087-1089.

Han, Y., Fu, T., Lu, J. and Xu, K. (2000) Characterisation and stability of hydroxyapatite coatings prepared by an electrodeposition and alkaline treatment process. *Journal materials research A,* **54**, 96-101.

Han, Y, Hong, S.H. and Xu, K. (2003) Structure and in vitro bioactivity of titania-based films by micro-arc oxidation, *Surface and Coatings Technology*, **168**, 249-258.

Han, Y. and Xu, K. (2004) Photoexcited formation of bone apatite-like coatings on micro-arc oxidized titanium, *Journal of Biomedical Research*, **71A**, 608-614.

Harle, J., Ki, H.W., Mordan, N., Knowles, J.C. and Salih, V. (2006) Initial responses of human osteoblasts to sol-gel modified titanium with hydroxyapatite and titania composition, *Acta Biomaterialia*, **2**, 547-556.

Hartman, R. P. A., (1998) Electrohydrodynamic atomization in the cone-jet mode: from physical modeling to powder production. Netherlands organization for scientific research

Hartman, R.P.A., Brunner, D.J., Camelot, D.M.A., Marijnissen, J.C.M., and Scarlett, B. (1999) Electrohydrodynamic atomization in the cone-jet mode physical modeling of the liquid cone and jet. *Journal of Aerosol Science*, **30**, 823-849.

Hartman, R.P.A., Brunner, D.J., Camelot, D.M.A., Marijnissen, J.C.M., and Scarlett, B. (2000) Jet break-up in electrohydrodynamic atomization in the cone-jet mode. *Journal of Aerosol Science*, 31, 65-95.

Hasan, .M, Haseeb, A.S.M.A., Masjuki, H.H. and Saidur, R. (2010) Adhesion and wear behavior of nanostructured titanium oxide thin films. *International Journal of Mechanical and Materials Engineering*, **5**, 5-10.

Hayati, I., Bailey, A.I., and Tadros, F. (1987a) Investigations in to the mechanisms of Electrohydrodynamic spraying of liquids;Effect of electric field and the environment on pendant drops and factors affecting the formation of stable jets amd atomization. *Journal of Colloid and Interface Science,* **117**, 205-221.

Hayati, I., Bailey, A.I. and Tadros, F. (1987b) Investigations in to the mechanisms of Electrohydrodynamic spraying of liquids; Mechanism of stable jet formation and electrical forces acting on a liquid cone, *Journal of Colloid and Interface Science*, **117**, 222-230.

He, J., Zhou, W., Zhou, X., Zhong, X., Zhang, X. Wan, P., Zhu, B. and Chen, W. (2008) T he anatase phase of nanotopography titania plays an important role on osteoblast cell morphology and prpliferation, *Journal of Materials Science: Materials in Medicine*, **19**, 3465-3472.

Heimann, R.B., Kurzweg, H., Ivey, D.G. and Wayman, M.L. (1998) Microstructural and in vitro chemical investigations in to plasma sprayed bioceramic coatings. *Journal of Biomedical Materials Research B; Applied Biomaterials*, **43**, 441-450.

Heimann, R.B. (1999) Design of novel plasma sprayed hydroxyapatite bond coat bioceramic systems. *Journal of Thermal spray technology*, **8**, 597-603.

Heimann, R.B., Schürmann, N. and Müller, R.T. (2004) *In vitro* and *in vivo* performance of Ti6Al4V implants with plasma-sprayed osteoconductive hydroxylapatite–bioinert titania bond coat “duplex” systems: an experimental study in sheep. *Journal of Materials Science: Materials in Medicine,* **15**, 1045-1052.

Heimann, R.B. (2006) Thermal spraying of biomaterials. *Surface Coatings and Technology*, **20**, 2012-2019.

Heimann, R.B. and Wirth, R. (2006) Formation and transformation of amorphous calcium phosphates on titanium alloy surfaces during atmospheric plasma spraying and their subsequent in vitro performance. *Biomaterials***, 27**, 823-831.

Hench, L.L, Splinter, R.J. and Allen,. W.C (1971) Bonding mechanisms at the interface of ceramic prosthetic materials, *Journal of Biomedical Materials Research*, **2**, 117-141.

Hench, L.L. and Paschall, H.H. (1973) Direct chemical bond of bioactive glass-ceramicmaterials to the muscle, *Journal of Biomedical Materials Research*, **4**, 25-42.

Hench, L.L. (1991) Bioceramics from concept to clinic. *Journal of the American Ceramic Society*, **74,** 1487-1510.

Hench, L.L. (1998) Bioceramics. *Journal of the American Ceramic Society*, **81**, 1705-1728.

Hsu, H.C., Wu, S.C., Lin, C.H. and Ho, W.F. (2009a) Electrolytic deposition of hydroxyapatite coating on thermal treated Ti-40Zr. *Journal of Materials Science: Materials in Medicine*, **20**, 1825–1830.

Hsu, H.C., Wu, S.C., Yang, C.H., and Ho, W.F. (2009b) ZrO_2/hydroxyapatite coating on titanium by electrolytic deposition. *Journal of Materials Science; Materials in Medicine*, **20**, 615-619.

Hu, L., Yoko, T., Kozuko, H. and Sakka, S. (1992) Effects of solvent on properties of sol-gel derived TiO_2 coating films. *Thin Solid Films*, **219**, 18-23.

Huang, H.H., Ho, C.T., Lee, T.H, Lee, T.L., Liao, K.K, and Chen, F.L. (2004) Effect of surface roughness of ground titanium on initial cell adhesion, *Biomolecular Engineering***, 21**, 93-97.

Huang, P., Xu, K., and Han, Y. (2005) Preparation and apatite layer formation of plasma electrolytic oxidation film on titanium for biomedical application. *Materials Letters*, **59**, 185-189.

Hwang, B.H., Chang, C.L., Hsu, C.S. and Fu, C.Y. (2007) Electrostatic spray deposition of NiO/CGO films, *Journal of Physics D; Applied Physics*, **40**, 3448-3455.

Iglesias, T.P. and Peon-Fernandez, J. (2001) A mixing rule for the permittivity of binary mixtures in a frame work of a weak fluctuations model, *Journal of Materials Science Letters*, **20,** 1333-1334.

Im, K.H., Lee, S.B., Kim, K.M. and Lee, Y.K. (2007) Improvement of bonding strength to titanium surface by sol–gel derived hybrid coating of hydroxyapatite and titania by sol–gel process. *Surface & Coatings Technology*, **202,** 1135–1138.

Inadome, T., Hayashi, K., Nakashima, Y., Tsumura, H. and Sugioka, Y. (1995) Comparison of bone-implant interface shear strength of hydroxyapatite-coated and alumina coated metal implants, *Journal of Biomedical Materials Research*, **29**, 19-24.

ISO Implants for surgery: Coating for hydroxyapatite ceramics*, ISO*, 1996, 1-8.

Inagaki, M., Yokogawa, Y., and Kameyama, T. (2003) Formation of highly oriented hydroxyapatite in hydroxyapatite /titanium coatings by radio frequency thermal plasma spraying. *Journal of Materials Science; Materials in Medicine*, **14**, 919-922.

Itiravoving, P., Promasa, A., Laipraser, T., Techaponwara-Chai, T., Kuptniratsaikul, S., Thankakit, V. and Heimann, R.B. (2003) *Journal of the Medical Association of Thailand*, **86**, 5422.

Jaenicke, S., Chuan, G.K., Raju, V. and Nie, Y.T. (2008) Structural and morphological control in the preparation of high surface area zirconia, *Catalysis Surveys from Asia*, **12**, 153-169.

Jarcho,M. (1981) Calcium phosphate ceramics as hard tissue prosthetics*, Clinical Orthopaedics and Related Research*, **157**, 259-278.

Jarcho, M., Kay, J.F., Gumaer, K.I., Doremus, R.H, and Dorebeck, H.P. (1979) Tissue cellular and subcellular events at the bone-ceramic Hydroxyapatite interface. *Journal of Bioengineering*, **1**, 79.

Jasty, M., Maloney, W.J., Bragdon, C., O'Connor, D.O., Harve, T. and Harris, W.H. (1991) The initiation of failure in cemented femoral components of hip arthroplasties, *The Journal of Bone and Joint Surgery*, **73B**, 551-558.

Jaworek, A. and Krupa, A. (1999) Classification of the modes of EHD spraying. *Journal of Aerosol Science,* **30**, 873-893.

Jayasinghe, S. N., and Edirisinghe, M. J. (2002) Effect of viscosity on the size of relics produced by electrostatic atomization. *Journal of Aerosol Science*, **33**, 1379-1388.

Jayasinghe,S.N, and Edirisinghe, M.J (2004) Electrostatic atomisation of a ceramic suspension. *Journal of the European Ceramic Society*, **24**, 2203-2213.

Jeffcoat, M.K., McGlumpy, E.A., Reddy, M.S., Geurs, N.C. and Proskin, H.M. (2003) A comparison of hydroxyapatite (HA)-coated threaded, HA coated cylindric and titanium threaded endosseous dental implants. *International Oral and Maxillofacial Implants*, **18**, 406-410.

Ji,H., Ponton, C.B., and Marquis, P.M, (1992) Microstructural characterisation of Hydroxyapatite coatings on titanium, *Journal of Materials Science: Materials in Medicine*, **3**, 283-287.

Ji, H. and Marquis, P.M. (1993) Effect of heat treatment on the microstructure of plasma-sprayed hydroxyapatite coating. *Biomaterials*, **14,** 64-68.

Jones, A. R., and Thong, K. C. (1971) The production of charged monodisperse fuel droplets by electrical dispersion. *Journal of Physics D: Applied Physics,* **4**, 1159-1166.

Jung, K.T. and Bell, A.T. (2000) The effects of synthesis and pretreatment conditions on the bulk structure and surface properties. *Journal of Molecular Catalysis A: Chemical*, **163**, 27-42.

Kanbara, T. Yajima, Y. and Yoshinari, M. (2011) Wear behavior of tetragonal zirconia polycrystal versus titanium and titanium alloy*, Biomedical Materials*, **6**, 1-6.

Kanta, A., Sedeva, R. and Ralston, J. (2005) Thermally and photo-induced changes in the water wettability of low surface wettability of low surface area silica and titania*. Langmuir*, **21**, 2400-2407.

Kates, S.L, Kates, O.S. and Mendelson, D.A (2007) Advances in the medical management of osteoporosis, Injury. *International Journal of the Care of the Injured*, **383**, S17-S23.

Kaewwiset, W., Onreabroy, W. and Limsuwan, P. (2008) Effect of annealed temperatures on the morphology of TiO_2 films, *Kasetgart Journal of Natural Science*, **42**, 340-345.

Kieswetter, K., Schwartz, Z., Hummert, T.W., Cochran, D.L., Simpson, J. and Dean, D.D. (1996) Surface roughness modulates the local production of growth factors and cytokines by osteoblast-like MG63 cells, *Journal of Biomedical Materials Research*, **32**, 55-63.

Kelly, J.R. and Denry, I. (2007) Stabilized zirconia as a structural ceramic: An overview*, Dental Materials*, **1134**, 1-10.

Kemmitt, T., Al-Islam, N.I. and Gainsford, G.J. (2000) Isolation and structural characterization of triethanolamino-titanatranes: x-ray structures of partial hydrolysis condensates*, Inorganic Chemistry*, **39**, 6067-6071.

Kern, T., Yang, Y., Glover, R. and Ong, J.L. (2005) Effect of heat-treated titanium surfaces on protein adsorption and osteoblast precursor cell initial attachment. *Implant Dentistry*, **14**, 70-76.

Khor, K.A, Gu, Y.W,, Quek, C.H. and Cheang, P (2003) Plasma spraying of functionally graded hydroxyapatite-Ti–6Al–4V coatings*,.Surface and Coatings Technology*, **168,** 195-201.

Khor, K.A., Fu, L., Lim, V.J.P, and Cheang, P. (2000) The effects of ZrO_2 on the phase compositions of plasma sprayed HA/YSZ composite coatings. *Materials Science and Engineering*, **A276**, 160-166.

Khor, K.A., Gu, Y.W., Pan, D. and Cheang, P. (2004) Microstructure and mechanical properties of plasma sprayed HA/YSZ/Ti–6Al–4V composite coatings. *Biomaterials*, **25**, 4009–4017.

Kim, H.M., Miyaji, F., Kokubo, T, and Nakamura, T. (1999) Graded structure of bioactive titanium prepared by chemical treatment. *Journal of Biomedical Materials Research***, 45**, 100-107.

Kim, D.J., Hahn, H.S., Oh, S.H. and Kim, E.J. (2002) Influence of calcinations temperature on structural and optical properties of TiO_2 thin films prepared by sol-gel dip coating, *Materials Letters*, **57**, 355-360.

Kim, D.H., Kong, Y.M., Lee, S.H., Lee, I.S., Kim, H.E., Heo, S.J. and Koak, J.Y. (2003) Composition and crystallisation of hydroxyapatite coating layer formed by electron beam deposition. *Journal of American Ceramic Society*, **86**, 186-188.

Kim, H.W., Koh, Y.H., Li, L.H., Lee, S. and Kim, H.E. (2004) Hydroxyapatite coating on titanium substrate with titanium buffer layer processed by sol-gel method. *Biomaterials*, **25**, 2533-2538.

Kim, H.W., Kim, H.E., Salih, V. and Knowles, J.C. (2005) Hydroxyapatite and Titania Sol–Gel composite coatings on titanium for hard tissue implants; mechanical and *in vitro* biological performance, *Journal of Biomedical Materials Research B; Applied biomaterials*, **72B**, 1-8.

Kim, D.Y., Kim, M., Kim, H.E., Koh, Y.H., Kim, H.W. and Jang, J.H., (2009) Formation of hydroxyapatite within porous TiO_2 layer by micro-arc oxidation coupled with electrophoretic depsotion. *Acta biomaterialia*, **5**, 2196-2205.

Klein, C.P.A.T., Patka, P., Van der lubbe, Wolke, J.G.C and de Groot, K. (1991) Plasma sprayed coatings of tetracalcium, hydroxyl-apatite and alpha tcp on titanium alloy: an interface study, *Journal of Biomedical Materials Research*, **25**, 53-65.

Klein C.P.A.T., Wolke J.G.C., Blieck-Hogervorst, J.M.A., and de Groot, K.(1994) Calcium phosphate plasma sprayed coatings and their stability; an *in vivo* study. *Journal of Biomedical Materials Research*, **28,** 909-917.

Klokkevold, P.R., Nishimura, R.D., Adachi, M. and Caputo, A. (1997) Osseointegration enhanced by chemical etching of the titanium surface: a torque removal study in the rabbit, *Clinical Oral Implants Research*, **8,** 442-447.

Klokkevold, P.R., Johnson, P., Dadgostari, S., Caputo, A., Dadyostari, S., Caputo, A., Davies, J.E. and Nishimura, K.D. (2001) Early endosseous integration enhanced by dual acid etching of titanium: A torque removal study in the rabbit. *Clinical Oral Implants and Related Research*, **12**, 350-357.

Kokubo, T., Kim, H.M. and Kawashita, M. (2003) Novel bioactive materials with different mechanical properties. *Biomaterials*, **24**, 2161-2175.

Kokubo, T. and Takadama, H. (2006) How useful is SBF in predicting *in vivo* bone activity, *Biomaterials*, **27**, 2907-2915.

Koparde, V.N. and Cummings, P.T. (2005) Molecular dynamics simulation of titanium dioxide nanoparticle sintering. *Journal of Physics and Chemistry B*, **109**, 24280-24287.

Krishna, D.S.R., Breme, Y.L. and Sun, Y. (2001) Thick rutile on titanium for tribological applications. *Tribology International*, **40**, 329-334.

Kumazawa, H., Han, Y. and Sada, E. (1993) Synthesis of spherical zirconia fine particles by controlled hydrolysis of zirconium tetrabutoxide in 1-propanol, *The Chemical Engineering Journal*, **51**, 129-133.

Kuroda, K., Shida, H., Ichino, R. and Okido, M. (2001) Osteoconductivity of titania/hydroxyapatite composite films formed using pulse electrolysis, *Materials Transactions*, **48**, 321-331.

Kurzweg, H., Heimann, R.B., and Troczynski, T. (1998a) Adhesion of thermally sprayed hydroxyapatite bond coat systems measured by a novel peel test. *Journal of Materials Science; Materials in Medicine*, **9**, 9-16.

Kurzweg, H., Heimann, R.B., Trocynski, T. and Wayman, M.L. (1998b) Development of plasma-sprayed bioceramic coatings with bond coats on titania and zirconia. *Biomaterials*, **19**, 1507-1511.

Kweh, S.W.K, Khor, K.A. and Cheang, P. (2000) Plasma-sprayed hydroxyapatite (HA) coatings with flame-spheroidized feedstock; microstructure and mechanical properties. *Biomaterials*, **21**, 1223-1234.

Kweh, S.W.K., Khor, K.A. and Cheang P. (2002) *In vitro* investigation of plasma sprayed Hydroxyapatite (HA) coatings produced from flame sprayed feedstock. *Biomaterials*, **23**, 775-785.

Lahiri, D., Benaduce, A.P., Rouzaud, F., Solomon, J., Keshri, A.K., Kas, L. and Agatwal, A. (2011). Wear behavior and in vitro cytotoxicity of wear debris generated from hydroxyapatite-carbon nano-tube composite coating, *Journal of Biomedical Materials Research***, 96A**, 1-12.

Lajeunesse, D., Kiebzak, G.M., Frondoza, C.G. & Sacktor, B. (1991) Regulation of osteocalcin secretion by human primary bone cells and by the human osteosarcoma cell line MG-63. *Bone and Mineral* **14**: 237-250.

Lamy, D., Pierre, A.C. and Heimann, R.B. (1996) Hydroxyapatite coatings with a bond coat on biomedical implants by plasma projection. *Journal of Materials Research*, **11**, 680-686.

Lee, Y., Wang, C., Huang, T., Chen C., Kao, C. and Ding, S. (2005) *In vitro* characterisation of post-heat treated plasma sprayed hydroxyapatite coatings. *Surface Coatings and Technology*, **197**, 367-374.

Lee, E.J, Lee, S.H, Kim, H.W, Kong, Y.M and Kim, H.E.(2005) Fluoridated apatite coatings on Titanium obtained by electron beam deposition. *Biomaterials*, **26**, 3843-3851.

Lee, S.H, Kim, H.E. and Kim, H.W. (2007) Nano sized hydroxyapatite coatings on Ti substrate with TiO2 buffer layer by e-beam deposition. *Journal of the American Ceramic Society*, **90**, 50-56.

Leeuwenburgh, S.G.C, Wolke, J.G.C, Schoonman, J. and Jansen, J.A. (2003) Electrostatic spray deposition (ESD) of calcium phosphate coatings, *Journal of Biomedical Materials Research*, **66A**, 330-334.

Leeuwenburgh, S.G.C, Wolke, J.G.C, Schoonman, J. and Jansen, J.A. (2005) Influence of deposition parameters on morphological properties of biomedical calcium phosphate coatings prepared using electrostatic spray deposition. *Thin Solid Films*, **472**, 105-113.

Leeuwenburgh, S.G.C., Heine, M.C, Wolke, J.G.C, Pratsinis, S.E, Schoonman, J. and Jansen, J.A. (2006) Morphology of calcium phosphate coatings for biomedical applications deposited using electrostatic spray deposition. *Thin Solid Films*, 503, 69-78.

Lewis, G. (2000) Hydroxyapatite-coated bioalloy surfaces: current status and future challenges. *Biomedical Materials and Engineering*, **10**, 157-188.

Li, H., Khor, K.A. and Cheang, P. (2002) Titanium dioxide reinforced hydroxyapatite coatings deposited by high velocity oxy-fuel (HVOF) spray. *Biomaterials*, **23**, 85-91.

Li, H., Khor, K.A. and Cheang, P. (2002) Properties of heat treated calcium phosphate coatings deposited by high velocity oxy fuel spray (HVOF), *Biomaterials*, **23**, 2105-2112.

Li, H., Khor, K.A. and Cheang, P. (2003) Impact formation and microstructure and characterization of thermal sprayed hydroxyapatitetitania composite coatings, *Biomaterials*, **24**, 949-957.

Li, H., Khor, K.A., Kumar, R. and Cheang, P. (2004) Characterization of hydroxyapatite/nano zirconia composite coatings deposited by high velocity oxy-guel (HVOF) spray process, *Surface and Coatings Technology*, **182**, 227-236.

Li, L.H., Kim, H.W., Lee, S.H., Kong, Y.M. and Kim, H.E. (2005) Biocompatibility of titanium implants modified by micro-arc oxidation and hydroxyapatite coating, *Journal of Biomedical Materials Research A*, **11**, 48-54.

Li, X., Huang, J., Ahmad, Z. and Edirisinghe, M. (2007A) Electrohydrodynamic coating of metal with nano-sized Hydroxyapatite, *Biomedical Materials and Engineering*, **17**, 335-346.

Li, D., Marquez, M. and Xia, Y. (2007) Capturing electrified nano droplets under Rayleigh instability by coupling electrospray with a sol-gel reaction. *Chemical Physics Letters***, 445**, 271-275.

Li, X., Huang, J. and Edirisinghe, M. (2008) Development of nano-Hydroxyapatite coating by electrohydrodynamic atomisation spraying, *Journal of Materials Science; Materials in Medicine*, **19**, 1545-1551.

Liao, C., Lin, F., Chen, K. and Sun, J. (1999) Thermal decomposition and reconstitution of hydroxyapatite in air atmosphere, *Biomaterials*, **20**, 1807-1813.

Lim, V.J.P., Khor, K.A., Fu, L. and Cheang, P. (1999) Hydroxyapatite-zirconia composite coatings via the plasma spraying process. *Journal of Materials Processing Technology*. **89-90**, 491-496.

Lin, H., Xu, H., Zhang, X. and de Groot, K. (1998) Tensile tests of interface between bone and plasma sprayed HA coating-Titanium implant. *Journal of Biomedical Materials Research; Applied Biomaterials*, **43A**, 113-122.

Lin, C.M. and Yen, S.K. (2004) Characterisation and bond strength of electrolytic HA/TiO_2 double layers for orthopaedic applications, *Journal of Materials Science; Materials in Medicine*, **15**, 1237-1246.

Lin, C.M. and Yen, S.K. (2005) Characterisation and bond strength of electrolytic HA/TiO_2 double layers for orthopaedic applications, *Journal of Materials Science; Materials in Medicine*, **16**, 889-897.

Liu, J.Q., Luo, Z.S., Cui, F.Z., Duan, X.F. and Peng, L.M. (2000) High-resolution transmission electron microscopy investigations of a highly adhesive hydroxyapatite coating/titanium interface fabricated by ion-beam-assisted deposition. *Journal of Biomedical Materials Research*, **52**, 115–118.

Liu, J.X., Yang, D.Z., Shi, F. and Cai, Y.J (2003) Sol-gel deposited TiO2 on NiTi surgical alloy for biocompatibility improvement, *Thin Solid Films*, **429**, 225-230.

Liu., X., Chu.P.K., and Ding.C. (2004) Surface modification of titanium,titanium alloys,and related materials for biomedical applications. *Materials Science and Engineering*, **47**, 49-121.

Liu, F., Song, Y., Wang, F., Shimizu, T., Igarashi, and Zhao, L. (2005A) Formation, characterization of hydroxyapatite on titanium by microarc oxidation and hydrothermal treatment. *Journal of Bioscience and Bioengineering*, **100**, 100-104.

Liu, X., Zhoa, X., Fu, R.K.Y., Ho, P.Y.J, Ding, C. and Chu, P.K. (2005) Plasma-treated nanostructured TiO2 surface supported biomimetic growth of apatite, *Biomaterials*, **26**, 6143-6150.

Liu, X., Huang, A., Ding, C., and Chu, P. (2006) Bioactivity and cytocompatility of zirconia (ZrO_2) films is fabricated by cathodic arc deposition, *Biomaterials*, **27**, 3904-3911.

Liu, X., Zhao, X., Li, B., Cao, C., Dong, Y., and Chu, P.K. (2008) UV-Irradiation induced bioactivity on TiO_2 coatings with nanostructural surface, *Acta Biomaterialia*, **4**, 544-552.

Lu, Y.P, Zhu, S.T, Li, S.T., Song, Y.J., Li, M.S., and Lei, T.Q., (2003) Plasma sprayed graded titanium–hydroxyapatite coatings. *Materials Science and Technology*, **19**, 259-263.

Lu, Y.P., Song, Y.Z., Zhu, R.F., Li, M.S., and Lei, T.Q (2003) Factors influencing phase compositions and structure of plasma sprayed hydroxyapatite coatings during heat treatment, *Applied Surface Science*, **206**, 345-354.

Lugscheider, E., Knepper, M., and Heimberg, M. (1994) Cytotoxicity investigation of plasma sprayed calcium phosphate coatings. *Journal of Materials Science: Materials in Medicine,* **5,** 371-375.

Lynn, A.K. and DuQuesnay, D.L., (2002A) Hydroxyapatite-coated Ti6Al4V part 1: The effect of coating thickness on mechanical fatigue behavior. *Biomaterials*, **23**, 1937-1946.

Lynn, A.K., and DuQuesnay, D.L. (2002B) Hydroxyapatite-coated Ti6Al4V part 2: The effect of post deposition heat treatment at low temperatures. *Biomaterials*, **23**, 1947-1953.

Mahalingham, S. and Edirisinghe, M.J. (2007) Characterization of electrohydrodynamically prepared titanium dioxide films, *Materials Science and Processing; Applied Physics A*, **89**, 987-993.

Marinha, D., Rossignol, C., and Djurado, P. (2009) Influence of electrospraying parameters on the microstructure of $La_{0.6}$ $Sr_{0.4}$ $CO_{0.2}$ $F_{0.8}O_{3\alpha}$ films for SOFCs, *Journal of Solid State Chemistry*, **182**, 1742-1748.

Marinucci, L., Ballani, S., Becchetti, E., Belcastro, S. Guerra, M., Calvitti, M., Lilli C., Calvi, E.M., and Locci, P. (2005) Effect of titanium surface roughness on human osteoblast proliferation and gene expression *in vitro*. *The international Journal of Oral and Maxillofacial Implants*, **21**, 719-725.

Martin, J.Y., Schwartz, Z, Hummert, T.W., Schraub, D.M., Simpson, J., Lankford, J., Dean, D.D., Cochran, D.L., and Boyan, B.D. (1995) Effect of titanium surface roughness on proliferation, differentiation and protein synthesis of human osteoblast-lie cells (MG63). *Journal of Biomedical Materials Research*, **29**, 389-401.

Mathews, N.R., Morales, E.R., Cortes-Jacome, M.A., Antonio-Toledo, J.A (2009) TiO_2 thin films-influence of annealing temperature on structural, optical and photocatalytic properties, *Solar Energy*, **83**, 1499-1508.

Meesters, G.M.H., Vercoulen, P.H.W., Marijnissen, J.C.M., and Scarlett, B. (1992) Generation of micron-sized droplets from the Taylor cone. *Journal of Aerosol Science*, **23**, 37-49.

Mehotra, R.C. (1988), Synthesis and reactions of metal alkoxides. *Journal of Non-crystalline Solids*, **100**, 1-5.

Miao, P. Balachandran, W. and Xiao, P. (1999) Formation of ceramic thin films using electrospray in cone-jet mode, *Industry Applications Conference*, **4,** 2487-2493.

Miao, P. Balachandran, W. and Xiao, P. (2002) Formation of ceramic thin films using electrospray in cone-jet mode, *Industry Applications; IEEE Transactions*, **38**, 50-56.

Mohammadi, Z., Ziael-Moayyed, A.A. and Mesgar, A.S.M. (2007), Adhesive and cohesive properties by indentation method of plasma-sprayed hydroxyapatite coatings, *Applied Surface Science***, 253**, 4960-4965.

Morscher, E., Hefti, A. and Aedbi, O. (1998) Severe osteolysis after third body wear due to hydroxyapatite particle from acetabular cup coating, *Journal of Bone and Joint Surgery*, **80B**, 267-272.

Mu, Y., Kobayashi, T., Sumiat, M., Yamamoto, A. and Hanawa, T. (2000) Metal ion release from titanium with active oxygen species generated by rat macrophages *in vitro*. *Journal of Biomedical Materials Research*, **49**, 238-243.

Muller, R.T. and Patsalis, T. (1997) Shear and tensile strength of hydroxyapatite coating under loading conditions; an experimental study in dogs, *Archives of Orthopaedic Trauma and Surgery*, **116**, 334-337.

Mustafa, K., Wennerberg, A., Wroblewski, J., Huhenby, K., Lopez, B.S. and Arvidson, K. (2001) Determining optimal surface roughness of TiO_2 blasted titanium implant material for attachment, proliferation and differentiation of cells derived from human mandibular alveolar bone*, Clinical Oral Implants Research*, **12**, 515-525.

Mutoh, M., Kaieda, S., and Kamimura, K (1979) Convergence and disintegration of liquid jets induced by an electrostatic field. *Journal of Applied Physics*, **50**, 3174-3179.

Myer, K., (2003) Standard handbook of biomedical engineering and design, McGraw-Hill.

Neague, R., Perednis D., Princivalle A. and Djurado, E. (2005) Initial stages in zirconia coatings using ESD, *Chemistry of Materials*, **17**, 902-910.

Neagu, R., Perednis D., Princivalle A. and Djurado, E. (2006) Zirconia coatings deposited by electrostatic spray by electrostatic spray deposition. *Chemistry of Materials*, **16**, 3733-3739.

Nguyen, T. and Djurado, E. (2001) Deposition and characterization of nanocrystalline tetragonal zirconia films using electrostatic spray deposition. *Solid State Ionics*, **138**, 191-197.

Nie, X., Leyland, A. and Matthews, A. (2000), Deposition of layered bioceramic Hydroxyapaite and Titania coatings on Titanium alloys using a hybrid technique of micro-arc oxidation and electrophoresis. *Surface and Coatings Technology*, **125**, 407-414.

Niederberger, M.and Pinna, N. (2009) Metal oxide nanoparticles in organic solvents; synthesis, formation and assembly applications, Springer-Verlag London, LTD.

Ning, C.Y., Wang, Y.J., Chen, X.F., Zhao, N.R., Ye, J.D. and Wu, G. (2005) Mechanical performances and microstructural characteristics of plasma-sprayed bio-functionally gradient HA–ZrO_2–Ti coatings, *Surface and Coatings Technology*, **200**, 2403-2408.

Noymer, P.D and Garel, M. (2000) Stability and atomisation characteristics of electrohydrodynamic jets in the cone-jet and multi jet modes, *Journal of Aerosol Science*, **31**, 1165-1172.

Oliva, J., Oliva, A, an Oliva, J. D (2010) Five year success rate of 831 consecutively placed zirconia dental implants in humans: A comparison of the different rough surfaces, International *Journal of Oral and Maxillofacial Implants*, **25**, 336-344.

Olofinjana, A.O., Bell, J.M., and Jamting, A.K. (2000) Evaluation of the mechanical properties of sol-gel deposited titania films using ultra-micro indentation, method, *Wear*, **241**, 174-179.

Ong, J.L. and Lucas, L.C. (1994) Post deposition heat treatments for ion beam sputter deposited calcium phosphate coatings. *Biomaterials*, **15**, 337-341.

Ong, J.L., Carnes, D.L., and Bessho, K. (2004) Evaluation of titanium plasma-sprayed and plasma sprayed hydroxyapatite implants *in vivo*, *Biomaterials*, **25**, 4601-4606.

Osathanon, T., Bespinyowong, K., Arkornnuit, M., Takashi, H., and Pavasant, P. (2011) Human osteoblast-like cell spreading and proliferation on Ti-6Al-7Nb surfaces of varying roughness. *Journal of Oral Science*, **53**, 23-30.

Ozeki, K., Yuhta, T., Fukui, Y., Aoki, A. and Nishimura, I. (2002) A functionally graded titanium/ hydroxyapatite film obtained by sputtering, *Journal of Materials Science; Materials in Medicine,* **1**, 253-258.

Pan, J., Liao, H., Leygrof, C., Thierry, D., and Li, J. (1998) Variation of oxide films on titanium induced by osteoblast-like cell culture and the influence of an H_2O_2 pretreatment. *Journal of Biomedical Materials Research*, **40**, 244-256.

Park, J.B., (1979) Biomaterials: An introduction ,London, Plenum Press.

Park, J.B and Lakes, S. (1992) Biomaterials: an introduction, 2nd edition, Plenum press, New York.

Park, E., Condrate, R..A, Hoelzer, D.T., Fischman, G.S. (1998) Interfacial characterisation of plasma spray coated calcium phosphate on Ti-6AL-4V, *Journal of Materials Science; Materials in Medicine*, **9**, 643-649.

Park, J. and Lakes, R.S. (2001) Biomaterials, 3rd Edition, Springer science and business media, New York, NY, USA

Patsi, M.E., Hautaniemei, J.A., Rahiala, H.M, Peltola, T.O. and Kangashniemi, I.M.O (1998) Bonding strengths of tiania sol-gel derived coatings on titanium, *Journal of Sol-gel Science and Technology*, **11**, 55-66.

Piconni, C., and Maccauro, G. (1999) Zirconia as a ceramic biomaterial. *Biomaterials*, **20**, 1–25.

Pilliar, R.M. (1983) Powder metal-made orthopaedic implants with porous surface for fixation by tissue growth. *Clinical Orthopaedics and Related Research*, **176**, 42-51.

Pilliar, R.M., Lee, J.M. and Maniutopoulos, G. (1986) Observations on the effect of movement on bone ingrowrh in to metal surfaced implants, *Clinical Orthopaedics and Related Research,* **208**, 108-113.

Piveteau, L.D., Gasser, B. and Schlapbach, L. (2000) Evaluating of sol-gel titanium dioxide coatings containing calcium phosphate for m*et al* implant application. *Biomaterials*, **21**, 2193-2201.

Pradhan, S.S., Sahoo, S., and Pradhan, S.K. (2010) Influence of annealing temperature on the structural, mechanical and wetting properties of TiO_2 deposited y RF magnetron sputtering. *Thin Solid Films*, **518**, 6904-6908.

Princivalle, A., Perednis, D., Neagu, R., and Djurado, E. (2004) Microstructural investigations of nanostructured La(Sr)$MnO_{3-\sigma}$ films deposited by electrostatic spray deposition, *Chemistry of Materials*, **16**, 3733-3739.

Princivalle, A., Perednis, D., Neagu, R., and Djurado, E. (2005) Porosity control of LSM/YSZ cathode coating deposited by electrospraying. *Chemistry of Materials*, **17**, 1220-1227.

Qiu, S. and Kalita, S.J. (2006) Synthesis, processing and characterization of nano-crystalline titanium dioxide, *Materials Science and Engineering*, **4**, 435-436, 322-327.

Qiu, D., Wang, A. and Yin, Y. (2010) Characterization and corrosion behavior of hydroxyapatite/zirconia composite coating on NiTi fabricated by electrochemical deposition. *Applied Surface Science*, **257**, 1774-1778.

Radin, S.R. and Ducheyne, P. (1992) Plasma spraying induced changes of calcium phosphate ceramic charactersitics and the effect on *in vitro* stability. *Journal of Materials Science: Materials in Medicine*, **3**, 33-42.

Ramires, P.A., Romoito, A., Cosentino, F. and Milella, E. (2001) The influence of titania/hydroxyapatite composite coatings on the in vitro osteoblasts behavior. *Biomaterials*, **22**, 1467-1474.

Ratner, B.D., Hoffmann, A.S., Schoen, R.J. and Lemons, J.E. (2012) Biomaterials science: An introduction to materials in medicine, Acaemic Press.

Ravaglioli, A. and Krajewski, A. (1992) Bioceramics; materials, properties, applications, London, Chapman and Hall, 44-45.

Rayleigh, L. (1882) On the equilibrium of liquid conducting masses charged with electricity. *Philosophical Magazine*, **14**, 184-186.

Razaei, M., Alavi, S.M., Sahebdelfar, S., Yan, Z.F., Teunnisen, H., Jacobsen, J.H. and Sehested, J. (2007) Synthesis of pure tetragonal zirconium oxide with high surface area, *Journal of Materials Science*, **42**, 1228-1237.

Rehman, I. and Bonfield, W. (1997) Characterization of hydroxyapatite and carbonated apatite by photo acoustic FTIR spectroscopy. *Journal of Materials Science; Materials in Medicine*, **8**, 1-4.

Rho, J., Tsui, T.Y. and Pharr, G.M. (1997) Elastic properties of human cortical and trabecular lamellar bone measured by nanoindentation. *Biomaterials*, **18**, 1325-1330.

Rohanizadeh, R., LeGeros, R.Z., Harsono, M. and Bendavid, A. (2005) Adherent apatite coating on titanium substrate using chemical deposition. *Journal of Biomedical Materials Research*, **72A**, 428-438.

Rokkum, M.,Reigstad, A. and Johansson, C (2002) HA particles can be released from well-fixed HA coated stems histopathology of biopsies from 20 hips 2-8 years, *Acta Orthopaedica Scandinavica*, **73**, 298-306.

Rosell-Lampert, J. and Fernandez-De La Mora, J. (1994) Generation of mono-disperese 0.3-4 μm in diameter from electrified cone-jets of higher conducting and viscous liquids. *Journal of Aerosol Science*, **25**, 1093-1119.

Rupp, F., Scheideler, L.,Rehbein, D., Axmann, D. and Geis-Gerstorfer, J. (2004) Roughness induced dynamic changes of wettability of acid etched titanium implants. *Biomaterials*, **25**, 1429-1439.

Ruys, A.J., Zeigler, K.A., Standard, O.C., Brandwood, A., Milthorpe, B.K. and Sorrell, C.C. (1992) In Ceramics: Adding the Value, edited by M. J.Bannister (CSIRO, Melbourne, 1992) p. 605.

Sader, M.S., Balduino, A., Soares, G.D. and Barojevic, R. (2005) Effect of three distinct treatments of titanium surface on osteoblast attachment, proliferation and differentiation. *Clinical Oral Implants Research*, **16**, 667-675

Saeri, M.R., Afshar, A., Ghorbani, M., Ehsani, N. and Sorrell, C.C. (2003) The wet precipitation process of hydroxyapatite, *Materials Letters*, **57**, 4064-4069.

Sanchez, C., Livage, J., Henry, M. and Babonneau, F. (1998) Chemical modification of alkoxide precursors. *Journal of Non-crystalline Solids*, **100**, 65-76.

Santos, V., Zeni, M., Bergmann, C.P., and Hehemberger, J.M. (2008) Correlation between thermal and tetragonal/monoclinic nanostructured zirconia powder obtained by sol-gel process, *Reviews on Advanced Materials Science*, **17**, 62-70.

Sarkar, D., Mohapatra, D., Ray, S., Bhattacharyya, S., Adak, S. and Mitra, N. (2007) Synthesis and characterization of sol-gel derived ZrO_2 doped Al_2O_3 powder, *Ceramics International*, **33**, 1275-1282.

Sato, M., Aslani, A., Sambito, M.A., Kalkhoran, N.M., Slamovich, E.B., and Webster, T.J. (2008) Nanocrystalline hydroxyapatite/titania coatings on titanium improves osteoblast adhesion, *Journal of Biomedical Materials Research*, **84A**, 265-272.

Seal, B.L., Otero, T.C. and Panitch, A. (2001) Polymeric biomaterials for tissue and organ regeneration. *Materials Science and Engineering R-Reports*, **34**, 147-230.

Shea, J.E. and Miller, S.C. (2005) Skeletal function and structure; implications for tissue targeted therapeutics*. Advanced Drug Delivery Reviews*, **57**, 945-957.

Shui, J.L., Yu, Y. and Chen, C.H. (2006) Deposition conditions in tailoring the morphology of highly porous reticular films prepared by electrostatic spray deposition (ESD) technique. *Applied Surface Science*, **253**, 2379-2385.

Shukla, S. and Seal, S. (2003) Phase stabilization in non-crystalline zirconia. *Reviews on Advanced Materials Science*, **5,** 117-120.

Simse, S.J., Ayers, R.A and Bateman, T.A. (1997) Porous materials for bone engineering. In Liu, D-M and Dixit, V. (Eds) Porous materials for tissue engineering, Materials Science Forum, Switzerland, Trans-Tech Publications, 151-182.

Si, H.Y., Sun, Z.H., Wang, X., Zi, W.W. and Zhang, H.L. (2009) Voltage-dependent morphology, wettability and photo-current response of anodic porous titanium dioxide films. *Microporous and Mesoporous Materials*, **119**, 75-81.

Singh, A. and Mehotra, R.C. (2004) Novel heterometallic alkoxide coordination systems of polyols (glycols, di- and tri-ethanolamines) derivedfrom the corresponding homometallic moieties. *Coordination Chemistry Reviews*, **248**, 101-118.

Smith, D.P.H (1986) The electrohydrodynamic atomization of liquids, *IEEE Transactions on Industry Applications*, **1A-22**, 527-535.

Soballe, K., Hansen, E.S., Rasmussen, H.B., Jorgensen, P.H. and Bunger, C. (1992) Tissue ingrowth in titanium and hydroxyapatite-coated implants during stable and unstable mechanical conditions. *Journal of Orthopaedic Research*, **10**, 285-299.

Song, W.H., Jun, Y.K,. Han, Y. and Hong, S.H (2004) Biomimetic apatite coatings on micro-arc oxidized titania, *Biomaterials*, **25**, 3343-3349.

Sopyan, I., Mei, M., Ramesh, S., and Khalid, K.A. (2007) Porous hydroxyapatite for artificial bone applications. *Science and Technology of Advanced Materials*, **8**, 116-123.

Sousa, S.R and Barbosa, M.A., (1993) Corrosion resistance of Titanium in saline physiological solutions with Calcium Phosphate and proteins. *Clinical Materials*, **14**, 287-294.

Sousa, S.R. and Barbosa, M.A. (1995) The effect of Hydroxyapatite thickness on m*et al* ion release from stainless steel substrates. *Journal of Materials Science: Materials in Medicine*, **6**, 818-823.

Sousa, S.R., and Barbosa, M.A (1996) Effect of hydroxyapatite thickness on m*et al* ion release from Ti6Al4V substrates *Biomaterials,* **17**, 397-404.

Spikjsma, G.I, Seisenbaeva, G.A, Fischer, A., Boumweeste, H.J.M, Blank, D.H.A., and Kessler, V.G. (2009) The molecular composition of non-modified and acac-modified propoxide and butoxide precursors of zirconium and hafnium dioxides*. Journal of Sol-gel Science and Technology*, **51**, 10-22.

Stadlinger, B., Hennig, M., Eckelt, U., Kublisch, E. and Mai, R. (2010) Comparison of zirconia and titanium implants after a short healing period; A pilot study in mini pigs, *International Journal of Oral and Maxillofacial Surgery*, **39**, 585-592.

Su, M. and Wang, J. (2011) Preparation and humidity sensitivity of multi-layered zirconia thin films by sol-gel method. *Sensor Letters*, **9**, 670-674.

Subbarao, E.C. (1981) Zirconia-an overview. In: Heuer AH, Hobbs LW, editors. Science and technology of zirconia. Columbus, OH: The American Ceramic Society, 1–24.

Suchanek, W. and Yoshimura, M. (1998) Processing and properties of Hydroxyapatite-based bimaterials for use as hard tissue replacement implants, *Journal of Materials Research*, **13**, 94-115.

Sun, L.M., Berndt, C.C., Gross, K.A. and Kucuk, A. (2001) Material fundamentals and clinical performance of plasma sprayed hydroxyapatite coatings; A review. *Journal of Biomedical Materials Research*, **58**, 570-592.

Sun, L., Berndt, C.C., Khor, K.A., Cheang. H.N. and Gross. K.A. (2002) Surface characteristics and dissolution behaviour of plasma-sprayed hydroxyapatite. *Journal of Biomedical Materials Research***, 62**, 228-236.

Takeda, S. and Fukawa, S. (2005) The role of surface OH groups in surface chemical properties of metal oxide films. *Materials Science and Engineering B*, **119,** 265-267.

Tang, K., and Gomez, A. (1994) On the structure of an electrostatic spray of monodisperse droplets. *Physics of Fluids*, **6**, 2317-2332.

Tang, K., and Gomez, A. (1996) Monodisperse electrosprays of low electric conductivity liquids in the cone-jet mode. *Journal of Colloidal Interface and Science*, **184**, 500-511.

Tang, H., Guo, O.Y., Jia, D. and Zhou, Y. (2010) High bone-like apatite-forming ability of mesoporous titania films, *Microporous and Mesoporous Materials*, **131**, 366-372.

Taniguchi, I., Van Landschoot, R.C., and Schoonman, J. (2003) Fabrication of La1-xSrxCO1-yFeyO3 thin films by electrostatic spray deposition, *Solid State Ionics*, **156**, 1-13.

Taniguchi, I. and Hozokawa, T. (2008) Deposition of SDC and NIO-SDC thin films and their surface morphology control by electrostatic spray deposition, *Journal of Alloys and Compounds*, **460**, 464-471.

Taylor, G.I. (1964) Disintegration of water drops in an electric Field. *Proceedings of the Royal Society of London. Series A, Mathematical and Physical Science*, **280**, 383-397.

Teoh, S.H. (2004) Engineering matertials for biomedical applications, Singapore, World scientific.

Torchia, M.E., lassen, R.A. and Blanco, A.J. (1996) Total hip arthroplasty with cement inpatients less than twenty years old. *The Journal of Bone and Joint Surgery*, **78A**, 995-1003.

Tracey, B.M. and Doremus, R.H. (1984) Direct electron microscopy studies of the bone-hydroxylapatite interface, *Journal of Biomedical Materials Research*,**18**, 719-726.

Tsui, Y.C., Doyle, C. and Clyne, T.W. (1998) Plasma sprayed hydroxyapatite coatings on titanium substrates; part 1: mechanical properties and residual stress levels. *Biomaterials*, **19**, 2015-2029.

Uchida, M., Kim, H.M., Miyuji, F., Koubo, T. and Naamura, T. (2002A) Apatite formation on zirconium metal treated with aqueous NaOH, *Biomaterials*, **23**, 313-317.

Uchida, M, Kim, H.M., Kokubo, T., Tanaka, K. and Nakamura, T. (2002B) Structural dependence of apatite formation on zirconia gels in a simulated body fluid, *Journal of The Ceramic Society of Japan*, **110**, 710-715.

Uchida, M., Kim, H.M., Kokubo, T., Fujibayashi, S. and Nakamura, T. (2003) Structure dependence of apatite formation on titania gels in a simulated body fluid, *Journal of Biomdical Materials Research*, **64A**, 164-170.

Vaartstra, B.A, Huffman, J.C, Gradeff, P.S., Hubert-Pfalzdraf, L.G., Dabvan, J.C, Parraud, S., Yunlu, K. and Coulton, .G. (1990) Alcohol adductsof alkoxides. Intramolecular hydrogen bonding as a general structural feature. Inorganic Chemistry, 29, 3126-3131.

Van Blitterswijk, C.A., Grote, J.J., Kuypers, W., Daems, W.T. and de Groot. K. (1986) Macroport tissue in growth; a quantitative and qualitative study on hydroxyapatite ceramic. *Biomaterials,* **7**, 137-144.

Van Noort, R. (1987) Titanium: The implant material of today, *Journal of Materials Science*, **22**, 3801-3811.

Vandrovcova, M., Hanus, J., Drabi, M., Kylian, O., Biederman, H., Lisa, V. and Bacaova, L. (2012) Effect of different surface nano roughness of titanium dioxide films on the growth pf human osteoblast-like MG63 cells, *Journal of Biomedical Materials Research*, **100**, 1016-1032.

Verma, A., Basu, A., Bashi, A.K. and Agnihotry, S.A. (2005A) Structural,optical and electrochemical properties of sol-gel derived TiO_2 films; Annealing effects. *Solid State Ionics*, **176**, 2285-2295.

Verma, A., Sumanta, S.B., Baksh, A.K, and Agnihotry, S.A. (2005B) Effect of stabilizer on structural, optical and electrochemical properties of sol-gel derived TiO_2 films. *Solar Energy Materialls and Solar Cells*, **88**, 47-64.

Verma, A. and Agnihotry, S.A. (2007) Thermal treatment effe3ct on nanostructured TiO_2 films deposited using diethanolamine stabilized precursor sol. *Electrochemica Acta,* **52** , 2701-2709.

Verma, A., Kar, M., and Singh, D. (2010) Aging effect of diethanolamine derived precursor sol on TiO_2 films deposited at different annealing temperature. *Journal of Sol-gel Science and Technology*, **54**, 129-138.

Vogel, J., Russel, C., Gunther, G., Hartmann, P., Vizethum, F. and Bergner, N. (1996) Characterisation of plasma sprayed hydroxyapatite by P-MAS-NMR and the effect of subsequent annealing. *Journal of Materials Science: Materials in Medicine*, **7**, 495-499.

Wang, B.C., Lee, T.M., Chang, E. and Yang, C.Y. (1993) The shear strength and failure mode of plasma sprayed hydroxyapatite coating to bone: The effect of coating thickness, *Journal of Biomedical Materials Research*, **27**, 1315-1327.

Wang, H., Eliaz, N., Xiang, Z., Hsu, H.P., Spector, M., and Hobbs, L.W. (2006) Early bone apposition *in vivo* on plasma sprayed and electrochemically deposited hydroxyapatite coatings on titanium alloy, *Biomaterials*, **27**, 4192-4203.

Wang, G., Meng, F., Ding, C., Chu P.K., and Liu, X. (2010) Microstructure, bioactivity and osteoblast behavior of monoclinic zirconia coating with nanostructured surface. *Acta Biomaterialia,* **6**, 990-1000.

Ward, D.A. and Ko, E.E. (1993) Synthesis and structural transformation of zirconia aerogels. *Chemistry of Materials*, **5**, 956-969.

Wasa, K., Kitabatake, M. and Adachi, H. (2004) Materials technology; sputtering of compound materials, America, William Andrew Inc.

Watanabe, H., Sato, K., Kokubon, K., Saaki, H. and Yoshinari, M. (2012) Change in surface properties of zirconia and initial attachment of osteoblast-like cells with hydrophilic treatment, *Dental Materials Journal*, **31**, 806-814.

Wei, M., Ruys, A.J., Swain, M.V., Kim. S.H., Milthorpe, B.K. and Sorrell, C.C. (1999) Interfacial bond strength of electrophoretically deposited hydroxyapatite coatings on metals, *Journal of Materials Science; Materials in Medicine,***10**,401-409.

Wei, M., Ruys, A.J, Milthorpe, B.K., Sorrell, C.C., and Evans, J.H. (2001) Electrophoretic deposition of Hydroxyapatite coatings on metal substrates; a nanoparticulate dual coating approach, *Journal of Sol-gel Science and Technology*, **21**, 39-48.

Wei, M., Ruys, A.J., Swain, M.V., Milthorpe, B.K. and Sorrell, C.C. (2005) Hydroxyapatite – coated metals; interfacial reactions during sintering, *Journal of Materials Science: Materials in Medicine,* 16, 101-106.

Wen, J., Leng, Y., Chen, J. and Zhang., C. (2000) Chemical gradient in plasma-sprayed HA coatings, *Biomaterials,* **21**, 1339-1343.

Wen, C.E., Xu, W., Hu, W.Y. and Hodgson., P.D. (2007) Hydroxyapatite/titania sol–gel coatings on titanium–zirconium alloy for biomedical applications. *Acta Biomaterialia*, **3**, 403-410.

Weng, J., Liu, X., Zhang, X. and Ji, X. (1994) Thermal decomposition of Hydroxyapatite structure induced by Titanium and its dioxide. *Materials Science Letters*,**13,**159-161.

Weng, J., Liu,Q., Wolke, J.G.C. Zhang, X. and de Groot, K. (1997) Formation and characterics of the apatite layer on plasma-sprayed hydroxyapatite coatings in simulated body fluid. *Biomaterials*, 18, 1027-1035.

Wennerberg, A. (1998) The importance of surface roughness for implant incorporation, *International Journal of Machine Tools and Manufacture*, **38**, 657-662.

Wenzel, R.N. (1936) Resistance of solid surfaces to wetting by water. *Industrial and Engineering Chemistry*, **28**, 988-994.

Whitehead, R.Y., Lucas, L.C. and Lacefield, W.R. (1993) The effect of dissolution on plasma sprayed Hydroxyapatite coatings on titanium. *Clinical materials*, **12**, 31-39.

Widonia, J., Eiden-Assmann, S. and Maret, G. (1995) *European Journal of Inorganic Chemistry*, 3148-3155.

Wilert, H.G., Ludwig, J. and Semlits, C.G.M. (1974) Reaction of bone to methacrylate after hip arthroplasty; a long term gross, light microscopic and scanning electron microscope study. *Journal of Bone and Joint Surgery*, **86A**, 1368-1382.

Wilhelm, O., Madler, L., Pratsinis, S.E (2003) Electrospray evaporation and deposition. *Journal of Aerosol Science*, **34**, 815-836.

Willman, G. (1999), Coating of implants with hydroxyapatite-materials; connections between bone and metal, *Advances in Engineering Materials*, **1**, 95-105.

Wolke, J.GC., de Groot, K., and Jansen, J.A. (1998) Dissolution and adhesion behaviour of radio frequency magnetron sputtered CaP coatings, *Journal of Materials Science*, **33**, 3371-3376.

Xiao, X.F., Liu, R.F. and Zheng, Y.Z. (2005) Hydoxyapatite/titanium composite coating prepared by hydrothermal–electrochemical technique. *Materials Letters*, **59**,1660-1664.

Xiao, X.F., Liu, R.F. and Zheng, Y.Z., (2006) Hydrothermal-electrochemical codeposited hydoxyapatite/yttria-stabilized zirconia composite coating. *Journal of Materials Science,* **41***,* 3417-3424*.*

Xu, W., Hu, W.Y, Li, M.H., Ma, Q.Q., Hodgson, P.D. and Wen, C.E. (2006) Sol-gel derived HA/TiO_2 double coatings on Ti scaffolds for orthopaedics applications. *Transactions of the non-ferrous metals society of China,* **16**, 209-216.

Yamamoto, D., Kawai, I., Kuroda, K., Ichino, R., Okido, M. and Si, K.I (2011) Osteoconductivity of anodized titanium with controlled micron-level surface toughness*, Materials Transactions*, **52**, 1650-1654.

Yang, C.Y., Wang, B.C., Chang, E., and Wu, B.C. (1995) Bond degradation at the plasma-sprayed HA coating /Ti-6Al-4V alloy interface; an *in vitro* study. *Journal of Materials Science; Materials in Medicine*, **6**, 258-265.

Yang, C., Weng,. J, Chen, J.. Feng, J., Yang, Z. and Zhang, X. (1996) Water vapour treated hydroxyapatite coatings after plasma spraying and their characteristics. *Biomaterials,* **17,** 419-424.

Yang, Y.C. and Chang, E. (2001) Influence of residual stress on bonding strength and fracture of plasma sprayed hydroxyapatite coatings on Ti-6AL-4V substrate. *Biomaterials*, **22**, 1827-1836.

Yang, Y.C and Chang, E. (2003) The bonding of plasma sprayed hydroxyapatite coatings to titanium; the effect of processing, porosity and residual stress. *Thin Solid Films***, 444**, 260-275.

Yang, Y.C., Chang, E. and Lee, S.Y. (2003) Mechanical properties and young's modulus of plasma sprayed Hydroxyapatite coating on Titanium substrate in simulated body fluid, *Journal of Biomedical Materials Research,* **67A**, 886-899.

Yang, Y.C. and Chang, E. (2003) The bonding of plasma sprayed hydroxyapatite coatings to titanium; the effect of processing, porosity and residual stress. *Thin Solid Films*, **444**, 260-275.

Yang, C.W., Lee, T.M., Lui, T.S., and Chang, E. (2006) Effect of post vacuum heating on the microstructural feature and bonding strength of plasma-sprayed hydroxyapatite coatings. *Materials Science and Engineering C,* **26**, 1395 – 1400.

Yang, Y.C. (2007) Influence of residual stress on bonding strength of the plasma-sprayed hydroxyapatite coating after the vacuum heat treatment. *Surface & Coatings Technology*, **201**, 7187–7193.

Yankee, S.J., Pletka, B.J. and Salsbury, L. (1991) Quality control of hydroxyapatite coating; the surface preparation stage in; Proceedings of the fourth national thermal spray conference, Pittsburgh PA, USA ,4-10 May, 475-479.

Yao, Z., Jiang, Y., Jiang, Z., Wang, F. and Wu, Z. (2008) Preparation and structure of ceramic coatings containing Zirconium oxide on Ti alloy by plasma electrolytic oxidation. *Journal of Materials Processing Technology,* **205**, 303-307

Yen, S.K., Chou, S.H., Wu, S.J., Chang, C.C., Lin, S.P. and Lin, C.M. (2006) Characterisation of electrolytic HA/ZrO_2 double layers coatings on TI6Al4V implant alloy, *Materials Science and Engineering C*, **26**, 65-77.

Yezek, L.; Rowell, R.L.; Larwa. M.and Chibowski, E. (1998) Changes in the zeta-potential of colloidal titanium dioxide after exposure to a radio frequency electric field using a circulating sample , *Colloids and surfaces. A, Physicochemical and engineering aspects*, **141**, 67-72

Yoldas, B.E. (1982) Effect of variations in polymerized oxides on sintering and crystalline transformations. *Journal of the American Ceramic Society*, **65**, 387-393.

Yue, S., Pilliar, R.M. and Weatherly, G.C,. (1984) The fatigue strength of porous coated Ti6Al4V implant alloy, *Journal of Biomedical Materials Research*,**18**,1043-1058.

Zeleny, J. (1914) The electrical discharge from liquid points and a hydrostatic method of measuring the electric intensity at their surfaces. *The Physical Review*, **3**, 69-91.

Zeleny, J. (1915) On the conditions of instability of electrified drops, with applications to the electric discharge from liquid points. *Proceedings of the Cambridge Philosophical Society,* **18**, 17-24.

Zeleny, J. (1917) Instability of electrified liquid surfaces. *The Physical Review* **17**, 1-8.

Zhang, T., Gawne D.T, and Bao.Y (1997) The influence of process parameters on the degradation of thermally sprayed polymer coatings, *Surface Coatings and Technology*, **96,** 337-344.

Zhang, Q., Chen, J., Feng, J., Cao, Y., Deng, C. and Zhang, X. (2003) Dissolution and mineralisation behaviours of HA coatings. *Biomaterials*, **24**, 4741-4748.

Zhang, S., Xianting, Z., Yongsheng, W., Kui, C., and Wenjian, W., (2006) Adhesion strength of sol–gel derived fluoridated hydroxyapatite coatings, *Surface & Coatings Technology*, **200**, 6350–6354.

Zhang, S., Sun, J., Xu, Y., Qian, S., Wang, B., Liu, F. and Lie, X. (2012) Biological behavior of osteoblast-like cells on titanium and zirconia films deposited by cathodic arc deposition. *Biointerphases*, **7**, 1-4.

Zhang, S., Sun, J., Xu, Y., Qian, S., Wang, B., Liu, F. and Lie, X. (2012) Biological behavior of osteoblast-like cells on titanium and zirconia films deposited by cathodic arc deposition. *Biointerphases*

Zheng, X., Huang, M., Ding, C., (2000) Bond strength of plasma-sprayed hydroxyapatite/Ti composite coatings, *Biomaterials*, **21**, 841-849.

Zhao, J., Fan, W., Wu, D. and Sun, Y. (2000) Synthesis of highly stabilized zirconia sols from zirconia n-propoxide –diglycol system, *Journal of Non-crystalline Solids*, **261**, 15-20.

Zhao, Z.W. and Tay, B. (2006) Study of nanorystal TiO_2 thin films by thermal annealing. *Journal of Electroceramics*, **16**, 489-493.

Zhao, Y.T., Zhang, Z., Dai, Q.X., Lin, D.Y. and Li, S.M. (2006) Microstructure and bond strength of HA(+ZrO2+Y2O3)/Ti6Al4Vcomposite coatings fabricated by RF magnetron sputtering, *Surface & Coatings Technology*, **200**, 354 – 536.

Zhao, Y., Xiong, T. and Huang, W. (2010) Effect of heat treatment on bioactivity of anodic titania films, *Applied Surface Science*, **256**, 3073-3076.

Zykova, A., Safonov, V., Smolik, J., Rogowska, R. Lukiyanchenko, R., Vyrva, O. and Yakorin, S. (2012) The corrosion properties of zirconium and titanium load-bearing implant materials with protective oxide coatings, 13th International Conference on Plasma Surface Engineering, September 10-14 2012, Garmish-Parten Kirchen, Germany, 388-391.